Control of instabilities and turbulence by fast particles in fusion plasmas

Jean-Baptiste Girardo

▶ **To cite this version:**

Jean-Baptiste Girardo. Control of instabilities and turbulence by fast particles in fusion plasmas. Plasma Physics [physics.plasm-ph]. Ecode doctorale de l'Ecole Polytechnique (EDX), 2015. English. NNT : . tel-01276865

HAL Id: tel-01276865

https://pastel.hal.science/tel-01276865

Submitted on 20 Feb 2016

HAL is a multi-disciplinary open access archive for the deposit and dissemination of scientific research documents, whether they are published or not. The documents may come from teaching and research institutions in France or abroad, or from public or private research centers.

L'archive ouverte pluridisciplinaire **HAL**, est destinée au dépôt et à la diffusion de documents scientifiques de niveau recherche, publiés ou non, émanant des établissements d'enseignement et de recherche français ou étrangers, des laboratoires publics ou privés.

Control of instabilities and turbulence by fast particles in fusion plasmas

Thèse présentée par
Jean-Baptiste Girardo

en vue d'obtenir le titre de
Docteur de l'École Polytechnique

Soutenue le 11 septembre 2015 à Cadarache

Pr Yanick Sarazin	Institut de Recherche sur la Fusion par confinement Magnétique (IRFM, Cadarache, France)	Directeur de thèse
Dr Rémi Dumont	Institut de Recherche sur la Fusion par confinement Magnétique (IRFM, Cadarache, France)	Responsable CEA
Pr Boris Breizman	Université du Texas à Austin (UT, Austin, Etats-Unis)	Rapporteur
Dr Philipp Lauber	Institut Max Planck de recherche en Physique des Plasmas (IPP, Garching, Allemagne)	Rapporteur
Pr Peter Beyer	Aix-Marseille Université (AMU, Marseille, France)	Examinateur
Dr Xavier Garbet	Institut de Recherche sur la Fusion par confinement Magnétique (IRFM, Cadarache, France)	Examinateur
Dr Sergei Sharapov	Centre de recherche de Culham sur l'Energie de Fusion (CCFE, Culham, Royaume-Uni)	Examinateur
Pr Jean-Marcel Rax	École Polytechnique (l'X, Palaiseau, France)	Président du jury

Octobre 2012 - Septembre 2015

Remerciements

Pendant les trois années de travail qui ont été nécessaires pour réaliser cette thèse, j'ai été formidablement aidé et soutenu par ma famille, mes amis, collègues et encadrants. Je leur suis profondément reconnaissant.

Je souhaiterais ici remercier / I here wish to thank

- the referees and members of the jury: Boris Breizman, Philipp Lauber, Rémi Dumont, Yanick Sarazin, Peter Beyer, Xavier Garbet, Sergei Sharapov and Jean-Marcel Rax ;
- mes encadrants à Cadarache: Rémi Dumont, Yanick Sarazin et Xavier Garbet ;
- l'Ecole Doctorale de l'Ecole Polytechnique (EDX) ;
- the fusion scientists with whom I worked at Cadarache, JET or elsewhere, in particular Sergei Sharapov, Jurrian Boom, Jacob Eriksson, Michael Fitzgerald, Nick Hawkes, Vasily Kiptily, Ivan Lupelli, Mervi Mantsinen, Mireille Schneider, Fulvio Zonca ;
- la hiérarchie de l'IRFM et du SCCP[1], notamment Alain Bécoulet, Jean-Michel Bernard, Nathalie Borio, Tuong Hoang, Valérie Icard, Emmanuel Joffrin, Clément Laviron, Xavier Litaudon, Pascale Monier-Garbet ;
- les collègues et amis stagiaires, thésards, post-docs, permanents que j'ai cotoyés durant ces trois années, notamment Alberto, Alexandre F., Alexandre S., Antoine, Axel, Billal, Camille, Chantal, Charles, Claudia, Clément, Clothilde, Cristian, Damien, David M., David Z., Davide, Didier, Dmitri, Dmitro, Emelie, Etienne, Fabien, Farah, François, Francesco, Frédric, Gabor, Grégoire, Guillaume, Guilhem, Hugo A., Hugo B., Jae-Heon, James, Jean-Claude, João, Johnny, Julien, Joan, Jorge, Laurent C., Laurent V., Ling-Feng, Marina, Maxim, Mervat, Nicolas F., Nicolas N., Olivier F., Olivier T., Patrick M., Patrick T., Peter, Pierre, Philippe, Roland, Romain, Thomas, Tuomas, Vianney, Virginie, Walid, Yves, Yue ;

[1] Service Chauffage et Confinement du Plasma

- toute l'équipe BIPS[1], qui m'a accueilli lors de mon arrivée chez Fusion for Energy ;
- le corps des Mines, qui m'a soutenu dans ma démarche, notamment Yannick d'Escatha, Marie-Solange Tissier, Pierre-Edouard Gille, Jérôme Gosset, Aurélie Gracia, Etienne Hans, Isabelle Vallet ;
- mes amis, notamment Alban, Aliénor et Pierre, Anne, Adrien, Timothée et Etienne, Antoine, Anton, Audrey, Baptiste et Irina, Benjamin, Benoit, Bernard, Blandine et Cyril, Clément, Damien, Edouard, Emmanuel, Julie, Malik, Marie, Martin, Nicolas, Norman, Pierre-Etienne, Rafik, Raphaël, Sara et Valentin, Sébastien, Simon, Valentine, Xavier, Xin ;
- ma famille : Papa, Maman, Pépé, Mémé, Papaï, Mamany, Claudine, ainsi que notamment Tati, Yves et Marie, Jacques et Malou, Noëlle et Albert, Catherine et Daniel, Thierry et Véronique.

Je prie par avance tous ceux que j'aurais pu bien involontairement oublier d'accepter mes excuses.

[1] Buildings, Infrastructure and Power Supplies project team

Table of Contents

List of Figures

List of Tables

Foreword

The present PhD thesis addresses the interaction of fast particles with instabilities and turbulence in fusion plasmas. We focus on three types of instabilities: the internal kink mode, which underlies sawtooth activity in tokamaks, the Energetic particle driven Geodesic Acoustic Mode (EGAM), and the Ion Turbulent Gradient (ITG) modes, which underlie turbulence. The interaction of fast particles with sawteeth and turbulence is considered under the angle of stability control: how can fast particle provide mitigation of those processes?

Fast particles in tokamaks are born from three main sources: Neutral Beam Injection (NBI), Ion Cyclotron Resonant Heating (ICRH) and alpha particles. Out of those sources, the first two can be, to some extent, controlled by the operator. They may be used on purpose to damp or excite plasma instabilities.

Since studies published in the late 80s - early 90s [Coppi 1988, Coppi 1989, Porcelli 1991], it has been known that trapped fast particles can, through their interaction with the internal kink mode, modulate the frequency of sawteeth. Results from experiments carried out in JET (European tokamak located in the UK) showing such sawtooth stabilization are presented in the present manuscript. In those experiments, the fast particles are deuterons first accelerated by NBI to about 100 keV, and then accelerated by 3rd harmonic ICRH to energies in the MeV range. The effects of those fast particles on sawteeth are studied for the first time in JET with ITER-Like Wall (ILW). They are interpreted in the framework of Porcelli's model, and found to be strongly stabilizing, consistently with the observations. A 2.5 s long sawtooth is studied, a record duration for JET with ILW; during this sawtooth the plasma parameters, in particular the fast particle distribution and the q-profile, are remarkably stable in time. Explanations for the sawtooth crashes, while fast particle provided such stabilization, are discussed: in two of the four considered discharges, tornado modes, which are known to expel fast particles from the core plasma, are observed just before the crashes. In the other two discharges, the inward propagation of a cold front triggered by Edge Localized Modes (ELMs), and preceding the sawtooth crash, is observed.

The impact of fast particles on the internal kink mode, and therefore on sawteeth, is a direct effect: by pumping energy from the mode, or on the contrary yielding energy to it, the fast particles can damp or excite the instability. The impact of fast particles on ITG modes studied in the present manuscript, and therefore on turbulence, is of a different kind: it is indirect. Indeed, this interaction occurs through so called Energetic particle driven Geodesic Acoustic Modes (EGAMs), which are similar to Geodesic Acoustic Modes (GAMs). GAMs were discovered in the 60s [Winsor 1968]; they were later shown, in the 00s, to have interaction with drift wave modes [Hallatschek 2001, Jakubowski 2002, Ramisch 2003, Miyato 2004, Nagashima 2005, Angelino 2006, Miki 2007, Waltz 2008, Conway 2011, Sasaki 2012, Xu 2012]. In particular, it was found that under certain circumstances, they could mitigate turbulence. However, GAMs are not easily triggered nor controlled by an operator. EGAMs, on the contrary, are excited by fast particles and may thus, to some extent, be controlled by an operator. It has recently been shown in numerical simulations that EGAMs interact with turbulence [Zarzoso 2013]; however the nature of this interaction, and in particular whether EGAMs damp or excite ITG modes, remains to be established. The similarity between GAMs and EGAMs suggests that EGAMs should be able to mitigate ITG modes, at least in certain ranges of plasma parameters. Based on this remark, the excitation of EGAMs by fast particles, and the relation between GAMs and EGAMs, are studied analytically in the present thesis. This is the first part of the interaction of fast particles with turbulence. The second part is the impact of EGAMs on ITG modes, discussed in the present work through a non-linear three wave parametric decay model.

All the notations used in the present thesis are summarized in a dedicated section at the end of the manuscript.

Chapter 1

Introduction

In this chapter, we first recall the basic physics which governs nuclear fusion in magnetically confined plasmas, present the magnetic geometry of tokamaks, and give the main characteristics of particle orbits in such devices. Subsequently, we give a brief introduction to the fluid and gyrokinetic theories which allow one to model the plasma in conditions relevant for thermonuclear fusion. Finally, we detail a few conventions used in the present manuscript and which may not be universally acknowledged, and give the outline of the present manuscript.

The present chapter is largely based on well-established references: [Hazeltine 2003, Rax 2005, Rax 2011, Wesson 2011]. They will most of the time not be explicitly cited in the passages below.

1.1 A few words about nuclear fusion in tokamaks

We here briefly recall a few aspects of controlled nuclear fusion in tokamaks, based on [Hazeltine 2003, Rax 2005, Mora 2011, Rax 2011, Wesson 2011]. Other types of magnetic confinement machines, not described in the present manuscript, include linear mirror machines, stellarators and reversed field pinch machines.

1.1.1 Reaction rate - Cross sections

In a magnetic plasma made of two types of ions a and b, the rate N of reactions per time unit and per volume unit reads as follows:

$$N = n_a n_b \langle \sigma(v) v \rangle_v, \tag{1.1}$$

where n_a is the density of ions a, n_b is the density of ions b, σ is the cross section of the fusion interaction between the two species of ions, v is the relative velocity between two ions of species a and b, and $\langle ... \rangle_v$ means the average over v weighted by the corresponding

distribution function.

Figure 1.1 presents the evolution of the $\langle \sigma(v)v \rangle_v$ factor according to temperature for three couples of elements: deuterium - deuterium (D-D), deuterium - tritium (D-T) and deuterium - helium 3 (D-He3). To get the figure, a Maxwellian distribution function was used to compute $\langle ... \rangle_v$. For further elements about this computation, one can refer to [Wesson 2011] or [Mora 2011].

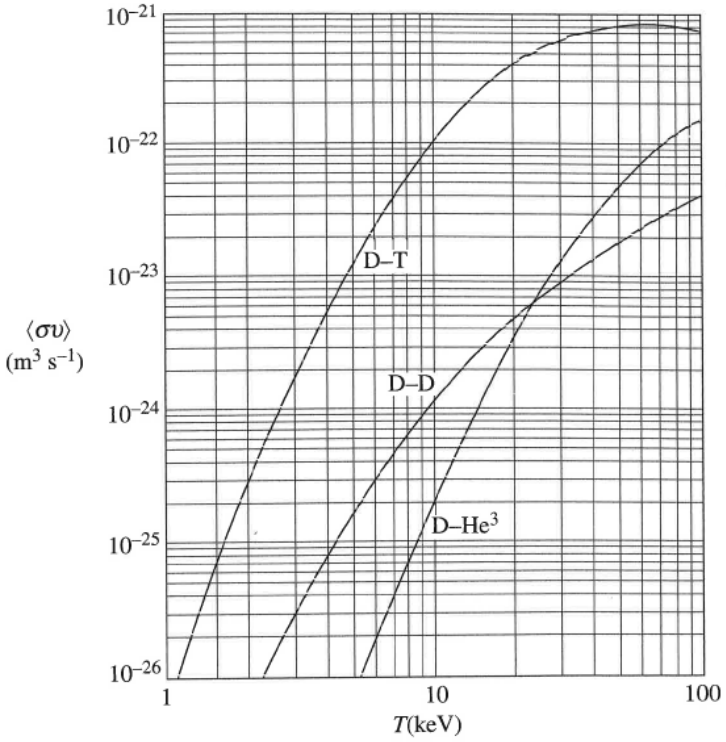

FIGURE 1.1 – Average cross sections of D-T, D-D and D-He3 reactions as a function of temperature (Source : [Wesson 2011]).

When collisions occur, those three couples of elements can give birth to the following reactions:

$$\begin{aligned} \mathrm{D} + \mathrm{T} &\longrightarrow \mathrm{He4} + \mathrm{n} + 17.59\ \mathrm{MeV}, \\ \mathrm{D} + \mathrm{D} &\begin{cases} \xrightarrow{50\%} \mathrm{He3} + \mathrm{n} + 3.27\ \mathrm{MeV}, \\ \xrightarrow{50\%} \mathrm{T} + \mathrm{H} + 4.03\ \mathrm{MeV}, \end{cases} \\ \mathrm{D} + \mathrm{He3} &\longrightarrow \mathrm{He4} + \mathrm{H} + 18.3\ \mathrm{MeV}, \end{aligned}$$

where n designates a neutron.

In the range of temperatures 1 keV - 100 keV, at given densities, we can see that D-T has by far the highest $\langle \sigma(v)v \rangle_v$ factor. The latter reaches its maximum around 60 keV;

however what is needed is not the maximisation of $\langle\sigma(v)v\rangle_v$ but of the reaction rate $n_a n_b \langle\sigma(v)v\rangle_v$. In the case of deuterium and tritium, calling n_i the total density of ions, $n_\mathrm{D} n_\mathrm{T}$ reaches its maximum for $n_\mathrm{D} = n_\mathrm{T} = \frac{n_i}{2}$. The reaction rate then reads $\frac{n_i^2}{4} \langle\sigma(v)v\rangle_v$. We will see further below (Section 1.1.1) that the pressure $p_i = n_i T_i$ in a tokamak, where T_i is the ion temperature, is constrained by technological and scientific issues. Calling p_max the maximum value of p_i, the reaction rate reads

$$N = p_\mathrm{max}^2 \frac{\langle\sigma v\rangle_v}{4T_i^2}, \tag{1.2}$$

where p_max is independent of the temperature and $\langle\sigma v\rangle_v$ is a function of the temperature only.

We can now see that the expression we need to maximize is $\frac{\langle\sigma v\rangle_v}{T_i^2}$. As shown in Figure 1.1, for values of T_i below 10 keV, $\langle\sigma v\rangle_v$ grows faster than T_i^2, while it grows slower than T_i^2 after $T_i = 20$ keV. Consequently, the optimum temperature range for D-T fusion is 10-20 keV.

1.1.2 Ignition criterion

Various criteria have been set up to predict what conditions may be favourable for controlled fusion to occur; among those, the ignition criterion is one of the most relevant.

Ignition is reached when the energy released by fusion in the plasma compensates the energy losses, or in other words when no external power is required to sustain the reaction. It is characterized by

$$P_\mathrm{fus\to pla} \geq P_\mathrm{loss}, \tag{1.3}$$

where $P_\mathrm{fus\to pla}$ is the power of fusion reactions transferred to the plasma and P_loss is the power of losses on the edge of the plasma (by radiation, conduction or convection).

In the case of D-T fusion, only the alpha particles transfer their energy to the plasma. Neutrons quickly escape out of the tokamak without having time to communicate their energy to the plasma. In fusion power plants, those neutrons will slow down in a water-cooled tritium breeding blanket; the water thus heated will be used to generate electricity.

Let us call E_α the energy that an alpha particle takes away from a D-T reaction, and let us call V the volume of the plasma. Assuming all the energy of the alpha-particles is transferred to the bulk ions, and assuming $n_\mathrm{D} = n_\mathrm{T} = \frac{n}{2}$, we can write

$$P_\mathrm{fus\to pla} = \left\langle \frac{n^2}{4} \langle\sigma v\rangle_v \right\rangle_x E_\alpha V, \tag{1.4}$$

where $\langle ... \rangle_x$ stands for the space average operator $\frac{1}{V}\int_V ...(dx)^3$.

Besides, under the hypothesis that energy losses are essentially conductive and convective, P_{loss} can be written as follows:

$$P_{\text{loss}} = \frac{W}{\tau_{\text{E}}}, \tag{1.5}$$

where W is the internal energy of the plasma, and τ_{E} is the characteristic energy confinement time. Radiative, bremsstrahlung and synchrotron losses have been neglected. In a simplified D-T plasma where electrons and ions have the same uniform temperature T_i, and where the density n_i is uniform, the internal energy reads $W = 2 \cdot \frac{3}{2} n_i T_i V = 3 n_i T_i V$ (the factor 2 appears to take into account both ion and electron internal energies). The energy confinement time depends on collisional and turbulent transports; which in turn depend on the plasma parameters. One of those parameters is the temperature: when the temperature rises, the energy confinement time decreases.

Taking into account the expressions of $P_{\text{fus}\to\text{pla}}$ and P_{loss} here above described, the ignition criterion becomes

$$n_i \tau_{\text{E}} \geq \frac{12\, T_i}{\langle \sigma v \rangle_v \; E_\alpha}. \tag{1.6}$$

The right hand side term of inequality (1.6) depends only on T_i, and reaches its minimum around 30 keV, as shown in Figure 1.2.

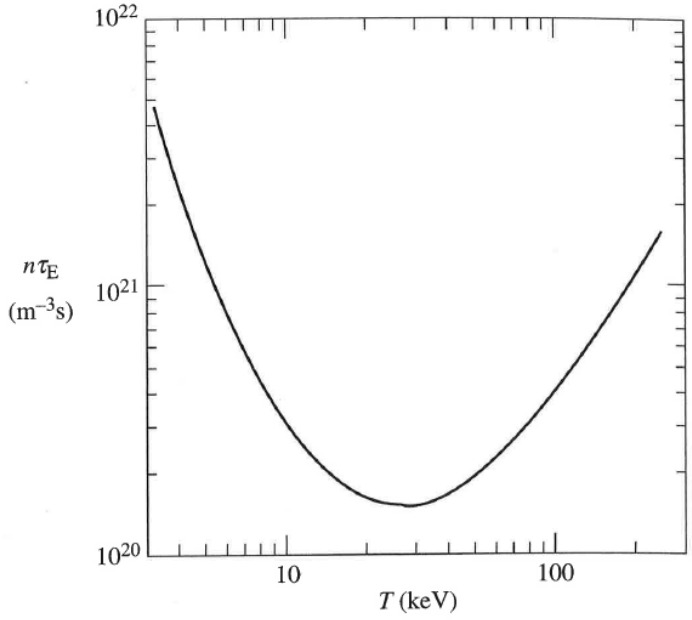

FIGURE 1.2 – Condition on $n\tau_{\text{E}}$ for ignition in the case of a D-T plasma, with flat density and temperature profiles (Source : [Wesson 2011]).

1.1.3 Triple product

Taking into account the dependence of τ_{E} on temperature, as well as synchrotron losses which increase rapidly with temperature, the ideal temperature for a burning plasma is not 30 keV, but 10-20 keV as mentioned above. In this range of temperature, $\langle \sigma v \rangle_v$ can be approximated with 10 % error bars as follows:[1]

$$\langle \sigma v \rangle_v = T_i^2 \times 1.1 \cdot 10^{-24} \quad \mathrm{m}^3 \cdot \mathrm{s}^{-1}, \text{ where } T_i \text{ is in keV.} \tag{1.7}$$

Considering that $E_\alpha = 3.5$ MeV, we obtain the following inequality, called *triple product* inequality:

$$n_i T_i \tau_{\mathrm{E}} \geq 3 \cdot 10^{21} \ \mathrm{keV} \cdot \mathrm{s} \cdot \mathrm{m}^{-3}. \tag{1.8}$$

It is recalled that this inequality is valid only for T_i comprised in the range 10 keV - 20 keV, and for flat radial density and temperature profiles.

For parabolic density and temperature profiles, the value of the right hand side is somewhat higher:

$$\hat{n}_i \hat{T}_i \tau_{\mathrm{E}} \geq 5 \cdot 10^{21} \ \mathrm{keV} \cdot \mathrm{s} \cdot \mathrm{m}^{-3}, \tag{1.9}$$

where $\hat{n}_i$ and $\hat{T}_i$ are the peak density and temperature values, encountered on the magnetic axis (see Section 1.2.1 below for the definition of the magnetic axis in a tokamak). In engineering units, the same inequality reads

$$\hat{n}_i \hat{T}_i \tau_{\mathrm{E}} \geq 8 \quad \mathrm{bar} \cdot \mathrm{s}. \tag{1.10}$$

To better understand what the triple product means for magnetic fusion, it is a good idea to write it differently. Let us define the β_i parameter of ions as the kinetic pressure of the ions divided by the magnetic pressure:

$$\beta_i = \frac{n_i T_i}{\frac{B^2}{2\mu_0}}, \tag{1.11}$$

where μ_0 is the vacuum magnetic permeability and B is the norm of the magnetic field.

It is possible to define the β_e parameter of electrons in the same way:

$$\beta_e = \frac{n_e T_e}{\frac{B^2}{2\mu_0}}, \tag{1.12}$$

[1] This approximation is valid only between 10 keV and 20 keV. In particular, away from the range 10 keV - 20 keV, $\langle \sigma v \rangle_v$ does not behave like T^2.

where, consistently, n_e and T_e are respectively the density and temperature of electrons.

Finally, the overall β parameter of the plasma can be defined as

$$\beta = \frac{n_e T_e + n_i T_i}{\frac{B^2}{2\mu_0}}. \tag{1.13}$$

Sticking to the simple case of the D-T plasma with parabolic density and temperature profiles, and where $T_i = T_e$, β_0 on the magnetic axis reads

$$\beta_0 = \frac{2\hat{n}_i \hat{T}_i}{\frac{B_0^2}{2\mu_0}}, \tag{1.14}$$

where B_0 is the value of the magnetic field on the magnetic axis.

This expression of β can then be injected into inequality (1.9) to get

$$B_0^2 \beta_0 \tau_{\mathrm{E}} \geq 4 \ \mathrm{T}^2 \cdot \mathrm{s}. \tag{1.15}$$

It is important to remember that this expression is valid only when the following conditions are fulfilled together: D-T plasma, temperature in range 10 keV - 20 keV, same ion and electron temperatures, parabolic profiles of density and temperature.

In particular, we can here see that the product $\hat{n}_i \hat{T}_i$ is a function of β_0 and B_0 only. As discussed below, β_0 and B_0 are constrained by scientific and engineering issues. Therefore, the product $\hat{n}_i \hat{T}_i$ is constrained by those issues, and this justifies the assumption made in Section 1.1.1, namely the existence of an upper boundary for the plasma pressure.

1.1.4 How can we improve each factor of the triple product?

To understand better how criterion (1.15) can be fulfilled, let us focus on each of the three factors B_0^2, β_0 and τ_{E}, in tokamaks.

- $\boldsymbol{B_0^2}$

  B_0 appears at first glance as an advantageous parameter to modify, since its impact on the ignition criteria is proportional to its square. In tokamaks, B_0 is usually of the order of a few Teslas. For instance, in the JET tokamak (European tokamak, located in the UK), B_0 has a value of 3.5 T; in the Tore Supra tokamak (France) it has a value of 4.5 T; and in the ITER tokamak (international tokamak, currently in construction in France) its intended value is 5.3 T (source: [Rax 2011]). Some machines, such as Alcator C-mod (US), regularly perform discharges at higher values of B_0: over 8 T. Besides, some other machines, such as Ignitor (tokamak in project, Italy), have been in discussion for long, with the intention of reaching even higher magnetic fields on the toroidal axis: a value of 13 T in the case of Ignitor. However, such projects still

have to come to reality: the main problem with high B_0 is the magnetic pressure $\sim \frac{B_0^2}{2\mu_0}$ the coils have to withstand, which, like the ignition criterion, varies as B_0^2. For $B_0 = 5$ T, this pressure is of the order of 100 bars. If $B_0 = 13$ T, it is over 650 bars.

A further issue is the width of the Scrape-Off Layer (SOL), which varies like $1/B^\alpha$, with α of the order of unity [Loarte 1999, Eich 2011, Goldston 2012]. The SOL is a zone of the outer plasma in which flux surfaces are not closed; the particles in this layer are guided by the magnetic field lines to the divertor, situated at the bottom of the tokamak. The width of the SOL determines the size of the power deposition layer on the divertor. Reducing the width of the SOL may lead to a dramatic increase in the power density deposited on the divertor.

- **β_0**

  In usual toroidal tokamaks, that is to say in tokamaks with large aspect ratio $\frac{R_0}{a} \sim 3$, β_0 is of the order of a few percent, which is quite low. So called *spherical* tokamaks can have a much higher β_0, which can reach 40 %. Such tokamaks are in fact still toroidal from a topological point of view, but their minor radius a is almost equal to their major radius R_0, so that the global machine is almost spherical. They are characterized by $\frac{R_0}{a} \sim 1$, and only depart from spheres by the vertical cylindrical hole they host in their core. The tokamaks MAST (UK) and NSTX (USA) are examples of spherical tokamaks, with $\frac{R_0}{a} \approx 1.3$.

  Those machines have several drawbacks, one of the main being the small size of the central post. Indeed, it has to host all Toroidal Field (TF) magnetic coils; and it is usually too small to host a central solenoid. If one wants to use superconductors for the coils, then the cryogenic system has to be hosted as well. In addition, the materials in that cylinder are very exposed to neutrons; the power thus received may be superior to 10 MW.m^{-2}, which means that metals in the cylinder hole are at risk of being transmuted and deformed.

- **τ_E**

  According to classical scaling laws, the energy confinement time is determined by several characteristics of the plasma; in particular the volume V, the kinetic pressure p and the magnetic field B. τ_E also depends on the transport (classical, neoclassical, turbulent) experienced by the plasma. One of the key goals of the study of turbulence is to reduce transport in order to increase τ_E (see Section 2.3).

  Let us assume that one managed to reduce turbulence, so that τ_E did not follow the scaling laws and increased at given B, p and V. The consequence would be a reduction in the power of the plant, at given size. Indeed, as written above, ignition

requires

$$P_{\text{fus}\to\text{pla}} \geq P_{\text{loss}}. \tag{1.16}$$

When steady-state is reached, this criterion turns into

$$P_{\text{fus}\to\text{pla}} = P_{\text{loss}}, \tag{1.17}$$

where it is recalled that $P_{\text{fus}\to\text{pla}}$ is the fusion power transferred to the plasma, *i.e.* the power of alpha particles in the case of a burning D-T plasma. If a power plant delivers 1 GW_{elec} to the electrical grid, then it requires about 3 GW_{th} of thermal power, taking into account Carnot yield. Assuming this power comes entirely from the neutrons of the D-T reactions, it means that $P_{\text{fus}\to\text{pla}}$ is about 750 MW.

Let us now recall the expression (1.5) of P_{loss}: $P_{\text{loss}} = \frac{3nTV}{\tau_{\text{E}}}$. We consequently have the following relationship:

$$P_{\text{fus}\to\text{pla}} = \frac{3nTV}{\tau_{\text{E}}}. \tag{1.18}$$

If τ_{E} increases at given n, T, V, then the power of the plant must be reduced through its dependence on $P_{\text{fus}\to\text{pla}}$, while the size of the plant, and hence its cost, remains constant.

1.2 Tokamaks: geometry and particle trajectories

1.2.1 Geometry of the magnetic field B

In a toroidal device designed for the magnetic confinement of charged particles, the magnetic field needs to have a poloidal component as well as a toroidal component. In tokamaks, the toroidal field is generated by poloidal coils disposed around the vacuum chamber, while the poloidal field is generated by a toroidal current carried by the plasma itself. Tokamaks are usually axisymmetric devices (contrary to stellarators for instance, in which the poloidal field is generated by external coils). The combination of the toroidal and poloidal components of the magnetic field yields helical field lines wrapped on nested magnetic surfaces, called flux surfaces. The flux surfaces have the topology of a torus; the inner-most one has a minor radius equal to zero and is in fact reduced to a mere line: this line is called the magnetic axis.

The geometry of tokamaks can be described by the following set of three coordinates: (ψ, θ, φ), where ψ is the poloidal magnetic flux counted from the magnetic axis and normalized to 2π, θ is the flux coordinate poloidal angle counted from the low field side

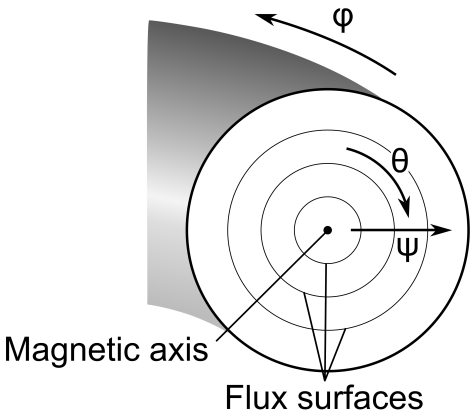

FIGURE 1.3 – Illustration of the set of coordinates (ψ, θ, φ) in the case of circular, concentric flux surfaces.

equatorial plane, and φ is the toroidal angle. ψ is a flux label, *i.e.* it is constant on a given flux surface and uniquely characterizes each flux surface. It verifies $\psi \sim r^2$, where r is the minor radius (distance between a given point and the magnetic axis). The ratio between the major radius (distance between a given point and the torus symmetry axis) and the minor radius is called the aspect ratio. The inverse aspect ratio $\varepsilon = \frac{r}{R_0}$, where R_0 is the major radius of the magnetic axis, is commonly used as a small parameter in calculus.

The flux coordinate poloidal angle θ is defined to ensure that the safety factor

$$q = \frac{\mathbf{B} \cdot \boldsymbol{\nabla}\varphi}{\mathbf{B} \cdot \boldsymbol{\nabla}\theta} \tag{1.19}$$

is a function of ψ only. This definition of θ differs from the geometrical one by a term of order ε which depends on ψ and θ. Figure 1.3 shows the set of coordinates (ψ, θ, φ) here used; the orientations have been chosen so that the set be direct.

In an axisymmetric tokamak, the magnetic field $\mathbf{B}$ can be written

$$\mathbf{B} = I(\psi)\boldsymbol{\nabla}\varphi + \boldsymbol{\nabla}\varphi \times \boldsymbol{\nabla}\psi, \tag{1.20}$$

where I is a function of ψ only, which can be expressed as

$$I(\psi) = \frac{qR^2}{\mathcal{J}}. \tag{1.21}$$

In this expression, R is the major radius and $\mathcal{J} = (\boldsymbol{\nabla}\psi \times \boldsymbol{\nabla}\theta \cdot \boldsymbol{\nabla}\varphi)^{-1}$ is the Jacobian of the Cartesian coordinates with respect to the (ψ, θ, φ) coordinates.

The corresponding vector potential reads

$$\mathbf{A} = \psi_{\mathrm{T}} \boldsymbol{\nabla}\theta - \psi \boldsymbol{\nabla}\varphi, \tag{1.22}$$

where ψ_{T} is the toroidal flux normalized to 2π; and the current density reads

$$\mathbf{J} = -\frac{I'(\psi)}{\mu_0}\mathbf{B} - \frac{dP}{d\psi} R^2 \boldsymbol{\nabla}\varphi, \tag{1.23}$$

where the pressure P is a function of ψ only.

According to the Ampère theorem, at first order in ε, the magnetic field verifies

$$B = B_0 \frac{R_0}{R}, \tag{1.24}$$

where B_0 is the norm of the magnetic field on the magnetic axis.

At order zero in ε, the norm B of the total magnetic field is equal to B_0:

$$B = B_0. \tag{1.25}$$

In flux coordinates, q reads at first order in ε

$$q(\psi) = \frac{r B_0}{R_0 B_{\mathrm{P}}}, \tag{1.26}$$

where B_{P} is the norm of the poloidal magnetic field.

In the case of concentric circular flux surfaces, the major radius coordinates reads

$$R = R_0 + r\cos\theta. \tag{1.27}$$

In practice, in tokamaks, the flux surfaces are not always circular. For instance, in JET the flux surfaces have a somewhat "D" shape; and they will have a similar shape in ITER. On the contrary, in Tore Supra, the flux surfaces are circular. However, even in this last case, they are not really concentric. Indeed, the plasma tends to shift outwards under the combined effects of self-induction and pressure: this results in the so-called Shafranov shift, which is stronger for the inner flux surfaces than for the outer ones. The Shafranov shift adds a term $\Delta(r)$ to the expression of R. $\Delta(r)$ comprises one term of order 2 in ε and one term of the order of β (ratio of the kinetic pressure to the magnetic pressure). Therefore, at small β and at first order in ε, the Shafranov shift needs not be taken into account, and the expression of R presented here above remains correct for circular flux surfaces.

1.2.2 Parallel and perpendicular directions

In magnetized plasmas, such as the ones which are encountered in tokamaks, the magnetic field provides strong anisotropy. At each spatial position, the magnetic field defines a privileged direction, called the parallel direction, and a normal surface referred to as the perpendicular direction. Vectors are usually decomposed into their parallel and perpendicular components (where it is therefore implied that *parallel* means *parallel to the equilibrium magnetic field* and *perpendicular* means *perpendicular to the equilibrium magnetic field*).

The unit vector in the parallel direction $\mathbf{b}$ is defined as follows:

$$\mathbf{b} = \frac{\mathbf{B}}{B}. \tag{1.28}$$

In the case of circular flux surfaces, in flux coordinates, $\mathbf{b}$ reads, at first order in ε,

$$\mathbf{b} = \mathbf{e}_\varphi + \frac{r}{q(\psi)R_0}\mathbf{e}_\theta, \tag{1.29}$$

where $\mathbf{e}_\theta$ is the unit vector in the poloidal direction, and $\mathbf{e}_\varphi$ is the unit vector in the toroidal direction. In that case, the parallel gradient reads

$$\nabla_\parallel = \mathbf{b}\cdot\boldsymbol{\nabla} \tag{1.30}$$

$$= \frac{1}{R}\left[\partial_\varphi + \frac{1}{q}\partial_\theta\right]. \tag{1.31}$$

Remark: in the case of circular, concentric flux surfaces, the three coordinates (ψ, θ, φ) define an orthogonal basis. Therefore no distinction between covariant and contravariant components needs to be made. This is, however, not the case in general.

1.2.3 Particle trajectories

When they are immersed in a stationary and uniform magnetic field, and in the absence of any other forces, charged ions can move freely in the direction of the field, while they describe circles in the perpendicular direction, with frequency $\omega_c = \frac{e_i B}{m_i}$ and radius $\rho_\mathrm{L} = \frac{v_\perp}{\omega_c}$, where B is the norm of the magnetic field, e_i is the charge of the ions, m_i is the mass of the particles and $v_\perp$ is the perpendicular velocity. This latter part of their movement is called the cyclotron gyration, the corresponding frequency is called the cyclotron frequency and the corresponding radius is called the Larmor radius. The combination of the free motion along the magnetic field and of the cyclotron gyration yields a helical trajectory. In tokamaks, however, the magnetic field is not uniform: although the helical trajectory here above described remains valid at first order, some additional features need to be taken into account. They are detailed below.

In the rest of the manuscript, electrons are treated adiabatically and collisional phenomena are not taken into account; this is why we have here chosen to focus on ions (electrons are mentioned in the paragraph on drift velocities only), and why no reference to collision characteristics is made.

Motion invariants

Some quantities can be, under certain conditions, identified as motion invariants. Among the quantities presented below, some are said to be *adiabatic* invariants. This means that they are invariant only under the following conditions: the spatial variations of the magnetic field $\mathbf{B}$ occur on large scales compared to the thermal ion Larmor radius $\rho_i = \sqrt{m_i T_i}/eB$, and the time variations of $\mathbf{B}$ occur on large scales compared to the cyclotron period of time ω_c^{-1}.

Only three independent invariants can be built. The energy, the magnetic moment and the canonical moment presented here below are independent. The longitudinal invariant can be expressed as a combination of those three independent invariants.

- Energy: $H = \frac{1}{2} m_i v_\parallel^2 + \mu B + e_i \phi$,
  where $v_\parallel$ is the parallel velocity, μ is the magnetic moment, and ϕ is the electric potential. The energy is a motion invariant only if the electric field varies slowly compared to the cyclotron rotation.

- Magnetic moment: $\mu = \frac{m_i v_\perp^2}{2B}$.
  The magnetic moment is an adiabatic invariant.

- Canonical momentum: $P_\varphi = m_i R v_\varphi - e_i \psi$,
  where v_φ is the toroidal velocity. The invariance of the canonical momentum is deduced from the independence of the motion Lagrangian with regard to the toroidal angle in the case of an axisymmetric tokamak. In practice, due to the finite number of toroidal field coils (for instance 32 non superconducting coils in JET, to be compared to 18 superconducting coils in Tore Supra or ITER), the toroidal magnetic field is not perfectly axisymmetric.

- Longitudinal invariant: $J = 2 \int_{-\theta_t}^{\theta_t} m_i v_\parallel dl$,
  where $\theta_t > 0$ is the poloidal angle of the trapped orbit turning points (the difference between trapped and passing ions in tokamaks is explained a few lines below). The longitudinal invariant is an adiabatic invariant which concerns trapped particles only. The integration path denoted by dl is made along the banana motion.

Trapped and passing orbits

In the absence of any electric field and collisions, the kinetic energy $E = \frac{1}{2} m_i v_\parallel^2 + \mu B$

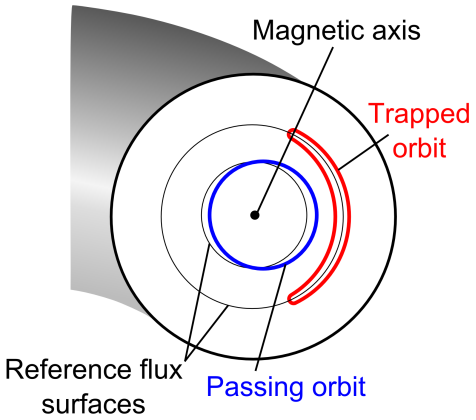

FIGURE 1.4 – Illustration of a passing orbit and a trapped orbit projected on a poloidal section, each represented with their reference flux surfaces.

of each ion is conserved, while μ is an adiabatic invariant. Therefore, the variations of $v_\parallel$ and B during the motion are directly linked. In the case of circular, concentric flux surfaces this link reads, at first order in the inverse aspect ratio,

$$v_\parallel^2 = \frac{2}{m_i}[E - \mu B_0(1 - \varepsilon\cos\theta)]. \tag{1.32}$$

This relation implies that $E - \mu B_0(1 - \varepsilon\cos\theta)$ must always be non-negative. If there exists a poloidal angle θ for which $E - \mu B_0(1 - \varepsilon\cos\theta)$ is null, then the ion will be *mirrored* by the magnetic field. It will not be able to reach the high field side of the tokamak (θ of the order of π), and will be confined to the low field side (θ of the order of zero). Such a particle is called a *trapped particle*. On the contrary, if the parallel energy of the ion is high enough for it to never fall to zero, then the particle is said to be a *passing particle*. The trapping condition corresponds to the case $E < \mu B_{\max} = \mu B_0(1 + \varepsilon)$. Using the definition of $E = \frac{1}{2}m_i v_\parallel^2 + \mu B$, this conditions can be recast as follows:

$$\left.\frac{v_\parallel}{v_\perp}\right|_{\theta=0} < \sqrt{2\varepsilon}. \tag{1.33}$$

Figure 1.4 shows the projection on a poloidal surface of a trapped orbit (in red) and of a passing orbit (in blue). Due to their shape, trapped orbits are also called *banana orbits*, and the corresponding motion is usually called *bounce motion*. The toroidal motion of ions is not represented in Figure 1.4: at the same time as they go to and fro in the poloidal direction, trapped particles also go to and fro in the toroidal direction; while passing particles have helical orbits rotating in the poloidal and toroidal directions.

The proportion η of trapped ions with respect to the total number of ions is of the order of the inverse aspect ratio:

$$\eta \sim \sqrt{\varepsilon}. \tag{1.34}$$

Passing and trapped orbits do not exactly lie on a flux surface: they deviate slightly from their reference surface due to the curvature and gradient drifts (see below). Those deviations from the reference flux surface are of the following order, for thermal trapped (δ_b) and passing (δ_p) ions:

$$\delta_b \sim \frac{q\rho_i}{\sqrt{\varepsilon}}, \tag{1.35}$$

$$\delta_p \sim q\rho_i. \tag{1.36}$$

Characteristic frequencies

The following frequencies are characteristic of the ion trajectories. Frequencies corresponding to collisions are not indicated here.

- Cyclotron frequency: $\omega_c = \frac{e_i B}{m_i}$.
  The cyclotron frequency concerns both trapped and passing particles; it corresponds to their motion around the magnetic field lines.

- Toroidal passing frequency: $\omega_\varphi = \frac{v_\parallel}{R}$.
  The toroidal passing frequency concerns passing particles only; it corresponds to their motion in the toroidal direction.

- Transit frequency (= poloidal passing frequency): $\omega_\parallel = \frac{v_\parallel}{qR}$.
  The transit frequency concerns passing particles only; it corresponds to their motion in the poloidal direction.

- Bounce frequency: $\omega_b \sim \frac{v_\mathrm{T}}{qR_0}\sqrt{\varepsilon}$,
  where $v_\mathrm{T} = \sqrt{\frac{T}{m}}$ is the thermal velocity. The bounce frequency concerns trapped particles only; it corresponds to their motion in the poloidal direction.

- Toroidal precession frequency: $\omega_d \sim \frac{qv_\mathrm{T}}{R_0}\frac{\rho_\mathrm{L}}{a}$.
  The toroidal precession frequency concerns trapped particles only. In addition to the bounce motion, trapped particles experience a slow motion in the toroidal direction. Indeed, on a banana orbit, since the parallel velocity reads $v_\parallel = \sqrt{\frac{2}{m}}\sqrt{E-\mu B}$, the particles go faster on the outer branch, where B is lower, than on the inner branch, where B is higher. The velocity difference between the two branches reads

  $$\delta v_\parallel = \frac{2}{m}\frac{\mu B_0}{2v_\parallel}\frac{\delta_b}{R_0}. \tag{1.37}$$

  This difference accounts for the toroidal precession, with frequency

  $$\omega_d \sim \frac{\delta v_\parallel}{R_0}. \tag{1.38}$$

The toroidal precession implies that although they will never make a whole poloidal turn, trapped particles will on the contrary eventually make a whole toroidal turn (see Figure 1.5) with frequency ω_d.

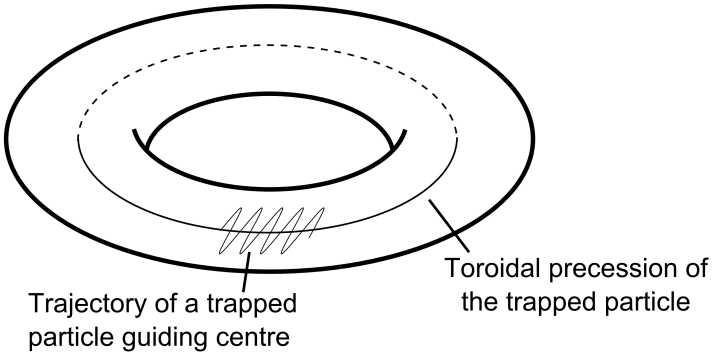

FIGURE 1.5 – Illustration of the trajectory of a trapped particle guiding centre, where the bounce motion is visible, and where the toroidal precession is identified.

Drift velocities

In tokamaks, the magnetic field is not uniform, and the particles are usually submitted to an electric field in addition to the magnetic field. In such situations, in addition to the helical motion around the field lines, they experience so-called drift velocities. The main drift velocities are the $\mathbf{E} \times \mathbf{B}$ (read "E cross B", where $\mathbf{E}$ is the electric field) drift, the curvature drift, and the gradient drift. Together, the curvature drift and the gradient drift are called the magnetic drift.

In the presence of an electric field $\mathbf{E}$, the ions are subject to the following $\mathbf{E} \times \mathbf{B}$ drift velocity:

$$\mathbf{v}_{\mathrm{E}} = \frac{\mathbf{E} \times \mathbf{b}}{B}. \tag{1.39}$$

When the magnetic field is curved and has a perpendicular gradient, the ions are subject to the following magnetic drift velocity, where the first part represents the curvature drift, and the second part represents the gradient drift:

$$\mathbf{v}_g = \frac{m_i v_\parallel^2}{e_i B} \boldsymbol{\kappa} + \frac{\mu B}{e_i B} \frac{\mathbf{b} \times \boldsymbol{\nabla} B}{B}. \tag{1.40}$$

In this expression, $\boldsymbol{\kappa}$ is the curvature of the magnetic field. It reads $\boldsymbol{\kappa} = (\mathbf{b} \times \boldsymbol{\nabla} B + \mathbf{rot}\ \mathbf{B}|_\perp)/B$, where the $\mathbf{rot}\ \mathbf{B}|_\perp$ term can be neglected when the plasma has a low β_i (ratio of the kinetic pressure to the magnetic pressure).

The $\mathbf{E}\times\mathbf{B}$ and magnetic drift also affect electrons (just replace m_i with m_e and e_i with $-e$, where m_e is the electron mass and e is the elementary Coulomb charge). However, they do not have the same effect: the $\mathbf{E}\times\mathbf{B}$ drift drives electrons and ions in the same direction, and therefore does not create any charge separation. On the contrary, the magnetic drift drives electrons and ions in opposite directions, thereby creating a charge separation.

Together, the $\mathbf{E}\times\mathbf{B}$ and the magnetic drifts explain why a poloidal magnetic field is needed in a tokamak: without the poloidal field, the magnetic drift would create a vertical charge separation; this charge separation would in turn be at the origin of an $\mathbf{E}\times\mathbf{B}$ drift, and the latter would cause the expulsion of the particles from the tokamak. By allowing a compensation of the vertical drift, the poloidal field prevents the charge separation caused by the magnetic drift from occurring.

1.3 A brief introduction to fluid and gyrokinetic theories

The kinetic and fluid theories provide models of the plasma, in the framework of which the time evolution of the relevant parameters can be computed. In the fluid theory, a three-dimension problem is considered (see Section 1.3.2 below), while in the kinetic theory six dimensions are taken into account, corresponding to spatial and velocity coordinates (see Section 1.3.1): the kinetic theory therefore provides a more complex framework than the fluid theory. While some aspects of plasma physics in tokamaks may be treated in both fluid and kinetic theories, it is sometimes necessary to resort to the kinetic model. This is in particular the case if Finite Larmor Radius (FLR) and Finite Orbit Width (FOW) effects are to be considered, or if Landau resonances in the velocity space are to be taken into account. For instance, the study of the excitation of Energetic particle driven Geodesic Acoustic Modes (EGAMs) requires a Landau resonance to be taken into account (see Chapter 3).

1.3.1 Gyrokinetic theory: time evolution and quasi-neutrality equations

In the kinetic model, on a microscopic scale, each particle is characterized by its spatial coordinates (3 dimensions) and its velocity coordinates (3 dimensions). On mesoscopic and macroscopic scales, the particles are described by a distribution function $f(\mathbf{x},\mathbf{v},t)$ which depends on the six phase space variables (physical space and velocity), plus on time. The number of particles having a velocity $[\mathbf{v};\mathbf{v}+\mathbf{dv}]$ at a position $[\mathbf{x};\mathbf{x}+\mathbf{dx}]$ is given by $f(\mathbf{x},\mathbf{v},t)(dv)^3(dx)^3$. A different distribution function is established for each species

present in the tokamak, and therefore the equations presented below are to be solved once for each species. In the present manuscript, however, the electrons are treated in a simplified way, according to the adiabatic theory (see below the paragraph dealing with the quasi-neutrality equation).

The distribution function evolves in time because of the interactions of particles with the surrounding electromagnetic field, with other particles (collisions) and external sources. Under the assumption that over infinitesimal times, the position and velocity of any given particle experience only infinitesimal variations, the time evolution of the distribution function is described by the Fokker-Planck equation

$$\frac{df}{dt} = C(f) + S, \tag{1.41}$$

where $C(f)$ is the collision operator and describes collisions between particles, while S is a source term which describes the injection of any given quantity (energy, momentum, particles...) in the system. $\frac{d}{dt}$ designates the particle derivative:

$$\frac{d}{dt} = \partial_t + \frac{d\mathbf{x}}{dt} \cdot \partial_{\mathbf{x}} + \frac{d\mathbf{v}}{dt} \cdot \partial_{\mathbf{v}}. \tag{1.42}$$

In the absence of source and collision terms, the Fokker-Planck equation is called the **Vlasov equation**, and reads

$$\frac{df}{dt} = 0. \tag{1.43}$$

The Vlasov equation is a 6 dimensional (6D) equation. However, in magnetized plasmas such as those encountered in tokamaks, this equation can be turned into a 5 dimensional (5D) equation, considering that the cyclotron motion of a particle around the magnetic field lines occurs both on a fast time scale and a small spatial scale. The aim of deriving such a 5D equation usually is to model perturbation phenomena in the vicinity of equilibrium states. Depending on the ordering hypotheses which are made on the perturbations, different kinds of 5D equations can be derived from the Vlasov equation. We here briefly present two of them; further details can be found in [Brizard 2007].

Drift-kinetic equation

The drift-kinetic equation is valid under the following ordering hypotheses:

$$\frac{\omega}{\omega_c} \ll 1, \tag{1.44}$$

$$k_\perp \rho_i \sim \rho_* \ll 1, \tag{1.45}$$

$$\frac{e\tilde{\phi}}{T_i} \sim 1 \text{ or smaller}, \tag{1.46}$$

where ω is the characteristic frequency of the perturbation, ω_c is the cyclotron frequency, $k_\perp$ is the characteristic perpendicular wave vector of the perturbation, $\rho_i = \sqrt{m_i T_i}/eB$ is the fluid ion Larmor radius, $\rho_* = \rho_i/a$ is the normalized ion Larmor radius, a is the minor radius of the tokamak, e is the elementary electric charge, T_i is the ion temperature, m_i is the ion mass, B is the norm of the equilibrium magnetic field and $\tilde{\phi}$ is the perturbed electric potential. In the drift-kinetic ordering, no requirement on the amplitude of the perturbed electric potential is made; while the condition $k_\perp \rho_i \ll 1$ requires the characteristic length of the perturbation to be much larger than the ion Larmor radius. This last condition restricts the types of perturbations which can be studied within the drift-kinetic model.

At low β and for electrostatic perturbations, the drift-kinetic equation reads, at order 1 in ρ_*,

$$\partial_t f + \left(\frac{\mathbf{b} \times \boldsymbol{\nabla} \tilde{\phi}}{B} + \frac{m v_\parallel^2 + \mu B}{eB} \frac{\mathbf{b} \times \boldsymbol{\nabla} B}{B} + v_\parallel \mathbf{b} \right) \cdot \boldsymbol{\nabla} f + \left(-\frac{e}{m} \nabla_\parallel \tilde{\phi} - \frac{\mu}{m} \nabla_\parallel B + v_\parallel \frac{\mathbf{b} \times \boldsymbol{\nabla} \tilde{\phi}}{B} \cdot \frac{\boldsymbol{\nabla} B}{B} \right) \partial_{v_\parallel} f = 0. \tag{1.47}$$

Gyrokinetic equation

In the case of electrostatic perturbations, the gyrokinetic equation is valid under the following ordering hypotheses:

$$\frac{\omega}{\omega_c} \ll 1, \tag{1.48}$$

$$\frac{e\tilde{\phi}}{T_i} \sim \rho_* \ll 1, \tag{1.49}$$

$$k_\perp \rho_i \sim 1 \text{ or smaller.} \tag{1.50}$$

Contrary to what happens in the drift-kinetic case, the amplitude of the perturbed electric potential has to remain small in the gyrokinetic ordering; but as a compensation more freedom is enjoyed on the characteristic length of the perturbation, which can be as small as the ion Larmor radius.

At low β and for electrostatic perturbations, the gyrokinetic equation reads, at order 1 in ρ_*,

$$\partial_t f + \left(\frac{\mathbf{b} \times \boldsymbol{\nabla} J_0 \tilde{\phi}}{B} + \frac{m v_\parallel^2 + \mu B}{eB} \frac{\mathbf{b} \times \boldsymbol{\nabla} B}{B} + v_\parallel \mathbf{b} \right) \cdot \boldsymbol{\nabla} f + \left(-\frac{e}{m} \nabla_\parallel J_0 \tilde{\phi} - \frac{\mu}{m} \nabla_\parallel B + v_\parallel \frac{\mathbf{b} \times \boldsymbol{\nabla} J_0 \tilde{\phi}}{B} \cdot \frac{\boldsymbol{\nabla} B}{B} \right) \partial_{v_\parallel} f = 0, \tag{1.51}$$

where J_0 is the gyroaverage operator.

In practice, in the present manuscript, the gyrokinetic equation is used with the fol-

lowing ordering:

$$k_\perp \rho_i \sim \delta, \tag{1.52}$$

where δ is a small parameter verifying

$$\rho_* \ll \delta \ll 1. \tag{1.53}$$

The gyrokinetic equation is solved in conjunction with the quasi-neutrality equation. Assuming that the electrons behave adiabatically, in the gyrokinetic ordering with $k_\perp \rho_i \sim \delta$, the quasi-neutrality equation reads, at order 1 in ρ_* and order 2 in δ:

$$n_e \frac{e}{T_e}\Big(\tilde{\phi} - \big\langle \tilde{\phi} \big\rangle_{\mathrm{FS}}\Big) = \mathrm{div}\Big(\frac{m_i n_i}{eB^2}\boldsymbol{\nabla}_\perp \tilde{\phi}\Big) + \int \left(1 + \frac{1}{2}\frac{\mu B}{T_i}\rho_i^2 \nabla_\perp^2\right) f \, (dv)^3 - n_i, \tag{1.54}$$

where n_e is the equilibrium electron density, T_e is the electron temperature, $\langle \cdot \rangle_{\mathrm{FS}}$ denotes the average on a flux surface, and n_i is the equilibrium ion density.

Remark: that the electrons behave adiabatically means that their inertia is considered to be small and that they are therefore always in equilibrium with the surrounding medium. In particular, they are considered to respond immediately to an electric potential perturbation, according to the Maxwellian equilibrium distribution function: $\tilde{n}_e \sim n_e \frac{e\tilde{\phi}}{T_e}$.

1.3.2 Fluid theory - Ideal MHD closure

The 6D kinetic theory can be reduced to a 3 dimensional (3D) fluid theory by integration on the velocity space. The variables are then the moments of the distribution function, defined as follows: the moment of order ι (where ι is a non-negative integer) is the integral over $\mathbf{v}$ of the particle distribution function multiplied by a factor of order v^ι.

The following moments are amongst the most commonly used:

- density: $n = \int f (dv)^3$.
  The density is a moment of order 0;
- fluid velocity: $\mathbf{u} = \frac{1}{n}\int \mathbf{v} f (dv)^3$.
  The fluid velocity is a moment of order 1;
- pressure tensor: $\mathbf{P} = m\int (\mathbf{v}-\mathbf{u}) \otimes (\mathbf{v}-\mathbf{u}) f (dv)^3$.
  The pressure tensor is a moment of order 2. The scalar pressure p is equal to the third of the trace of the pressure tensor $\mathbf{P}$. The temperature of a species is defined as the ratio of the scalar pressure to the density;
- heat flux: $\mathbf{Q} = \frac{m}{2}\int |\mathbf{v}-\mathbf{u}|^2 (\mathbf{v}-\mathbf{u}) f (dv)^3$.
  The heat flux is a moment of order 3.

The fluid equations are obtained from the kinetic equation, multiplied by factors of order v^ι and then integrated over $\mathbf{v}$. A fluid equation of order ι always contains a moment of order $\iota + 1$, which means that the set of fluid equations to be solved is infinite. Consequently, to get a finite number of self-consistent, closed equations, approximations have to be made; such approximations are called fluid closures. Various fluid closures have been developed, we will here present one of them: the ideal MagnetoHydroDynamic (MHD) closure. The question of fluid closures remains open for further refinement, it is an on-going research area.

Ideal MHD closure

In the ideal MHD model, the following assumptions are made: at order 0 in the normalized Larmor radius ρ_*, the parallel electric field is null ($E_\parallel = 0$) and the fluid velocity is the sum of a parallel component and of an electric drift velocity: $\mathbf{u} = u_\parallel \mathbf{b} + \frac{\mathbf{E}\times\mathbf{b}}{B}$. Those features can be summed up in the following equation:

$$\mathbf{E} + \mathbf{u} \times \mathbf{B} = 0. \tag{1.55}$$

In addition, $\mathbf{u}$ is assumed to be the same for all species, the pressure tensor is assumed to be isotropic (therefore only the scalar pressure is needed), and the heat flux is assumed to be negligible.

Under those hypotheses, the ideal MHD equations are:

$$\frac{d\rho_m}{dt} + \rho_m \operatorname{div} \mathbf{u} = 0, \tag{1.56}$$

$$\rho_m \frac{d\mathbf{u}}{dt} + \boldsymbol{\nabla} p - \mathbf{J} \times \mathbf{B} = 0, \tag{1.57}$$

$$\frac{dp}{dt} + \frac{5}{3} p \operatorname{div} \mathbf{u} = 0, \tag{1.58}$$

where ρ_m is the mass density. Those equations are complemented by the Maxwell equations to form a closed set of equations.

1.4 Conventions used in the present manuscript

Some conventions are commonly used in the field of plasma physics for nuclear fusion, but may not be used in other fields. Some other conventions may not be unanimously acknowledged, even in the field of plasma physics. To be sure that no ambiguity arises from the choices of conventions made in the present manuscript, they are here explicitly stated.

- The word *axisymmetric* is used to describe an object (field, device such as a tokamak...) which is invariant by a rotation of **any angle** around a symmetry axis.

The implication of *axisymmetric* is therefore here stronger than invariance by a mere rotation of π around the symmetry axis.

- The word *frequency* here stands for either *frequency*, written f, or *pulsation*, written ω, without distinction; it needs to be understood according to the context. There is a factor 2π between the usual meanings of *frequency* and *pulsation*: $\omega = 2\pi f$.

- A difference should be made between observed MHD or turbulent activity and the underlying instabilities. In the present manuscript, sawtooth activity and turbulence are considered, along with the respective underlying internal kink mode and Ion Temperature Gradient (ITG) modes. The underlying modes are said to be unstable when their amplitudes evolve in time like $e^{\gamma t}$, where t stands for the time, and $\gamma > 0$ is the growth rate. Of course, such an evolution is necessarily limited in time: the modes cannot have an infinite amplitude. In most cases, saturation occurs: the modes stop growing and may be damped by some non-linear process. After a while, the conditions for linear growth may be gathered again, and the cycle starts anew. The resulting process of growth and decay of the underlying modes corresponds to observed sawtooth activity or turbulence.

  Sensu stricto, only instabilities may be stabilized: it is the case for the internal kink mode and ITG modes, but not for sawtooth activity and turbulence as those are not strictly speaking instabilities. Nonetheless, it is common to say that sawtooth activity and turbulence are stabilized, meaning in fact that the underlying processes are stabilized. Such an extended meaning is used in the present manuscript.

- The gradient of a tensor $\mathbf{F}$ of order 1 (*i.e.* a vector) is computed as follows, in Cartesian coordinates:

$$\boldsymbol{\nabla}\mathbf{F} = \begin{bmatrix} \partial_x F_x & \partial_y F_x & \partial_z F_x \\ \partial_x F_y & \partial_y F_y & \partial_z F_y \\ \partial_x F_z & \partial_y F_z & \partial_z F_z \end{bmatrix}.$$

  With this convention, the differential of $\mathbf{F}$ applied in $\mathbf{x}$ to a vector $\mathbf{h}$ can be expressed as

$$\mathrm{d}\mathbf{F}(\mathbf{x})(\mathbf{h}) = \boldsymbol{\nabla}\mathbf{F}|_{\mathbf{x}} \cdot \mathbf{h},$$

  where $\cdot$ is the tensor product contracted once.

  Attention: in some other conventions, not used in the present manuscript, a different order is adopted in the expression of $\boldsymbol{\nabla}\mathbf{F}$, and the differential then reads $\mathrm{d}\mathbf{F}(\mathbf{x})(\mathbf{h}) = \mathbf{h} \cdot \boldsymbol{\nabla}\mathbf{F}|_{\mathbf{x}}$.

- The divergence of a vector $\mathbf{F}$ is written $\mathrm{div}\,\mathbf{F}$.

- The curl of a vector $\mathbf{F}$ is written **rot F**.
- The vectorial product of two vectors $\mathbf{F}$ and $\mathbf{G}$ is written with the sign $\times$: $\mathbf{F} \times \mathbf{G}$.
- The Boltzmann constant is set equal to 1 in equations, and the temperature is expressed in energy units. To get the temperature in SI units, simply divide the temperature in energy units by the actual Boltzmann constant $k_B = 1.38{\cdot}10^{-23}$ J/K.

1.5 Outline

The present manuscript starts with two introductory chapters, which reflect some aspects of the academic knowledge in plasma physics.

A general introduction on thermonuclear fusion and tokamak plasmas is proposed in Chapter 1 here above.

In Chapter 2, a focus is given on the instabilities studied in the present manuscript. Sawtooth activity, along with the underlying internal kink mode, is presented. Porcelli's model [Porcelli 1991], which predicts the stabilization of the internal kink mode by fast particles, is described. An overview of ITG modes, which underlie turbulence, is provided; the physics of GAMs and EGAMs is introduced.

The developments of this thesis are presented in Chapters 3 to 5. The stabilization of sawteeth by fast particles is studied from an experimental point of view, while the stabilization of ITG modes via EGAMs is discussed through theoretical and analytical modelling.

In chapter 3, we report on the stabilization of sawteeth by fast particles in the tokamak JET, in the framework of Porcelli's theoretical model. The energetic deuterons are produced by 100 keV NBI combined with 3rd harmonic ICRH.

In chapter 4, we analyse the link between GAMs and EGAMs: do they belong to the same mode branch? Depending on the answer, EGAMs may or may not have the same impact as GAMs on turbulence. Through a linear, analytical model, in which the fast particles are represented by a Maxwellian bump-on-tail distribution function, we find that the answer depends on several parameters.

In chapter 5, we discuss the interaction between EGAMs and ITG modes. A non-linear three wave parametric interaction model is developed, in which the possibility of the excitation of two ITG modes by a single EGAM is studied. We conclude that such

a phenomenon cannot occur locally. However, assuming the ITG is linearly unstable in the core plasma, and taking into account radial propagation, an ITG mode may be non-linearly excited in the outer region even if it is linearly stable.

Chapter 2

Sawteeth; EGAMs; turbulence: overview of three types of plasma instabilities which interact with fast particles.

2.1 The stakes

Plasma instabilities

A tokamak is designed to provide magnetic confinement to a steady-state plasma. The features of the magnetic field geometry and the particle trajectories described in Section 1.2 correspond to the case of an equilibrium plasma. However, the plasma is driven away from this ideal equilibrium state whenever a perturbation arises. If the equilibrium is stable (situation illustrated in Figure 2.1-a), the plasma will return to its equilibrium state as soon as the perturbation ceases. On the contrary, if the equilibrium is unstable (situation illustrated in Figure 2.1-c), the plasma will not return to its equilibrium state when the perturbation ceases: as soon as it has left its equilibrium state, the plasma will be self-driven to a different state.

In practice, an unstable equilibrium cannot be maintained in an experiment, since the slightest perturbation is enough to drive the plasma away from this equilibrium. Such a situation can be compared to a pendulum consisting of a mass held at the extremity of a rigid bar. There are two equilibrium positions for such a pendulum: in one of them the bar is vertical and the mass is down; in the other one the bar is also vertical but the mass is up. Only the first case corresponds to a stable equilibrium; the second one corresponds to an unstable equilibrium: if the mass moves by even a fraction of degree, it will be driven by gravity down to its stable equilibrium position, assuming the pendulum is dissipative.

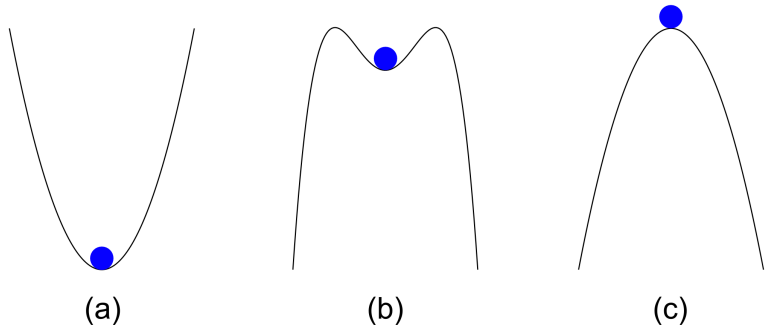

FIGURE 2.1 – Illustration of (a) stable equilibrium, (b) metastable equilibrium, (c) linearly unstable equilibrium.

Between stable and unstable equilibria, there exist metastable equilibria (situation illustrated in Figure 2.1-b). In such situations, the amplitude of the perturbation matters: if the perturbation is small, the system remains close to its equilibrium value, like in the case of a stable equilibrium. If the perturbation is large enough, the system is driven away from its equilibrium, like in the case of an unstable equilibrium.

Fusion plasmas in tokamaks are known to be subject to rich dynamics ranging from stable oscillations to fast-growing instabilities. Those oscillations and instabilities are characterized by their frequencies and spatial structures (toroidal, poloidal and radial structures, usually given by the corresponding wave vectors). They are most of the time studied with Fourier analysis or similar tools: a given oscillation or instability is therefore usually called a *mode*. Some classes of modes exhibit well-defined frequencies and spatial structures, while some others correspond to a wide range of frequencies and have more complex spatial structures.

For a few words on the definition of underlying instabilities, refer to Section 1.4.

Understanding the excitation mechanisms of the modes encountered in fusion plasmas and learning to control them is of tremendous importance in the view of next step tokamak experiments such as ITER. A class of particles present in tokamaks is particularly relevant regarding their interactions with instabilities: those are fast ions which, under certain circumstances, can trigger or damp instabilities. A review of the impact of energetic particles in plasmas in view of burning experiments can be found in [Gorelenkov 2014].

Fast ions

Fast ions are defined as ions which have a kinetic energy which is several times larger than the thermal energy. In tokamaks, the thermal energy is about 10-20 keV, while there are three main sources of fast ions:

- alpha particles from D-T reactions;
  in a power plant, the main fusion reactions will be deuterium-tritium reactions. They will produce fast alpha particles (helium 4) at an energy of about 3.5 MeV. Such a population of fast alpha particles is isotropic: their energy is as much contained in their parallel velocity as in their perpendicular velocity;

- NBI-accelerated ions;
  Neutral Beam Injection (NBI) is one of the means used to heat fusion plasmas to the 10-20 keV range. Ionized particles are accelerated in dedicated accelerators outside the tokamak and are neutralized before being injected in the plasma. They then transfer their energy via collisions. To be able to reach the core plasma before being ionized, those particles need to have a sufficiently high energy: it is about 100 keV in JET. In ITER, they should have an energy of about 1 MeV. The parallel velocity and the perpendicular velocity of fast ions born from NBI have the same order of magnitude;

- ICRH-accelerated ions;
  Ion Cyclotron Resonant Heating (ICRH) is another means used to heat fusion plasmas. An electromagnetic wave is produced in the plasma by dedicated apparatus. The range of frequency used is of the order of a few tens of MHz, and the fast particles can be accelerated to energies of the order of a few MeV. The population of fast ions born from ICRH is highly anisotropic: their fast kinetic energy is almost entirely comprised in their perpendicular velocity, while their parallel velocity remains similar to that of thermal particles.

Focus on sawteeth, EGAMs and turbulence

In this manuscript, we will focus on three distinct phenomena: sawteeth, EGAMs and turbulence.

Sawteeth occur in the core plasma and are responsible for sudden drops of the electron temperature. They have been extensively studied, in conjunction with the internal kink mode, neoclassical tearing modes and magnetic reconnection issues [Bussac 1975, Kadomtsev 1975, Waelbroeck 1989, Aydemir 1992, Zakharov 1993]. It has been shown that, under certain circumstances, sawteeth oscillations can be stabilized by kinetic ions [White 1988, White 1989, Porcelli 1991, Edery 1992, Porcelli 1992, Zabiego 1994, Porcelli 1996, Angioni 2002, Graves 2005]. In Chapter 3, the stabilization of sawteeth in JET by fast deuterium beam ions accelerated to the 100 keV range by NBI, and then to the MeV energy range by 3rd harmonic ICRH, is analysed in the framework of Porcelli's model [Porcelli 1991]. In view of this analysis, an overview of sawteeth phenomena is presented in Section 2.2 below, with focus on the aspects relevant for the study presented in Chapter 3.

Turbulence is a widely observed phenomenon in all tokamaks; it causes energy transport from the core to the edge plasma. This turbulent transport is a major hurdle on the road to burning plasma, as it involves high losses of energy, thus leading to the reduction of the energy confinement time τ_E (see Section 1.1 about the importance of τ_E). Some electrostatic modes, known as Geodesic Acoustic Modes (GAMs) and first described in the early days of research on nuclear fusion plasmas [Winsor 1968], have recently been found to interact with turbulence [Hallatschek 2001, Jakubowski 2002, Ramisch 2003, Miyato 2004, Nagashima 2005, Angelino 2006, Miki 2007, Conway 2011, Sasaki 2012, Xu 2012]. This opens the way to a possible reduction of turbulent transport. GAMs are damped in thermal plasma; however fast ions have been found to excite GAM-like modes, called Energetic particle driven Geodesic Acoustic Modes (EGAMs) [Fu 2008, Berk 2010, Qiu 2010, Zarzoso 2012b, Kolesnichenko 2013]. In Chapter 4, the relation between GAMs and EGAMs is investigated, to better understand to which extent those modes may behave in a similar way or not, and may have a similar mitigating impact on turbulence or not. In Chapter 5, the relation between EGAMs and Ion Temperature Gradient (ITG) turbulence is examined, through a parametric decay model. In view of the studies reported in those two chapters, an overview of the physics of ITG turbulence, GAMs and EGAMs is presented in Section 2.3 below, with focus on the aspects relevant for Chapters 4 and 5.

2.2 Overview of sawteeth phenomena

Sawteeth are thus called because of the shape they give to the timelines of electron temperature: Figure 2.2 shows characteristic sawtooth activity. A thorough presentation of sawteeth phenomena can be found in [Nicolas 2013]. We focus in the present section on the aspects relevant for Chapter 3.

Sawtooth crashes are usually caused by the excitation of the internal kink mode, described in Section 2.2.1 below. Sawtooth crashes are often accompanied by magnetic reconnection, can trigger Neoclassical Tearing Modes (NTMs), and can expel impurities from the core plasma. Those aspects are presented in Section 2.2.2. Finally, the stabilization of sawteeth by trapped fast particles is discussed in Section 2.2.3.

2.2.1 Internal kink mode

The internal kink mode [Bussac 1975] is an instability which can arise in tokamaks wherever the safety factor q drops below 1. It is called *internal* for the lowest values of q are encountered in the core plasma, close to the magnetic axis. The word *kink* is due to the first observations of those instabilities, in Z-pinch machines: when exposed to a strong enough co-radial magnetic field, the plasma started to twist like a snake. It was found that

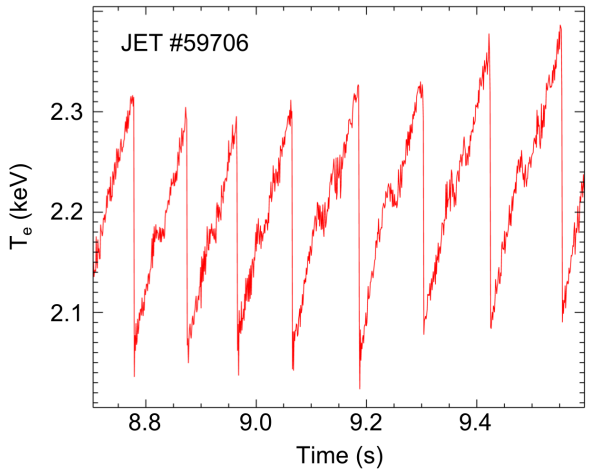

FIGURE 2.2 – Core electron temperature timeline from Electron Cyclotron Emission (ECE) measurements during JET discharge #59706, exhibiting characteristic sawtooth activity.

a strong enough longitudinal magnetic field could provide stabilization. The particular role of the safety factor q in tokamaks is reminiscent of the ratio between co-radial and longitudinal fields needed to provide stabilization in Z-pinch machines.

The internal kink mode appears as a possible instability in the ideal MHD model (described in Sec. 1.3.2). It is characterized by the spatial displacement $\boldsymbol{\xi}$ of any given fluid element with respect to its equilibrium position, in interaction with perturbations $\tilde{\mathbf{B}}$, $\tilde{\mathbf{J}}$ and $\tilde{p}$ of respectively the magnetic field, the current and the pressure. If there exists a displacement $\boldsymbol{\xi}$ which corresponds to a decrease in the plasma potential energy, then the plasma equilibrium is unstable and the internal kink mode can appear. The displacement $\boldsymbol{\xi}$ which arises is the one which corresponds to the highest potential energy drop.

In the large aspect ratio approximation ($\varepsilon = r/R_0 \ll 1$, where ε is the inverse aspect ratio), for a monotonous radial q profile and neglecting the inertia, the internal kink mode has the following ideal structure:

$$\boldsymbol{\xi} = \xi_0 e^{i\varphi - i\theta}(\mathbf{e}_r - i\mathbf{e}_\theta) + c.c. \quad \text{for } r < r_1, \tag{2.1}$$

$$\boldsymbol{\xi} = 0 \quad \text{for } r > r_1, \tag{2.2}$$

where r_1 is the minor radius of the $q = 1$ surface, ξ_0 is a constant and *c.c.* means *complex conjugate*. The ideal internal kink mode thus exhibits an $(m, n) = (1, 1)$ structure, where m is the poloidal mode number and n the toroidal mode number, with a rigid body displacement within the $q = 1$ surface. This rigid body displacement occurs perpendicularly to the equilibrium magnetic field: at first order in the inverse aspect ratio, the parallel displacement is null. The plasma outside the $q = 1$ surface is not affected; a discontinuity in the ideal solution therefore occurs at $r = r_1$. This discontinuity can be smoothed out

by taking into account the inertia in a small layer around $r = r_1$.

2.2.2 Sawteeth main features

Sawtooth crashes are known to be associated with magnetic reconnection [Kadomtsev 1975, Waelbroeck 1989, Zakharov 1993]. A magnetic reconnection is a reorganisation of the magnetic topology. It can occur when a flux surface breaks and a magnetic island appears: Figure 2.3 presents an illustration of a magnetic island with structure $(m, n) = (1, 1)$, where m is the poloidal mode number and n is the toroidal mode number. A magnetic island is a flux tube which is not centred on the magnetic axis. It is a perturbation which affects the equilibrium magnetic geometry and leads to particle or energy transport: mean profiles tend to flatten inside the island as a result of the fast parallel transport; and several islands can overlap, leading to stochastic field lines and enhanced radial transport.

Sawtooth crashes can lead to the excitation of Neoclassical Tearing Mode (NTMs) [Buttery 2004]. The excitation of those modes is more likely in the case of violent crashes, such as those which follow long sawteeth (usually called *monster* sawteeth). NTMs correspond to the reconnection of magnetic field lines on rational q surfaces. NTMs usually exhibit one of the following structures: $(m, n) = (3, 2)$ or $(m, n) = (2, 1)$. NTMs are thus called for they cause the *tearing* of magnetic flux surfaces, and are excited only when the magnetic island is large enough to compensate the stabilizing effect of the bootstrap current [Nicolas 2013], where the bootstrap current is a neoclassical effect of the radial pressure gradient. The mechanism of NTM destabilization is as follows: when a magnetic island appears, it locally causes a drop in the pressure gradient, which in turn results in a reduction of the bootstrap current. This current hole favours the growth of the magnetic island, and thus of the NTM.

It has recently been found that sawteeth can expel impurities from the core plasma [Nave 2003, Nakano 2009]. Impurities in tokamaks can be particularly harmful because of the energy losses they cause. Those energy losses are due in particular to line emission and bremsstrahlung. Line emission is high in the case of ions which are partially, but not entirely, ionized; while bremsstrahlung increases with Z_i^2, where Z_i is the ion charge number. In new generation tokamaks, divertors are coated with tungsten, which has a particularly high charge number $Z_i = 74$. It is partially ionized at $T = 10$ keV, with a high effective Z_i of about 50-60, thus leading to possible high power losses [Pütterich 2010]. Sawtooth crashes may prove very useful to avoid the accumulation of tungsten in the core.

Taking into account the features here above exposed, the question of the optimal sawtooth frequency remains open [Chapman 2011, Graves 2012]. Indeed, longer sawteeth correspond to higher and more stabilized core electron temperature, which is beneficial

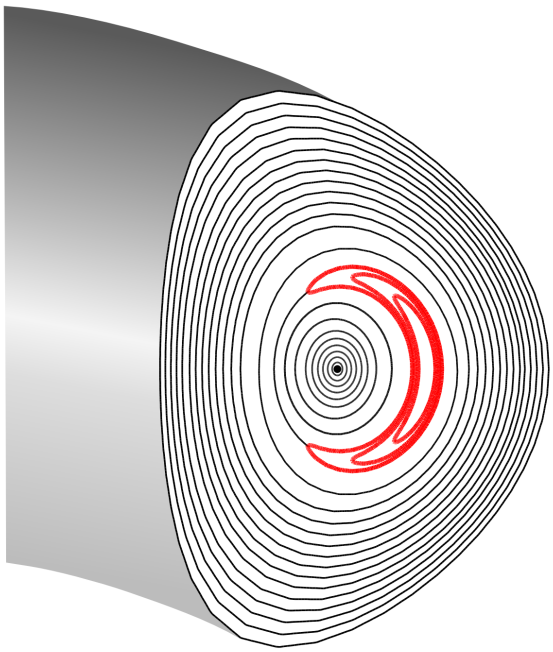

FIGURE 2.3 – Schematic representation of a magnetic island, evidenced in red. The black, solid lines represent the flux surfaces out of the magnetic island, with a D-shaped poloidal section. Figure obtained with the XTOR-2F code [Lütjens 2010, Février 2015].

for fusion. However, the crashes which follow those stabilized periods are more intense, cause higher T_e drops, and can cause harmful NTMs. Besides, shorter sawteeth periods may be beneficial to ensure that the core plasma always remains clear from impurities.

2.2.3 Sawteeth stabilization by fast particles

Under certain conditions, fast particles can stabilize sawteeth. In the literature, different mechanisms of stabilization have been evidenced; trapped fast particles in the core plasma are at the origin of one of them [Coppi 1988, Coppi 1989, Porcelli 1991, Porcelli 1996, Angioni 2002].

The contribution δW_{kin} of fast particles to the plasma potential energy in the presence of an internal kink mode is computed as follows:

$$\delta W_{\text{kin}} = \int (dx)^3 \int_{-\infty}^{t} dt' \, \tilde{\mathbf{J}}_k \cdot \tilde{\mathbf{E}}, \tag{2.3}$$

where $\tilde{\mathbf{J}}_k$ is the fast particle current density perturbation and $\tilde{\mathbf{E}}$ is the electric field perturbation, both created by the internal kink mode. Given the small ratio of the fast particle density to the thermal population density, $\tilde{\mathbf{E}}$ is essentially generated by thermal ions and can be related to the displacement $\boldsymbol{\xi}$ through the ideal MHD relation. $\tilde{\mathbf{J}}_k$ can be related to the fast particle pressure perturbation through the momentum balance equation,

neglecting inertial and collision terms.

In Sec. 2.2.1, the internal kink mode was derived within the ideal MHD framework. To take into account the fast particle perturbation, it is necessary to resort to the kinetic theory. The pressure is then obtained by integrating over the velocity coordinates; and equation (2.3) can be split into two terms. One of them is an adiabatic (in the convention of [Coppi 1990][1]) contribution: the fast particles follow the perturbation computed with the ideal MHD model. The other term is a non-adiabatic (still in the convention of [Coppi 1990]) contribution.

Under the following conditions:

$$\varepsilon, \rho_* \ll 1, \tag{2.4}$$

$$\omega \ll \omega_b, \tag{2.5}$$

$$\omega \ll \omega_\parallel \langle q-1 \rangle_{q<1}, \tag{2.6}$$

where ε is the inverse aspect ratio, ρ_* is the Larmor radius normalized to the tokamak minor radius, ω is the kink mode frequency, ω_b is the trapped fast particle bounce frequency, $\omega_\parallel$ is the passing fast particle transit frequency, and $\langle \cdot \rangle_{q<1}$ denotes the average over the volume within the $q = 1$ surface; the non-adiabatic contribution from passing fast particles can be neglected [Coppi 1990]. As for the non-adiabatic contribution from trapped particles, its structure is then aligned with the equilibrium magnetic field lines instead of being aligned with the kink mode: its spatial dependence is in $e^{i\varphi - iq\theta}$ instead of being in $e^{i\varphi - i\theta}$. This non-adiabatic contribution contains in particular a kinetic factor $\frac{1}{\omega - \omega_d}$, where ω_d is the trapped fast particle precession frequency; its sign therefore depends on the velocity of the considered fast particles. If $\omega > \omega_d$, then their contribution is usually destabilizing; on the contrary, if $\omega < \omega_d$ (that is to say, if the fast ions are fast enough), then their contribution is usually stabilizing. In practice, to meet this last condition, the fast particles need to have an energy of at least a few tens of keV.

If $\omega_d \sim \omega$, a resonance can occur between the internal kink mode and the fast particles: depending on the ratio of the fast ion kinetic pressure to the magnetic pressure β_k, fishbone modes are then triggered [Chen 1984, Porcelli 1991]. Fishbones are thus called because of the characteristic shape they give to magnetic perturbations measured with Mirnov coils [Mirnov 1971]: see Figure 2.4.

In JET, ICRH-generated fast particles can reach energies up to 2 MeV; the following ordering is therefore met: $\omega \ll \omega_d$, and the $\frac{1}{\omega - \omega_d}$ factor can be approximated as $-\frac{1}{\omega_d}$.

[1] Note that the definition of the adiabatic term adopted in [Coppi 1990], that is to say $\tilde{f}^{\mathrm{ad}} = -\boldsymbol{\xi}_\perp \cdot \boldsymbol{\nabla} f_{\mathrm{eq}}$, is not the one which is usually adopted in the literature.

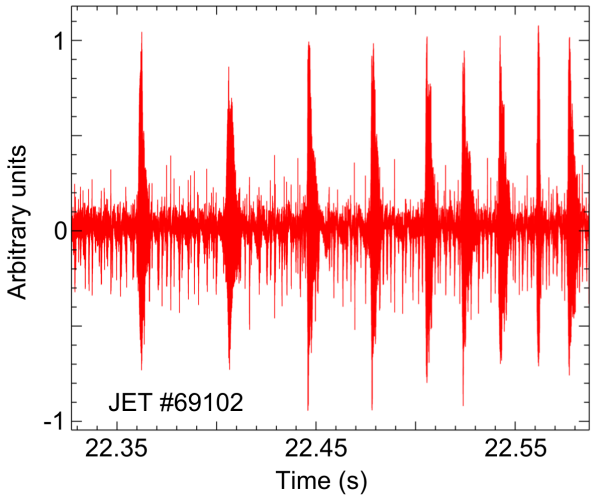

FIGURE 2.4 – Magnetic perturbation timeline from a Mirnov coil during JET discharge #69302 exhibiting characteristic fishbone activity.

The overall fast ion contribution then comprises two terms: see expression (3.10), from [Porcelli 1991]. One of them is usually stabilizing, while the other is usually destabilizing. The former is stronger when q is lower (and lower than 1 in any case), while the latter is stronger when the magnetic shear $s = rq'(r)/q$ is higher. Consequently, the fast particles closest to the magnetic axis usually have a stabilizing effect, while those further from the magnetic axis (but still within the $q = 1$ surface) have a destabilizing effect. It is therefore important for stabilization that the fast particles distribution be as peaked as possible on the magnetic axis.

Other mechanisms of sawtooth control by fast particles have been evidenced in the literature. In particular, ICRF current drive can modify the q-profile and thus the magnetic shear in the core plasma. Consequently, the ratio between the fast particle adiabatic and non-adiabatic contributions is modified. Passing ions with large orbit width, close to the $q = 1$ surface and with an asymmetric distribution in parallel velocity have also been shown to have an impact on sawtooth crashes.

2.3 Overview of ITG turbulence and GAMs/EGAMs

2.3.1 Turbulence: the ITG mode

Various turbulent (*i.e.* with high mode numbers) modes have been extensively studied: at low β, the main ones are the Ion Temperature Gradient (ITG) modes [Horton 1981], the Electron Temperature Gradient (ETG) modes [Drake 1988, Horton 1988], the Trapped Ion Modes (TIM) [Tagger 1977, Tang 1977, Biglari 1989], and the Trapped Electron Modes (TEM) [Kadomtsev 1970].

Among them, the ITG are one of the most frequent and harmful turbulent modes. They can be described in ballooning representation.

Ballooning representation

In ballooning representation [Glasser 1977, Lee 1977, Connor 1978, Connor 1979, Hazeltine 1990], the perturbed electric potential reads, at the lowest order in ρ_*,

$$\tilde{\phi}(\mathbf{x}_G, t) = e^{-i\omega t} e^{in\varphi} \sum_{\ell=-\infty}^{+\infty} \hat{\Phi}(\theta + 2\ell\pi) e^{-inq(\theta+2\ell\pi-\theta_0)} + c.c. \tag{2.7}$$

The sum over ℓ ensures the 2π-periodicity in θ. The function $\hat{\Phi}$ provides the poloidal shape of the modes; it has to decrease fast enough at infinity for $\hat{\Phi}^2$ to be integrable. It appears that ITG modes verify this integrability condition.

The modes are usually localized on the low field side, which is called the *bad curvature* region, for this is where the excitation of instability is the easiest: $\boldsymbol{\nabla} B$ and $\boldsymbol{\nabla} p$ there have the same orientation. On the contrary, the high field side is called the *good curvature* region, for $\boldsymbol{\nabla} B$ and $\boldsymbol{\nabla} p$ there have opposite orientations, which makes it harder for modes to be excited. This asymmetry in θ provides the name of the representation: the modes are localized on the low field side; this can be compared to an excrescence on that side, hence the name *ballooning*.

θ_0 is called the ballooning angle: under certain circumstances linked to the magnetic shear, θ_0 coincides with the value of the poloidal angle for which the mode is the strongest. The radial dependence is taken into account through the linearized dependence of q on r: $q = q_0 + (r - r_0)q_0'$, where r_0 is the minor radius of the reference resonance surface, $q_0 = q(r_0)$ and $q_0' = q'(r_0)$.

The representation here above is equivalent to the following expression:

$$\tilde{\phi}(\mathbf{x}_G, t) = e^{i[K_0(r-r_0)+n\varphi]} \sum_{m=-\infty}^{+\infty} \hat{\phi}\left(\frac{r - r_m}{d}\right) e^{-im\theta} + c.c., \tag{2.8}$$

where $\hat{\phi}$ is the small scale radial envelope, $K_0 = nq_0'\theta_0$ is the radial wave vector, r_m is the minor radius of a given resonance surface and verifies $q(r_m) = m/n$, m is the corresponding poloidal mode number, and $d = 1/nq_0'$ is the distance between two resonance surfaces. $\hat{\Phi}$ in expression (2.7) is the Fourier transform of the small scale radial structure $\hat{\phi}$.

It can be seen in expression (2.8) that, through K_0, the ballooning angle θ_0 also provides a large scale radial envelope. To explicitly get this structure, a supplementary function (not written here), which is the Fourier transform of the considered radial envelope and therefore depends on θ_0, has to be determined. Then, multiplying equation (2.8) by this function and integrating over θ_0 yields the large scale radial envelope.

It can be seen in expression (2.7) that the ballooning representation provides an $n(\varphi - q\theta)$ structure: the modes are aligned with the magnetic field lines. Given the 2π periodicity in θ and φ, the alignment of the modes with the magnetic field lines gives a particular role to the so-called *rational* flux surfaces. Those are flux surfaces on which the safety factor is rational: $q = \frac{m}{n}$, where m and n are not higher than a few tens. On such flux surfaces, the field lines are closed: starting from a given point in space, they will reach the same point again after m toroidal turns and n poloidal turns. This configuration enables a resonance to take place: a mode reaches its maximal intensity on the corresponding rational flux surface.

ITG mode structure

The ITG modes are expressed in the form of the ballooning representation; the $\hat{\Phi}$ function and the dispersion relation which provides the mode frequency ω are to be determined. We here consider the case of a mode excited by ions with a $Z_i = 1$ charge number, with equal electron temperature and ion temperature: $T_e = T_i$.

Looking for the poloidal shape $\hat{\Phi}$ under the form

$$\hat{\Phi} = \hat{\Phi}_0 e^{-\frac{(y-y_0)^2}{2\Delta^2}}, \tag{2.9}$$

where $\hat{\Phi}_0$ is a constant and $y = \theta - \theta_0$, one finds (see Appendix A for the computation):

$$y_0 = \theta_0(s_0 - 1)\left(1 - 2s_0 + 2\frac{k^2 s_0^2}{\Omega_g}\right)^{-1}, \tag{2.10}$$

$$\Delta^2 = -2\Omega_\parallel^2\left[2\frac{1+\Omega_n^*}{\Omega_p^*} + \left(2-\theta_0^2\right)\Omega_g - 2k^2 + \frac{\theta_0^2(s_0-1)^2\Omega_g^2}{(1-2s_0)\Omega_g + 2k^2 s_0^2}\right]^{-1}, \tag{2.11}$$

where $s_0 = r_0 q_0'/q_0$ is the magnetic shear on the reference resonance surface, $k = k_\theta \rho_i$ is the normalized poloidal wave vector, $k_\theta = nq_0/r_0$ is the poloidal wave vector, $v_\mathrm{T} = \sqrt{T_i/m_i}$ is the ion thermal velocity, $\Omega_\parallel = v_\mathrm{T}/qR\omega$ is the normalized transit frequency, $\Omega_g = 2k_\theta T_i/eBR\omega$ is the normalized fluid drift frequency, $\Omega_n^* = -k_\theta T_i n_i'(r)/\omega eBn_i$ is the normalized density diamagnetic frequency, and $\Omega_p^* = -k_\theta T_i p_i'(r)/\omega eBp_i$ is the normalized pressure diamagnetic frequency.

ITG stability

The dispersion relation reads (see Appendix A for the computation)

$$\left[2\frac{1+\Omega_n^*}{\Omega_p^*} + \left(2-\theta_0^2\right)\Omega_g - 2k^2 + \frac{\Omega_g^2\theta_0^2(s_0-1)^2}{(1-2s_0)\Omega_g + 2k^2 s_0^2}\right]^2 + 2\Omega_\parallel^2\left[(1-2s_0)\Omega_g + 2k^2 s_0^2\right] = 0. \tag{2.12}$$

To better understand this relation, let us consider a simple case, in the approximation $\theta_0 = 0$, $\Omega_\parallel \ll 1$ and $k \ll 1$. The dispersion relation then reads

$$\omega^2 + \omega\omega_n^* + \omega_{gf}\omega_p^* = 0, \tag{2.13}$$

where $\omega_{gf} = 2k_\theta T_i/eBR$ is the fluid drift frequency, $\omega_n^* = -k_\theta T_i n_i'(r)/eBn_i$ is the density diamagnetic frequency, and $\omega_p^* = -k_\theta T_i p_i'(r)/eBp_i$ is the pressure diamagnetic frequency.

The ITG frequency is thus the root of a second order polynomial. The mode is unstable if $\mathrm{Im}(\omega) > 0$: in the ordering here considered, this corresponds to the condition $(\omega_n^*)^2 - 4\omega_g\omega_p^* < 0$. This condition also reads

$$\left|\frac{p_i'(r)}{p_i}\right| > \frac{R}{8}\left|\frac{n_i'(r)}{n_i}\right|^2. \tag{2.14}$$

This inequality shows that a threshold in temperature gradient exists for the excitation of ITG modes. This threshold is a growing function of the density gradient: the density gradient is stabilizing, while the temperature gradient is destabilizing. A consequence is that, for a given density gradient, the actual temperature gradient in a tokamak cannot exceed the ITG threshold: if $|T_i'(r)/T_i|$ becomes steeper than the threshold, turbulence will start, causing radial transport, and the temperature gradient will then become lower.

2.3.2 Zonal flows and GAMs

The study of zonal flows and GAMs is of interest because of their interaction with turbulence. An overview of the excitation of zonal flows and GAMs, along with their interaction with turbulence, can be found in [Zarzoso 2012a]. Based on this description, we give below a brief presentation of those modes, with focus on GAMs in view of the study of EGAMs (see Section 2.3.3, Chapter 4, and Chapter 5).

Zonal flows

In tokamaks, in the presence of a radial electric field, an $\mathbf{E} \times \mathbf{B}$ poloidal velocity arises (see Section 1.2.3). If the electric field varies in r, then radially sheared poloidal flows can appear, leading to the reduction of turbulence [Biglari 1990, Waltz 1994, Hahm 1995, Hahm 1999]. The mechanism of turbulence mitigation by steady poloidal flows exhibiting radial shear is illustrated in Figure 2.5.

Various axisymmetric modes can lead to the excitation of radially sheared poloidal flows. In the literature, three types are usually distinguished: mean field flows, with a null frequency; low frequency modes, with a frequency of the order of a few kHz; and higher frequency modes, with a frequency of the order of a few 10 kHz. The latter cor-

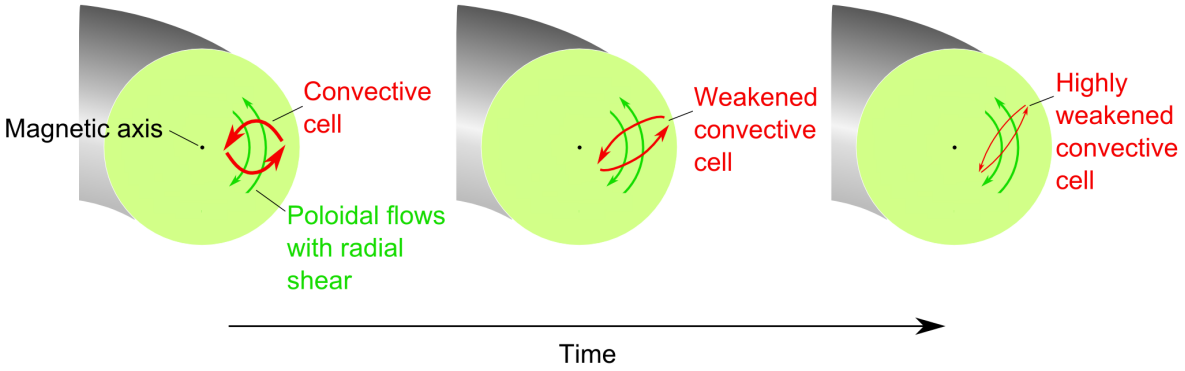

FIGURE 2.5 – Mitigation of a turbulent convective cell via radially sheared poloidal flows.

respond to GAM-like modes; while in the literature mean field flows and low frequency $n = 0$ modes may both be called zonal flows. This confusion is understandable as in most cases those two types interact in the same way with turbulence, since the frequency of low frequency modes is low enough compared to the frequency of turbulence to be assimilated to zero. In the present thesis, we have chosen the convention to give the name *zonal flows* to the low frequency modes.

Zonal flows are low-frequency modes (a few kHz) with an $(m, n) = (0, 0)$ structure: those modes correspond to poloidal flows driven by an $\mathbf{E} \times \mathbf{B}$ drift. Zonal flows have been found to be non-linearly excited by turbulence [Hasegawa 1979, Chen 2000, Diamond 2001, Malkov 2001, Diamond 2005]. They can therefore provide a saturation mechanism for turbulence: turbulent modes excite zonal flows, which in turn mitigate turbulence thanks to the radially sheared poloidal flows. This saturation mechanism is of interest in view of turbulence control; however a drawback is the difficulty for an operator to control the excitation of zonal flows.

GAMs

Geodesic Acoustic Modes (GAMs) are modes which are similar to zonal flows; in particular they have an axisymmetric $n = 0$ structure and exhibit a radial electric field. They differ from zonal flows in particular via their poloidal structure, since they have an $m = 1$ component in addition to the $m = 0$ component shared with zonal flows (see Figure 2.6), and via their frequency (a few 10 kHz), which is an order of magnitude higher than that of zonal flows. Note that the $m = 1$ component of GAMs exhibits a $\sin\theta$ structure, where θ is the poloidal angle counted from the equatorial plane: this component is null at first order on the equatorial plane, as shown in Figure 2.6. GAMs are thus called for they are caused by the geodesic curvature of the magnetic field (*geodesic* qualifies the component of the field curvature $(\boldsymbol{\nabla}\mathbf{b}) \cdot \mathbf{b}$ which is tangential to flux surfaces, by opposition to the

normal curvature which is perpendicular to flux surfaces), and for their frequency is of the order of the ion sound wave frequency:

$$\omega_{\mathrm{GAM}} \sim \frac{v_{\mathrm{T}}}{R}. \tag{2.15}$$

GAMs are Landau-damped in thermal plasmas, with a damping factor proportional to e^{-q^2}, where q is the safety factor. Since the safety factor is usually higher in the edge plasma, the damping of GAMs is smaller there; GAMs are therefore usually observed in the edge plasma. This fact is illustrated in Figure 2.6, and evidenced in Figure 2.7 which shows a reflectometry spectrogram from Tore Supra: the GAM there appears as a white line at frequency 8-18 kHz, for a normalized radius comprised between 0.75 and 0.95.

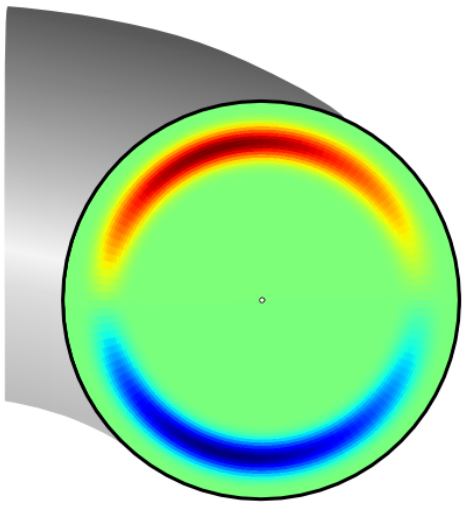

FIGURE 2.6 – Illustration of the GAM structure, obtained with the GYSELA code [Sarazin 2006, Grandgirard 2008, Sarazin 2010].

GAMs were discovered in the 60s [Winsor 1968], and later enjoyed renewed interest when they were found to have interaction with turbulence [Hallatschek 2001, Jakubowski 2002, Ramisch 2003, Miyato 2004, Nagashima 2005, Angelino 2006, Miki 2007, Conway 2011, Sasaki 2012, Xu 2012]. When considering the interaction of radially sheared poloidal flows with turbulence, the GAMs may seem flawed when compared to the zonal flows because of their higher frequency. Indeed, if the poloidal flows oscillate too quickly, then the turbulence may only be sensitive to the time average component of those flows, which is usually zero in the case of GAMs. For instance, simulations with a fluid code have shown that the effect of zonal flows on turbulence is, in the region of parameters then explored, largely dominant over the effect of GAMs [Miyato 2004]. However, the frequency of GAMs is generally low enough for an interaction with turbulence to occur (turbulence covers a wide range of frequencies, from 10 kHz to 1 MHz, with a peak around

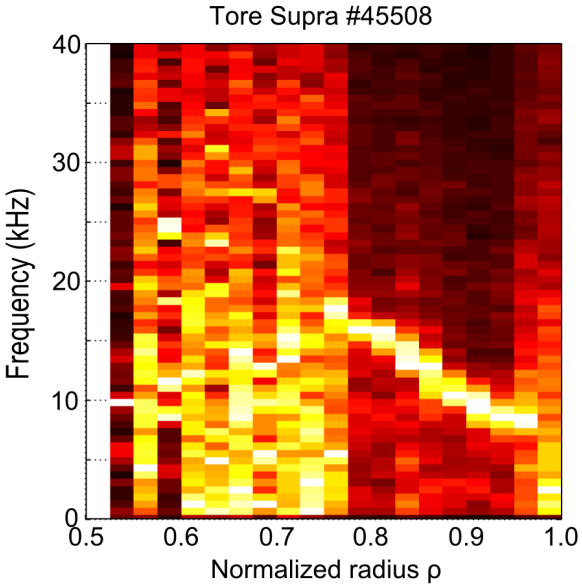

FIGURE 2.7 – Reflectometry spectrogram exhibiting the signature of a GAM in Tore Supra. Source: [Storelli 2014].

100 kHz.). In some cases, the effect of GAMs on turbulence may even be dominant over the effect of zonal flows [Waltz 2008]. In addition, the interaction of GAMs with turbulence may not be limited to a quench of convective cells via radially sheared poloidal flows: in [Miyato 2004], the onset of GAMs corresponds to a reduction of the heat flux, though no correlation is observed between the GAM oscillatory flows and the heat flux.

The ITG turbulence frequency ω_{ITG} is of the order of

$$\omega_{\mathrm{ITG}} \sim k_\theta \rho_i \frac{v_{\mathrm{T}}}{L_p}, \tag{2.16}$$

where $L_p = \frac{r}{p}\frac{dp}{dr}$ is the characteristic pressure gradient length. From a heuristic point of view, GAMs may interact with turbulence if $\omega_{\mathrm{GAM}} < \omega_{\mathrm{ITG}}$. This condition may be satisfied more easily in the edge plasma where L_p is usually lower than in the core plasma. This inequality also shows that ITG modes exhibiting large wave vectors k_θ may interact more easily with GAMs. A consequence of those two observations could be that GAMs interact with most ITG modes in the edge plasma, while they may interact mainly with small-scale modes in the core plasma. The radial mode structure also matters. The best interactions are expected when GAMs and ITG modes have similar radial wave vectors. See the end of Section 2.3.3 for a discussion on the EGAM radial structure.

Like in the case of zonal flows, it was found that GAMs can be non-linearly excited by turbulence [Itoh 2005, Chakrabarti 2007, Guzdar 2008, Zonca 2008, Hager 2012]. Therefore, they can provide a saturation mechanism for turbulence. However, like in the case

of zonal flows, a drawback is the difficulty for an operator to control the excitation of GAMs. At first glance, GAMs may therefore not seem as promising as zonal flows for turbulence control: the former have a higher frequency than the latter, which usually leads to a reduced impact on turbulence, and both seem hard to control. Still, GAMs have an asset: it has been found that GAM-like modes, called EGAMs, can be excited by fast ions. Since fast ions can be controlled, to some extent, by NBI and ICRH, the control of EGAMs by an operator may be easier than the control of zonal flows and GAMs. Then, if EGAMs were to have a mitigating impact on turbulence in certain ranges of parameters, they would provide a controlled way to reduce turbulent transport. Current knowledge on EGAMs is presented in Section 2.3.3.

2.3.3 EGAMs

We have seen in Section 2.3.2 that zonal flows and GAMs interact with turbulence. However those modes are hard to control, since they are naturally damped in thermal plasma (even in non-collisional plasma, because of Landau damping), and are usually excited non-linearly by turbulence itself, which leads to saturation but not proper control of turbulence.

It was found, in a JET experiment with Ion Cyclotron Resonant Heating (ICRH), that n=0 modes identified [Berk 2006, Boswell 2006] as Global GAMs could be driven unstable by trapped energetic ions. This observation led to the idea of controlling the GAMs, and perhaps plasma turbulence coupled to the GAMs, with energetic particles. Later, an experiment on DIII-D with counter-current Neutral Beam Injection (NBI) revealed modes, somewhat similar to those observed on JET, but at a frequency twice as low as the characteristic GAM frequency [Nazikian 2008, Berk 2010]. Studies [Fu 2008, Qiu 2010, Kolesnichenko 2013] aiming at explaining this experiment found new modes called Energetic-particle-driven GAMs (EGAMs), and investigated them. Those EGAMs were also detected [Zarzoso 2012b] in the 5D gyrokinetic code GYSELA [Sarazin 2006, Grandgirard 2008, Sarazin 2010], at about half the expected GAM frequency, like in the DIII-D experiment [Nazikian 2008]. Due to their similarity with GAMs, the EGAMs are good candidates for reducing turbulent transport, thanks to vortex shearing (see Section 2.3.2). However, recent numerical simulations suggest that the impact of EGAMs on turbulence may not always be as positive as expected, and requires further investigation [Zarzoso 2013]. EGAMs can also be responsible for fast ion losses under certain circumstances [Fisher 2012]. Those elements justify extensive study of EGAMs, to better understand the circumstances under which they can be excited by fast particles, and those under which they may have a mitigating impact on turbulence. In particular, understanding their links with GAMs may enable researchers to make use of similarities

between the two modes in the study of their interaction with turbulence.

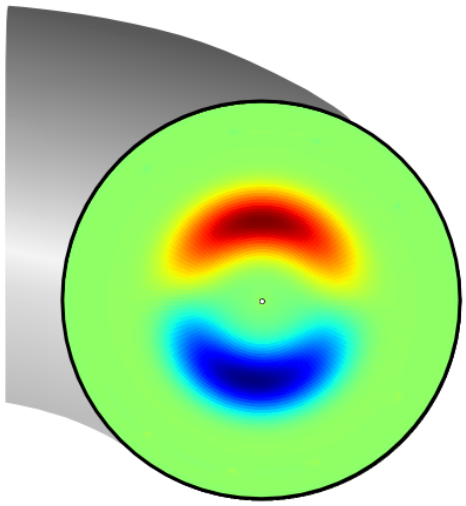

FIGURE 2.8 – Illustration of the EGAM structure, obtained with the GYSELA code [Sarazin 2006, Grandgirard 2008, Sarazin 2010].

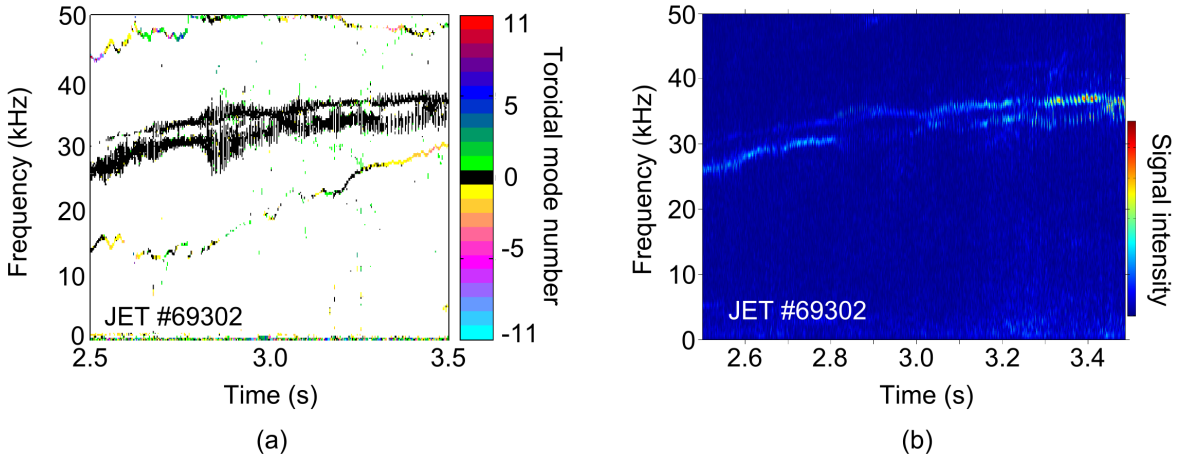

FIGURE 2.9 – Magnetic and reflectometry spectrograms exhibiting the signature of an EGAM in JET. (a) Magnetic spectrogram; data from Mirnov coils [Mirnov 1971]. (b) Reflectometry spectrogram; source: [Arnichand 2014].

Like GAMs, EGAMs have been observed in various tokamaks, and have an axisymmetric structure ($m = 0, 1; n = 0$), with the $m = 1$ component exhibiting a $\sin\theta$ phase. Unlike GAMs, they are excited by fast particles with a linear mechanism and usually appear in the core plasma, as illustrated in Figure 2.8, and evidenced in a JET discharge (see Figures 2.9 and 2.10). In addition, their frequency is usually different from that of GAMs [Nazikian 2008], by a factor which can vary between approximately 1 and 2, depending on the equilibrium conditions.

The experimental signature of an EGAM on JET is presented in Figure 2.9. The left hand-side graph is a magnetic spectrogram showing the toroidal mode number of each displayed mode. $n = 0$ is characterized by the black colour: the EGAM can clearly be seen at a frequency comprised between 25 and 38 kHz. The right hand-side graph is a reflectometry spectrogram, with a resonance position situated in the core plasma. The EGAM clearly appears at the same frequency as in the magnetic spectrogram. Reflectometry measurements during JET discharge #69302 were made at 4 different radial positions. In the spectrograms obtained from the two outer-most positions, no EGAM appears; while the EGAM is visible in the spectrograms obtained from the two inner-most positions. Those reflectometry results, which show the core localization of EGAMs, are summarized in Figure 2.10.

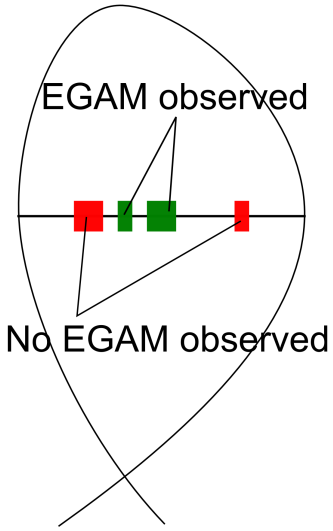

FIGURE 2.10 – Reflectometry measurements in JET: radial localization of EGAMs in discharge #69302. Reflectometry analysis: [Arnichand 2014]

Two conditions are required for EGAMs to be excited by fast particles: the availability of energy from the fast particles to be transferred to a potential mode, and a resonance between the fast particles and the mode to make the transfer of energy possible.

In practice, the first condition corresponds to the existence of a positive slope $\partial_E F_k > 0$ in the distribution function of fast particles with respect to the kinetic energy. The energy used to excite EGAMs therefore comes from the velocity space.

The second condition corresponds to a resonance between the EGAM and one of the fast particle characteristic frequencies (see Section 1.2.3). In practice, the resonance may occur with the bounce frequency of barely trapped particles, the value of which is close to the EGAM frequency. In JET discharge #69302, off-axis ICRH was applied on the high-field side: a population of anisotropic barely trapped fast particles was thus created,

with available energy that led to the excitation of EGAMs. The resonance may also occur with the transit frequency of passing fast particles, if the fast ion kinetic energy is low enough for the transit frequency to be close to the EGAM frequency. In DIII-D, EGAMs were excited by counter-passing NBI. The available energy came from the anisotropy of the fast particle distribution, while the transit frequency of the fast particles was found to be about twice as high as the detected EGAM frequency [Nazikian 2008]. In view of the analytical results presented in Chapter 4, this factor 2 between the fast particle transit frequency and the EGAM frequency is not in contradiction with the existence of a resonance. In particular, as can be seen on Figure 4.8, what matters is the resonance with the real frequency of the relevant root of the *GAM* dispersion relation. In the presence of fast particles, the imaginary part of this root changes and becomes positive, thus leading to the excitation of the EGAM; it is important to note that the real part can also change, by a factor of the order of 1 to 2.

As mentioned above, a major difference between GAMs and EGAMs is their radial structure and location. While GAMs are observed in the edge plasma, EGAMs are observed in the core plasma. It is worth noting that while EGAMs are electrostatic mode and are localized in the core plasma, they trigger magnetic fluctuations which can be detected by Mirnov coils at the edge of the plasma (see Figure 2.9). This observation suggests that EGAMs may have an underlying radial structure which extends from the core to the edge plasma. Numerical simulations of GAMs taking into account magnetic fluctuations were performed [Biancalani 2014] with the NEMORB code [Bottino 2011]: they did not reveal any change in the GAM oscillations with respect to simulations performed with electric field perturbations only. This is in agreement with the analytical theory developed in [Smolyakov 2010]. However, it was shown analytically that electromagnetic GAM side-bands $m = \pm 2$ may exist outside the magnetic surface on which the GAMs appear [Wahlberg 2009].

The issue of the EGAM radial structure is mentioned in the literature, in the framework of experiments [Berk 2006, Nazikian 2008] as well as from a theoretical point of view [Fu 2008, Zonca 2008, Qiu 2010]. The dependence of the GAM frequency ($\omega_{\mathrm{GAM}} \sim v_{\mathrm{T}}/R$) provides a radial continuum: at each radial position corresponds a given GAM frequency. Consequently, GAMs are well localized. On the contrary, dedicated theoretical developments [Fu 2008, Qiu 2010] suggest that EGAMs may correspond to a global eigenfunction of the radial dispersion relation, with a frequency distinct from the GAM continuum. This question of the EGAM radial structure is of particular importance in view of the study of the interaction with turbulence (see Chapter 5).

Chapter 3

Sawteeth stabilization with 3rd harmonic deuterium ICRF-accelerated beam in JET plasmas

In the present chapter, we report on sawtooth stabilization by fast deuterium (D) beam ions accelerated to about 100 keV by Neutral Beam Injection (NBI), and then to the MeV energy range by 3rd harmonic Ion Cyclotron Resonant Heating (ICRH). Four sawteeth from four different JET discharges are studied. JET is the Joint European Torus, a European tokamak located in the UK; it is currently the largest tokamak in the world. One of the studied sawteeth, in discharge #86775, is a 2.5 s long monster sawtooth, during which the fast particle population and the q-profile are remarkably stable. We will see that according to Porcelli's model, its crash is due to a fast occurring event. The stabilization of a sawtooth by 3rd harmonic deuterium ICRH in JET was already studied in [Gassner 2012], in discharge #74951. However, in that discharge, the fast particles did not exhibit a stable profile and the event causing the sawtooth crash occurred on a longer time scale (a few 100 ms). The present study can be found in [Girardo 2015].

The efficiency of sawtooth stabilization by the fast particles obtained in our experiments is assessed within Porcelli's model. We find that the stabilization provided by fast particles is strong, in accordance with the experiments. In particular, the model predicts higher stabilization in the case of discharge #86775, which is the discharge where the monster sawtooth was observed. We then aim at understanding the reasons which cause the sawtooth crashes, while fast particles provide such stabilization.

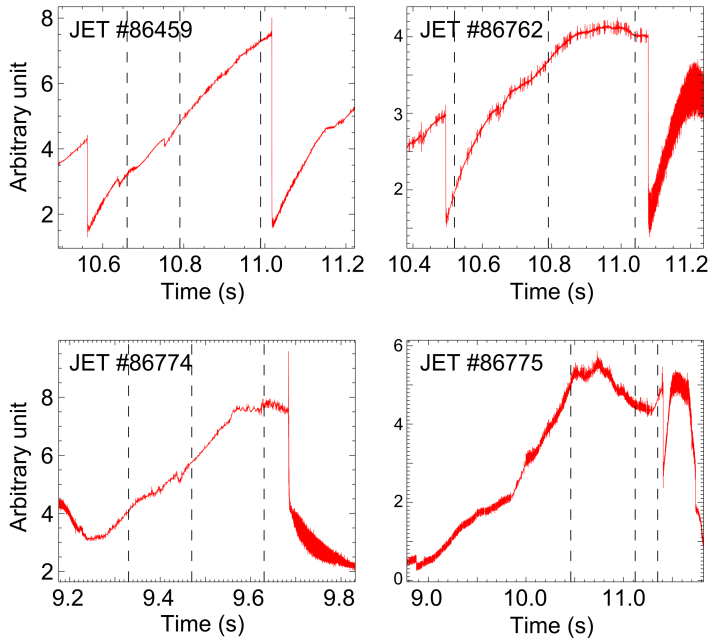

FIGURE 3.1 – Soft X-rays signals for the four sawteeth studied in the present chapter. Arbitrary units on y-axis. The time slices for which values are presented in Table 3.1 are here marked with dashed lines.

3.1 Presentation of the four considered JET discharges - Framework of the present study

Four sawteeth, from four different discharges (#86459, #86762, #86774 and #86775), are considered in the present study. Those four discharges were performed in June and July 2014, in JET with ITER-Like Wall (ILW) [Matthews 2011], at $B_0 \sim 2.3$ T, $I \sim 2$ MA, $R_0 \sim 3$ m and $a \sim 0.9$ m, where B_0 is the intensity of the magnetic field on the magnetic axis, I is the intensity of the toroidal plasma current, R_0 is the major radius of the magnetic axis and a is the minor radius of the plasma.

In all four cases, NBI and 3rd harmonic deuterium ICRH heating were on. For each discharge, four ICRH antennas were used with frequencies between 51.4 and 51.8 MHz, speeding up the NBI-accelerated particles from the 10-100 keV range to the MeV range.

In Figure 3.1, the soft X-ray signals corresponding to the four sawteeth are presented. The first sawtooth occurred in discharge #86459, lasting about 0.4 s. The second sawtooth was measured in discharge #86762, with a duration of over 0.5 s. The third sawtooth happened in discharge #86774 and lasted about 0.4 s. Finally, the fourth sawtooth occurred in discharge #86775: it was a record-long sawtooth in JET with ILW, with a duration of over 2.4 s.

The present study is carried out in the framework of a theoretical model developed by Porcelli in [Porcelli 1991]. According to this model, a sawtooth remains stable as long

as the potential energy functional $\delta\hat{W} = \delta\hat{W}_{\mathrm{MHD}} + \delta\hat{W}_{\mathrm{kin}}$ remains positive, where the MagnetoHydroDynamic (MHD) contribution $\delta\hat{W}_{\mathrm{MHD}}$ usually is negative, and therefore destabilizing, while the kinetic contribution $\delta\hat{W}_{\mathrm{kin}}$ can, under certain circumstances, be positive and therefore stabilizing. The MISHKA1 code [Mikhailovskii 1997] is used to retrieve $\delta\hat{W}_{\mathrm{MHD}}$ for the studied sawteeth. $\delta\hat{W}_{\mathrm{kin}}$ contains two parts: a part from the NBI-accelerated particles, here called $\delta\hat{W}_{\mathrm{NBI}}$, and a part from the ICRH-accelerated particles, here called $\delta\hat{W}_{\mathrm{ICRH}}$. $\delta\hat{W}_{\mathrm{NBI}}$ is computed with an analytical expression, validated for JET in [Angioni 2002]. The computation of $\delta\hat{W}_{\mathrm{ICRH}}$ is based on an integral formula from [Porcelli 1991], and numerical values are obtained with the HAGIS code [Pinches 1998]. The distribution of NBI-accelerated and ICRH-accelerated fast particles is obtained from the SPOT code [Schneider 2005], with input from the NEMO [Schneider 2011] and PION [Eriksson 1993] codes, and run using the RFOF library [Johnson 2011].

The effect of cyclotron current drive on sawteeth stabilization and destabilization has been studied in [Graves 2011]. Though such effects may in general cases have a substantial impact on sawteeth, they are not expected to be significant in our experiments as dipole ICRH was used.

Besides, three of the four studied discharges (#86762, #86774 and #86775) contained helium 3 (He3), in a proportion of 5 to 13 %. In those discharges, in addition to 3rd harmonic D heating, the ICRH may have led to some 2nd harmonic He3 heating. However, the power transferred to the plasma through 2nd harmonic He3 heating was found [Hellsten 2015] to be much lower than through 3rd harmonic D beam heating. For discharge #86775, in the steady-state plasma 0.4 s after the ICRH power reached flat top, the ICRH power absorbed by the D beam was 84 %, while the power absorbed by He3 was 3 % only, the remaining 13 % being absorbed by electrons. The difference in the absorbed powers can be explained as follows: the 2nd harmonic He3 resonance layer occurs at higher magnetic field than the 3rd harmonic D resonance, which means that the ICRH waves first crosses the 3rd harmonic D resonance before reaching the 2nd harmonic He3 resonance layer. In addition, the He3 ions were not pre-accelerated by NBI. Therefore, the effects of fast He3 particles have not been taken into account in the present work.

3.2 Bulk equilibrium reconstruction and MHD excitation of internal kink mode

For the bulk equilibrium reconstruction, the EFIT code has been run in conjunction with data from Motional Stark Effect (MSE) measurements. With this method, the accuracy of the q profile is estimated to be of the order of 10-15 % [Brix 2008]. To generate a straight field line coordinate system required for MHD analysis, the HELENA code

discharge		86459			86762	
$\boldsymbol{t}$**[s]**	10.66	10.79	10.99	10.52	10.79	11.04
$\boldsymbol{q}$ **on axis**	0.96	0.93	0.87	0.97	0.88	0.85
$\boldsymbol{R(q=1)}$ **[m]**	3.33	3.35	3.40	3.29	3.38	3.38
$\boldsymbol{s_1}$	0.14	0.19	0.38	0.08	0.32	0.36
$\boldsymbol{\delta\hat{W}_{\mathrm{MHD}}}$ **[10^{-3}]**	N/A	-0.86	-1.61	N/A	-2.28	-2.03

discharge		86774			86775	
t[s]	9.33	9.47	9.63	10.46	11.12	11.35
$\boldsymbol{q}$ **on axis**	0.99	0.95	0.85	0.75	0.71	0.69
$\boldsymbol{R(q=1)}$ **[m]**	3.33	3.36	3.43	3.42	3.42	3.43
$\boldsymbol{s_1}$	0.11	0.25	0.49	0.61	0.70	0.75
$\boldsymbol{\delta\hat{W}_{\mathrm{MHD}}}$ **[10^{-3}]**	N/A	-2.11	-3.06	-4.41	-4.34	-4.37

Table 3.1 – For the four studied sawteeth, four values are presented at different time slices: q on axis, computed with HELENA; the radial position of the $q = 1$ surface (equatorial plane, low field side), computed with HELENA; the magnetic shear on the $q = 1$ surface s_1, computed with HELENA; and the MHD potential energy functional $\delta\hat{W}_{\mathrm{MHD}}$, computed with MISHKA1. The time slices here mentioned are indicated in Figure 3.1 with dashed lines.

[Huysmans 1991] has then been used. The results are presented in Table 3.1.

The equilibrium computed by HELENA has been used as an input to the MISHKA1 code [Mikhailovskii 1997] to compute the MHD growth rate of the internal kink mode for the four studied sawteeth, at different times, with accuracy estimated to be of the order of 3 % [Gassner 2012]. This MHD growth rate has then been converted to the MHD potential energy functional $\delta\hat{W}_{\mathrm{MHD}}$ as described in [Porcelli 1991]:

$$\delta\hat{W}_{\mathrm{MHD}} = -\frac{s_1}{2\pi}\gamma\tau_{\mathrm{A}}, \tag{3.1}$$

where γ is the internal kink mode growth rate, $s_1 = \bar{r}_1 q'(\bar{r}_1)$ is the magnetic shear on the $q = 1$ surface, $\bar{r}_1 = r_1\sqrt{\kappa_1}$ is the average minor radius of the $q = 1$ surface, r_1 is the minor radius of the $q = 1$ surface on the equatorial plane, κ_1 is the ellipticity of the $q = 1$ surface, $\tau_{\mathrm{A}} = \sqrt{3}R_0/v_{\mathrm{A}}$ is the Alfvén time, R_0 is the plasma major radius on the magnetic axis, $v_{\mathrm{A}} = B_0/\sqrt{\mu_0 n_i m_i}$ is the Alfvén speed, B_0 is the norm of the magnetic field on the magnetic axis, μ_0 is the vacuum magnetic permeability, n_i is the peak ion density and m_i is the ion mass.

The results from MISHKA1 are presented in Table 3.1. Note that $\delta\hat{W}_{\mathrm{MHD}}$ has been computed only when q on axis had a value equal to or lower than 0.95: when q is too close to 1, numerical computations are not accurate enough; and expression (3.1) is valid only for largely unstable situations, that is to say when q on axis is much lower than 1.

3.3 NBI contribution to $\delta\hat{W}_{\mathrm{kin}}$

Let us recall that $\delta\hat{W}_{\mathrm{kin}} = \delta\hat{W}_{\mathrm{NBI}} + \delta\hat{W}_{\mathrm{ICRH}}$.

The NBI contribution reads [Angioni 2002]:

$$\delta\hat{W}_{\mathrm{NBI}} = \frac{\sqrt{2}\mu_0}{2\pi B_0^2 \varepsilon_1^{1/2}} \left[\frac{3}{2} \int_0^{\rho_1} \frac{\rho^{1/2}}{\rho_1^{3/2}} p_{\mathrm{NBI}} d\rho - p_{\mathrm{NBI}}(\rho_1) \right], \tag{3.2}$$

where p_{NBI} is the pressure of NBI-accelerated fast particles, and ρ_1 is the normalized radial position of the $q = 1$ surface. It is found in [Angioni 2002] that this analytical expression gives, in the case of JET NBI, very good agreement with values obtained from numerical codes modelling kinetic-MHD modes interactions. The radial pressure profiles of the NBI-accelerated ions are obtained with the SPOT code [Schneider 2005] coupled with the NBI deposition simulation code NEMO [Schneider 2011]. They are assumed to be stable during the time scales of interest, since the neutral particle injection was stable during the considered sawteeth, and since NBI fast particles are not expected to be affected by the tornado modes observed in discharges #86459 and #86762 (their energy is too low).

The results are presented in Figure 3.4 and discussed in Section 3.7. Note that the NBI contribution $\delta\hat{W}_{\mathrm{NBI}}$ is generally small compared to the ICRH contribution $\delta\hat{W}_{\mathrm{ICRH}}$.

3.4 ICRH-accelerated fast particles distribution

ICRH ions are known to be mostly trapped and it is assumed that their banana tips are coincident with the ICRH resonant layer (situated in the central region, close to the magnetic axis in our experiments). Following [Hellesen 2013], we here use an extension of the classical Stix model [Stix 1975, Hellesen 2013] to high harmonics. In the central region, the radial variations of the background electron temperature and density are slow compared to the radial variations of the fast particle density. The following ansatz for the distribution function is thus employed:

$$F_{k,\mathrm{ICRH}} = \lambda f_\rho(\rho) f_{\mathrm{E}}(E_k) \delta(\Lambda - \Lambda_0), \tag{3.3}$$

where λ is a normalization factor, $\rho = r/\bar{a}$ is the normalized minor radius coordinate, r is the minor radius coordinate, $\bar{a} = a\sqrt{\kappa_a}$ is the average minor radius of the plasma, a is the minor radius of the plasma measured on the equatorial plane, κ_a is the ellipticity of the plasma at $r = a$, $\Lambda = \mu_k B_0 / E_k$ is the pitch coordinate, $E_k = 1/2 m_k v^2$ is the kinetic energy, m_k is the mass of the fast particles, $\mu_k = m_k v_\perp^2 / 2B$ is the magnetic moment, $v_\perp$ is the norm of the perpendicular velocity, v is the total norm of the velocity, and B is the norm of the magnetic field.

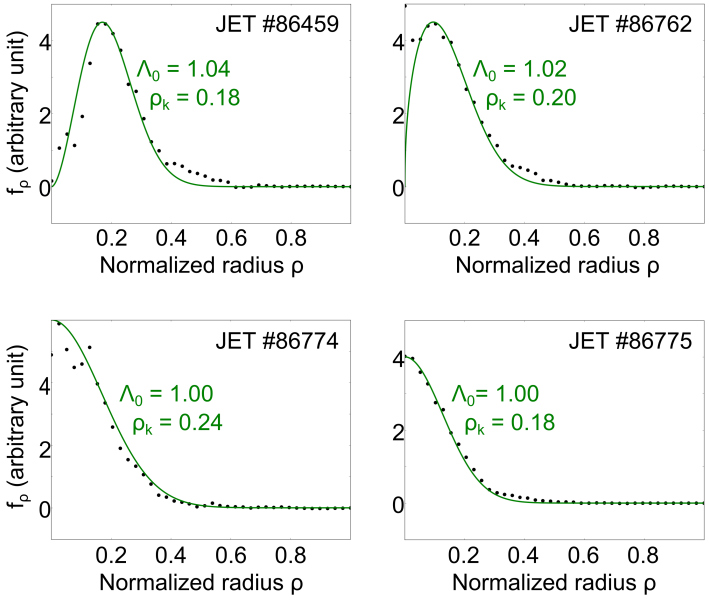

FIGURE 3.2 – Radial fast ion distribution: data from SPOT (black circles) and corresponding fits (green solid lines) - discharges #86459, #86762, #86774 and #86775.

Λ_0 is the value of the pitch on the ICRH resonance layer. In the four discharges, the magnetic field was chosen to ensure that the resonance layer would be situated close to the magnetic axis: consequently Λ_0 is close to 1.0 in the four discharges. We find $\Lambda_0 = 1.04$ in discharge #86459, $\Lambda_0 = 1.02$ in discharge #86762, and $\Lambda_0 = 1.00$ in discharges #86774 and #86775. The influence of Λ_0 on sawtooth stabilization according to Porcelli's model is discussed in Section 3.7.

A Gaussian-like shape of the radial distribution function is assumed:

$$f_\rho(\rho) = \rho^\alpha e^{-(\rho/\rho_k)^2}, \tag{3.4}$$

where ρ_k is the characteristic length of the radial distribution, and α is a constant used to ensure that the maximum of the distribution function is reached on the resonance layer. The ICRH-accelerated fast particle distribution is modelled with the SPOT code [Schneider 2005], with the use of the NEMO code [Schneider 2011] (for the NBI deposition), the RFOF library [Johnson 2011] (for the interaction between the ions and the ICRF wave) and the PION code [Eriksson 1993] (for the propagation of the ICRF wave in the plasma). The numerical results, along with the corresponding fits, are presented in Figure 3.2.

The TOFOR diagnostic [Gatu Johnson 2008] has been used to measure the energy distribution of the neutrons emitted by reactions with fast deuterium. From this energy distribution of the neutrons, it has been possible [Hellesen 2010a, Hellesen 2010b, Eriks-

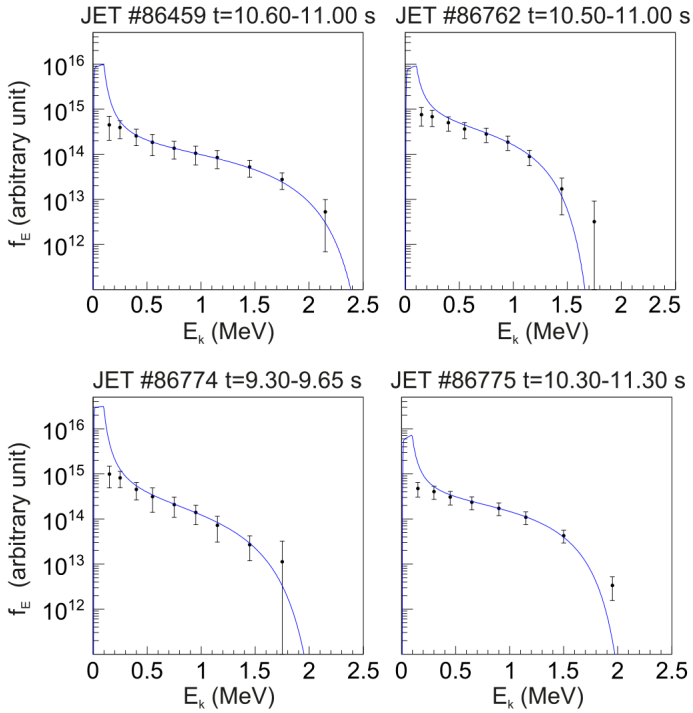

FIGURE 3.3 – Energy distribution retrieved from TOFOR measurements (circle marks with error bars) and analytic fit (full line curve) - discharges #86459, #86762, #86774 and #86775.

discharge	86459	86762	86774	86775
$\boldsymbol{W_{k,\mathrm{ICRH}}}$ **[kJ]**	322	252	249	615

Table 3.2 – $W_{k,\mathrm{ICRH}}$ for the studied discharges: data from SPOT.

son 2013, Hellesen 2013] to estimate the energy distribution f_{E} of the fast deuterium particles. The estimated energy distributions are shown in Figure 3.3, along with analytic distributions obtained by solving a Fokker-Planck equation derived in [Stix 1975]. More details about this Fokker-Planck modelling can be found in [Hellesen 2013]. In Figure 3.3, the cut-off energies in the analytic distributions have been adjusted so that the resulting neutron energy distribution be in agreement with the TOFOR measurements. It can be seen that the deuterium distributions are similar for the four studied sawteeth, with cut-off energies varying between 1.6 and 2.4 MeV.

Note that in Figures 3.2 and 3.3, the y-axis units are arbitrary; what matters is the relative profile of the distribution only: the normalization of the distribution functions is contained in λ in expression (3.3), this λ being determined below in Section 3.5.

3.5 Normalization of the ICRH distribution function

In expression (3.3), f_ρ and f_{E} provide the profiles of the fast particle distribution function, but none of those functions yields the normalization of $F_{k,\mathrm{ICRH}}$. This normalization is represented by λ, a constant in space and velocity which is determined in this section for each studied discharge, using the total energy of the ICRH-accelerated fast particles $W_{k,\mathrm{ICRH}}$. It is necessary to determine λ for the computation of $\delta\hat{W}_{\mathrm{ICRH}}$ (see Section 3.6). $W_{k,\mathrm{ICRH}}$ is defined as

$$W_{k,\mathrm{ICRH}} = \int (dx)^3 (dv)^3 E_k F_{k,\mathrm{ICRH}}. \tag{3.5}$$

Taking into account expression (3.3) of $F_{k,ICRH}$ and the expressions of f_ρ and f_{E}, (3.5) can be written, at lowest order in the inverse aspect ratio $\varepsilon = r/R_0$, as

$$W_{k,\mathrm{ICRH}} = \frac{8\pi^2 R_0 \bar{a}^2}{m\sqrt{2m}} \int_{\rho_{\min}}^{1} d\rho \int_{-\theta_t}^{\theta_t} d\theta \int_0^{+\infty} dE_k \frac{\lambda \rho^{\alpha+1} e^{-(\rho/\rho_k)^2} f_{\mathrm{E}}(E_k) E_k^{3/2}}{\sqrt{1-\Lambda_0+\Lambda_0 \varepsilon \cos\theta}}, \tag{3.6}$$

where θ is the poloidal angle counted from the equatorial plane and $\rho_{\min}$ is the minimum value of ρ reached by fast particles.

Defining

$$c_{r\theta} = \int_{\rho_{\min}}^{1} \int_{-\theta_t}^{\theta_t} \frac{\rho^{\alpha+1} e^{-(\rho/\rho_k)^2}}{\sqrt{1-\Lambda_0+\Lambda_0 \varepsilon \cos\theta}} \, d\theta d\rho, \tag{3.7}$$

$$c_{\mathrm{E}} = \int_0^{+\infty} E_k^{3/2} f_{\mathrm{E}}(E_k) dE_k, \tag{3.8}$$

$W_{k,\mathrm{ICRH}}$ reads:

$$W_{k,\mathrm{ICRH}} = \frac{8\pi^2 \lambda R_0 \bar{a}^2 c_{r\theta} c_{\mathrm{E}}}{m_k \sqrt{2m_k}}. \tag{3.9}$$

The numerical values of $W_{k,\mathrm{ICRH}}$ have been retrieved from SPOT results; they are indicated in Table 3.2. In discharges #86459, #86762 and #86775, the ICRH power was stable during the studied sawteeth; therefore $W_{k,\mathrm{ICRH}}$ can be considered as stable over time. In discharge #86774, the studied sawtooth occurred during a power ramp-up: this ramp-up was not taken into account in SPOT, a time-averaged power value being used instead. However, the rationale presented in Section 3.7 is not altered by this fact: what matters is the evolution of $\delta\hat{W}_{\mathrm{kin}}$ in time, which is found to increase. Taking into account the ICRH power ramp-up in discharge #86774 would only accentuate the increase of $\delta\hat{W}_{\mathrm{kin}}$ over time, and would thus not bring any significant change to the global picture.

3.6 ICRH contribution to $\delta\hat{W}_{\mathbf{kin}}$

3.6.1 Expression of $\delta\hat{W}_{\mathbf{ICRH}}$

To compute $\delta\hat{W}_{\mathrm{ICRH}}$, an integral expression, equation (11) of [Porcelli 1991], is used. This expression is valid in the following limit: when the parallel pressure of fast particles is small compared to their perpendicular pressure, and when the internal kink mode frequency is small compared to the banana drift frequency (condition (2) in [Porcelli 1991]). This limit is relevant to our experiments for the ICRH-accelerated particles, which are in the MeV range (see TOFOR results in Section 3.4).

Thus,

$$\delta\hat{W}_{\mathrm{ICRH}} = \frac{\pi\mu_0\varepsilon_1}{2B_p^2(\bar{r}_1)\bar{r}_1}\left(\frac{2}{m_k}\right)^{3/2}\int_0^{\bar{r}_1} drr\int_{1-\varepsilon}^{1+\varepsilon} d\Lambda\Lambda I_b\frac{I_cI_d - I_q^2}{I_d}\int_0^{+\infty} dE_kE_k^{3/2}\frac{\partial F_{k,\mathrm{ICRH}}}{\partial r}, \tag{3.10}$$

where $\varepsilon_1 = \bar{r}_1/R_0$ is the inverse aspect ratio at the $q = 1$ surface, $B_p(\bar{r}_1) = \bar{r}_1B_0/R_0$ is the poloidal component of the magnetic field on the $q = 1$ surface, $I_b = \frac{v\tau_b}{Rq}$, $I_c = \langle\cos\theta\rangle_b$, $I_d = \langle\cos\theta\rangle_b + s\langle\theta\sin\theta\rangle_b$, $I_q = \langle\cos(q\theta)\rangle_b$, $\langle\cdot\rangle_b$ represents the average over the bounce motion, $v = \sqrt{2E_k/m_k}$ is the velocity of the particle, and τ_b is the bounce period.

Taking into account the expression of $F_{k,\mathrm{ICRH}}$,

$$\frac{\partial F_{k,\mathrm{ICRH}}}{\partial r} = \frac{\lambda}{\bar{a}}\left(\frac{\alpha}{\rho} - \frac{2\rho}{\rho_k^2}\right)\rho^\alpha e^{-(\rho/\rho_k)^2}\delta(\Lambda - \Lambda_0)f_{\mathrm{E}}(E_k). \tag{3.11}$$

Using equation (3.9) to replace λ in this expression, $\delta\hat{W}_{\mathrm{ICRH}}$ reads

$$\delta\hat{W}_{\mathrm{ICRH}} = \frac{\mu_0W_k}{4\pi c_{r\theta}\bar{a}\bar{r}_1^2B_0^2}\int_{\rho_{\min}}^{\rho_1} d\rho\rho^{\alpha+1}\left(\frac{\alpha}{\rho} - \frac{2\rho}{\rho_k^2}\right)e^{-(\rho/\rho_k)^2}I(\Lambda_0), \tag{3.12}$$

where $I(\Lambda_0)$ is defined as $\Lambda I_b\frac{I_cI_d - I_q^2}{I_d}$ evaluated at $\Lambda = \Lambda_0$.

3.6.2 Computation of $I(\Lambda_0)$ with HAGIS

The HAGIS code is used to compute the orbit of fast test particles; ellipticity and Finite Orbit Width (FOW) effects are taken into account. From those orbits, $I(\Lambda_0)$ is computed numerically. The output of HELENA is used for the safety factor and the magnetic shear radial profiles; those profiles are used to numerically compute the integral over ρ in expression (3.12). The results are presented in Figure 3.4 and discussed in Section 3.7.

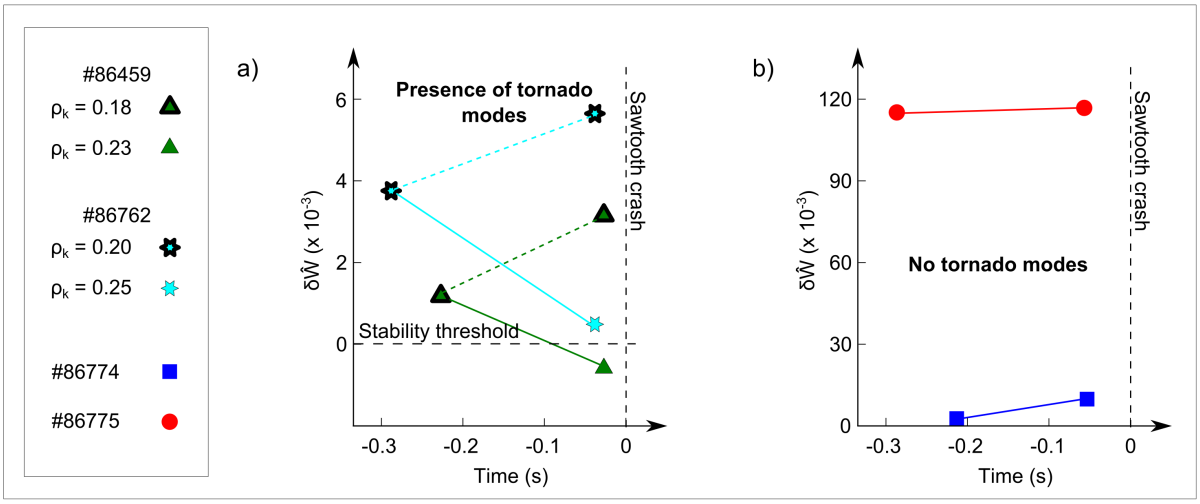

FIGURE 3.4 – Evolutions of $\delta\hat{W} = \delta\hat{W}_{\mathrm{MHD}} + \delta\hat{W}_{\mathrm{kin}}$ in the case of discharges #86459 and #86762 (figure a), as well as discharges #86774 and #86775 (figure b), as functions of time before the sawtooth crashes. For discharges #86459 and #86762, different values of ρ_k have been assumed: the dashed lines show the evolution of $\delta\hat{W}$ for stationary values of ρ_k; the full lines show the expected evolution of $\delta\hat{W}$ assuming ρ_k increases in time. For discharges #86774 and #86775, the full lines show the evolution of $\delta\hat{W}$ taking into account the stability of ρ_k as indicated by the timelines from the neutron cameras.

3.7 Predictions of the model: sawteeth stabilization

The evolutions of $\delta\hat{W} = \delta\hat{W}_{\mathrm{MHD}} + \delta\hat{W}_{\mathrm{kin}}$ are shown in Figures 3.4 a) and 3.4 b). According to Porcelli's theory, a sawtooth crash is due to occur when $\delta\hat{W}$ becomes negative.

In the case of discharges #86459 and #86762, the dashed lines show the evolution of $\delta\hat{W}$ assuming ρ_k (characteristic length of the ICRH fast particles radial distribution) remains constant. This evolution is unlikely, considering the tornado modes which occurred during those two discharges (see Section 3.8.1 below). The full lines show the expected evolution of $\delta\hat{W}$, assuming ρ_k increases during the tornado modes activity. In Figure 3.4-a), an increase of 0.05 in ρ_k has been retained, consistent with the observations made in a JET discharge exhibiting similar features [Gassner 2012]. In discharges #86459 and #86762, gamma-rays signals were too low to retrieve any useful data, and neutron cameras were not in activity, thus prohibiting the direct experimental observation of the fast particle radial redistribution.

In the case of discharges #86774 and #86775, neutron cameras [Adams 1993] with horizontal and vertical lines of sight were available (see Figure 3.5). Thanks to the reaction $\mathrm{D}_{\mathrm{fast}} + \mathrm{D}_{\mathrm{th}} \rightarrow n + {}^3\mathrm{He}$, a broadening of the radial distribution of the fast deuterons during the sawteeth would have been observable on the neutron cameras signals (the signals from the outer channels would have increased while the signals from the inner channels would have decreased, like in [Gassner 2012]). However, in discharges #86774

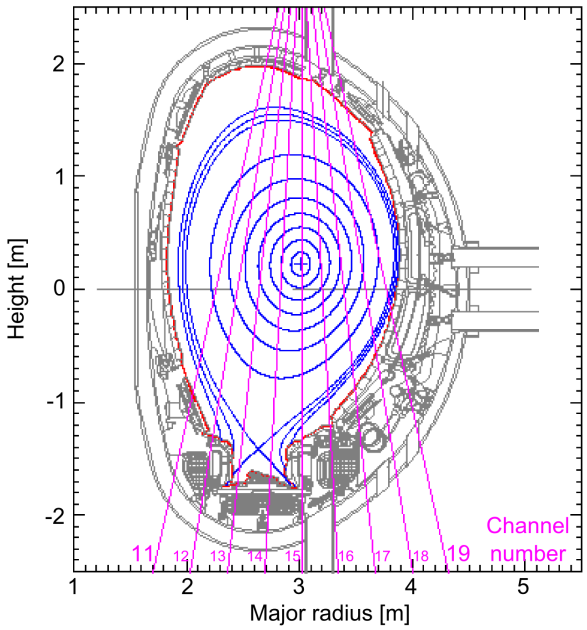

FIGURE 3.5 – Lines of sight of vertical neutron cameras in JET. The blue circles correspond to the magnetic flux surfaces computed with EFIT in discharge #86775, at time t=10.96 s.

and #86775, no significant evolution of the neutron cameras signals was observed during the studied sawteeth (see Figure 3.6), which means that the fast particles were not expelled from within the $q = 1$ surface. In particular, in the case of discharge #86775, the fast particle population was remarkably stable. This is consistent with the fact that no tornado modes were observed (see Section 3.8.1 below). Consequently, the time evolution of $\delta\hat{W}$ has been plotted at constant ρ_k for those two discharges.

It can be observed in Figure 3.4-b) that $\delta\hat{W}$ does not get closer to the crash threshold ($\delta\hat{W} = 0$) when time goes by. On the contrary, $\delta\hat{W}$ tends to get further from the threshold. This fact can be interpreted considering that the fast particle distribution features (Λ_0, ρ_k, $W_{k,\mathrm{ICRH}}$) remain the same, while the radial position of the $q = 1$ surface increases (see Table 3.1) and q on axis decreases. Consequently, the fast particles are found to be contained deeper and deeper within the $q = 1$ surface as time increases, and they are more stabilizing [Porcelli 1991, Porcelli 1992]. The evolutions of $\delta\hat{W}$ computed for discharges #86774 and #86775 show that the sawtooth crashes for those discharges must have been caused by events which are fast (a few 10 ms) compared to the sawtooth characteristic period, since no evolution of $\delta\hat{W}$ in the direction of a crash is observed during the sawtooth.

It can be observed in Figure 3.4-a) that $\delta\hat{W}$ is highly sensitive to the value of ρ_k: this is consistent with the theory [Porcelli 1991, Porcelli 1992]. In discharges #86459 and #86762, without any increase of ρ_k, Porcelli's model would not predict the sawtooth

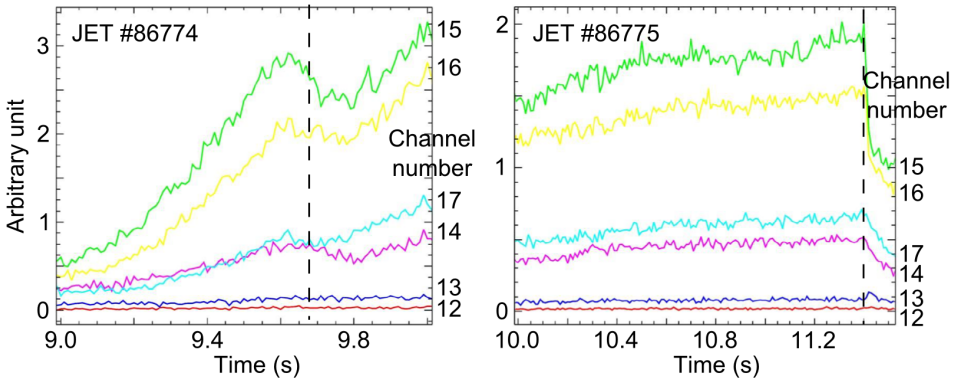

FIGURE 3.6 – Timelines from neutron cameras, vertical channels 12 to 17, discharges #86774 and #86775. The dashed lines show the times of the sawtooth crashes.

crash, since $\delta\hat{W}$ then increases over time and gets further from the crash threshold. On the contrary, taking into account an increase of ρ_k is consistent with the onset of the crash, in the framework of Porcelli's model.

The absolute values of $\delta\hat{W}$ depend strongly not only on ρ_k but also on Λ_0. The closer Λ_0 is to 1.0, the more stabilizing the fast particles are. This is consistent with the fact that when $\Lambda_0 = 1.0$, the fast particles are contained deeper within the $q = 1$ surface and are therefore more stabilizing. It may be difficult to determine Λ_0 with the accuracy necessary for the computation of $\delta\hat{W}$: the needed accuracy is of the order of 1% for the value of B_0 (magnetic field on axis), which is not met by EFIT with MSE. However, contrary to ρ_k, Λ_0 is expected to remain stable over times of a few hundreds of milliseconds, and the time evolution of $\delta\hat{W}$ is hardly sensitive to the value retained for Λ_0. This means that even if the original error made on Λ_0 is higher than 1%, this does not affect the rationale here exposed: what really matters is that Λ_0 is stable during the considered time scales, and that $\delta\hat{W}$ increases over time if ρ_k remains constant.

It can finally be observed in Figure 3.4 that $\delta\hat{W}$ is much higher in the case of discharge #86775 than in the other three cases. This is consistent with the fact that the corresponding sawtooth was much longer (over 2.5 s) than the other three studied sawteeth. This high value of $\delta\hat{W}$ can be explained by the high value of the fast particle energy (see Table 3.2) and by the favourable radial position of the fast particles ($\Lambda_0 = 1$ and small ρ_k: see Figure 3.2) in the case of discharge #86775.

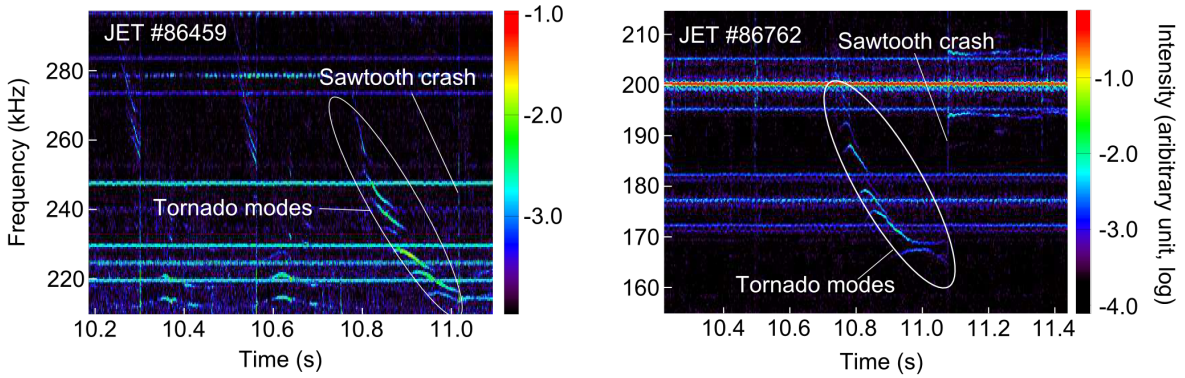

FIGURE 3.7 – Tornado modes measured with FIR interferometry - discharges #86459 and #86762.

3.8 Explanation for the crashes

3.8.1 Tornado modes

Tornado modes [Saigusa 1998, Kramer 2004] are observed in discharges #86459 and #86762 with Far InfraRed (FIR) interferometry (Figure 3.7). Those tornado modes have an overall duration of more than 0.2 s before the sawtooth crashes. Tornado modes are known to be at the origin of the expulsion of some fast particles from within the $q = 1$ surface, as has been observed in the tokamaks JT-60 in Japan [Saigusa 1998], TFTR in the USA [Bernabei 2000], DIII-D in the USA [Bernabei 2001], and JET [Gassner 2012]. In particular, the JET discharge studied in [Gassner 2012] was very similar to the discharges considered in the present study (same magnetic field on axis, same plasma current, same 3rd harmonic deuterium ICRH). Such expulsion of fast particles during the sawteeth means that the stabilizing effect of the fast particles is strongly reduced; this can lead to the crash of the sawteeth, as exposed in [Bernabei 2000, Bernabei 2001, Gassner 2012]. In our experiments, the expulsion of the fast particles outside the $q = 1$ surface can be modelled as the increase of ρ_k during the sawtooth periods. Porcelli's model then shows that this expulsion of fast particles is consistent with the crashes and sufficient to account for them: see Section 3.7 and Figure 3.4-a).

In the case of discharges #86774 and #86775, no tornado modes were observed. One can notice that the two discharges exhibiting tornado modes were the two with $\Lambda_0 > 1.0$, while the two-discharges with $\Lambda_0 = 1.0$ did not exhibit tornado modes.

3.8.2 ELMs - Inward propagation of a cold front

In discharges #86774 and #86775, as can be seen in Figure 3.8, significant drops in the radio-frequency (RF) coupled power are observed just before the sawtooth crashes: a drop of 31 % in the case of discharge #86774, and a drop of 43 % in the case of discharge #86775. Could those power drops be at the origin of a decrease in the stabilizing fast

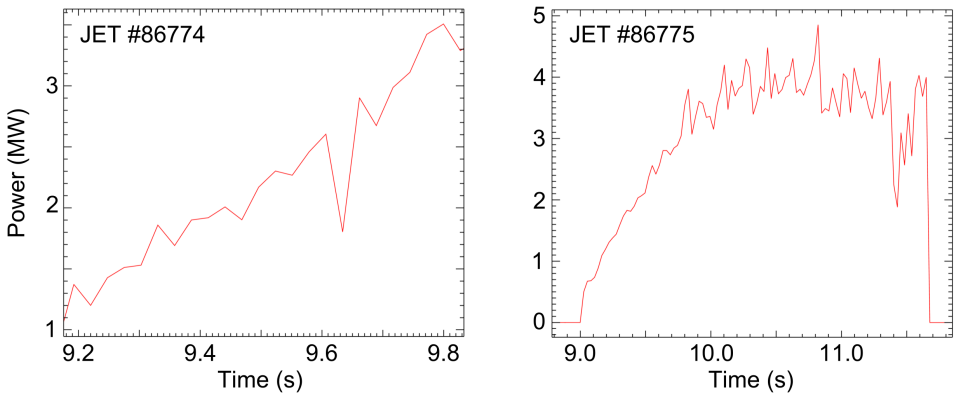

FIGURE 3.8 – ICRH coupled power - discharges #86774 and #86775.

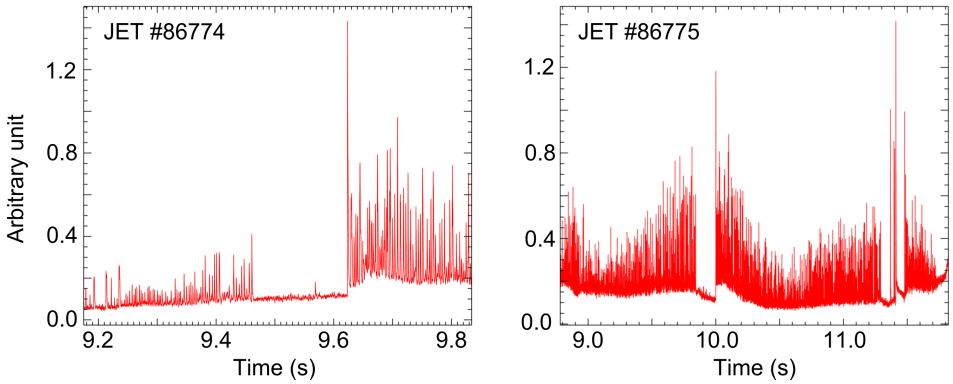

FIGURE 3.9 – ELMs (D alpha) - discharges #86774 and #86775.

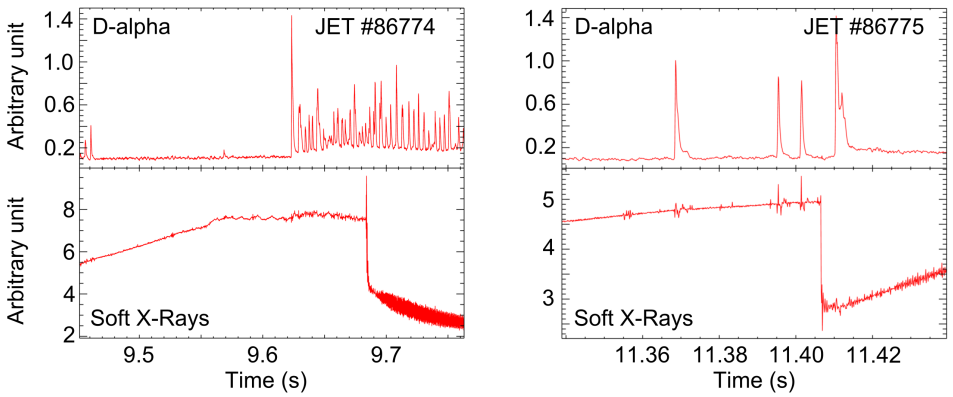

FIGURE 3.10 – ELMs (D alpha) and Soft X-Rays, with focus on crash times - discharges #86774 and #86775.

particle population within the $q = 1$ surface, thus leading to the observed crashes? The slowing down time for the fast particle population can be estimated with the Spitzer time τ_s [ITER 1999]:

$$\tau_s = \frac{3(2\pi)^{3/2} T_e^{3/2} \varepsilon_0^2 m_k}{n_e \sqrt{m_e} e^4 \ln \Lambda}, \tag{3.13}$$

where T_e is the electron temperature, ε_0 the vacuum permittivity constant, m_e is the electron mass, e the elementary Coulomb charge and $\ln \Lambda$ is the Coulomb logarithm. With the set of parameters corresponding to the four discharges here considered, $\ln \Lambda$ reads [NRL 2011]

$$\ln \Lambda = 24 - \ln\left(\frac{\sqrt{n_e}}{T_e}\right), \tag{3.14}$$

where n_e is in m^{-3} and T_e is in eV. For discharge #86774, expression (3.13) yields $\tau_s = 0.6$ s, while it yields $\tau_s = 0.9$ s for discharge #86775. In comparison, the times between the RF power drops and the sawtooth crashes are one order of magnitude lower: it is comprised between 0.04 and 0.08 s for discharge #86774, while it is comprised between 0.005 and 0.04 s for discharge #86775. Those intervals correspond to the time intervals between two measurements of the RF power.

Another hypothesis is that the RF power drops have been caused by ELM bursts, and that in addition to causing the RF power drops, those ELM bursts have also triggered the sawtooth crashes. The measured activity of D-alpha transition is represented in Figure 3.9 for discharges #86774 and #86775 during the studied sawteeth.

In the case of discharge #86774, one major ELM burst occurs at $t = 9.62$ s, while no other significant burst occurs before. This burst takes place about 60 ms before the sawtooth crash, as can be seen in Figure 3.10 where D-alpha activity and soft X-ray signals are represented together, with a focus on the crash time.

In the case of discharge #86775, two periods of major ELM activity are recorded: one around $t = 10.0$ s, which does not have any significant impact on the coupled ICRH power, and one around $t = 11.4$ s, at the same time as the sawtooth crash. It can be seen in Figure 3.10 that in the second period of ELM activity, the first burst occurs about 40 ms before the sawtooth crash. That the first period of ELM activity should have had no impact on the coupled ICRH power makes it likely that the intensity of ELMs was then weaker than during the second period of activity; and this is consistent with the fact that it should not have triggered any sawtooth crash either. It is also consistent with the fact that during the first period of ELM activity ($t = 10.0$ s), $\delta\hat{W}_{\mathrm{MHD}}$ computed with MISHKA1 was about twice as low as during the second period ($t = 11.4$ s), thus indicating that the internal kink mode was not as easy to be destabilized during the first

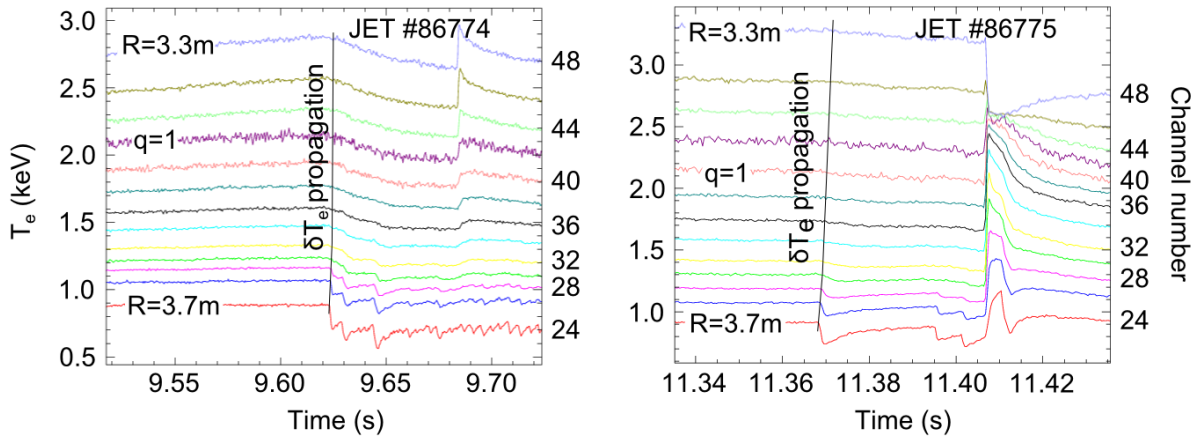

FIGURE 3.11 – Time evolution of the electron temperature in discharge #86774 measured with various ECE channels, corresponding to various radial positions comprised between $R = 3.3$ m (channel 48) and $R = 3.7$ m (channel 24). The $q = 1$ surface corresponds approximately to channel 42 in the case of discharge #86774, and to channel 40 in the case of discharge #86775.

period of ELM activity as during the second period.

It has been reported in [Sarazin 2002] that some large ELM bursts can generate a strong perturbation δT_e which propagates inwards at a velocity of the order of a few 100 m·s^{-1}. In the two discharges of interest, the $q = 1$ surface is situated quite far from the magnetic axis, at $R = 3.43$ m on the equatorial plane, low field side (see Table 3.1). Thus, the δT_e perturbation can reach this surface after travelling about 50 cm, which correspond to less than 5 ms. This time value is lower than the time which elapses between the first ELM burst of interest and the sawtooth crash in both discharges #86774 (60 ms) and #86775 (40 ms), which makes it possible for the ELM bursts to be at the origin of the sawtooth crashes.

Figure 3.11 shows the time evolution of the electron temperature in discharges #86774 and #86775 measured with various Electron Cyclotron Emission (ECE) channels, corresponding to various radial positions comprised between $R = 3.3$ m (channel 48) and $R = 3.7$ m (channel 24). On those two figures, the propagation of the cold front (δT_e perturbation) can be seen and is identified with a solid black line. In the case of discharge #86775, the cold front does not appear in Figure 3.11 clearly enough for immediate identification; this is why larger scale plots have been represented in Figure 3.12. Note that in that last figure, only the vertical scale (corresponding to the electron temperature) has been increased with respect to Figure 3.11, while the x-axis scale has been kept similar to that of Figure 3.11.

The inward propagating perturbation triggered by ELM bursts was measured in

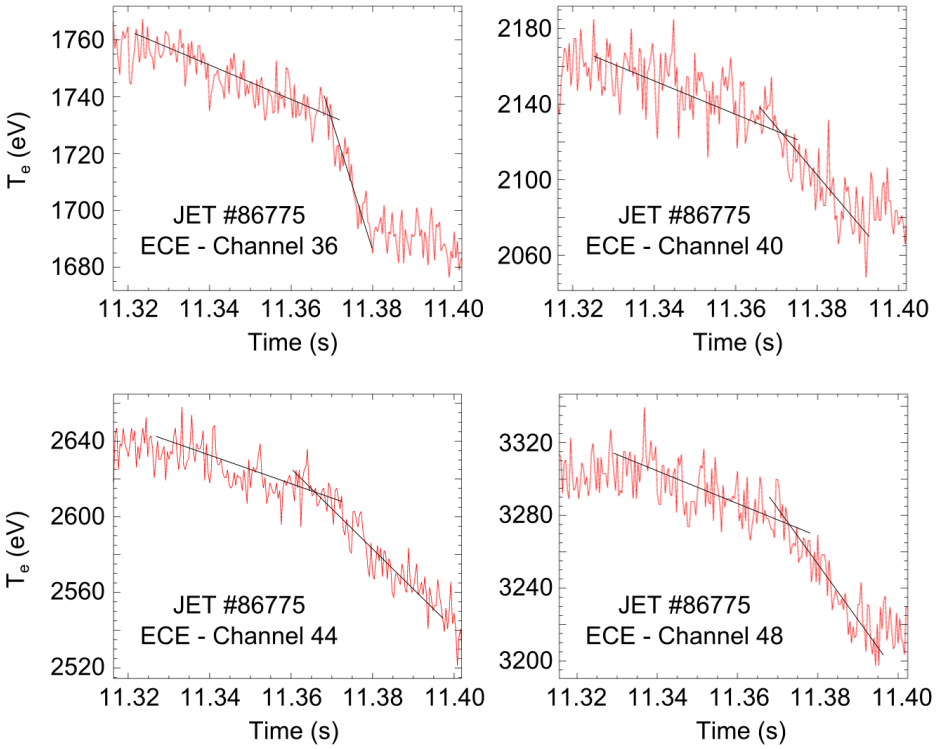

FIGURE 3.12 – Details of the time evolution of the electron temperature in discharge #86775 measured by four different ECE channels (channels 36, 40, 44 and 48), showing the propagation of the cold front to the $q = 1$ surface (corresponding approximately to channel 40) and beyond (channels 44 and 48).

[Sarazin 2002] on T_e and is here measured experimentally on T_e as well. However other plasma parameters are likely to be affected by the inward propagating front, and be perturbed at the same time as the electron temperature. The mechanism of sawtooth destabilization by such perturbations triggered by ELM bursts is not clear yet. Those perturbations may have an impact on the $q = 1$ layer, and in particular on the magnetic shear s_1; but this hypothesis has not been confirmed and the exact mechanism remains to be determined.

3.9 Conclusion

Four sawteeth in four different JET discharges have been analysed. The application of Porcelli's model to those sawteeth, with the help of the equilibrium codes EFIT and HELENA, of the MHD code MISHKA1, of the fast-particle codes SPOT and HAGIS has enabled us to check that fast particles produced by NBI and 3rd harmonic deuterium ICRH had a strong stabilizing effect on the internal kink mode. Despite the stabilization thus gained, the four sawtooth all ended up crashing. Two mechanisms that can explain those crashes have been observed.

The first one is the appearance of tornado modes before the sawtooth crashes in

discharges #86459 and #86762. Tornado modes are known [Saigusa 1998, Bernabei 2000, Bernabei 2001, Gassner 2012] to expel fast particles from within the $q = 1$ surface, leading to the loss of their stabilizing effect. In such situations, fast particles are not only the cause of the sawtooth stabilization, they are also the cause of the sawtooth crashes, since they are at the origin of the tornado modes which eventually trigger the sawtooth crashes.

The second one is an inward propagating perturbation δT_e of the electron temperature, triggered by major ELM bursts. The inward propagation of the perturbation occurs at ballistic velocities [Sarazin 2002] (~ 160 m·s^{-1}): the time of the propagation from the edge of the plasma to the $q = 1$ surface is therefore under 5 ms in JET. This phenomenon is believed to be at the origin of the sawtooth crashes in discharges #86774 and #86775. An implication of this hypothesis is that the cause for sawtooth crashes comes from outside the $q = 1$ surface, and not from the very particles which provide stabilization.

A limit of the present study is that the possible mechanism of the interaction between the cold front in discharges #86774 and #86775 and the internal kink mode has not been analysed. Further theoretical and experimental analyses are required for that.

One of the sawteeth studied in the present chapter had a duration of about 2.5 s. However, monster sawteeth may not be desired in burning plasmas: on the one hand, they correspond to higher and more stabilized core electron temperature, which is beneficial for fusion; on the other hand, the crashes which follow such sawteeth are more intense, cause higher T_e drops, and can cause harmful NTMs. The issue of plasma impurities also matters: sawteeth can expel impurities, and high frequency sawteeth may be beneficial to avoid the accumulation of high Z ions in the core plasma. For more details, one may read [Chapman 2011, Graves 2012].

Chapter 4

Relation between GAMs and EGAMs

The relation between GAMs and EGAMs is somewhat unclear and remains to be explained: it is the purpose of this chapter. The present study can be found in [Girardo 2014]. Through a linear, analytical model, the relation between GAMs and EGAMs is investigated. The fast particles are modelled by a Maxwellian bump-on-tail distribution function, in which only deeply passing ions are retained.

The link between GAMs and EGAMs is found to depend on several parameters: the safety factor q, the fast ion parallel velocity $\bar{u}_{\|}$ normalized to the thermal velocity, the ratio τ_k of the fast ion distribution width to the bulk ion temperature, the ratio T_t/T_e of the bulk ion temperature to the electron temperature, the mass m_k and the charge number Z_k of the fast ions. Those parameters are explored in the following ranges: $1 \leq q \leq 3$; $2 \leq \bar{u}_{\|} \leq 4$; $0.1 \leq \tau_k \leq 2$ and $0.5 \leq T_t/T_e \leq 2$; while the masses and charge numbers correspond to those of hydrogen (H), deuterium (D), tritium (T) and helium 3 (He3). For low values of q and m_k; for high values of $\bar{u}_{\|}$, τ_k and T_t/T_e, the EGAM originates from the GAM. On the contrary, for high values of q and m_k; for low values of $\bar{u}_{\|}$, τ_k and T_t/T_e, the GAM is not the mode which becomes unstable when fast particles are added: the EGAM then originates from a distinct mode, which is strongly damped in the absence of fast particles.

Note that such a split in the nature of the EGAM depending on the parameters of the plasma was already exposed in [Fu 2008]. The present analysis gives further information about this split; the origin of the two branches is clarified. In particular, it is here established that one of the two branches (the so called *Landau EGAM*) originates from a branch of Landau modes which already exist and are stable in the absence of fast particles. When kinetic particles are added, one of the stable Landau modes sees its frequency rise progressively to the upper part of the complex plane, and turns into an excited mode. In addition, the present model takes into account the possibility of having different species for thermal ions on the one hand, and kinetic particles on the other hand. This leads to interesting results, in particular regarding the excitation threshold of the EGAM, which

is found to be very low under certain circumstances (Figure 4.7).

The analysis carried out in this chapter allows one to better understand the ways in which the real frequency and the growth rate of the GAMs and EGAMs can be modified. This is important in particular to better apprehend the interaction of GAMs and EGAMs with turbulence. After exposing the linear, analytical model which has been used in the present work to study the link between GAMs and EGAMs, we detail the results which were obtained through numerical resolution of the dispersion relation. Those results are then discussed.

4.1 Model

4.1.1 Equations

The equilibrium magnetic field is $\mathbf{B} = I(\psi)\boldsymbol{\nabla}\varphi + \boldsymbol{\nabla}\varphi \times \boldsymbol{\nabla}\psi$. We use an electrostatic approximation, *i.e.* fluctuations of the magnetic field are not considered. φ is the toroidal angle, ψ is the magnetic poloidal flux normalized to 2π, and the poloidal angle is written θ. (ψ, θ, φ) constitutes a direct set of coordinates in which the safety factor q depends on ψ only. The aspect ratio $\frac{R_0}{a}$, where a is the minor radius of the tokamak and R_0 the major radius on the magnetic axis, is assumed to be large. The distribution functions of the thermal ion and kinetic ion gyro-centres are called, respectively, f_t and f_k (t for *thermal* and k for *kinetic*). The total ion gyro-centre distribution function f_G thus reads: $f_\mathrm{G} = f_t + f_k$. Since most equations for f_t and f_k are identical, the subscript s (for *species*) will be used instead of t or k whenever possible, and only one equation will be written. The gyrokinetic equation for the ion distribution functions f_s reads

$$\frac{\partial f_s}{\partial t} + \mathbf{v}_{d,s} \cdot \boldsymbol{\nabla}_\perp f_s + v_\parallel \nabla_\parallel f_s + \frac{dE_s}{dt}\frac{\partial f_s}{\partial E_s} = 0, \tag{4.1}$$

where the subscript s stands for species s and can be replaced with either t or k, $E_s = \frac{1}{2}m_s v_\parallel^2 + \mu_s B$ is the kinetic energy, $\mu_s = \frac{m_s v_\perp^2}{2B}$ is the magnetic moment and B is the intensity of the magnetic field. $\mathbf{v}_{d,s}$ is the drift velocity comprising the electric drift $\frac{\mathbf{b}\times\boldsymbol{\nabla}\tilde{\phi}}{B}$, the gradient drift $\frac{\mu_s B}{e_s B}\frac{\mathbf{b}\times\boldsymbol{\nabla}B}{B}$ and the curvature drift which reads $\frac{m_s v_\parallel^2}{e_s B}\frac{\mathbf{b}\times\boldsymbol{\nabla}B}{B}$ in the low β limit. e_s stands for the electric charge of species s, m_s stands for the mass of species s, $\mathbf{b}$ is the unitary vector directed along the magnetic field, β is the ratio of the kinetic energy to the magnetic energy. In the present work, the long wavelength limit is considered, so that the gyro-averaged electric potential $J_0\tilde{\phi}$ is simply replaced by the electric potential $\tilde{\phi}$ itself. μ_s is an adiabatic motion invariant and the kinetic energy varies according to the

electric energy transfers:

$$\frac{d\mu_s}{dt} = 0, \tag{4.2}$$

$$\frac{dE_s}{dt} = -e_s\big(\mathbf{v}_{d,s} + v_\parallel \mathbf{b}\big) \cdot \boldsymbol{\nabla}\tilde{\phi}. \tag{4.3}$$

The equilibrium electric field is assumed to be small, so that $\tilde{\phi}$ represents the perturbed part only of the electrostatic potential. The electrons are considered adiabatic:

$$\tilde{n}_e = n_e \frac{e}{T_e}\Big(\tilde{\phi} - \Big\langle\tilde{\phi}\Big\rangle_{\mathrm{FS}}\Big), \tag{4.4}$$

where n_e is the equilibrium density of electrons, $\tilde{n}_e$ is the perturbed density of electrons, T_e is the electron temperature, e is the elementary Coulomb charge and $\langle\cdot\rangle_{\mathrm{FS}}$ stands for the average on a magnetic flux surface.

The distribution function of the ions of species s is decomposed into an equilibrium part F_s and a perturbed part $\tilde{f}_s$:

$$f_s = F_s\Big(1 + \tilde{f}_s\Big). \tag{4.5}$$

With those notations, the overall ion gyro-centre distribution function f_{G} reads

$$f_{\mathrm{G}} = \sum_s f_s = f_t + f_k = F_t\Big(1 + \tilde{f}_t\Big) + F_k\Big(1 + \tilde{f}_k\Big). \tag{4.6}$$

The quasi-neutrality equation $\tilde{n}_e = Z_t\tilde{n}_t + Z_k\tilde{n}_k$ reads (see Appendix B)

$$n_e\frac{e}{T_e}\Big(\tilde{\phi} - \Big\langle\tilde{\phi}\Big\rangle_{\mathrm{FS}}\Big) = \sum_{s\in\{t,k\}}\left[\mathrm{div}\Big(\frac{m_s n_s}{eB^2}\boldsymbol{\nabla}_\perp\tilde{\phi}\Big) + Z_s\int F_s\tilde{f}_s\,(dv)^3\right], \tag{4.7}$$

where, for species s, Z_s is the charge number, $\tilde{n}_s$ is the perturbed density, and n_s is the equilibrium density. The n_s verify: $n_e = Z_t n_t + Z_k n_k$. The gyrokinetic equation is linearized in $\tilde{f}_s$ and $\tilde{\phi}$; the equilibrium radial gradients are neglected. The computation is executed up to order 1 in $\rho_* = \rho_i/a$, where ρ_i is the ion Larmor radius.

In the case of GAMs and EGAMs, two Fourier modes are predominantly excited: $(m,n) = (0,0)$ and $(1,0)$ where m is the poloidal mode number, and n is the toroidal mode number. For the density and for the electrostatic potential $(1,0)$ modes, the $\sin\theta$ part is predominant over the $\cos\theta$ part, where θ is counted from the equatorial plane.

4.1.2 GAM Dispersion Relation

The bulk plasma particles at equilibrium are represented by a local Maxwellian distribution:

$$F_t = n_t \left(\frac{m_t}{2\pi T_t} \right)^{\frac{3}{2}} e^{-\frac{E_t}{T_t}}, \tag{4.8}$$

where the subscript t stands for *thermal*.

In the absence of fast particles, with $Z_t = 1$, the dispersion relation of the GAM reads

$$\frac{1}{q^2} + A_1(\Omega_t) - \frac{N_1(\Omega_t)^2}{D_1(\Omega_t)} = 0, \tag{4.9}$$

with

$$A_1(\Omega_t) = \mathcal{Z}(\Omega_t) \left(\Omega_t^3 + \Omega_t + \frac{1}{2\Omega_t} \right) + \Omega_t^2 + \frac{3}{2}, \tag{4.10}$$

$$N_1(\Omega_t) = \mathcal{Z}(\Omega_t) \left(\Omega_t^2 + \frac{1}{2} \right) + \Omega_t, \tag{4.11}$$

$$D_1(\Omega_t) = \mathcal{Z}(\Omega_t)\Omega_t + 1 + \frac{T_t}{T_e}, \tag{4.12}$$

$$\Omega_t = qR\sqrt{\frac{m_t}{2T_t}}\omega, \tag{4.13}$$

where ω is the frequency of the mode, q is the safety factor, R_0 is the major radius on the magnetic axis, and $\mathcal{Z}$ is the plasma dispersion function [Fried 1961]. This dispersion relation is the same as the one obtained in [Zonca 2008].

4.1.3 EGAM Dispersion Relation

The bulk plasma particles at equilibrium are still represented by a local centred Maxwellian distribution, while the fast particles are represented by a shifted Maxwellian distribution (here called *bump-on-tail* distribution) in parallel velocity:

$$F_k = \frac{n_k}{2} \left(\frac{m_k}{2\pi T_t \tau_k} \right)^{\frac{3}{2}} \left[e^{-\frac{m_k \left(v_\parallel - \bar{v}_\parallel \right)^2 + 2\mu_k B}{2T_t \tau_k}} + e^{-\frac{m_k \left(v_\parallel + \bar{v}_\parallel \right)^2 + 2\mu_k B}{2T_t \tau_k}} \right], \tag{4.14}$$

where the subscript k stands for *kinetic* and $\bar{v}_\parallel$ is the position of the bump of the distribution function on the $v_\parallel$ axis. Note that the distribution function of the fast particles is a centred Maxwellian in perpendicular velocity, and that it is even in parallel velocity: consequently, no parallel momentum is injected [Elfimov 2014]. In addition, the distribution function (4.14) can be recast as a function of motion invariants only; in particular only

highly passing particles are considered and the parallel velocity is considered as a motion invariant (see Appendix B). τ_k is a temperature-like, dimensionless parameter which describes the width of the bumps in $v_\parallel$. For the model to be consistent, the bumps need to be larger than the small variation of $v_\parallel$ during a poloidal turn which has been neglected. This imposes a condition on τ_k:

$$\tau_k \gg \frac{\varepsilon^2}{\bar{u}_\parallel^2}, \tag{4.15}$$

where

$$\bar{u}_\parallel = \sqrt{\frac{m_k}{2T_t}}\bar{v}_\parallel. \tag{4.16}$$

For $\bar{u}_\parallel = 2.8$ and $\varepsilon = 0.3$, this condition numerically reads $\tau_k \gg 0.011$.

In the presence of fast particles described by such a bump-on-tail distribution function, the dispersion relation of the EGAM reads

$$\frac{1}{q^2} + A_1(\Omega_t) + A_2(\Omega_k) - \frac{\left[N_1(\Omega_t) + N_2(\Omega_k)\right]^2}{D_1(\Omega_t) + D_2(\Omega_k)} = 0, \tag{4.17}$$

where

$$A_1(\Omega_t) = \frac{n_e}{n_t + n_k\frac{m_k}{m_t}}\frac{n_t}{n_e}\left\{\mathcal{Z}(\Omega_t)\left[\Omega_t^3 + \Omega_t + \frac{1}{2\Omega_t}\right] + \Omega_t^2 + \frac{3}{2}\right\}, \tag{4.18}$$

$$A_2(\Omega_k) = \frac{m_k}{m_t}\frac{n_e}{n_t + n_k\frac{m_k}{m_t}}\frac{n_k}{2n_e}\left\{\left[\mathcal{Z}\left(\frac{\Omega_k - \bar{u}_\parallel}{\sqrt{\tau_k}}\right)\left[1 - \frac{\bar{u}_\parallel}{\Omega_k}\right]\right.\right. \tag{4.19}$$

$$\left.\left. + \mathcal{Z}\left(\frac{\Omega_k + \bar{u}_\parallel}{\sqrt{\tau_k}}\right)\left[1 + \frac{\bar{u}_\parallel}{\Omega_k}\right]\right]\left[\frac{\Omega_k^3}{\tau_k^{3/2}} + \frac{\Omega_k}{\sqrt{\tau_k}} + \frac{\sqrt{\tau_k}}{2\Omega_k}\right] + 2\frac{\Omega_k^2}{\tau_k} + 3 - \frac{\bar{u}_\parallel\sqrt{\tau_k}}{\Omega_k^2}\mathcal{Z}\left(\frac{\bar{u}_\parallel}{\sqrt{\tau_k}}\right)\right\}, \tag{4.20}$$

$$N_1(\Omega_t) = Z_t\sqrt{\frac{n_e}{n_t + n_k\frac{m_k}{m_t}}}\frac{n_t}{n_e}\left\{\mathcal{Z}(\Omega_t)\left[\Omega_t^2 + \frac{1}{2}\right] + \Omega_t\right\}, \tag{4.21}$$

$$N_2(\Omega_k) = Z_k\frac{1}{\sqrt{\tau_k}}\sqrt{\frac{m_k}{m_t}}\sqrt{\frac{n_e}{n_t + n_k\frac{m_k}{m_t}}}\frac{n_k}{2n_e}\left\{\left[\mathcal{Z}\left(\frac{\Omega_k - \bar{u}_\parallel}{\sqrt{\tau_k}}\right)\left[1 - \frac{\bar{u}_\parallel}{\Omega_k}\right]\right.\right. \tag{4.22}$$

$$\left.\left. + \mathcal{Z}\left(\frac{\Omega_k + \bar{u}_\parallel}{\sqrt{\tau_k}}\right)\left[1 + \frac{\bar{u}_\parallel}{\Omega_k}\right]\right]\left[\frac{\Omega_k^2}{\tau_k} + \frac{1}{2}\right] + 2\frac{\Omega_k}{\sqrt{\tau_k}} - \frac{\bar{u}_\parallel}{\Omega_k}\mathcal{Z}\left(\frac{\bar{u}_\parallel}{\sqrt{\tau_k}}\right)\right\}, \tag{4.23}$$

$$D_1(\Omega_t) = Z_t^2\frac{n_t}{n_e}\{\mathcal{Z}(\Omega_t)\Omega_t + 1\} + \frac{T_t}{T_e}, \tag{4.24}$$

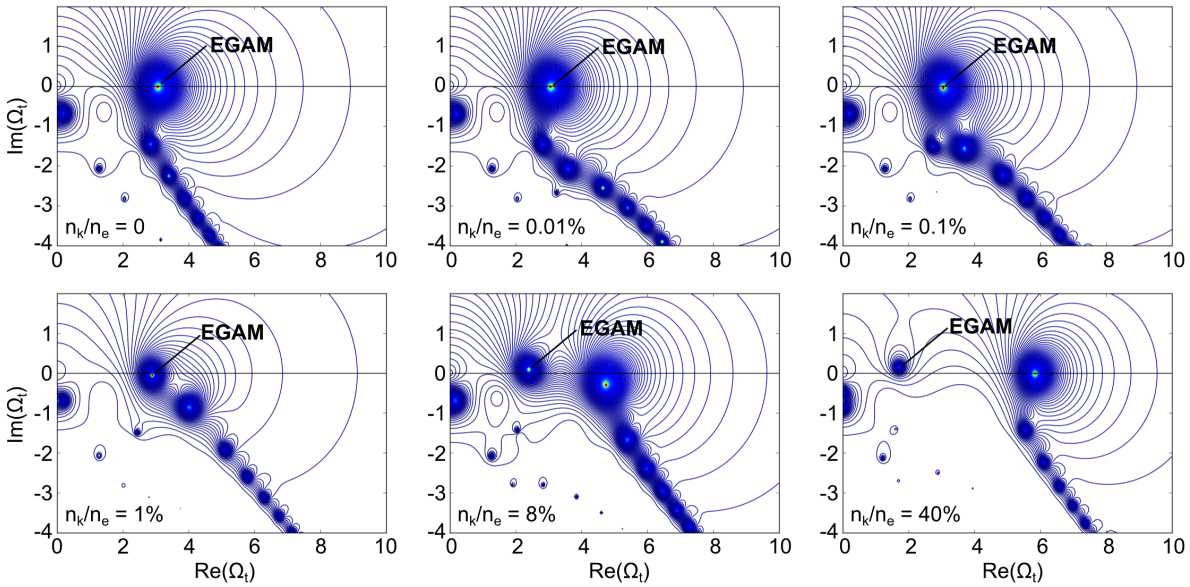

FIGURE 4.1 – Contour representations of $|D(\Omega_t)|^{-1}$ in the complex plane for $q = 1.6$, $T_t/T_e = 1$, for various concentrations of fast ions, from 0 to 40%. The bulk and fast ions belong to the same species (D-D), with $\bar{u}_\parallel = 2.8$ and $\tau_k = 1$.

$$D_2(\Omega_k) = \frac{Z_k^2}{\tau_k}\frac{n_k}{2n_e}\left\{\mathcal{Z}\left(\frac{\Omega_k - \bar{u}_\parallel}{\sqrt{\tau_k}}\right)\frac{\Omega_k}{\sqrt{\tau_k}}\left[1 - \frac{\bar{u}_\parallel}{\Omega_k}\right] + \mathcal{Z}\left(\frac{\Omega_k + \bar{u}_\parallel}{\sqrt{\tau_k}}\right)\frac{\Omega_k}{\sqrt{\tau_k}}\left[1 + \frac{\bar{u}_\parallel}{\Omega_k}\right] + 2\right\}, \tag{4.25}$$

and where

$$\Omega_k = qR\sqrt{\frac{m_k}{2T_t}}\omega. \tag{4.26}$$

The details of the derivation of this dispersion relation can be found in Appendix B. The dispersion relation (4.9) is recovered in the absence of fast particles, *i.e.* for $n_k = 0$, and for $Z_t = 1$.

4.2 Results

4.2.1 Impact of the safety factor q on the link between GAMs and EGAMs

The dispersion relation (4.17) is numerically solved for various parameters of the bulk plasma and of the fast particles. Calling D the left hand-side of that relation, we look for the zeros of D as a function of Ω_t, Ω_k being itself a linear function of Ω_t: $\Omega_k = \sqrt{\frac{m_k}{m_t}}\Omega_t$. In Figures 4.1 and 4.2 shown are the contour representations of $|D(\Omega_t)|^{-1}$ in the complex plane for $q = 1.6$ and $q = 3$, for various concentrations of fast ions. The solutions of the

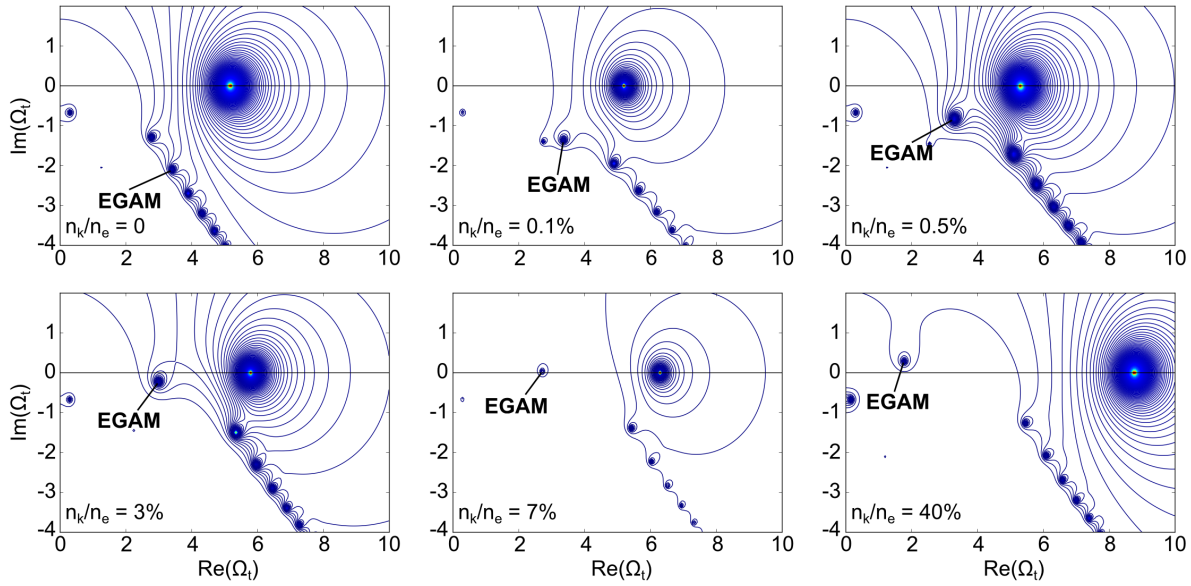

FIGURE 4.2 – Contour representations of $|D(\Omega_t)|^{-1}$ in the complex plane for $q = 3$, $T_t/T_e = 1$, for various concentrations of fast ions, from 0 to 40%.The bulk and fast ions belong to the same species (D-D), with $\bar{u}_{\|} = 2.8$ and $\tau_k = 1$.

dispersion relation correspond to the high values of $D^{-1}(\Omega_t)$, which are recognizable as the fully filled circles. In particular, one can see that in the absence of fast particles, no circle is present in the upper part of the complex plane, where $\mathrm{Im}(\Omega_t) > 0$ (which corresponds to excited modes). One zero of the dispersion relation is present slightly below the real axis: it is the GAM. Several zeros are present in the lower complex plane (where $\mathrm{Im}(\Omega_t) < 0$): those zeros correspond to highly damped modes, which are therefore observed neither in experiments nor in simulations. When fast particles are added, the positions of the roots evolve, and when the fast particle concentration becomes high enough, one of the roots crosses the real axis and finds itself in the upper plane.

In those figures, the EGAM is defined as the only mode which lies in the upper plane above a certain fast-particle density threshold, and which is therefore the only mode to be excited. During its evolution, this mode is labelled as an EGAM in Figures 4.1 and 4.2. Another mode lies very close to the real axis above a certain fast particle density threshold, at a real frequency greater than that of the EGAM. However, this mode is never excited. The GAM is defined as the only mode which lies very close to the real axis in the absence of fast particles. When fast particles are added, it can either turn into an EGAM (Figure 4.1) or remain on the real axis (Figure 4.2) and thus not be excited.

In Figure 4.1, when the proportion of fast particles increases, the GAM becomes an EGAM: this mode is called an *EGAM from GAM*. At the same time, a mode which was deeply damped in the absence of fast particles progressively gets nearer to the real axis. The behaviour of the modes in Figure 4.2 is different. When the proportion of fast parti-

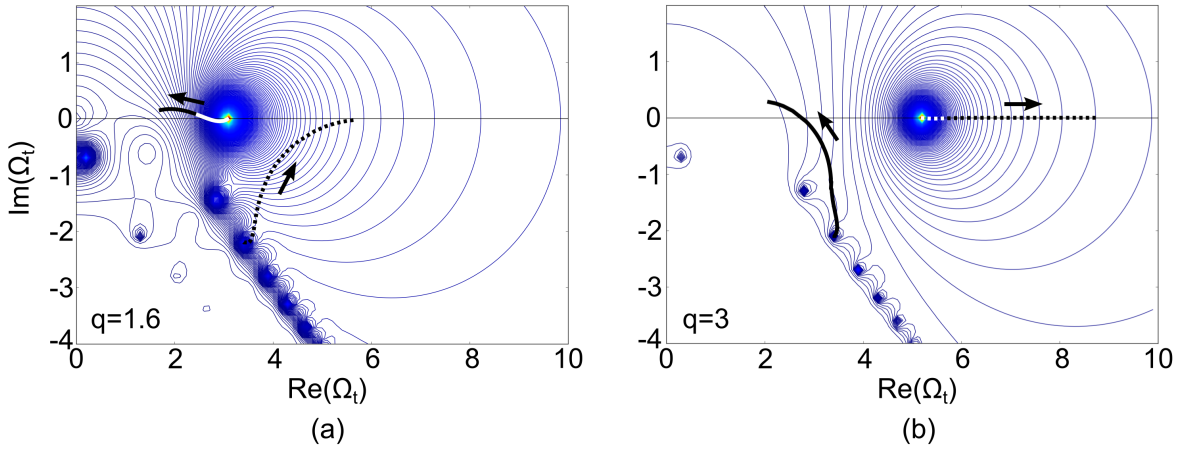

FIGURE 4.3 – Background (blue curves): contour representation of $|D(\Omega_t)|^{-1}$ in the complex plane, in the absence of fast ions, for $q = 1.6$ (a) or $q = 3.0$ (b). In both cases, $T_t/T_e = 1$. Black curves: evolution of the GAM and EGAM frequencies when the proportion of fast ions n_k/n_e varies from 0 to 40%. The bulk and fast ions belong to the same species (D-D), with $\bar{u}_{\|} = 2.8$ and $\tau_k = 1$.

cles increases, the GAM remains close to the real axis, and does not turn into an excited mode. At the same time, a mode which was deeply damped in the absence of fast particles progressively moves towards the upper plane, crosses the real axis and then gets excited: this mode is called a *Landau EGAM*. It is worth noting that the link between GAMs and EGAMs is thus different according to the value of the safety factor q: for $q = 1.6$, the EGAM originates from the GAM; while for $q = 3$, the GAM and the EGAM belong to different mode branches. The existence of two different kinds of EGAMs has also been shown numerically [Zarzoso 2014] with the gyrokinetic code NEMORB [Jolliet 2007, Bottino 2011].

In Figure 4.3 shown are the contour representations (in blue) of $|D(\Omega_t)|^{-1}$ in the complex plane for $q = 1.6$ and $q = 3$, in the absence of fast particles. Those two contour representations are the same as the ones in Figures 4.1 and 4.2 in the absence of fast particles. Atop those contour representations, the evolutions of some zeros of the dispersion relation when the proportion of fast particles increases from 0 to 40% (black curves) are superposed. The evolutions of those zeros are numerically computed; the evolutions of the other zeros are not represented as they are not significant. In Figure 4.3-a), drawn with the same parameters as Figure 4.1, one can see that the GAM becomes an EGAM (solid black line). At the same time, a mode which was deeply damped in the absence of fast particles gets very close to the real axis, but does not cross it (dashed black line). In Figure 4.3-b), drawn with the same parameters as Figure 4.2, one can see that the GAM does not turn into an EGAM: the GAM stays about the real axis, but never enters the upper plane (dashed black line). At the same time, a mode which was deeply damped in the ab-

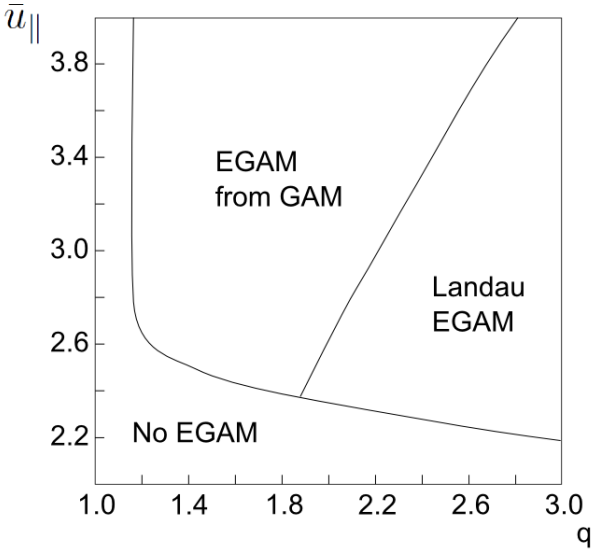

FIGURE 4.4 – Phase diagram: type of EGAM as a function of q and $\bar{u}_{\|}$, for D-D particles, with $T_t/T_e = 1$ and $\tau_k = 1$.

sence of fast particles goes up, crosses the real axis, and yields an EGAM (solid black line).

Figure 4.3-b) was obtained with the same parameters as those used in [Zarzoso 2012b]: $q = 3$, $T_t/T_e = 1$, $\bar{u}_{\|} = 2.8$, $\tau_k = 1$, $m_k/m_t = 1$, $Z_k = Z_t = 1$ (NB: due to different normalizations, $\bar{\zeta} = 4$ in [Zarzoso 2012b] corresponds to $\bar{u}_{\|} = 2.8$ in the present work). In that figure, we can see that the frequency of the EGAM is approximately half the frequency of the GAM which would be obtained in the absence of fast particles. For the real part of Ω_t, we thus recover with a linear, analytical model the result which had previously been obtained in [Zarzoso 2012b] with the non-linear, 5D gyrokinetic code GYSELA, and which had also been obtained experimentally in DIII-D [Nazikian 2008].

4.2.2 Impact of other parameters

The safety factor q is not the only parameter to have an impact on the link between GAMs and EGAMs. The phase diagrams reproduced as Figures 4.4 and 4.5 show, for various sets of parameters, three different zones in which the EGAM either originates from the GAM, is a Laudau EGAM, or is not excited at all (at least up to a fast particle fraction of 40%). Those sets of parameters are respectively $(q, \bar{u}_{\|})$, $(q, T_t/T_e)$ and (q, τ_k). In the zones labelled as *EGAM from GAM*, the EGAM is excited and originates from the GAM: the situation corresponds to the one which appears in Figures 4.1 and 4.3-a). In the zones labelled as *Landau EGAM*, the EGAM is excited and originates from a mode which is deeply damped in the absence of fast particles: the situation corresponds to the one which appears in Figures 4.2 and 4.3-b).

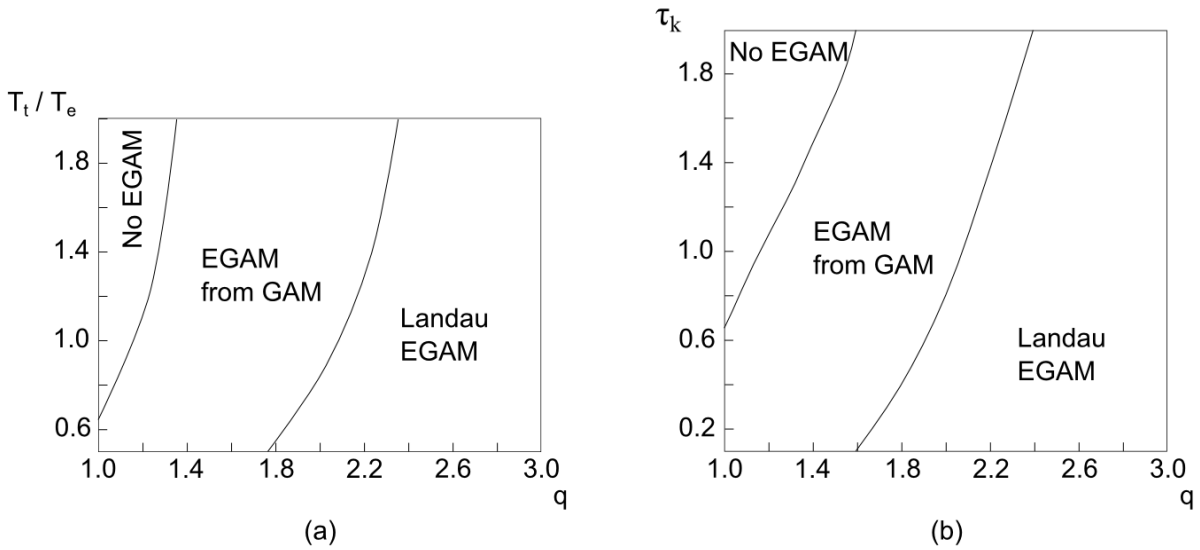

FIGURE 4.5 – Phase diagrams: type of EGAM, for D-D particles, (a) as a function of q and T_t/T_e with $\tau_k = 1$ or (b) as a function of q and τ_k with $T_t/T_e = 1$. In both cases, $\bar{u}_{\|} = 2.8$.

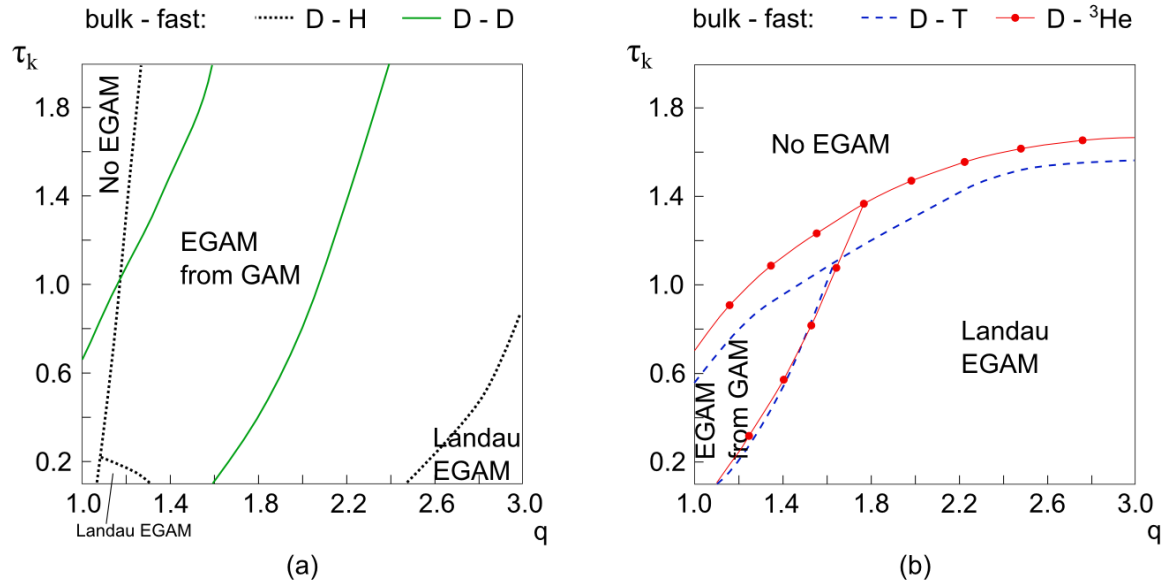

FIGURE 4.6 – Phase diagrams: type of EGAM as a function of q and τ_k, with $\bar{u}_{\|} = 2.8$ and $T_t/T_e = 1$. (a) $D_{(bulk)}$ - $H_{(fast)}$ and D-D particles. (b) $D_{(bulk)}$ - $T_{(fast)}$ and $D_{(bulk)}$ - $He3_{(fast)}$ particles.

Figure 4.6-a) completes Figure 4.5-b): the three different zones *No EGAM*, *EGAM from GAM* and *Landau EGAM* are represented as functions of q and τ_k for two different kinds of fast particles, which have the same charge but different masses (hydrogen and deuterium). The thermal particles are deuterium in both cases.

Finally, Figure 4.6-b) gives further information about the impact of the charge number. In this figure, the same three zones are represented as functions of q and τ_k for two different kinds of fast particles, which have the same mass but different charges (tritium and helium 3). The thermal particles are deuterium in both cases.

Note that in Figures 4.4 to 4.6, the critical density above which the EGAM becomes unstable is different at each position in the diagram. Indeed, as noted in [Zarzoso 2012b], the excitation threshold depends on a certain number of parameters, including q, $\bar{u}_\parallel$, τ_k and T_t/T_e; this issue is further discussed in section 4.2.3. The *No EGAM* region refers to cases in which no EGAM is excited when the fraction of energetic particles n_k/n_e varies from 0 to 40%; an EGAM is considered to be excited when $\mathrm{Im}(\Omega_t)$ is positive, with a precision of 0.05. Diagrams 4.4 to 4.6 were obtained with a matrix of test points, with steps of 0.2 (for all parameters) between the points. For each test point, the dispersion relation (4.17) was numerically solved for different values of the fast particle density (from 0 to 40%).

4.2.3 Excitation threshold

The parameters of the bulk plasma and of the fast particles also have an impact on the excitation threshold of EGAMs. Figure 4.7 presents the growth rate of EGAMs in the case of $q = 1.8$ and deuterium as thermal particles, for different species of fast particles (H, D, T, and He3). For the considered parameters, Figure 4.6-a) shows that hydrogen and deuterium EGAMs originate from GAMs, while Figure 4.6-b) shows that tritium and helium 3 EGAMs are Landau EGAMs. This distinction is consistent with what can be observed in Figure 4.7: in the case of hydrogen and deuterium, $\lim_{n_k \to 0} \mathrm{Im}(\Omega_t) \approx 0$, which indicates that the EGAMs originate from GAMs. On the contrary, in the case of tritium and helium 3, $\lim_{n_k \to 0} \mathrm{Im}(\Omega_t) < 0$, which indicates that the EGAMs are Landau EGAMs. Such a difference in the excitation threshold between the two types of EGAMs should allow one to distinguish a Landau EGAM from an EGAM from GAM in experiments.

With the parameters used to produce Figure 4.7, for an experimentally reasonable density of fast particles of 5%, we can see that there is a huge difference between the different species. For heavy fast particles such as tritium and helium 3, the EGAMs (which are then Landau EGAMs) are still far from the excitation threshold. On the contrary, for lighter fast particles such as deuterium and especially hydrogen, a density of 5% corresponds to a region where the EGAMs (which are then EGAMs from GAMs) can be excited.

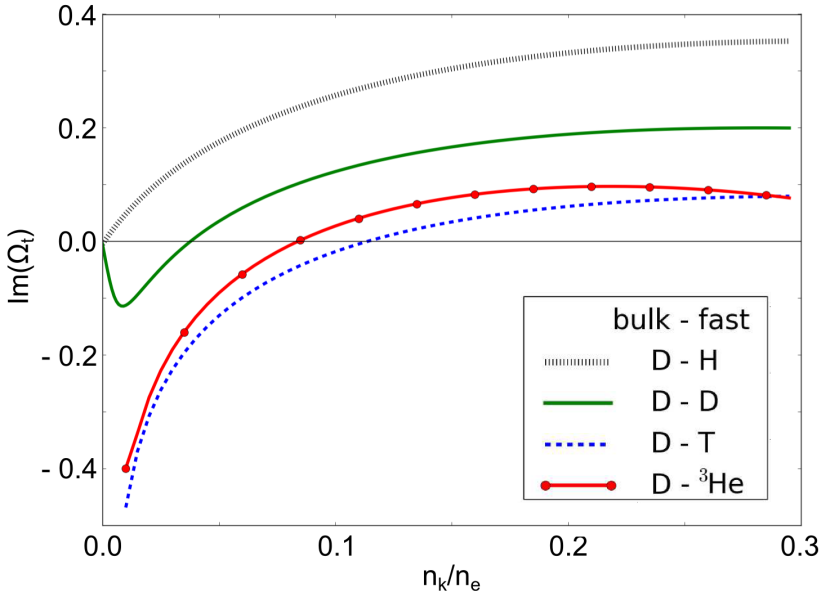

FIGURE 4.7 – normalized EGAM growth rate $\mathrm{Im}(\Omega)$ as a function of n_k/n_e, with $q = 1.8$, $\bar{u}_{\|} = 2.8$ $\tau_k = 1$ and $T_t/T_e = 1$, for D(bulk) - H(fast), D-D, D(bulk) - T(fast) and D(bulk) - He3(fast) particles. The EGAM is excited whenever $\mathrm{Im}(\Omega) > 0$.

In addition, it is worth noticing that there is no fast particle density threshold for the excitation of EGAMs in the hydrogen case, for the parameters used to compute Figure 4.7. It means that there exist certain cases in which EGAMs are very easily excited. This feature is related to the nature of the EGAM (the excitation is easier in the case of an EGAM from GAM). The behaviour of EGAMs at very low fast particle concentration is of notable interest for the study of the interaction of EGAMs with turbulence, and to understand the appearance of EGAMs in experiments.

4.3 Discussion

4.3.1 Limit $q \to 0$

When $q \to 0$, Figures 4.4 to 4.6 show that no EGAM is excited. Let us show that it is consistent with expression (4.17). First, let us show that, in the absence of fast particles , $|\Omega_{t,\mathrm{GAM}}|$ remains small (under a few unities) when $q \to 0$. Indeed, if $|\Omega_{t,\mathrm{GAM}}|$ were large, the hydrodynamic limit would be applicable, and the dispersion relation would read in that limit [Zonca 2008]: $1 - \frac{q^2}{\Omega_t^2}\left(\frac{7}{4} + \frac{T_e}{T_t}\right) + i\sqrt{\pi}q^2\Omega_t^3 e^{-\Omega_t^2} = 0$. Taking into account the constraint on Ω_t, which has to be above a few unities for the hydrodynamic limit to be valid, this equation has no solution (in Ω_t) when $q \to 0$. Therefore, the only possibility for $\Omega_{t,\mathrm{GAM}}$ to be a solution of the dispersion relation (4.9) is to be out of the hydrodynamic limit, that is to say to be smaller than a few unities. Let us now consider the EGAM frequency $\Omega_{t,\mathrm{EGAM}}$: it is expected to have the same order of magnitude as $\Omega_{t,\mathrm{GAM}}$, even

though there may be a ratio of several unities between the two frequencies. When q approaches 0, $\Omega_{t,\mathrm{EGAM}}$ is therefore to be looked for in a region of the type $|\Omega_t| < C$, where C is an arbitrary, positive constant of the order of a few unities. It can be checked with a numerical graphic representation of $D_1(\Omega_t) + D_2(\Omega_k)$ that this expression does not have any root satisfying $|\Omega_t| < C$, $\mathrm{Re}(\Omega_t) > 0$ and $\mathrm{Im}(\Omega_t) > 0$; which means that $1/(D_1(\Omega_t)+D_2(\Omega_k))$ is bounded in that region (called U from now on). In addition, since the plasma function $\mathcal{Z}(\Omega)$ is bounded for $\mathrm{Im}(\Omega) > C'$ (where C' can be any arbitrary, positive or negative constant), $A_1(\Omega_t) + A_2(\Omega_k) - \frac{[N_1(\Omega_t)+N_2(\Omega_k)]^2}{D_1(\Omega_t)+D_2(\Omega_k)}$ is bounded for Ω_t in U. It is important to note that this last expression does not have any explicit dependence on q, which implies that it remains bounded even when q approaches 0. Let us now consider the remainder of the dispersion relation: $\lim_{q\to 0} \frac{1}{q^2} = +\infty$. Therefore, when $q \to 0$, one part of the dispersion relation approaches infinity, while the other remains bounded for values of Ω_t in U: consequently, the dispersion relation (4.17) does not have any excited solution when $q \to 0$, which is consistent with what can be observed in Figures 4.4 to 4.6.

4.3.2 Limits $\bar{u}_\parallel \to 0$ and $\tau_k \to +\infty$

It can be observed in Figure 4.4 that when $\bar{u}_\parallel \to 0$, no EGAM is excited. To account for this phenomenon, it is to be remembered that the growth of the EGAM comes from the existence of a range of energy for which [Zarzoso 2012b, Fu 2008] $\frac{\partial f_k}{\partial E_k} > 0$. When $\bar{u}_\parallel \to 0$, the centres of the fast ion bumps move towards 0 in the phase space; the overall ion distribution function thus approaches a Maxwellian, for which $\frac{\partial f_k}{\partial E_k} > 0$ is nowhere verified. Consequently, no EGAM is expected to be excited, which is consistent with the observation in Figure 4.4. For the same reason, no EGAM is expected to be excited when $\tau_k \to +\infty$, which is consistent with Figures 4.5-b) and 4.6.

4.3.3 Impact of FLR/FOW effects on the growth rate

In Figure 4.7, in the D-D case, the growth rate becomes positive for $n_k/n_e = 4\%$ (± 0.5 percentage point). In the case of $q = 3$, we find that the growth rate of EGAMs in the D-D case, (with $\bar{u}_\parallel = 2.8$, $\tau_k = 1$ and $T_t/T_e = 1$) becomes positive for $n_k/n_e = 6\%$. This value is quite low compared with the excitation threshold obtained with the GYSELA code for the same parameters [Zarzoso 2012b]: the threshold value was then about $n_k/n_e = 15\%$. A possible explanation for this discrepancy is that GYSELA takes into account the Finite Larmor Radius (FLR) and Finite Orbit Width (FOW) effects, while the present model does not. Regarding the FOW effects, a numerical plot in [Biancalani 2014], based on a theoretical model from [Sugama 2006, Sugama 2008] shows that for large values of q ($q > 2$), the damping rate of GAMs in the absence of fast particles is several orders of magnitude larger when FOW effects are taken into account than when they are not.

Consequently, for large values of q, the EGAM growth rate is expected to be lower when FOW effects are taken into account than when they are not. In addition, regarding the FLR effects, the GYSELA simulations [Zarzoso 2012b] were performed over an annular domain $0.2 \leq r/a \leq 0.8$, where r is the radial coordinate, and a is the maximal value of r. This restricted choice of r/a led to higher values of the radial wave vector of the mode k_r, and therefore artificially increased the damping due to FLR effects. Both those FOW and FLR effects are consistent with the difference found in threshold values between the present analytical model and the GYSELA simulations [Zarzoso 2012b].

Note that according to the same numerical plot [Biancalani 2014], the FOW effects are expected to play a less significant role for low values of q ($q \leq 2$). As a matter of fact, simulations taking FOW effects into account made with the gyrokinetic code NEMORB, in the D-D case with parameters $q = 2$, $\bar{u}_{\parallel} = 2.8$, $\tau_k = 1$ and $T_t/T_e = 1$, indicate [Zarzoso 2014] that the EGAM excitation threshold is reached at $n_k/n_e = 5\%$. With the present analytical model, we find for the same parameters a threshold of $n_k/n_e = 4\%$. Contrary to what was found in the $q = 3$ case, the threshold values found in the $q = 2$ case are similar whether FOW effects are taken into account [Zarzoso 2014] or not (present model). This is consistent with [Biancalani 2014]. In that NEMORB case, the simulations were performed over a domain $0 \leq r/a \leq 1$, thus leading to reduced FLR effects with respect to the GYSELA case.

Further details about FOW/FLR effects and numerical analysis of EGAM excitation can be found in [Zarzoso 2014].

4.3.4 EGAM resonance

The resonance in the model happens for $\Omega_k = \bar{u}_{\parallel}$. When $\bar{u}_{\parallel}$ and $\Omega_{k,\mathrm{GAM}}$ have similar values, it is expected that the fast particles will preferentially excite the GAM mode (which is the least damped mode in the absence of fast particles), thus leading to an EGAM from GAM. In the absence of fast particles, when q increases, $\Omega_{k,\mathrm{GAM}}$ also increases [Zonca 2008], while numerical plots made in the present work indicate that the damped modes do not evolve significantly. If q increases from a configuration in which $\bar{u}_{\parallel}$ and $\Omega_{k,\mathrm{GAM}}$ have similar values (while $\bar{u}_{\parallel}$ remains the same), $\Omega_{k,\mathrm{GAM}}$ will increase and thus move away from $\bar{u}_{\parallel}$. At the same time, the damped modes will keep the same values, one of them having a real part close to $\bar{u}_{\parallel}$. The fast particles will then resonate with this damped mode and excite it, rather than the GAM which has moved away, thus leading to a Landau EGAM. Consistently, still starting from a configuration in which $\bar{u}_{\parallel}$ and $\Omega_{k,\mathrm{GAM}}$ have similar values, if $\bar{u}_{\parallel}$ decreases while q remains the same, $\bar{u}_{\parallel}$ will move away from $\Omega_{k,\mathrm{GAM}}$: the fast particles are therefore expected to excite a damped mode with a real part close to $\bar{u}_{\parallel}$ rather than the GAM, thus leading to a Landau EGAM. This analysis

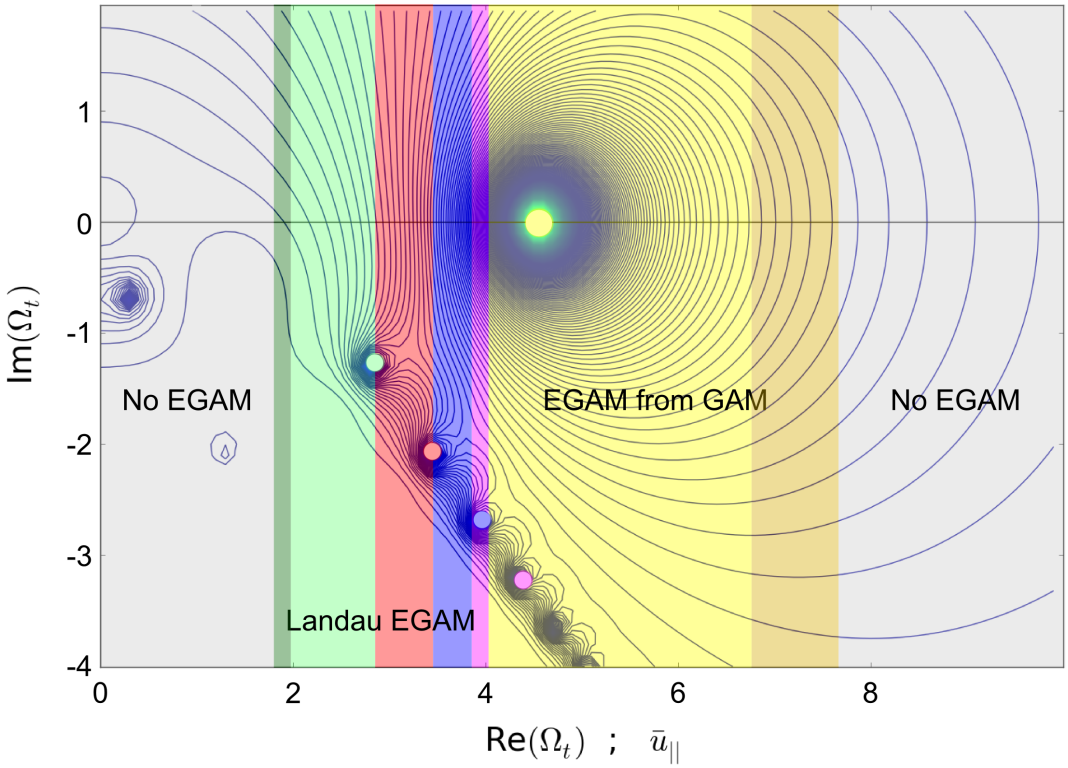

FIGURE 4.8 – Background: contour representation of $|D(\Omega_t)|^{-1}$ in the complex plane for $q = 2.6$, $T_t/T_e = 1$ and in the absence of fast ions. Coloured stripes: $\bar{u}_{||}$. This figure allows one to see the resonance link between $\bar{u}_{||}$ (coloured stripes) and the roots of the GAM dispersion relation in the absence of fast particles (coloured circles), when bulk and fast ions belong to the same species (D-D) and when $\tau_k = 0.4$. Reading example: for a value of 2.5, $\bar{u}_{||}$ is in the light green stripe. This means that it is the root tagged with a light green circle that will be excited and turn into the EGAM when fast particles are added.

is consistent with what can be observed in Figure 4.4: when q increases (for a given $\bar{u}_{||}$) or when $\bar{u}_{||}$ decreases (for a given q), there is a transition from the *EGAM from GAM* zone to the *Landau EGAM* zone. The almost straight-line limit between those two zones was also expected, as it reflects the role of $\bar{u}_{||}/q$ in the resonance $\omega_{\mathrm{GAM}} = \sqrt{2T_t/m_k}(\bar{u}_{||}/qR)$ (expressed in terms of the non-normalized frequency ω_{GAM}).

Figure 4.8 (on which bulk and fast particles belong to the same species, which means that $\Omega_k = \Omega_t$) gives a clear illustration of the resonance $\Omega_k = \bar{u}_{||}$ when $q = 2.6$ is fixed and $\bar{u}_{||}$ varies, with $\tau_k = 0.4$. It can be seen that the fast particles always excite a root of the dispersion relation which has a real part $\mathrm{Re}(\Omega_t)$ very close to $\bar{u}_{||}$; in fact it is the first mode which has a real frequency superior to $\bar{u}_{||}$ which is excited - with a preference for the GAM mode when two modes have similar real frequencies, given that this mode is already very close to the excitation threshold, and therefore requires less energy to be excited than the highly damped modes.

Below a certain value of $\bar{u}_\parallel$ ($\bar{u}_\parallel = 1.8$ in Figure 4.8), the EGAMs are not excited - we here remind that the EGAM is considered not to be excited when it never has a positive growth rate for fractions of fast particles ranging between 0 and 40%, with a precision of 0.05 for the growth rate $\mathrm{Im}(\Omega_t)$. For $\bar{u}_\parallel$ between 1.8 and 2 (in dark green in Figure 4.8), the EGAM is a Landau EGAM: it corresponds to a root of the dispersion relation which does not exist in the absence of fast particles, and which appears close to the root tagged with a light green circle when fast particles are added. For $\bar{u}_\parallel$ between 2 and 4, the Landau EGAMs come from roots which all exist in the absence of fast particles, and which are tagged with colour circles in Figure 4.8. For $\bar{u}_\parallel$ between 4 and 6.7, the EGAM comes from the GAM root (in light yellow in Figure 4.8).

Beyond a certain value of $\bar{u}_\parallel$ ($\bar{u}_\parallel = 7.6$ in Figure 4.8), the EGAMs are no more excited. $\bar{u}_\parallel$ is too far from the GAM frequency for a resonance to occur, and the other modes are too deeply damped. Between the *GAM from EGAM* range and the *no-EGAM* range, there is a zone (in dark yellow in Figure 4.8) where the origin of the EGAM remains unclear. The reason is that when fast particles are added, a deeply damped mode first moves to the real axis and joins the GAM root: those two modes then become undistinguishable. When the fraction of fast particles further increases, one of them turns into the EGAM while the other remains below the real axis.

When τ_k increases, the bumps of the fast-particle distribution function become larger, and consequently the possibilities of resonance between $\Omega_{k,\mathrm{GAM}}$ and $\bar{u}_\parallel$ increase. When such possibilities of resonance increase, a resonance with the GAM is preferred to a resonance with a damped mode, since the GAM is already much closer to the excitation threshold. This can be observed in Figures 4.5-b) and 4.6: when τ_k increases (for given values of q and $\bar{u}_\parallel$), there is a transition from the *Landau EGAM* zone to the *EGAM from GAM* zone.

4.4 Conclusion

The ratio of frequencies between the EGAM and the GAM close to 1/2 observed in experiments in DIII-D [Nazikian 2008] and in the non-linear code GYSELA [Zarzoso 2012b] is recovered with a linear model. A noticeable feature of this linear model is that quantitative results can be obtained in a few minutes through numerical computation on a personal computer. This model however exhibits some limitations. First, kinetic electrons are not taken into account, while they might play a role in the excitation of EGAMs, similarly to the effect observed for standard GAMs [Zhang 2010]. Second, trapped ions are not considered either. Finally, neither FLR nor FOW effects are taken into account. The

impacts of FLR/FOW effects on EGAMs, together with a detailed comparison of the analytic dispersion relation with gyrokinetic simulations, are analysed in [Zarzoso 2014].

Depending on the equilibrium parameters of the plasma, as well as on the parameters of the energetic particles, the GAMs and EGAMs belong or not to the same branch. The EGAM originates from the GAM in the following regions of the studied parameters: low values of the safety factor q and of the mass of the fast ions; high values of the energy of the fast ions, of the width of the fast particle distribution, and of the ratio of the bulk ion temperature to the electron temperature. On the contrary, the EGAM originates from a mode which is damped in the absence of fast particles (Landau EGAM) when the studied parameters are in the following regions: high values of the safety factor q and of the mass of the fast ions; low values of the energy of the fast ions, of the width of the fast particle distribution, and of the ratio of the bulk ion temperature to the electron temperature.

The difference between EGAMs originating from GAMs and Landau EGAMs may be observed in experiments through the different density thresholds required for their excitation (Figure 4.7). Information on the behaviour of EGAMs for low concentrations of fast particles can be retrieved from the present model and may be compared to experimental results. It may also be possible to differentiate the two types of EGAM through their radial profiles: since they have different origins, an EGAM from GAM and a Landau EGAM may have different radial structures. If this happened to be the case, it would then be possible to observe it in experiments. Clarification on the EGAM radial structure and the potential differences between different kinds of EGAMs requires additional theoretical and experimental work.

Differentiating the GAM from the EGAM in experiments has several interests. Contrary to the GAM, which arises from turbulence, the EGAM can give information on the fast particle distribution. For instance, the nature of the EGAM (*EGAM from GAM* or *Landau EGAM*) can give information on the mean velocity of the fast particles (parameter $\bar{u}_{\parallel}$ in Figure 4.8). Besides, if it is found from further investigation that the EGAMs have different radial structures depending on their nature, their impact on turbulence may prove different as well. Since the study of EGAMs is largely motivated by their impact on turbulence, it is worth trying to understand whether different types of interaction with turbulence may exist, depending on the EGAM type.

Chapter 5

Description of the interaction of EGAMs with ITG modes through a three wave parametric decay model

GAMs were found to have a mitigating impact on turbulence in [Hallatschek 2001, Jakubowski 2002, Ramisch 2003, Miyato 2004, Waltz 2008, Conway 2011, Xu 2012]. EGAMs were simulated [Zarzoso 2012b] with the gyrokinetic code GYSELA [Sarazin 2006, Grandgirard 2008, Sarazin 2010], and have been found to destabilize turbulence [Zarzoso 2013]. This impact of EGAMs on turbulence was unexpected, taking into account the similarity of GAMs with EGAMs. However, such a behaviour may occur only for a certain range of parameters. We present in this section a model of the parametric decay of an EGAM into two ITG waves. The aim is to understand under which conditions such a phenomenon may take place, and consequently how it can be avoided. After having introduced the numerical results showing the excitation of turbulence by EGAMs, we present the parametric interaction model. We then detail the local dispersion relation derived with this model, in the case of an EGAM decaying into two ITG modes. Finally, we discuss a possible one dimensional propagative mechanism of interaction between EGAM and ITG, within the parametric interaction model.

5.1 Gyrokinetic simulations show excitation of ITG modes by EGAMs

In this section, we comment on numerical simulations presented in [Zarzoso 2013]; more details about them can be found therein. Those simulations were carried out with the gyrokinetic code GYSELA.

Two sources play a role in the considered simulations:

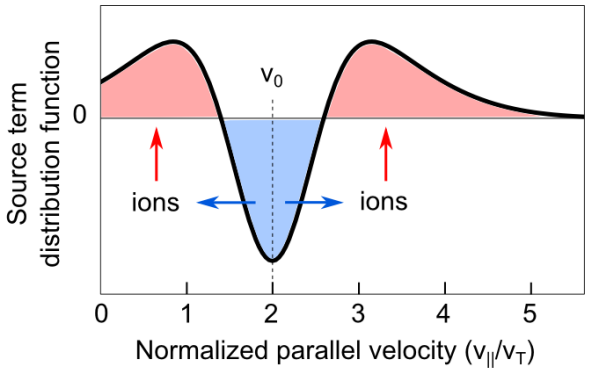

FIGURE 5.1 – Implementation of the fast ion source in GYSELA

- a thermal heat flux source is present at the core of the plasma, around the inner radial boundary of the simulation domain. It leads to an increase in temperature of the core plasma; a steep radial temperature gradient is thus created, enabling ITG turbulence to develop. This heat source does not cause positive energy slopes ($\partial_E f > 0$) to appear in the ion distribution function.

- an *ad hoc* fast particle source, the role of which is to trigger EGAMs. This fast particle source corresponds to a "pump" which removes particles from a given position on the parallel velocity axis and injects them at another position on the same axis (see Figure 5.1). This fast particle source has been designed to inject energy only, while it has no effect on momentum, density nor vorticity. This pump does modify the distribution function shape in the velocity space: it creates two bumps-on-tail in parallel velocity, which can trigger EGAMs when they grow large enough. Contrary to the thermal heat source, the fast particle source is localized almost everywhere in the radial simulation domain.

During the first part of the simulations, only the heat flux source is activated, while the fast particle source is turned off. The result is the appearance of ITG turbulence. When the turbulence reaches steady-state, the fast particle pump is turned on: it corresponds to the start of period A in Figures 5.2 and 5.3. During period A, the source of fast particles is active, but the bumps-on-tail are not large enough yet for EGAMs to be triggered; ITG turbulence remains active as if no fast particle source had been turned on. The fluctuations corresponding to this turbulence are visible in red and yellow in Figure 5.2 and in colours other than green in Figure 5.3.

During period B, it can be seen that turbulent fluctuations decrease in intensity, in particular for values of the minor radius superior to 0.5. This is due to the way the fast particle source is implemented in GYSELA: the particles pumped by the source are removed from a position in the velocity space which is resonant with ITG modes. The

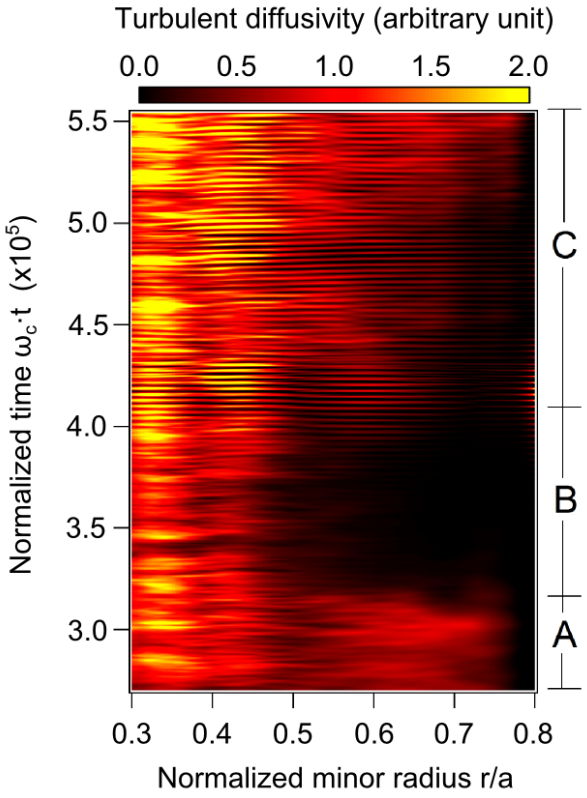

FIGURE 5.2 – Turbulent diffusivity (colour scale) as a function of the normalized minor radius (x-axis) and time (y-axis). Three periods, called A, B and C, are distinguished depending on the type of EGAM and ITG activity. Source: [Zarzoso 2013]

particle depletion in this particular velocity space region therefore accounts for the decrease in intensity of ITG turbulence. Note that during period B, EGAMs are still not observed in the simulations.

The beginning of period C corresponds to the appearance of EGAMs. At the same time, the ITG turbulence regains intensity. A difference in the ITG turbulence behaviour can be observed in Figure 5.2 between periods A and C: during period A, ITG turbulence seems to have a broadband frequency; while it is modulated by the EGAM frequency during period C. This last fact suggests that there is an interaction between EGAMs and ITG modes. However, against expectations, the appearance of EGAMs does not coincide with a reduction, but with an increase in turbulence intensity.

The interaction between EGAMs and ITG modes is also visible in Figure 5.3. At the end of period B, static oscillations appear at minor radius around 0.6. At that moment, those static oscillations appear as independent from other oscillations exhibiting an avalanche-like behaviour at minor radius 0.4-0.5. Then, during period C, a mixing between those static and avalanche-like oscillations occur.

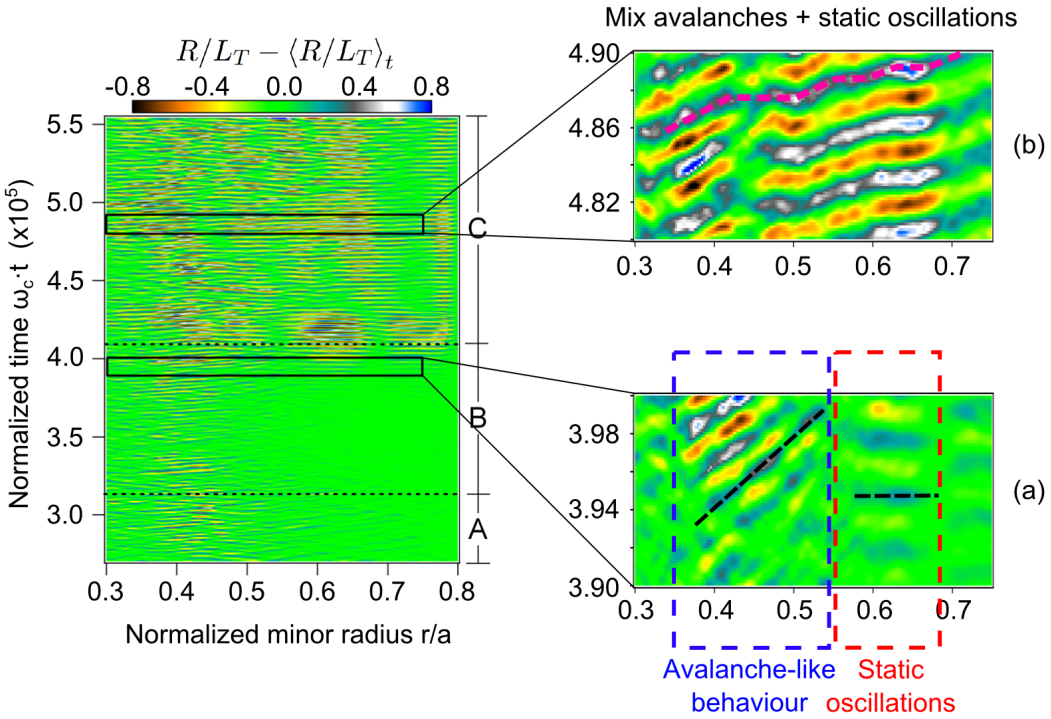

FIGURE 5.3 – Time fluctuating part of the inverse normalized temperature gradient length ($R/L_T - \langle R/L_T \rangle_t$, colour scale) as a function of the normalized minor radius (x-axis) and time (y-axis). Three periods, called A, B and C, are distinguished depending on the type of EGAM and ITG activity. Two zooms (a) and (b) are made on characteristic time slices exhibiting avalanche-like behaviours and static oscillations. Source: [Zarzoso 2013]

5.2 Presentation of the three wave parametric interaction model

We present in this section a parametric decay model which aims at understanding the interactions between EGAM and ITG modes observed in the GYSELA gyrokinetic simulations described in Section 5.1. This model takes into account three different waves: one is a pump wave, the existence of which is taken for granted. This pump wave decays into two other waves, called the daughter waves. The excitation of those two daughter waves is described by the parametric interaction model; their growth is a consequence of the pump wave decay.

Such a model was already considered in [Zonca 2008]. The pump wave was then an ITG mode, decaying into a GAM and another ITG mode: the situation is illustrated in Figure 5.4-a). We here consider a different situation: the pump wave is an EGAM, and the two daughter waves are ITG modes, as illustrated in Figure 5.4-b).

The interaction between the three waves is non-linear. In the gyrokinetic Vlasov

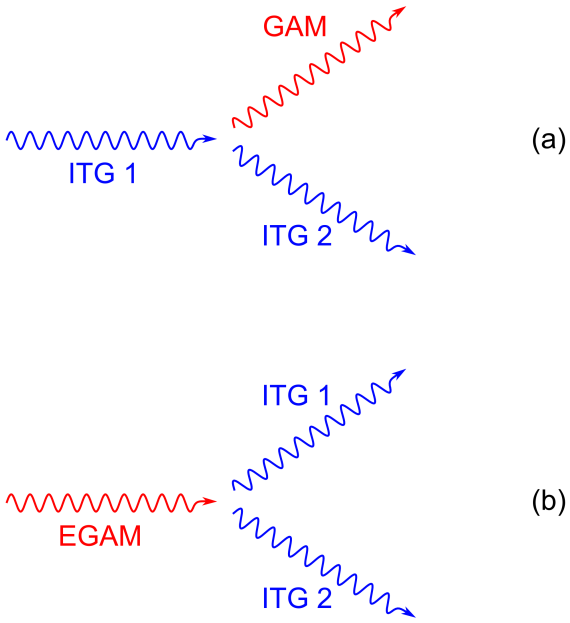

FIGURE 5.4 – Illustration of the three wave parametric interaction model

equation, the dominant non-linearity is assumed to be the $\mathbf{E} \times \mathbf{B}$ velocity; non-linearities in the velocity space are not taken into account in the present model. In the case studied in [Zonca 2008], it was shown that through this non-linear interaction, the daughter GAM and ITG waves could be driven unstable by the ITG pump wave. We here intend to check whether daughter ITG waves can be non-linearly driven unstable by an EGAM pump wave.

For the interaction between the three modes to occur, the wave vectors and frequencies need to be in agreement:

$$\mathbf{k}_{\mathrm{E}} = \mathbf{k}_1 - \mathbf{k}_2, \tag{5.1}$$

$$\omega_{\mathrm{E}} = \omega_1 - \omega_2, \tag{5.2}$$

where $\mathbf{k}_{\mathrm{E}}$ and ω_{E} are respectively the EGAM wave vector and real frequency, $\mathbf{k}_1$ and ω_1 are respectively the first ITG mode wave vector and real frequency, $\mathbf{k}_2$ and ω_2 are respectively the second ITG mode wave vector and real frequency.

Note that we here adopt a convention under which the mode frequencies can be either positive or negative. This may differ from other conventions sometimes used in the literature, under which all frequencies are considered positive. In practice, Figure 5.4-b) corresponds to a situation where the frequencies equality should read $\omega_{\mathrm{E}} = \omega_1 + \omega_2$ if all frequencies were positive. Therefore, for (5.2) to correspond to the situation shown in

Figure 5.4-b), the following signs for the frequencies should be considered:

$$\omega_{\mathrm{E}}, \omega_1 > 0, \tag{5.3}$$

$$\omega_2 < 0. \tag{5.4}$$

We will focus in Section 5.3 on situations which fulfil those conditions.

A consequence of equation (5.2) together with conditions (5.3) and (5.4) is that the EGAM frequency should be of the same order of magnitude as the ITG frequencies. This condition is fulfilled by the ordering considered in the present study.

Indeed, as described in Chapter 4,

$$\omega_{\mathrm{E}} \sim C\frac{v_{\mathrm{T}}}{R}, \tag{5.5}$$

where v_{T} is the ion thermal velocity and C is a constant of the order of 1 to 10. Besides, as indicated in (5.28),

$$\omega_{\mathrm{ITG}} \sim \delta^2 \omega_p *, \tag{5.6}$$

where δ is a small parameter defined in expression (5.10) and $\omega_p *$ is the pressure diamagnetic frequency defined in (5.41).

As mentioned in Section 5.3.1, $a\boldsymbol{\nabla}_\perp \ln f_{\mathrm{G,eq}}$ is assumed to be of order δ^{-3}.

Consequently,

$$\omega_{\mathrm{ITG}} \sim \frac{1}{\varepsilon}\frac{v_{\mathrm{T}}}{R}, \tag{5.7}$$

where ε is the inverse aspect ratio.

Considering that $\frac{1}{\varepsilon} \sim C$, we find indeed that

$$\omega_{\mathrm{E}} \sim \omega_{\mathrm{ITG}}. \tag{5.8}$$

The EGAM is an axisymmetric mode, *i.e.* $n = 0$ where n is the toroidal mode number, and has a low poloidal mode number: $m = 0, 1$. On the contrary, ITG modes usually have high toroidal and poloidal mode numbers (n and m are of the order of a few 10). Consequently, for condition (5.1) to be met, the two ITG modes need to have identical toroidal and poloidal mode numbers. Rigorously speaking, their poloidal mode numbers may differ by unity, a difference which is much smaller than the mode number themselves. The interaction with the EGAM can only take place through the radial wave vectors.

Given that the two ITG modes have, in the situation here considered, frequencies of opposite signs and toroidal wave vectors of the same sign, their phase velocities have opposite

signs. It is sometimes assumed that ITG waves can only travel in one single direction (the ion direction) in tokamaks. In fact, they may also travel in the electron direction. This has already been reported for instance in [Romanelli 1989, Romanelli 1990]. In those papers, depending on the plasma parameters, the ITG can travel in one or the other direction. In the present manuscript, we can infer from expressions (5.54) and (5.55) that two ITG modes can travel in opposite directions, including in situations when the two modes share the same plasma parameters (which is not the case in [Romanelli 1989, Romanelli 1990]). The condition for it to happen is that the two modes have different ballooning angles, one of them being superior to $\pi/2$.

The resolution of the model leads to equations of the following type:

$$\partial_t \phi_1 = \Lambda \phi_{\mathrm{E}} \phi_2, \tag{5.9}$$

where Λ is the non-linear coupling operator, ϕ_1 is the first ITG mode amplitude, ϕ_2 is the second ITG mode amplitude, and ϕ_{E} is the EGAM mode amplitude. Calling $\gamma = (\partial_t \phi_1)/\phi_1$ the non-linear ITG growth rate, the aim is to check whether γ can take real, positive values in the framework of the parametric interaction model.

5.3 Local model

We here derive the local dispersion relations in the case of an EGAM pump wave and two ITG daughter waves. The time evolution equations are deduced from the dispersion relations. Two branches arise, leading to different possible situations. Out of them only one is physically meaningful.

5.3.1 Derivation of the local dispersion relations

The non-linear dispersion relation is derived in the case where the linear part corresponds to one ITG mode, called the first ITG mode, while the non-linear part corresponds to the EGAM and the other ITG mode, called the second ITG mode. From this dispersion relation, the equation in which the linear part corresponds the second ITG mode, while the non-linear part corresponds to the EGAM and the first ITG mode, is then deduced.

More details about the present derivation can be found in Appendix C. The derivation of the linear part is similar to the derivation of the linear ITG mode exposed in Section 2.3.1 and Appendix A.

We first consider the gyrokinetic Vlasov equation up to order 1 in ρ_*, where $\rho_* = \rho_i/a$ is the normalized ion Larmor radius. A second small parameter δ is considered, of the

order of $k_\perp \rho_i$, where $k_\perp$ designates the order of magnitude of the perpendicular wave vectors. With the notations used below, $k_\perp$ may correspond to either k_θ, K_1, K_2 or k_r. The ordering is as follows:

$$\rho_* \ll \delta \sim k_\perp \rho_i \ll 1. \tag{5.10}$$

The ordering $\delta \ll 1$ means that we are here considering long wave lengths as compared to ρ_i.

The ion gyro-centre distribution function f_G is decomposed into an equilibrium part, called $f_\mathrm{G,eq}$, and a perturbed part called $\tilde{f}$. The perturbed part itself comprises three components $\tilde{f}_\mathrm{GE}$, $\tilde{f}_\mathrm{G1}$ and $\tilde{f}_\mathrm{G2}$ corresponding respectively to the EGAM, the first ITG mode and the second ITG mode. The equilibrium electric potential is assumed to be null. The perturbed electric potential, called $\tilde{\phi}$, comprises three components $\tilde{\phi}_\mathrm{E}$, $\tilde{\phi}_1$ and $\tilde{\phi}_2$ corresponding respectively to the EGAM, the first ITG mode and the second ITG mode. Those perturbations can be summed up as follows:

$$f_\mathrm{G} = f_\mathrm{G,eq} + \tilde{f}_\mathrm{GE} + \tilde{f}_\mathrm{G1} + \tilde{f}_\mathrm{G2}, \tag{5.11}$$

$$\tilde{\phi} = \tilde{\phi}_\mathrm{E} + \tilde{\phi}_1 + \tilde{\phi}_2. \tag{5.12}$$

The following orderings in δ and ρ_* are assumed for the EGAM perturbation,

$$\frac{e\tilde{\phi}_\mathrm{E}}{T_i} \sim \rho_* \delta^{-2}, \tag{5.13}$$

$$\frac{\tilde{f}_\mathrm{GE}}{f_\mathrm{G,eq}} \sim \rho_* \delta^{-1}, \tag{5.14}$$

and for the ITG perturbations,

$$\frac{e\tilde{\phi}_{1,2}}{T_i} \sim \rho_* \delta^{-1}, \tag{5.15}$$

$$\frac{\tilde{f}_\mathrm{G1,2}}{f_\mathrm{G,eq}} \sim \rho_* \delta^{-3}. \tag{5.16}$$

The ordering in ρ_* is imposed by the gyrokinetic equation (see [Brizard 2007]). The orderings in δ of $\tilde{\phi}_\mathrm{E}$ and $\tilde{f}_{1,2}$ correspond to the idea that the non-linear term in the $\mathbf{E} \times \mathbf{B}$ velocity is dominant. The orderings in δ of $\tilde{f}_\mathrm{GE}$ and $\tilde{\phi}_{1,2}$ are then deduced from the gyrokinetic Vlasov equations (see Appendix A for the ITG and Appendix B for the EGAM). $J_0 - 1$ applied to perturbed fields is of order δ^2 and $a\boldsymbol{\nabla}_\perp \ln f_\mathrm{G,eq}$ is assumed to be of order δ^{-3}.

The computation is carried out up to order 1 in ρ_* and -1 in δ. The equilibrium distribution function $f_\mathrm{G,eq}$ is assumed to be a Maxwellian. The ballooning representation

is used for ITG modes 1 and 2,

$$\tilde{\phi}_{1,2}(\mathbf{x}_{\mathrm{G}},t) = \phi_{1,2}(t)e^{-i\omega_{1,2}t}e^{in\varphi}\hat{\Phi}_{1,2}(\theta)e^{-ir_0k_\theta\theta - inq_0'x\theta + ixK_{1,2}} + c.c., \tag{5.17}$$

$$\tilde{f}_{\mathrm{G}1,2}\big(\mathbf{x}_{\mathrm{G}},v_\parallel,\mu,t\big) = f_{1,2}(t)e^{-i\omega_{1,2}t}e^{in\varphi}\hat{F}_{1,2}\big(\theta,v_\parallel,\mu\big)e^{-ir_0k_\theta\theta - inq_0'x\theta + ixK_{1,2}} + c.c., \tag{5.18}$$

while the EGAM is represented in the conventional form:

$$\tilde{\phi}_{\mathrm{E}}(\mathbf{x}_{\mathrm{G}},t) = \frac{T_i}{e}\phi_{\mathrm{E}}(t)e^{-i\omega_{\mathrm{E}}t}e^{ik_rx} + c.c. \tag{5.19}$$

In those expressions, q is the safety factor, $\phi_{\mathrm{E},1,2}(t)$ and $f_{1,2}(t)$ are the amplitudes of the modes, $K_{1,2} = n\theta_{1,2}q_0'$ is the ITG radial wave vector, $\theta_{1,2}$ is the ITG ballooning angle, n is the ITG toroidal mode number, $k_\theta = \frac{nq_0}{r_0}$ is the ITG poloidal wave vector, k_r is the EGAM radial wave vector, and *c.c.* means *complex conjugate*. We consider the safety factor to be linear: $q = q_0 + q_0'x$, where $q_0 = q(r_0)$, $q_0' = q'(r_0)$, $x = r - r_0$ and r_0 is the position (in the small radius coordinate) of the reference resonance surface. $\omega_{\mathrm{E},1,2}$ is the real part of the linear frequency (*i.e.* the frequency which is solution of the linear dispersion relation).

In practice, since the EGAM is the pump wave, its amplitude is assumed to be large and vary slowly compared to the amplitudes of the daughter waves (the ITG modes). Therefore, we will consider that ϕ_{E} is a constant.

To ensure interaction between the two ITG modes and the EGAM, the following relations are assumed:

$$\omega_{\mathrm{E}} + \omega_2 = \omega_1, \tag{5.20}$$

$$k_r + K_2 = K_1. \tag{5.21}$$

The following wave vectors and frequencies are defined:

$$k_{\perp 1,2} = \sqrt{(K_{1,2} - nq_0'\theta)^2 + k_\theta^2} \qquad \text{is the perpendicular ITG wave vector,} \tag{5.22}$$

$$ik_\parallel = \frac{\partial_\theta}{qR} \qquad \text{is the parallel wave vector,} \tag{5.23}$$

$$i\Omega_{1,2} = i\omega_{1,2} - \partial_t \qquad \text{is the comprehensive mode frequency,} \tag{5.24}$$

$$\omega_* = -k_\theta\frac{\partial_r \ln f_{\mathrm{G,eq}}}{B}\frac{T_i}{e} \qquad \text{is the diamagnetic frequency,} \tag{5.25}$$

$$\omega_{g1,2} = v_g[\sin\theta(K_{1,2} - nq_0'\theta) - \cos\theta k_\theta] \qquad \text{is the kinetic drift frequency,} \tag{5.26}$$

$$\omega_\parallel = v_\parallel k_\parallel \qquad \text{is the transit frequency.} \tag{5.27}$$

In expression (5.26), $v_g = \frac{mv_\parallel^2 + \mu B}{eBR}$ is the norm of the drift velocity.

A hydrodynamic limit is considered, with the following orderings:

$$\frac{\omega_*}{\Omega_{1,2}} \sim \delta^{-2}, \tag{5.28}$$

$$\frac{\omega_\parallel}{\Omega_{1,2}} \sim \delta, \tag{5.29}$$

$$\frac{\omega_{g1,2}}{\Omega_{1,2}} \sim \delta^2. \tag{5.30}$$

The gyrokinetic Vlasov equation then reads:

$$\begin{aligned} f_1(t)\hat{F}_1 = -f_{\mathrm{G,eq}}\frac{e}{T_i}\frac{\omega_*}{\Omega_1}\left(1 - \frac{\omega_{g1}}{\Omega_1} + \frac{\omega_\parallel}{\Omega_1} + \frac{\omega_\parallel^2}{\Omega_1^2} - \frac{1}{2}\frac{\mu B}{T_i}k_{\perp 1}^2\rho_i^2\right)\phi_1(t)\hat{\Phi}_1 \\ - \left(1 - \frac{\omega_{g1}}{\Omega_1} + \frac{\omega_\parallel}{\Omega_1} + \frac{\omega_\parallel^2}{\Omega_1^2}\right)\frac{iA}{\Omega_1}, \end{aligned} \tag{5.31}$$

where the linear part corresponds to the first ITG mode and the non-linear part A (see Appendix C for details) is related to the EGAM and the second ITG mode. A similar equation can be derived in which the linear part is related to the second ITG mode while the non-linear part corresponds to the EGAM and the first ITG mode

We here suppose that there is only one species of ions, and that its charge number is 1. The equilibrium density of ions and electrons is therefore the same, and is here called n_i. Assuming that the electron temperature T_e is equal to the ion equilibrium temperature T_i and neglecting the spatial variations of n_i, the quasi-neutrality equation reads

$$n_i\frac{e}{T_i}\phi_{1,2}(t)\hat{\Phi}_{1,2} = \int f_{1,2}(t)\hat{F}_{1,2}\left(1 - \frac{1}{2}\frac{\mu B}{T_i}\rho_i^2\left[k_\theta^2 + \left(K_{1,2} - nq_0'\theta\right)^2\right]\right)(dv)^3. \tag{5.32}$$

After integrating over the velocity, an integration is performed over θ, using a Gaussian form for the poloidal shape $\hat{\Phi}_{1,2}$, as suggested in Section 2.3.1. We suppose that $q \gg 1$.

The resulting dispersion relations read as follows:

$$\frac{e}{T_i}\phi_1(t)L_1(\Omega_1, K_1) = \frac{i}{\Omega_2}\Gamma_1(\Omega_1, \Omega_2, K_1, K_2)\frac{s_0(\theta_1 - \theta_2)k_\theta^2}{B}\phi_{\mathrm{E}}\phi_2(t), \tag{5.33}$$

$$\frac{e}{T_i}\phi_2(t)L_2(\Omega_2, K_2) = -\frac{i}{\Omega_1}\Gamma_2(\Omega_1, \Omega_2, K_1, K_2)\frac{s_0(\theta_1 - \theta_2)k_\theta^2}{B}\phi_{\mathrm{E}}\phi_1(t); \tag{5.34}$$

where the linear parts are

$$L_1(\Omega_1, K_1) = \frac{\Omega_1 + \omega_n^*}{\omega_p^*} + \frac{\omega_{gf}}{\Omega_1}\cos\theta_1 - k^2, \tag{5.35}$$

$$L_2(\Omega_2, K_2) = \frac{\Omega_2 + \omega_n^*}{\omega_p^*} + \frac{\omega_{gf}}{\Omega_2}\cos\theta_2 - k^2; \tag{5.36}$$

and the non-linear parts are

$$\begin{aligned}\Gamma_1(\Omega_1, \Omega_2, K_1, K_2) &= \frac{\omega_n^*}{\omega_p^*} \\ &+ \left[\frac{\cos\theta_2}{\Omega_2} + \frac{-s_0(\theta_1-\theta_2)\sin\theta_2 + \cos\theta_2}{\Omega_1}\right]\omega_{gf} - k^2\left[1 + (\theta_1-\theta_2)^2 s_0^2\right],\end{aligned} \tag{5.37}$$

$$\begin{aligned}\Gamma_2(\Omega_1, \Omega_2, K_1, K_2) &= \frac{\omega_n^*}{\omega_p^*} \\ &+ \left[\frac{\cos\theta_1}{\Omega_1} + \frac{s_0(\theta_1-\theta_2)\sin\theta_1 + \cos\theta_1}{\Omega_2}\right]\omega_{gf} - k^2\left[1 + (\theta_1-\theta_2)^2 s_0^2\right].\end{aligned} \tag{5.38}$$

In those expressions,

$$s_0 = \frac{r_0 q_0'}{q_0} \qquad \text{is the magnetic shear on the reference surface,} \tag{5.39}$$

$$\omega_n^* = -\frac{k_\theta}{B}\frac{T_i}{e}\frac{n_i'(r)}{n_i} \qquad \text{is the density diamagnetic frequency,} \tag{5.40}$$

$$\omega_p^* = -\frac{k_\theta}{B}\frac{T_i}{e}\frac{p_i'(r)}{p_i} \qquad \text{is the pressure diamagnetic frequency,} \tag{5.41}$$

$$\omega_{gf} = \frac{2k_\theta T_i}{eBR} = \frac{2nq_0 T_i}{er_0 BR} \qquad \text{is the fluid drift frequency,} \tag{5.42}$$

$$k = k_\theta \rho_i \qquad \text{is the normalized poloidal wave vector.} \tag{5.43}$$

In equation (5.33), the linear part is related to the first ITG mode, while the non-linear part corresponds to the EGAM and the second ITG mode. In equation (5.34), the linear part corresponds to the second ITG mode, while the non-linear part is related to the EGAM and the first ITG mode.

5.3.2 Time evolution equation

We assume that the two ITG modes are linearly marginally stable. This means that the linear frequencies, which are roots of the linear dispersion relations (5.35) and (5.36), are real. We perform an expansion of L_1 and L_2 around the linear frequencies. After differentiation in time, we find the same time evolution equations for ϕ_1 and ϕ_2:

$$\partial_{tt}\phi_1(t) = \Lambda_1\Lambda_2\phi_{\mathrm{E}}^2\phi_1(t), \tag{5.44}$$

$$\partial_{tt}\phi_2(t) = \Lambda_1\Lambda_2\phi_{\mathrm{E}}^2\phi_2(t), \tag{5.45}$$

where

$$\Lambda_1(\omega_1,\omega_2,K_1,K_2)=\frac{T_i}{e}\frac{s_0(\theta_1-\theta_2)k_\theta^2\Gamma_1(\omega_1,\omega_2,K_1,K_2)}{\omega_2 B\left[\frac{1}{\omega_p^*}-\frac{\omega_{gf}}{\omega_1^2}\cos\theta_1\right]}, \tag{5.46}$$

$$\Lambda_2(\omega_1,\omega_2,K_1,K_2)=-\frac{T_i}{e}\frac{s_0(\theta_1-\theta_2)k_\theta^2\Gamma_2(\omega_1,\omega_2,K_1,K_2)}{\omega_1 B\left[\frac{1}{\omega_p^*}-\frac{\omega_{gf}}{\omega_2^2}\cos\theta_2\right]}, \tag{5.47}$$

have been assumed to be independent of time.

Calling

$$\gamma^2=\Lambda_1\Lambda_2\phi_{\mathrm{E}}^2, \tag{5.48}$$

ϕ_1 and ϕ_2 can be expressed as $e^{\pm\gamma t}$.

For the two ITG modes to be linearly unstable, γ^2 needs to be positive. Otherwise, if γ^2 is negative, γ will be an imaginary number, which means that the ITG modes will be purely oscillatory and will not grow.

γ^2 has the same sign as

$$D=-\frac{\Gamma_1(\omega_1,\omega_2,K_1,K_2)\Gamma_2(\omega_1,\omega_2,K_1,K_2)}{\omega_1\omega_2\left[\frac{1}{\omega_p^*}-\frac{\omega_{gf}}{\omega_1^2}\cos\theta_1\right]\left[\frac{1}{\omega_p^*}-\frac{\omega_{gf}}{\omega_2^2}\cos\theta_2\right]}, \tag{5.49}$$

where ω_1 and ω_2 are respectively roots of equations (5.35) and (5.36).

Let us normalize the frequencies to ω_p^*:

$$\bar{\Omega}_n=\frac{\omega_n^*}{\omega_p^*}, \tag{5.50}$$

$$\bar{\Omega}_g=\frac{\omega_{gf}}{\omega_p^*}, \tag{5.51}$$

$$\bar{\Omega}_1=\frac{\omega_1}{\omega_p^*}, \tag{5.52}$$

$$\bar{\Omega}_2=\frac{\omega_2}{\omega_p^*}. \tag{5.53}$$

With those notations, $\bar{\Omega}_1$ and $\bar{\Omega}_2$ read

$$\bar{\Omega}_1=\frac{k^2-\bar{\Omega}_n}{2}+\varepsilon_1\frac{1}{2}\sqrt{\left(k^2-\bar{\Omega}_n\right)^2-4\bar{\Omega}_g\cos\theta_1}, \tag{5.54}$$

$$\bar{\Omega}_2=\frac{k^2-\bar{\Omega}_n}{2}+\varepsilon_2\frac{1}{2}\sqrt{\left(k^2-\bar{\Omega}_n\right)^2-4\bar{\Omega}_g\cos\theta_2}, \tag{5.55}$$

where $\varepsilon_1,\varepsilon_2=\pm1$ determine two different branches. As shown in Section 5.3.3 below,

only the $\varepsilon_1, \varepsilon_2 = +1$ branch is physically meaningful.

5.3.3 Determination of the physically meaningful branch

Two consistent ways are used to show that in expressions (5.54) and (5.55), only the $\varepsilon_1, \varepsilon_2 = +1$ branch is physically meaningful. We first consider the poloidal extension of the two ITG modes, which must be finite. We then consider the radial propagation of a linearly damped ITG mode, which must exhibit a group velocity in the direction of the reference resonance surface, thus conveying energy to the position where the mode is damped.

Finite poloidal extension of ITG modes

Let us consider the non-local ITG linear dispersion relation for the first ITG mode (see Appendix A for details on the derivation of this equation):

$$-\frac{1}{\Omega_{\mathrm{L1}}^2}\frac{v_{\mathrm{T}}^2}{q^2R^2}\partial_{\theta\theta}\hat{\Phi}_1 + \left[\frac{\Omega_{\mathrm{L1}}+\omega_n^*}{\omega_p^*} + \frac{\omega_{gf}}{\Omega_{\mathrm{L1}}}\left[1+(\theta-\theta_1)^2\left(s_0-\frac{1}{2}\right)+(\theta-\theta_1)\theta_1(s_0-1)-\frac{\theta_1^2}{2}\right]\right.$$
$$\left. - k^2\left[s_0^2(\theta-\theta_1)^2+1\right]\right]\hat{\Phi}_1 = 0, \tag{5.56}$$

where Ω_{L1} is the complex linear frequency of the mode. Contrary to what was supposed in Section 5.3.2, we here consider that Ω_{L1} has a small imaginary part, called γ_1, which will enable us to determine the sign of ε_1. The linear frequency thus reads

$$\Omega_{\mathrm{L1}} = \omega_1 + i\gamma_1. \tag{5.57}$$

A Gaussian function

$$\hat{\Phi}_1 = e^{-\frac{(\theta-\theta_1-y_1)^2}{2\Delta_1^2}} \tag{5.58}$$

is solution of equation (5.56). The expressions of parameters y_1 and Δ_1 are given in Section 2.3.1 and in Appendix A.

In the limit $s_0 \gg 1$, where s_0 is the magnetic shear, equation (5.56) becomes

$$\partial_{\theta\theta}\hat{\Phi}_1 + \left[k^2 s_0^2\,\Omega_{\mathrm{L1}}^2\frac{q^2R^2}{v_{\mathrm{T}}^2}(\theta-\theta_1)^2 - \zeta\right]\hat{\Phi}_1 = 0, \tag{5.59}$$

and the parameters of the Gaussian solution become

$$y_1 = 0, \tag{5.60}$$

$$\frac{1}{\Delta_1^2} = \iota_1 i|ks_0|\frac{qR}{v_\mathrm{T}}(\omega_1 + i\gamma_1), \tag{5.61}$$

where $\iota_1 = \pm 1$ remains to be determined. For the poloidal extension of the ITG mode to be finite, the real part of $\frac{1}{\Delta_1^2}$ needs to be positive, *i.e.* $\iota_1\gamma_1$ needs to be negative.

In equation (5.59), ζ is a parameter needed to ensure that expression (5.58) is a consistent solution of the equation. (5.58) being solution of (5.59) imposes that

$$\zeta = -\frac{1}{\Delta_1^2} = -\iota_1 i|ks_0|\frac{qR}{v_\mathrm{T}}(\omega_1 + i\gamma_1). \tag{5.62}$$

Besides, ζ has to be consistent with the constant term in θ in equation (5.56):

$$\frac{1}{\Omega_{\mathrm{L}1}^2}\frac{v_\mathrm{T}^2}{q^2R^2}\zeta = \frac{\Omega_{\mathrm{L}1} + \omega_n^*}{\omega_p^*} + \frac{\omega_{gf}}{\Omega_{\mathrm{L}1}}\cos\theta_1 - k^2, \tag{5.63}$$

where $1 - \frac{\theta_1^2}{2}$ has been replaced with $\cos\theta_1$.

The following equation must thus be satisfied by $\Omega_{\mathrm{L}1}$:

$$\frac{\Omega_{\mathrm{L}1} + \omega_n^*}{\omega_p^*} + \frac{\omega_{gf}}{\Omega_{\mathrm{L}1}}\cos\theta_1 - k^2 + \frac{1}{\Omega_{\mathrm{L}1}}\frac{v_\mathrm{T}}{qR}\iota_1 i|ks_0| = 0. \tag{5.64}$$

We recognize the linear dispersion relation (5.35) where an imaginary term has been added. This additional term is small in the limit $q \gg 1$.

Normalizing the frequencies to ω_p^*, this dispersion relation becomes

$$\bar{\Omega}_{\mathrm{L}1} + \bar{\Omega}_n + \frac{\bar{\Omega}_g}{\bar{\Omega}_{\mathrm{L}1}}\cos\theta_1 - k^2 + \frac{1}{\bar{\Omega}_{\mathrm{L}1}\omega_p^*}\frac{v_\mathrm{T}}{qR}\iota_1 i|ks_0| = 0, \tag{5.65}$$

where

$$\bar{\Omega}_{\mathrm{L}1} = \frac{\Omega_{\mathrm{L}1}}{\omega_p^*}. \tag{5.66}$$

The solution reads

$$\bar{\Omega}_{\mathrm{L}1} = \frac{k^2 - \bar{\Omega}_n}{2} + \varepsilon_1\frac{1}{2}\sqrt{\left(k^2 - \bar{\Omega}_n\right)^2 - 4\left(\bar{\Omega}_g\cos\theta_1 + \frac{1}{\omega_p^*}\frac{v_\mathrm{T}}{qR}\iota_1 i|ks_0|\right)}, \tag{5.67}$$

where one can see that γ_1 has the same sign as $-\varepsilon_1\iota_1$. $\gamma_1\iota_1$ being negative to ensure that $\hat{\Phi}_1$ has a finite poloidal extension thus corresponds to ε_1 being positive.

The same rationale applies to the second ITG mode, and we find that ε_2 must also be positive for the mode to have a finite poloidal extension.

Balance between energy source and convected flux

Like in the previous paragraph about the finite poloidal extension of the ITG modes, we here consider the non-local linear dispersion relation in the limit $s_0 \gg 1$:

$$\partial_{\theta\theta}\hat{\Phi}_1 + \left[k^2 s_0^2\,\Omega_{\mathrm{I}1}^2 \frac{q^2R^2}{v_{\mathrm{T}}^2}(\theta-\theta_1)^2 - \zeta\right]\hat{\Phi}_1 = 0, \tag{5.68}$$

with the same solution

$$\hat{\Phi}_1 = e^{-\frac{(\theta-\theta_1)^2}{2\Delta_1^2}}. \tag{5.69}$$

We are now interested in the imaginary part of $\frac{1}{\Delta_1^2}$: we consider a model in which the ITG mode propagates radially from the reference resonance flux surface. As the radial wave vector depends on r and increases when one gets away from the reference surface, a position comes where the hydrodynamic limit is no longer valid. A Landau resonance there takes place. If the ITG mode is linearly damped, the wave group velocity should be oriented towards the reference resonance surface: indeed, the energy is then provided to the mode by the Landau resonance at the radial positions where the hydrodynamic limit is no longer valid, while this energy is withdrawn from the mode at the radial positions around the reference layer, where linear damping occurs. On the contrary, if the ITG mode is linearly unstable, the wave group velocity should be oriented outwards, from the reference resonance surface [Pearlstein 1969]: indeed, the energy is then provided to the mode by the linear instability at the radial positions around the reference layer resonance, while it is withdrawn from the mode by the Landau resonance at the radial positions where the hydrodynamic limit is no longer valid.

Calling η the imaginary part of $1/(2\Delta_1^2)$:

$$\eta = \mathrm{Im}\left(\frac{1}{2\Delta_1^2}\right), \tag{5.70}$$

the oscillatory part of the Gaussian shape reads

$$\hat{\Phi}_1 = e^{-i\eta(\theta-\theta_1)^2}, \tag{5.71}$$

with

$$\eta = \frac{1}{2}\iota_1 |k s_0| \frac{qR}{v_\mathrm{T}} \omega_1. \tag{5.72}$$

In this expression, $\iota_1 = \pm 1$.

In the ballooning representation, the poloidal shape is the Fourier transform of the small scale radial shape. Therefore, in the present model, the small scale radial shape reads $e^{-\frac{\bar{x}^2}{i\eta}} = e^{i\frac{\bar{x}^2}{\eta}}$, where $\bar{x} = (r - r_0)/d$ is the normalized distance from the ITG reference resonance flux surface and $d = 1/nq_0'$ is the distance between two resonance surfaces. This radial shape can also be written under the form of a position-dependent wave vector:

$$e^{i\frac{\bar{x}^2}{\eta}} = e^{i\int K(x)dx}, \tag{5.73}$$

with

$$K(x) = 4\iota_1 \frac{x v_\mathrm{T}}{d^2 |k s_0| qR\omega_1}, \tag{5.74}$$

and where $x = r - r_0$.

The radial group velocity of the wave then reads

$$\frac{\partial \omega_1}{\partial K} = -4\iota_1 \frac{x v_\mathrm{T}}{d^2 |k s_0| qR K^2(x)}. \tag{5.75}$$

For a linearly damped ITG mode, the wave packet must propagate towards the reference resonance surface, which means that the group velocity must be negative for x positive. Therefore, in that case, $\iota_1 = +1$.

The same procedure as in the paragraph about the finite poloidal extension of the ITG modes can then be carried out: for the Gaussian shape to satisfy the linear dispersion relation (5.68) in the limit $s_0 \gg 1$, a constant term ζ needs to be taken into account. This ζ must be equal to both $-1/\Delta_1^2$ and to the constant term in the linear dispersion relation (5.56). We thus get the linear dispersion relation of the mode, and

$$\bar{\Omega}_{\mathrm{L}1} = \frac{k^2 - \bar{\Omega}_n}{2} + \varepsilon_1 \frac{1}{2}\sqrt{\left(k^2 - \bar{\Omega}_n\right)^2 - 4\left(\bar{\Omega}_g \cos\theta_1 + \frac{1}{\omega_p^*}\frac{v_\mathrm{T}}{qR}\iota_1 i |k s_0|\right)}. \tag{5.76}$$

In the case of a damped mode, *i.e.* for $\gamma_1 < 0$, we have seen that $\iota_1 = +1$ for the radial group velocity to have the correct sign. Consequently, ε_1 must be positive, which is consistent with the result obtained considering the finite poloidal extension of the mode.

5.3.4 Results of the local model

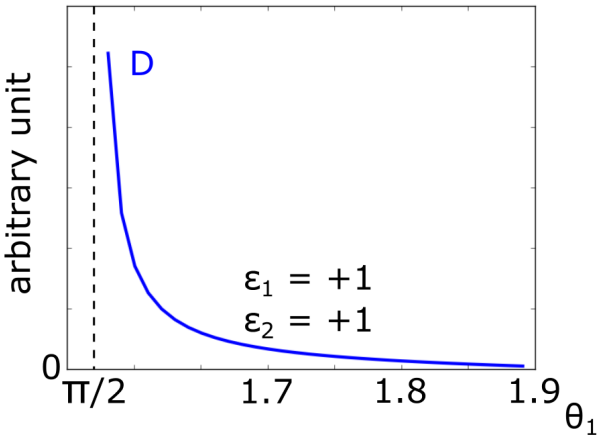

FIGURE 5.5 – D as a function of θ_1, in the case $\bar{\Omega}_g = 0.003$, $\bar{\Omega}_n = 0.2$, $k = 0.3$, and $s_0 = 1$.

Taking into account expressions (5.54) and (5.55) of $\bar{\Omega}_1$ and $\bar{\Omega}_2$, expression (5.49) can be re-written

$$D = -\varepsilon_1\varepsilon_2 \frac{\frac{\bar{\Omega}_g}{\bar{\Omega}_2} s_0(\theta_1-\theta_2)\sin\theta_1 - \bar{\Omega}_1 + \frac{\bar{\Omega}_g}{\bar{\Omega}_2}\cos\theta_1 - k^2 s_0^2(\theta_1-\theta_2)^2}{\sqrt{\left(k^2-\bar{\Omega}_n\right)^2 - 4\bar{\Omega}_g\cos\theta_1}} \times \frac{-\frac{\bar{\Omega}_g}{\bar{\Omega}_1} s_0(\theta_1-\theta_2)\sin\theta_2 - \bar{\Omega}_2 + \frac{\bar{\Omega}_g}{\bar{\Omega}_1}\cos\theta_2 - k^2 s_0^2(\theta_1-\theta_2)^2}{\sqrt{\left(k^2-\bar{\Omega}_n\right)^2 - 4\bar{\Omega}_g\cos\theta_2}}. \tag{5.77}$$

D depends on the following parameters: $\bar{\Omega}_g, \bar{\Omega}_n, k, \theta_1, \theta_2$ and s_0, under the constraint that $\bar{\Omega}_1$ and $\bar{\Omega}_2$ are real, *i.e.* $\left(k^2-\bar{\Omega}_n\right)^2 - 4\bar{\Omega}_g > 0$. Out of those parameters, the ballooning angles θ_1 and θ_2 play a significant role, in particular to ensure that $\bar{\Omega}_1$ and $\bar{\Omega}_2$ have opposite signs, as requested by (5.2). In addition, L_1 and Γ_1 on the one hand, and L_2 and Γ_2 on the other hand, are similar, which makes γ^2 close to minus a perfect square. Only the ballooning angles θ_1 and θ_2 break this symmetry between the first ITG mode and the second ITG mode.

We here consider the case $\theta_2 = 0$. Considering both $\theta_1 = 0$ and $\theta_2 = 0$ is impossible since $\bar{\Omega}_1$ and $\bar{\Omega}_2$ would then have the same sign, and γ^2 would then be negative. Another way to see it is that the ballooning angles of the ITG modes also provide the radial wave vectors K_1 and K_2: if the radial wave vectors of both the ITG modes are null, then no interaction with the EGAM can occur. However, considering that only the second ITG radial wave vector is null does not restrict the generality of the problem: the EGAM can still interact radially with the first ITG mode, while the second ITG mode provides poloidal and toroidal counterpart wave vectors for the first ITG mode.

To ensure that $\bar{\Omega}_1$ and $\bar{\Omega}_2$ have opposite signs, we consider the case $k^2 - \bar{\Omega}_n < 0$ with $\theta_1 > \pi/2$, as instructed by (5.54) and (5.55).

D is plotted in Figure 5.5 as a function of θ_1, for $\bar{\Omega}_g = 0.003$, $\bar{\Omega}_n = 0.2$, $k = 0.3$, and $s_0 = 1$: D is positive for the considered values of θ_1.

D being positive is equivalent to γ^2 being positive. Consequently, ITG modes can be driven non-linearly unstable by an EGAM pump wave in the framework of a local three wave parametric interaction model, under very stringent conditions. In particular, one of the two ITG modes should have a ballooning angle larger than $\pi/2$.

Let us now consider a non-local model, which could also explain the onset of ITG modes in the outer region, under less stringent conditions regarding the ballooning angle.

5.4 Model taking into account the ITG radial propagation

Turning back to the results of gyrokinetic simulations exposed in Section 5.1, an important feature is that during phase B, ITG modes were not entirely suppressed: they remained linearly unstable in the core region, while they were stable in the outer region. In the present section, we therefore reconsider the three wave parametric interaction model to include radial propagative effects.

The mode amplitudes ϕ_1 and ϕ_2 are now assumed to depend not only on t but also on x, where $x = r - r_0$ is the radial distance from the ITG reference resonance surface. $\phi_1(t,x)$ and $\phi_2(t,x)$ now provide the radial envelope of the modes, together with the linear ballooning angles θ_1 and θ_2. Ω_1 and Ω_2 still have the following meanings:

$$\Omega_1 = \omega_1 + i\partial_t, \tag{5.78}$$

$$\Omega_2 = \omega_2 + i\partial_t, \tag{5.79}$$

while K_1 and K_2 now stand for

$$K_1 = nq_0'\theta_1 - i\partial_x, \tag{5.80}$$

$$K_2 = nq_0'\theta_2 - i\partial_x, \tag{5.81}$$

where the ∂_x terms have been added with respect to the previous definitions of K_1 and K_2, to take into account the new dependence of ϕ_1 and ϕ_2 on x.

We here suppose that the second ITG mode is localized in the core region, where it is linearly unstable. An *ad-hoc* representation is chosen for this mode, which is assumed to

exhibit regular bursts:

$$\phi_2(t,x) = \sum_{i=0}^{+\infty} \Phi_2(x)\delta(t-t_i), \tag{5.82}$$

where the ITG bursts occur at times t_i, Φ_2 is a function localized in $x < x_2$, and x_2 denotes the limit between the region in which the ITG is linearly unstable, namely $x < x_2$, and the region in which the ITG is linearly stable, namely $x > x_2$. We here consider a situation which is the inverse of the one illustrated in Figure 5.4-a): instead of an ITG mode giving birth to another ITG mode plus an EGAM, we consider the case where an ITG mode and an EGAM give birth to another ITG mode, at a radial location different from the one of the mother ITG wave. This new situation is illustrated in Figure 5.6.

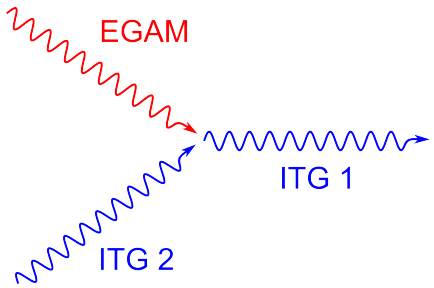

FIGURE 5.6 – Illustration of the three wave parametric interaction model - reverse process to the one shown in Figure 5.4-a).

Assuming $\theta_1 \neq 0$ and $\theta_2 = 0$, the dispersion relation in which the linear part corresponds to the first ITG mode and the non-linear part to the EGAM and the second ITG mode, reads

$$\frac{e}{T_i} L_1(\Omega_1, K_1)\phi_1(t,x) = \frac{i}{\Omega_2}\Gamma_1(\Omega_1,\Omega_2,K_1,K_2)\frac{s_0\theta_1 k_\theta^2 \hat{\Phi}_0}{B}\phi_{\mathrm{E}}\phi_2(t,x), \tag{5.83}$$

where

$$L_1(\Omega_1, K_1) = \frac{\Omega_1 + \omega_n^*}{\omega_p^*} + \frac{\omega_{gf}}{\Omega_1}\cos\theta_1 - k^2, \tag{5.84}$$

$$\Gamma_1(\Omega_1,\Omega_2,K_1,K_2) = \frac{\omega_n^*}{\omega_p^*} + \left[\frac{1}{\Omega_1} + \frac{1}{\Omega_2}\right]\omega_{gf} - k^2\left[\theta_1^2 s_0^2 + 1\right]. \tag{5.85}$$

L_1 is expanded not only around the linear complex frequency Ω_{L1}, but also around the linear radial wave vector $nq_0'\theta_1$:

$$L_1(\Omega_1,K_1) = L_1(\Omega_{\mathrm{L1}}, nq_0'\theta_1) + \frac{\partial L_1}{\partial \Omega_1}\cdot(\Omega_1 - \Omega_{\mathrm{L1}}) + \frac{\partial L_1}{\partial K_1}\cdot(K_1 - nq_0'\theta_1), \tag{5.86}$$

where $L_1(\Omega_{\mathrm{L}1}, nq_0'\theta_1) = 0$.

We define the following normalized coordinates:

$$\tau = \omega_c t, \tag{5.87}$$

$$X = \frac{x}{\rho_i}, \tag{5.88}$$

where ω_c is the cyclotron frequency and ρ_i is the fluid Larmor radius.

Assuming the first ITG mode is linearly marginally stable, *i.e.* $\gamma_1 = 0$, and taking into account expression (5.54) of ω_1, the dispersion relation reads

$$\partial_\tau \phi_1(\tau, X) + v_{g1}\partial_{\mathrm{X}}\phi_1(\tau, X) = \bar{\Lambda}_1 \phi_{\mathrm{E}}\phi_2(\tau, X), \tag{5.89}$$

where

$$\bar{\Lambda}_1(\omega_1, \omega_2, K_1, K_2) = \frac{\bar{\Omega}_1}{\bar{\Omega}_2} \frac{\Gamma_1(\omega_1, \omega_2, K_1, K_2) s_0 \theta_1 k^2}{\sqrt{\left(\bar{\Omega}_n - k^2\right)^2 - 4\bar{\Omega}_g \cos\theta_1}}, \tag{5.90}$$

$$v_{g1} = \frac{\bar{\Omega}_g}{\bar{\Omega}_c} \frac{1}{k s_0} \frac{\sin\theta_1}{\sqrt{\left(\bar{\Omega}_n - k^2\right)^2 - 4\bar{\Omega}_g \cos\theta_1}}, \tag{5.91}$$

$$\bar{\Omega}_c = \frac{\omega_c}{\omega_p^*}. \tag{5.92}$$

The following function ϕ_1 is a solution of equation (5.89):

$$\phi_1(\tau, X) = \bar{\Lambda}_1 \phi_0 \sum_{i=0}^{+\infty} \Phi_2[X - v_{g1}(\tau - \tau_i)] H(\tau - \tau_i), \tag{5.93}$$

where H is the Heaviside function and $\tau_i = \omega_c t_i$. For $\phi_1(t, x)$ to be non null in the outer region ($X > X_2$), v_{g1} needs to be positive. This condition corresponds to $\sin\theta_1 > 0$. Besides, one may observe that the group velocity depends strongly on the magnetic shear s_0: $v_{g1} \sim 1/s_0$. Low values of s_0 correspond to high values of v_{g1}. This suggests that the propagative model here described may be more efficient in low shear plasmas. The simulations presented in [Zarzoso 2013] exhibited a parabolic q-profile, with low magnetic shear (s between 0 and 0.4).

An illustration of the non-linear solution given by expression (5.93) is presented in Figure 5.7. To plot the figures, the following assumptions have been made:

$$\Phi_2(X) = e^{-\frac{X^2}{\Delta_{\mathrm{X}}^2}}, \tag{5.94}$$

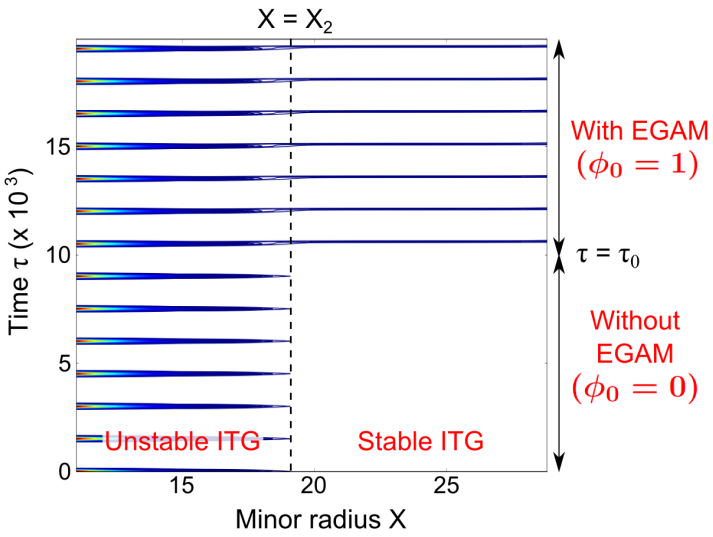

FIGURE 5.7 – Numerical representation of $|\phi_1| + |\phi_2|$, where ϕ_1 is given by expression (5.93) and ϕ_2 by expression (5.82). For $\tau < \tau_0$, $\phi_0 = 0$ which means that $\phi_1 = 0$; therefore only ϕ_2 appears in the figure. For $\tau > \tau_0$, $\phi_0 = 1$; therefore ϕ_1 and ϕ_2 appear in the figure. The colours correspond to the intensity of $|\phi_1|+|\phi_2|$. The following numerical values have been used: $\Delta_X = 6$, $\Delta_\tau = 50$, $\Delta_{\tau_i} = 1500$, $s_0 = 0.05$, $k = 0.3$, $\theta_1 = 0.7$, $\bar{\Omega}_n = 0.2$, $\bar{\Omega}_g = 0.003$, $\bar{\Omega}_c = 10$ and $\phi_0 = 0.1$.

$$\delta(\tau) = e^{-\frac{\tau^2}{\Delta_\tau^2}}, \tag{5.95}$$

$$\tau_{i+1} = \tau_i + \Delta_{\tau_i}, \tag{5.96}$$

where Δ_X, Δ_τ and Δ_{τ_i} are constant parameters. The numerical values are detailed in the caption of Figure 5.7. Regarding ϕ_0, one should remember that it is normalized to T_i/e, as mentioned in expression (5.19); a numerical value of $\phi_0 = 0.1$ has been used.

5.5 Conclusion

The results of the local model discussed in Section 5.3.4 show that a parametric excitation of linearly stable ITG waves by an EGAM is possible under stringent conditions (especially regarding the ballooning angle of one of the daughter ITG waves). This means that in the framework of this model, an EGAM may non-linearly excite linearly stable ITG waves. This result provides a possible explanation for the behaviour of EGAMs and ITG modes in the gyrokinetic simulations described in Section 5.1 [Zarzoso 2013]. It comes as a counter-example to the interaction which is expected between EGAMs and ITG modes: indeed, like GAMs [Hallatschek 2001, Jakubowski 2002, Ramisch 2003, Miyato 2004, Waltz 2008, Conway 2011, Xu 2012], EGAMs are expected to mitigate, rather than excite, ITG modes.

Based on the observation that during phase B, in the simulations presented in Section 5.1, ITG modes were not suppressed in the core region of the plasma, the radial propagation of ITG modes may also play a significant role. The model exposed in Section 5.4 shows indeed that the presence of a region in which ITG modes are linearly unstable, coupled with the presence of an EGAM as a pump wave, can cause the appearance of an ITG mode at a location where the ITG is linearly stable. The amplitude of the ITG mode which appears in this non-linear model is proportional to the amplitude of the linearly excited ITG mode; in the gyrokinetic framework, the former represents a small fraction of the latter. Note that in the numerical simulations, the EGAM amplitude which non-linearly links the ITG modes was not small, which may explain why the ITG had similar amplitudes in the core and outer regions during phase C. This propagative model provides a simple analytical explanation for the interaction between ITG modes and EGAMs observed in the GYSELA simulations, with less stringent conditions on the ballooning angle than in the case of the local model.

The analytical results here obtained call for more simulations, to assess the level of generality of the excitation of linearly stable ITG modes by an EGAM, in the presence of linearly unstable ITG modes at different radial location.

Chapter 6

Conclusions and perspectives

Fast particles are a key issue in tokamaks. First because their presence will be inevitable in burning D-T plasmas: alpha particles will be born at about 3.5 MeV, to be compared to a bulk plasma ion temperature of a few 10 keV. Second because they can, to some extent, be controlled by an external operator, through Neutral Beam Injection (NBI) and Ion Cyclotron Resonant Heating (ICRH), which are alternative fast particle sources to fusion reactions. Third because they interact with various plasma instabilities: this feature is of interest to stabilize or destabilize modes on purpose.

In the present manuscript, we focus on the interaction of fast particles with three plasma instabilities: a MagnetoHydroDynamic (MHD) instability, the internal kink mode, which underlies sawtooth activity; a kinetic instability, the Energetic particle driven Geodesic Acoustic Mode (EGAM); and via EGAMs the Ion Temperature Gradient (ITG) modes, which underlie turbulence.

In the case of sawtooth activity, the fast particles interact directly with the internal kink mode. Porcelli's model [Porcelli 1991] shows that trapped fast ions can stabilize the mode under certain conditions, in particular if they are localized close enough to the magnetic axis. We report in Chapter 3 on strong sawtooth stabilization by deuterons accelerated to about 100 keV by NBI, and subsequently to the MeV range by third harmonic ICRH. The contributions of NBI and ICRH to the stabilization of sawteeth are computed in the framework of Porcelli's model, with the help of different numerical codes. As a result, the fast particles are found to be stabilizing in the four studied discharges, in accordance with the experiments. A monster sawtooth of about 2.5 s appears in one of the studied discharges, namely #86775; the sawteeth in the other three studied discharges are somewhat shorter. This observation is consistent with the results from Porcelli's model, which predict that among the four studied discharges, the strongest sawtooth stabilisation provided by fast particles is in discharge #86775. This 2.5 s long sawtooth is remarkable under various aspects: it is record in JET with ITER-Like Wall (ILW), and the discharge

parameters are constant during the sawtooth, in particular the fast ion distribution and the q-profile.

In two of the four studied discharges, tornado modes are observed before the sawtooth crashes. Tornado modes are known to expel fast particles from the core plasmas, and are believed to be here responsible for the sawteeth crashes. In the other two discharges, cold fronts due to Edge Localized Modes (ELMs) are observed just before the sawtooth crashes. Those cold fronts may be at the origin of the sudden onset of the internal kink mode, while stabilization is provided by the energetic particles, and while neutron cameras show that the population of fast particles in the core plasma does not decrease up to the very moment of the crash.

In the case of turbulence, the interaction between fast particles and ITG modes is indirect; it occurs through another mode: the Energetic particle driven Geodesic Acoustic Mode (EGAM). EGAMs are similar to Geodesic Acoustic Modes (GAMs). In Chapter 4, a local linear dispersion relation of EGAMs is derived, and the relation between GAMs and EGAMs is analysed. Depending on the plasma and fast particle parameters, the EGAM can either originate from a mode which is Landau-damped in the absence of fast particles and is excited in the presence of fast particles, or from the GAM itself which is slightly damped in the absence of fast particles and is excited when fast particles are present. In the first case, the EGAM is called a *Landau EGAM*; in the second case the EGAM is called an *EGAM from GAM*. There also exist ranges of parameters in which the EGAM cannot be excited at all.

In Chapter 5, gyrokinetic simulations published in [Zarzoso 2013] are considered. Those simulations suggest that instead of reducing turbulence, EGAMs can on the contrary enhance turbulence. An analytical, non-linear three wave parametric interaction model is developed to better understand the behaviour of EGAMs and ITG modes observed in the simulations. Considering the toroidal and poloidal structures of EGAMs and ITG modes, the interaction can only occur through the radial wave numbers. A local dispersion relation shows that the non-linear excitation of two linearly stable ITG modes by an EGAM is possible under stringent conditions (stringent especially regarding the ballooning angle of one of the two daughter ITG waves). This result provides a possible explanation for the excitation of ITG modes observed in the GYSELA simulations. However, it brings a counter-example to the expectations that EGAMs would mitigate ITG-driven turbulence, the latter being based on the similarity between GAMs and EGAMs and the mitigating impact of GAMs on turbulence described in [Hallatschek 2001, Jakubowski 2002, Ramisch 2003, Miyato 2004, Waltz 2008, Conway 2011, Xu 2012]. A three wave interaction propagative model is also found to provide a possible explanation for the excitation of ITG modes observed in the GYSELA simulations, under less stringent conditions on the ballooning angle: if ITG modes are linearly unstable in the core region

and linearly stable in the outer region, the EGAM can act as a pump to non-linearly make ITG modes appear in the outer region. The group velocity depends strongly on the plasma shear; it suggests that this mechanism may be dominant in low shear plasmas. It turns out that the gyrokinetic simulations presented in [Zarzoso 2013] exhibit low shear plasmas.

Several paths may be explored to carry on the work performed on sawtooth stabilization. The absence of tornado modes in two of the four studied discharges, while they are present in the other two discharges, is unexplained. The magnetic shear $s = rq'(r)/q$ and the β parameter are expected to play a role. Besides, it happens that the two discharges in which tornado modes are not present are those in which the ICRH resonant layer is best centred on the magnetic axis: is there a link between those two observations?

The possible interaction between ELMs and sawteeth via the inward propagation of a cold front also remains to be explained. Analytical study of this interaction is needed to understand the possible mechanisms at stake, the conditions under which such an interaction may occur. This analytical study may be carried out along with numerical simulations combining edge and core plasmas. On the experimental side, a statistical survey may be carried out to help determine the link between ELMs and sawteeth: what is the proportion of sawtooth crashes preceded by an ELM-triggered inward propagating cold front? Conversely, how many ELM bursts may be triggered by sawtooth crashes?

Regarding the interaction of fast particles with turbulence via EGAMs, the results exposed in the present manuscript open the way for further research. The analytical work carried out in the framework of the present thesis shed new light on the gyrokinetic simulations presented in [Zarzoso 2012b, Zarzoso 2013]. These analytical results may in turn be used as guidelines to design further gyrokinetic simulations. Regarding the relation between GAMs and EGAMs, non-linear simulations carried out in the various ranges of parameters explored in Chapter 4, including with various fast ion species, should provide interesting results, further validating the linear analytical model or, on the contrary, pointing out some limitations. Regarding the interaction between EGAMs and ITG modes, simulations with the GYSELA code may be carried on: a priority could be the improvement of the fast particle source in the code, which would be made more flexible. The goal is to carry out simulations in which the ITG modes would not be damped by the fast particle source prior to the appearance of the EGAMs. Different ranges of plasma, or fast particle parameters could be explored: in particular, the magnetic shear, which seems to play a key role in the non-linear interaction between EGAMs and ITG modes, could be varied. Other parameters, including the values of the safety factor q, may be varied to take into account the different types of EGAMs exposed in Chapter 4. Due to their closer link to GAMs, EGAMs from GAM may be better at mitigating turbulence than Landau EGAMs.

Along with numerical simulations, further analytical work may also be carried out. The non-local three wave interaction model exposed in Section 5.4 may be extended to take into account a self-consistent form for the linearly unstable ITG mode (here called ITG 2), for which an *ad-hoc* form has been chosen so far. This may lead to the non-linear excitation of the linearly stable ITG mode (here called ITG 1) as a true instability, with a growth rate of its own, rather than as a mode whose amplitude is a fraction of ITG 2's.

Analytical work also includes the study of a key aspect of EGAMs: their radial mode structure. We have seen in Sections 2.3.2 and 2.3.3 that GAMs and EGAMs are observed at different radial locations. GAMs are observed in the edge plasma, while EGAMs are localized in the core plasma but have a magnetic component which is detected by Mirnov coils, outside of the plasma. An EGAM seems to be a coherent mode, with a well defined frequency: how is this frequency determined with respect to the radial position of the mode? That is to say, to compute the EGAM frequency, where should the ion temperature or the value of q be evaluated on the minor radius axis? If those parameters vary quickly in r, could the mode still have a wide radial extension? The answers to those questions are important to better assess the impact of EGAMs on turbulence, to understand whether they may provide a radial link for turbulence spreading from the core to the edge plasma, or on the contrary whether they may be able to trigger an Internal Transport Barrier (ITB).

Appendices

Appendix A

Linear ITG derivation

A.1 Gyrokinetic Vlasov equation

In the present appendix, we use the gyrokinetic model described in Section 1.3.1 to derive the linear ITG poloidal shape (2.10)-(2.11) and dispersion relation (2.12). The derivation is based on [Garbet 2001, Sarazin 2009].

The following variables are used: $(\mathbf{x}_\mathrm{G}, v_\parallel, \mu)$, where the subscript G denotes the gyro-centre position. $v_\parallel$ is the parallel velocity, μ is the magnetic moment. The latter is an adiabatic invariant, which means that $d_t\mu = 0$.

We here consider an electrostatic perturbation. This means that the magnetic field fluctuations are not taken into account: $\mathbf{B}(\mathbf{x}_\mathrm{G}, t) = \mathbf{B}_\mathrm{eq}(\mathbf{x}_\mathrm{G})$. The equilibrium electric potential is assumed to be null; the electric potential is therefore reduced to its perturbed part $\tilde{\phi}$. In agreement with the gyrokinetic hypotheses, $e\tilde{\phi}/T_i$ is assumed to be of order 1 in ρ_*.

The distribution function of gyro-centres f_G is decomposed into an equilibrium part $f_\mathrm{G,eq}$ and a perturbed part $\tilde{f}_\mathrm{G}$:

$$f_\mathrm{G}(\mathbf{x}_\mathrm{G}, v_\parallel, \mu, t) = f_\mathrm{G,eq}(\mathbf{x}_\mathrm{G}, v_\parallel, \mu) + \tilde{f}_\mathrm{G}(\mathbf{x}_\mathrm{G}, v_\parallel, \mu, t). \tag{A.1}$$

The perturbation of the distribution function is assumed to be of order 1 in ρ_*: $\tilde{f}_\mathrm{G}/f_\mathrm{G,eq} \sim \rho_*$.

The gyrokinetic equation reads, at first order in ρ_*:

$$\partial_t f_\mathrm{G} + \mathbf{v}_{\mathrm{G}\perp} \cdot \boldsymbol{\nabla}_\perp f_\mathrm{G} + v_\parallel \nabla_\parallel f_\mathrm{G} + d_t v_\parallel \cdot \partial_{v_\parallel} f_\mathrm{G} = 0, \tag{A.2}$$

with

$$\mathbf{v}_{\mathrm{G}\perp} = \mathbf{v}_{\mathrm{E}} + \mathbf{v}_g, \tag{A.3}$$

$$\mathbf{v}_{\mathrm{E}} = \frac{\mathbf{b}\times\boldsymbol{\nabla} J_0\tilde{\phi}}{B}, \tag{A.4}$$

$$\mathbf{v}_g = \frac{mv_\parallel^2+\mu B}{eB}\frac{\mathbf{b}\times\boldsymbol{\nabla}B}{B} + \frac{mv_\parallel^2}{eB}\frac{\mathbf{rot}\ \mathbf{B}}{B}\bigg|_\perp. \tag{A.5}$$

In this expression, $\mathbf{v}_{\mathrm{E}}$ is the electric drift velocity, $\mathbf{v}_g$ the gradient and curvature drift velocity and J_0 is the gyro-average operator. The magnetic field $\mathbf{B}$ is to be evaluated at the gyro-centre position. The last term in the expression of $\mathbf{v}_g$, that is to say $\frac{mv_\parallel^2}{eB}\frac{\mathbf{rot}\ \mathbf{B}}{B}\big|_\perp$, can be neglected when the plasma has a low β, which is what we will here consider.

Still up to the first order in ρ_* and at low β:

$$d_t v_\parallel = -\frac{e}{m}\nabla_\parallel J_0\tilde{\phi} + v_\parallel \mathbf{v}_{\mathrm{E}}\cdot\frac{\boldsymbol{\nabla}B}{B}. \tag{A.6}$$

In this expression, only highly passing particles are considered, which means that the term $\frac{e}{m}\mu\nabla_\parallel B$ has not been taken into account.

In addition to ρ_*, a second small parameter is introduced, $\delta\sim k_\perp\rho_i$, with the following ordering:

$$\rho_* \ll \delta \ll 1, \tag{A.7}$$

were ρ_i is the ion Larmor radius and $k_\perp$ represents a characteristic value of the perpendicular wave vector. In terms of the notations used below, $k_\perp$ here means either k_θ or K_0. Taking into account δ, the following orderings are considered:

$$\frac{e\tilde{\phi}}{T_i} \sim \rho_*\delta^{-1}, \tag{A.8}$$

$$\frac{\tilde{f}_{\mathrm{G}}}{f_{\mathrm{G,eq}}} \sim \rho_*\delta^{-3}. \tag{A.9}$$

The second ordering comes from the fact that $\frac{e\tilde{\phi}}{T_i}\frac{f_{\mathrm{G,eq}}}{\tilde{f}_{\mathrm{G}}}\sim\delta^2$ (see the derivation below). In the computation, we will keep terms up to order 1 in ρ_* and -1 in δ. J_0-1 applied to perturbed fields is of order δ^2: $J_0-1\approx\frac{1}{2}\frac{\mu B}{T_i}\rho_i^2\nabla_\perp^2$. $ak_\perp = k_\perp\rho_i a/\rho_i$ is of order $\delta\rho_*^{-1}$ (a is the value of the minor radius of the tokamak). $a\boldsymbol{\nabla}_\perp \ln f_{\mathrm{G,eq}}$ is assumed to be of order δ^{-3}. The orderings in δ here assumed are consistent with those considered for the non-linear interaction of an EGAM with ITG modes (see Section 5.3.1).

Removing all non-linear and equilibrium terms, the gyrokinetic equation reads, with

the conventions here adopted:

$$\partial_t \tilde{f}_{\mathrm{G}} + \frac{\mathbf{b}\times\boldsymbol{\nabla} J_0\tilde{\phi}}{B}\cdot\boldsymbol{\nabla}_\perp f_{\mathrm{G,eq}} + \frac{mv_\parallel^2+\mu B}{eB}\,\frac{\mathbf{b}\times\boldsymbol{\nabla}B}{B}\cdot\boldsymbol{\nabla}_\perp\tilde{f}_{\mathrm{G}} + v_\parallel\nabla_\parallel\tilde{f}_{\mathrm{G}} - \frac{e}{m}\nabla_\parallel J_0\tilde{\phi}\,\partial_{v_\parallel} f_{\mathrm{G,eq}} + v_\parallel\frac{\mathbf{b}\times\boldsymbol{\nabla}J_0\tilde{\phi}}{B}\cdot\frac{\boldsymbol{\nabla}B}{B}\partial_{v_\parallel} f_{\mathrm{G,eq}} = 0. \tag{A.10}$$

A Maxwellian distribution function is assumed for the equilibrium distribution function:

$$f_{\mathrm{G,eq}} = n_0\left(\frac{m}{2\pi T_i}\right)^{3/2} e^{-\frac{mv_\parallel^2}{2T_i}-\frac{\mu B}{T_i}}. \tag{A.11}$$

Therefore:

$$\boldsymbol{\nabla}_\perp f_{\mathrm{G,eq}}|_{v_\parallel,\mu} = \mathbf{e}_r\,\frac{\partial}{\partial r} f_{\mathrm{G,eq}}\bigg|_{\varepsilon,\mu} - \frac{\mu\boldsymbol{\nabla}_\perp B}{T_i} f_{\mathrm{G,eq}}, \tag{A.12}$$

$$\partial_{v_\parallel} f_{\mathrm{G,eq}} = -\frac{mv_\parallel}{T_i} f_{\mathrm{G,eq}}. \tag{A.13}$$

Taking into account those last two relations, and after having removed high order terms, the gyrokinetic equation reads

$$\partial_t\tilde{f}_{\mathrm{G}} + \frac{\mathbf{b}\times\boldsymbol{\nabla}J_0\tilde{\phi}}{B}\cdot\mathbf{e}_r\,\frac{\partial}{\partial r} f_{\mathrm{G,eq}}\bigg|_{\varepsilon,\mu} + \frac{mv_\parallel^2+\mu B}{eB}\,\frac{\mathbf{b}\times\boldsymbol{\nabla}B}{B}\cdot\boldsymbol{\nabla}_\perp\tilde{f}_{\mathrm{G}} + v_\parallel\nabla_\parallel\tilde{f}_{\mathrm{G}} + \frac{ev_\parallel}{T_i}\nabla_\parallel\tilde{\phi}\, f_{\mathrm{G,eq}} = 0. \tag{A.14}$$

In the case of concentric circular poloidal sections, this equation can be recast as

$$\partial_t\tilde{f}_{\mathrm{G}} - \frac{\partial_\theta J_0\tilde{\phi}}{rB}\partial_r f_{\mathrm{G,eq}} - v_g\left(\sin\theta\partial_r + \frac{\cos\theta}{r}\partial_\theta\right)\tilde{f}_{\mathrm{G}} + v_\parallel\left(\frac{\partial_\varphi}{R}+\frac{\partial_\theta}{qR}\right)\tilde{f}_{\mathrm{G}} + f_{\mathrm{G,eq}}\frac{ev_\parallel}{T_i}\left(\frac{\partial_\varphi}{R}+\frac{\partial_\theta}{qR}\right)\tilde{\phi} = 0, \tag{A.15}$$

where $v_g = \frac{mv_\parallel^2+\mu B}{eBR}$.

The ballooning representation (see Section 2.3.1) is used to express $\tilde{\phi}$ and $\tilde{f}_{\mathrm{G}}$:

$$\tilde{\phi}(\mathbf{x}_{\mathrm{G}},t) = e^{-i\omega t}e^{in\varphi}\sum_{\ell=-\infty}^{+\infty}\hat{\Phi}(\theta+2\ell\pi)e^{-inq(\theta+2\ell\pi-\theta_0)} + c.c., \tag{A.16}$$

$$\tilde{f}_{\mathrm{G}}\big(\mathbf{x}_{\mathrm{G}}, v_{\parallel}, \mu, t\big) = e^{-i\omega t} e^{in\varphi} \sum_{\ell=-\infty}^{+\infty} \hat{F}\big(\theta + 2\ell\pi, v_{\parallel}, \mu\big) e^{-inq(\theta+2\ell\pi-\theta_0)} + c.c., \tag{A.17}$$

where q is the safety factor and *c.c.* means *complex conjugate*. We consider the safety factor to be linear: $q = q_0 + q_0' x$, where $q_0 = q(r_0)$, $q_0' = q'(r_0)$, $x = r - r_0$ and r_0 is the position (in the small radius coordinate) of the reference resonance surface.

Keeping only the $\ell = 0$ component; defining $K_0 = n\theta_0 q_0'$ and $k_\theta = \frac{nq_0}{r_0}$, the ballooning representation reads as follows:

$$\tilde{\phi}(\mathbf{x}_{\mathrm{G}}, t) = e^{-i\omega t} e^{in\varphi} \hat{\Phi}(\theta) e^{-ir_0 k_\theta \theta - inq_0' x\theta + ixK_0} + c.c., \tag{A.18}$$

$$\tilde{f}_{\mathrm{G}}\big(\mathbf{x}_{\mathrm{G}}, v_{\parallel}, \mu, t\big) = e^{-i\omega t} e^{in\varphi} \hat{F}\big(\theta, v_{\parallel}, \mu\big) e^{-ir_0 k_\theta \theta - inq_0' x\theta + ixK_0} + c.c. \tag{A.19}$$

Inserting those expressions into equation (A.15), we get

$$\begin{aligned}
&- i\omega e^{-i\omega t} e^{in\varphi} \hat{F} e^{-ir_0 k_\theta \theta - inq_0' x\theta + ixK_0} \\
&\quad - \partial_\theta \left(1 + \frac{1}{2}\frac{\mu B}{T_i}\rho_i^2 \nabla_\perp^2\right) e^{-i\omega t} e^{in\varphi} \hat{\Phi} e^{-ir_0 k_\theta \theta - inq_0' x\theta + ixK_0} \frac{\partial_r f_{\mathrm{G,eq}}}{rB} \\
&\quad - v_g \left(\sin\theta \partial_r + \frac{\cos\theta}{r}\partial_\theta\right) e^{-i\omega t} e^{in\varphi} \hat{F} e^{-ir_0 k_\theta \theta - inq_0' x\theta + ixK_0} \\
&\quad + v_\parallel \left(\frac{\partial_\varphi}{R} + \frac{\partial_\theta}{qR}\right) e^{-i\omega t} e^{in\varphi} \hat{F} e^{-ir_0 k_\theta \theta - inq_0' x\theta + ixK_0} \\
&\quad + f_{\mathrm{G,eq}} \frac{e v_\parallel}{T_i} \left(\frac{\partial_\varphi}{R} + \frac{\partial_\theta}{qR}\right) e^{-i\omega t} e^{in\varphi} \hat{\Phi} e^{-ir_0 k_\theta \theta - inq_0' x\theta + ixK_0} = 0.
\end{aligned} \tag{A.20}$$

Due to ordering considerations, once out of the exponentials, θ or x do not need to be derived any more. Besides, $\frac{\rho_i^2}{T_i}$ does not have any spatial dependence (except through B, but B is here assumed to be constant). $\hat{F}$ and $\hat{\Phi}$ depend slowly on θ, and are therefore not to be derived except in parallel gradients. Equation (A.20) can therefore be recast as

$$\begin{aligned}
&- i\omega \hat{F} + \frac{\left(ik_\theta + \frac{inq_0' x}{r_0}\right)\left(1 - \frac{1}{2}\frac{\mu B}{T_i} k_\perp^2 \rho_i^2\right)\hat{\Phi}}{B} \partial_r f_{\mathrm{G,eq}} + v_\parallel f_1(t) \frac{\partial_\theta \hat{F}}{qR} \\
&\quad - v_g \left(\sin\theta (iK_0 - inq_0'\theta) - \cos\theta \left(ik_\theta + \frac{inq_0' x}{r_0}\right)\right) \hat{F} \frac{\partial_\theta \hat{\Phi}}{qR} + f_{\mathrm{G,eq}} \frac{e v_\parallel}{T_i} = 0.
\end{aligned} \tag{A.21}$$

We define the perpendicular wave vector $k_\perp$ and the parallel wave vector $k_\parallel$ as follows:

$$k_\perp^2 = (K_0 - nq_0'\theta)^2 + k_\theta^2, \tag{A.22}$$

$$ik_\parallel = \frac{\partial_\theta}{qR}. \tag{A.23}$$

We define the diamagnetic frequency ω_*, the kinetic drift frequency ω_{gk}, and the parallel frequency $\omega_\parallel$ as follows:

$$\omega_* = -k_\theta \frac{\partial_r \ln f_{\mathrm{G,eq}}}{B} \frac{T_i}{e}, \tag{A.24}$$

$$\omega_{gk} = v_g[\sin\theta(K_0 - nq_0'\theta) - \cos\theta k_\theta], \tag{A.25}$$

$$\omega_\parallel = v_\parallel k_\parallel. \tag{A.26}$$

Taking into account those definitions, and considering that $\frac{x}{r_0}$ is small, equation (A.21) now reads

$$\hat{F} = -f_{\mathrm{G,eq}} \frac{e}{T_i} \frac{\omega_* \left(1 - \frac{1}{2}\frac{\mu B}{T_i} k_\perp^2 \rho_i^2\right) - \omega_\parallel}{\omega + \omega_{gk}} \hat{\Phi} + \frac{\omega_\parallel}{\omega} \hat{F}. \tag{A.27}$$

Assuming the following orderings:

$$\frac{\omega_*}{\omega} \text{ is of order } \delta^{-2}, \tag{A.28}$$

$$\frac{\omega_\parallel}{\omega} \text{ is of order } \delta, \tag{A.29}$$

$$\frac{\omega_{gk}}{\omega} \text{ is of order } \delta^2, \tag{A.30}$$

this expression can be recast as

$$\hat{F} = -f_{\mathrm{G,eq}} \frac{e}{T_i} \frac{\omega_*}{\omega} \left(1 - \frac{\omega_{gk}}{\omega} + \frac{\omega_\parallel}{\omega} + \frac{\omega_\parallel^2}{\omega^2} - \frac{1}{2}\frac{\mu B}{T_i} k_\perp^2 \rho_i^2\right) \hat{\Phi}. \tag{A.31}$$

A.2 Quasi-neutrality equation

The gyrokinetic quasi-neutrality equation reads (see Section 1.3.1)

$$n_i \frac{e}{T_e} \left(\tilde{\phi} - \left\langle \tilde{\phi} \right\rangle_{\mathrm{FS}}\right) = \mathrm{div}\left(\frac{m_i n_i}{eB^2} \boldsymbol{\nabla}_\perp \tilde{\phi}\right) + \int J_0 \cdot \left(f_{\mathrm{G,eq}} + \tilde{f}_{\mathrm{G}}\right) (dv)^3 - n_i. \tag{A.32}$$

We have here supposed that there is only one species of ions, and that its charge number is 1. The equilibrium density of ions and electrons is therefore the same, and is here called n_i. $\left\langle \tilde{\phi} \right\rangle_{\mathrm{FS}}$ is the flux-surface average of the electrostatic potential. $f_{\mathrm{G,eq}}$ is the equilibrium ion distribution function; it verifies $\int J_0 \cdot f_{\mathrm{G,eq}} \, (dv)^3 = n_i$ at order 1 in ρ_*. We assume that the electron temperature T_e is equal to the ion temperature T_i. The spatial variations of n_i are neglected.

Using the ballooning representation, considering that $\hat{F}$ depends slowly on θ, that $\frac{x}{r_0}$

is small, and eliminating high order terms, the quasi-neutrality equation can be recast as

$$n_i \frac{e}{T_i}\hat{\Phi} = \int \hat{F}\left(1 - \frac{1}{2}\frac{\mu B}{T_i}\rho_i^2\left[k_\theta^2 + (K_0 - nq_0'\theta)^2\right]\right)(dv)^3. \tag{A.33}$$

Recalling expression (A.31), this expression transforms into

$$\frac{e}{T_i}\hat{\Phi} = -\int \frac{f_{\mathrm{G,eq}}}{n_i}\frac{e}{T_i}\frac{\omega_*}{\omega}\left(1 - \frac{\omega_g}{\omega} + \frac{\omega_\parallel^2}{\omega^2} - \frac{\mu B}{T_i}k_\perp^2\rho_i^2\right)\hat{\Phi}\,(dv)^3. \tag{A.34}$$

Defining

$$\omega_n^* = -\frac{k_\theta}{B}\frac{T_i}{e}\frac{n_i'(r)}{n_i}, \tag{A.35}$$

$$\omega_p^* = -\frac{k_\theta}{B}\frac{T_i}{e}\frac{p_i'(r)}{p_i}, \tag{A.36}$$

$$v_{\mathrm{T}}^2 = \frac{T_i}{m}, \tag{A.37}$$

$$s_0 = \frac{r_0 q_0'}{q_0}, \tag{A.38}$$

where $p_i = n_i T_i$ is the ion pressure, and integrating over the velocity, the equation becomes

$$\left[\frac{\omega + \omega_n^*}{\omega_p^*} + \frac{2k_\theta T_i}{\omega e B R}[\cos\theta + s_0(\theta - \theta_0)\sin\theta] + v_{\mathrm{T}}^2\frac{k_\parallel^2}{\omega^2} - k_\theta^2\rho_i^2\left[s_0^2(\theta - \theta_0)^2 + 1\right]\right]\hat{\Phi} = 0. \tag{A.39}$$

Let us define the fluid drift frequency ω_{gf} and the normalized poloidal wave vector k:

$$\omega_{gf} = \frac{2k_\theta T_i}{eBR} = \frac{2nq_0 T_i}{er_0 BR}, \tag{A.40}$$

$$k^2 = k_\theta^2\rho_i^2. \tag{A.41}$$

The frequencies of the problem are renormalized to the ITG frequency ω:

$$\Omega_g = \frac{\omega_{gf}}{\omega} = \frac{2k_\theta T_i}{\omega e B R} = \frac{2nq_0 T_i}{\omega e r_0 B R}, \tag{A.42}$$

$$\Omega_p^* = \frac{\omega_p^*}{\omega}, \tag{A.43}$$

$$\Omega_n^* = \frac{\omega_n^*}{\omega}, \tag{A.44}$$

$$\Omega_\parallel = \frac{v_{\mathrm{T}}}{qR\omega} \tag{A.45}$$

$$y = \theta - \theta_0. \tag{A.46}$$

A new variable y is defined as a translation of the variable θ:

$$y = \theta - \theta_0. \tag{A.47}$$

With those definitions, the equation becomes

$$\left[\frac{1+\Omega_n^*}{\Omega_p^*} + \Omega_g[\cos(y+\theta_0) + s_0 y \sin(y+\theta_0)] - \Omega_\parallel^2 \partial_{yy} - k^2\left[s_0^2 y^2 + 1\right]\right]\hat{\Phi} = 0. \tag{A.48}$$

In the limit $y \ll 1$, $\theta_0 \ll 1$, the cosine and sine functions can be expanded:

$$\cos(y+\theta_0) = 1 - \frac{(y+\theta_0)^2}{2}, \tag{A.49}$$

$$y\sin(y+\theta_0) = y(y+\theta_0), \tag{A.50}$$

thus leading to

$$-\partial_{yy}\hat{\Phi} + \left[\frac{1+\Omega_n^*}{\Omega_\parallel^2\Omega_p^*} + \frac{\Omega_g}{\Omega_\parallel^2}\left[1 + y^2\left(s_0 - \frac{1}{2}\right) + y\theta_0(s_0-1) - \frac{\theta_0^2}{2}\right] - \frac{k^2}{\Omega_\parallel^2}\left[s_0^2y^2+1\right]\right]\hat{\Phi} = 0. \tag{A.51}$$

A.3 Linear ITG dispersion relation

Let us rewrite equation (A.51) under the following shape:

$$\partial_{yy}\hat{\Phi} - \lambda(y-\alpha)^2\hat{\Phi} - \mu\hat{\Phi} = 0. \tag{A.52}$$

By identification of the terms of the second order polynomial in y:

$$\lambda = \left(s_0 - \frac{1}{2}\right)\frac{\Omega_g}{\Omega_\parallel^2} - \frac{k^2}{\Omega_\parallel^2}s_0^2, \tag{A.53}$$

$$2\lambda\alpha = -\theta_0(s_0-1)\frac{\Omega_g}{\Omega_\parallel^2}, \tag{A.54}$$

$$\lambda\alpha^2 + \mu = \frac{1+\Omega_n^*}{\Omega_\parallel^2\Omega_p^*} + \frac{\Omega_g}{\Omega_\parallel^2} - \frac{\theta_0^2}{2}\frac{\Omega_g}{\Omega_\parallel^2} - \frac{k^2}{\Omega_\parallel^2}. \tag{A.55}$$

Consequently, the three parameters λ, α and μ read

$$\lambda = \left(s_0 - \frac{1}{2}\right)\frac{\Omega_g}{\Omega_\parallel^2} - \frac{k^2}{\Omega_\parallel^2}s_0^2, \tag{A.56}$$

$$\alpha = \frac{\theta_0(s_0-1)\Omega_g}{(1-2s_0)\Omega_g + 2k^2s_0^2}, \tag{A.57}$$

$$\mu = \frac{1}{2\Omega_{\parallel}^2}\left[2\frac{1+\Omega_n^*}{\Omega_p^*} + \left(2-\theta_0^2\right)\Omega_g - 2k^2 + \frac{\theta_0^2(s_0-1)^2\Omega_g^2}{(1-2s_0)\Omega_g + 2k^2 s_0^2}\right]. \tag{A.58}$$

We suppose that $\hat{\Phi}$ has the following shape:

$$\hat{\Phi} = \hat{\Phi}_0 e^{-\frac{(y-y_0)^2}{2\Delta^2}}, \tag{A.59}$$

where $\hat{\Phi}_0$ is a constant, and where we want to determine y_0, Δ and ω.

With this expression, the second order derivative in y reads

$$\partial_{yy}\hat{\Phi} - \frac{(y-y_0)^2}{\Delta^4}\hat{\Phi} + \frac{1}{\Delta^2}\hat{\Phi} = 0, \tag{A.60}$$

and we can infer, by identification:

$$\lambda = \frac{1}{\Delta^4}, \tag{A.61}$$

$$\alpha = y_0, \tag{A.62}$$

$$\mu = -\frac{1}{\Delta^2}. \tag{A.63}$$

The dispersion relation can then easily be written:

$$\mu^2 = \lambda, \tag{A.64}$$

which can be recast as

$$\left[2\frac{1+\Omega_n^*}{\Omega_p^*} + \left(2-\theta_0^2\right)\Omega_g - 2k^2 + \frac{\theta_0^2(s_0-1)^2\Omega_g^2}{(1-2s_0)\Omega_g + 2k^2 s_0^2}\right]^2 + 2\Omega_{\parallel}^2\left[(1-2s_0)\Omega_g + 2k^2 s_0^2\right] = 0. \tag{A.65}$$

Appendix B

Linear EGAM derivation

We present in this appendix the major steps of the derivation of the EGAM dispersion relation (4.17). The model takes into account three species: two ion species (thermal ions and kinetic ions), and the electrons. Throughout the calculus, the subscripts t, k and e are used to denote respectively the thermal ions, the kinetic ions and the electrons. Whenever an equation is the same for thermal and kinetic ions, it is written only once for simplicity purpose, and the subscript s (standing for *species*) is used. This means that whenever the subscript s is met in an equation, it can be substituted indifferently with t or k.
The quasi-neutrality equation is solved taking into account the three species. This equation is coupled to two gyrokinetic equations for the ions, while an adiabatic representation is used for the electrons.

B.1 Gyrokinetic equation, for thermal and kinetic ions

The equation used for species s (where it is recalled that s stands indifferently for t - *thermal* - or k - *kinetic*) is the gyrokinetic equation (4.1). We recall that the distribution function of the ions of species s is decomposed into an equilibrium part F_s and a perturbed part $\tilde{f}_s$:

$$f_s = F_s\Big(1 + \tilde{f}_s\Big) \tag{B.1}$$

The model is electrostatic, *i.e.* no fluctuation of the magnetic field is taken into account.

The thermal ion equilibrium is described by a Maxwellian distribution function (expression (4.8)). The temperature and density equilibrium radial profiles are assumed to be flat, which means that F_t depends on the kinetic energy of the particles E_t only.

The kinetic ion equilibrium is described by a so-called bump-on-tail function, consisting in two Maxwellian functions shifted in parallel velocity (expression (4.14)).

Note that the fast particles are accelerated in the parallel direction only: the fast particle parallel velocity is of the order of a few times the thermal velocity, while their perpendicular velocity is of the order of the thermal velocity itself. In addition, the aspect ratio R_0/a is assumed to be large. Consequently, the vast majority of the fast particles here considered are highly passing. Their parallel velocity can therefore be considered as a motion invariant, $\bar{v}_\parallel$ can be chosen to be a constant (*i.e.* independent of r and θ), and the distribution function (4.14) can be recast as a function of motion invariants only:

$$F_k = n_k \left(\frac{m_k}{2\pi T_t \tau_k} \right)^{\frac{3}{2}} e^{-\frac{\frac{1}{2} m_k \bar{v}_\parallel^2 + E_k}{T_t \tau_k}} \cosh\left(\frac{m_k v_\parallel \bar{v}_\parallel}{T_t \tau_k} \right). \tag{B.2}$$

Two different kinds of expansions are performed:
a) the equations are linearized according to the perturbed quantities ($\tilde{f}_t$, $\tilde{f}_k$ and $\tilde{\phi}$);
b) the equations are expanded up to the first order in ρ_*, consistently with the order at which the gyrokinetic equations used in the model are valid. ρ_* is defined as ρ_i/a where ρ_i is the ion Larmor radius and a the minor radius of the tokamak. Note that this expansion is valid for both thermal and kinetic ions: kinetic ions are accelerated only in the parallel direction, which means that ρ_* is the same for thermal and kinetic ions.

After linearisation according to the perturbed quantities, the gyrokinetic equation for species s reads

$$F_s \partial_t \tilde{f}_s + \mathbf{v}_E \cdot \boldsymbol{\nabla}_\perp F_s + F_s \mathbf{v}_{g,s} \cdot \boldsymbol{\nabla}_\perp \tilde{f}_s + F_s v_\parallel \nabla_\parallel \tilde{f}_s + d_t E_s \partial_{E_s} F_s = 0. \tag{B.3}$$

Neither F_t nor F_k have any spatial dependence: consequently $\boldsymbol{\nabla}_\perp F_s = 0$.

Besides, the kinetic energy of species s varies according to the electric energy transfers: $d_t E_s = -e_s v_\parallel \nabla_\parallel \tilde{\phi} - e_s \mathbf{v}_{g,s} \cdot \boldsymbol{\nabla}_\perp \tilde{\phi}$. Consequently, the gyrokinetic equation for species s can be recast as

$$\partial_t \tilde{f}_s = \left(\mathbf{v}_{g,s} \cdot \boldsymbol{\nabla}_\perp + v_\parallel \nabla_\parallel \right) \left(\frac{e}{T_t} \tilde{\phi} Z_s T_t \partial_{E_s} \log F_s - \tilde{f}_s \right), \tag{B.4}$$

where $Z_s = e_s/e$ is the charge number of species s and e is the elementary Coulomb charge.

Since the GAM and the EGAM are axisymmetric modes, the perturbed quantities $\tilde{f}_t$, $\tilde{f}_k$ and $\tilde{\phi}$ are independent of the toroidal angle φ. In the case of a tokamak with circular, concentric magnetic flux surfaces, we have, in flux coordinates:

$$\mathbf{v}_{g,s} \cdot \boldsymbol{\nabla}_\perp = v_{g,s} \left(\sin\theta \partial_r + \frac{\cos\theta}{r} \partial_\theta \right), \tag{B.5}$$

$$v_\parallel \nabla_\parallel = \frac{v_\parallel}{qR} \partial_\theta, \tag{B.6}$$

where $v_{g,s} = \frac{m_s v_\parallel^2 + \mu_s B}{e_s R B}$.

The radial extension of the EGAM is assumed to be significantly smaller than the minor radius of the tokamak. Therefore, in expression (B.5), only the $\sin\theta\partial_r$ term is retained as it is assumed to be dominant over the $\frac{\cos\theta}{r}\partial_\theta$ term.

A decomposition of $\tilde{f}_t$, $\tilde{f}_k$ and $\tilde{\phi}$ is performed on a Fourier basis:

$$\tilde{f}_s = \sum_{\substack{\omega,m=0 \\ k_r=-\infty}}^{+\infty} [f^c_{sm}\cos m\theta + f^s_{sm}\sin m\theta] e^{i(k_r r - \omega t)}, \tag{B.7}$$

$$\tilde{\phi} = \frac{T_t}{e} \sum_{\substack{\omega,m=0 \\ k_r=-\infty}}^{+\infty} [\phi^c_m\cos m\theta + \phi^s_m\sin m\theta] e^{i(k_r r - \omega t)}, \tag{B.8}$$

where the electric potential has been normalized to T_t/e.

At leading order in ρ_*, the first two poloidal harmonics of equation (B.4) read

$$2\omega f_{s0} = v_{g,s}k_r[f^s_{s1} - \phi^s_1 Z_s T_t \partial_{E_s}\log F_s], \tag{B.9}$$

$$i\omega f^c_{s1} = \frac{v_\parallel}{qR}[f^s_{s1} - \phi^s_1 Z_s T_t \partial_{E_s}\log F_s], \tag{B.10}$$

$$i\omega f^s_{s1} = -i\phi_0 v_{g,s}k_r Z_s T_t \partial_{E_s}\log F_s - \frac{v_\parallel}{qR}\,[f^c_{s1} - \phi^c_1 Z_s T_t \partial_{E_s}\log F_s]. \tag{B.11}$$

Note that those harmonics have been expressed up to the first order in ρ_* only. To get them, $k_r\rho_i$ has been assumed to be of order $\rho_*^{1/2}$, leading to the following orderings (which can easily be checked *a posteriori*): $v_\parallel/qR\omega$ is of order 0 in ρ_*; ϕ^s_1/ϕ_0, f^s_{s1}/ϕ_0, f^c_{s1}/ϕ_0 and $v_{g,s}k_r/\omega$ are of order 1/2 in ρ_*; f_{s0}/ϕ_0 and ϕ^c_1/ϕ_0 are of order 1 in ρ_*. While f^c_{s1}/ϕ_0 is of order 1/2 in ρ_*, it is important to remark that its integral in velocity at that order is null, which means that n^c_{s1}/ϕ_0, is of order 1 in ρ_*, where $n^c_{s1} = \int F_s f^c_{s1}(dv)^3/n_s$.

Defining $\omega_{g,s} = v_{g,s}k_r$ and $\omega_\parallel = v_\parallel/qR$, equations (B.9) to (B.11) can, after some linear combinations, be recast as follows:

$$f_{s0} = -Z_s T_t \partial_{E_s}\log F_s \frac{\omega^2\omega_{g,s}\phi^s_1 + \omega\omega^2_{g,s}\phi_0}{2\omega\left(\omega^2 - \omega^2_\parallel\right)}, \tag{B.12}$$

$$f^s_{s1} = -Z_s T_t \partial_{E_s}\log F_s \frac{\omega\omega_{g,s}\phi_0 + \omega^2_\parallel\phi^s_1 + i\omega\omega_\parallel\phi^c_1}{\omega^2 - \omega^2_\parallel}. \tag{B.13}$$

Equation (B.10) has been used to derive equations (B.12) and (B.13), but it will not be useful any more in what follows: it has therefore not been copied again. It is to be recalled that equations (B.12) and (B.13) are valid indifferently for thermal and kinetic ions (just replace the subscript s with t or k).

B.2 Quasi-neutrality equation, taking into account thermal ions, kinetic ions and adiabatic electrons

The perturbed quasi-neutrality equation reads $\tilde{n}_e = Z_t\tilde{n}_t + Z_k\tilde{n}_k$.

The perturbed density of ion species s reads, in the gyrokinetic framework at first order in ρ_*, as the integral of the perturbed gyro-centre distribution function, plus a polarisation term:

$$\tilde{n}_s = \mathrm{div}\left(\frac{m_s n_s}{e_s B^2}\boldsymbol{\nabla}_\perp\tilde{\phi}\right) + \int F_s\tilde{f}_s\,(dv)^3. \tag{B.14}$$

Taking into account equations (B.14) and (4.4), the perturbed quasi-neutrality equation reads

$$n_e\frac{e}{T_e}\left(\tilde{\phi} - \left\langle\tilde{\phi}\right\rangle_{\mathrm{FS}}\right) = \mathrm{div}\left(\frac{m_t n_t + m_k n_k}{eB^2}\boldsymbol{\nabla}_\perp\tilde{\phi}\right) + \int\left[Z_t F_t\tilde{f}_t + Z_k F_k\tilde{f}_k\right](dv)^3. \tag{B.15}$$

Defining $\rho_s^2 = \frac{m_s T_t}{e^2B^2}$ where the subscript s stands for either k or t, neglecting the equilibrium spatial variations with regard to the perturbation spatial variations, and dividing by n_e, the quasi-neutrality equation can be recast as

$$\frac{e}{T_e}\left(\tilde{\phi} - \left\langle\tilde{\phi}\right\rangle_{\mathrm{FS}}\right) = \frac{e}{T_t}\left[\frac{n_t}{n_e}\rho_t^2 + \frac{n_k}{n_e}\rho_k^2\right]\boldsymbol{\nabla}_\perp^2\tilde{\phi} + \frac{1}{n_e}\int\left[Z_t F_t\tilde{f}_t + Z_k F_k\tilde{f}_k\right](dv)^3. \tag{B.16}$$

Using Fourier decompositions (B.7) and (B.8), defining $\rho_a^2 = \frac{n_t}{n_e}\rho_t^2 + \frac{n_k}{n_e}\rho_k^2$, and assuming (like was done in the gyrokinetic equation calculus) that ∂_r is dominant over $\frac{\partial_\theta}{r}$, the first two harmonics of the quasi-neutrality equation can be written, at first order in ρ_*, as

$$\rho_a^2 k_r^2\phi_0 = Z_t\int\frac{F_t}{n_e}\,f_{t0}\,(dv)^3 + Z_k\int\frac{F_k}{n_e}\,f_{k0}\,(dv)^3, \tag{B.17}$$

$$\frac{T_t}{T_e}\phi_1^c = Z_t\int\frac{F_t}{n_e}\,f_{t1}^c\,(dv)^3 + Z_k\int\frac{F_k}{n_e}\,f_{k1}^c\,(dv)^3, \tag{B.18}$$

$$\frac{T_t}{T_e}\phi_1^s = Z_t\int\frac{F_t}{n_e}\,f_{t1}^s\,(dv)^3 + Z_k\int\frac{F_k}{n_e}\,f_{k1}^s\,(dv)^3. \tag{B.19}$$

Reporting equations (B.12) and (B.13) into equations (B.17) and (B.19), considering that $-T_t\partial_{E_t}\log F_t = 1$, and removing the odd terms in $v_\parallel$ (which disappear when integrated), we get the following system:

$$\begin{aligned}\rho_a^2 k_r^2\,\phi_0 = {}& \frac{Z_t^2}{2}\phi_1^s\int\frac{F_t}{n_e}\frac{\omega\omega_{g,t}}{\omega^2-\omega_\parallel^2}\,(dv)^3 + \frac{Z_t^2}{2}\phi_0\int\frac{F_t}{n_e}\frac{\omega_{g,t}^2}{\omega^2-\omega_\parallel^2}\,(dv)^3\\ & - \frac{Z_k^2}{2}\phi_1^s\int\frac{T_t\partial_{E_k}F_k}{n_e}\frac{\omega\omega_{g,k}}{\omega^2-\omega_\parallel^2}\,(dv)^3 - \frac{Z_k^2}{2}\phi_0\int\frac{T_t\partial_{E_k}F_k}{n_e}\frac{\omega_{g,k}^2}{\omega^2-\omega_\parallel^2}\,(dv)^3,\end{aligned} \tag{B.20}$$

$$\frac{T_t}{T_e}\phi_1^s = Z_t^2\phi_0\int\frac{F_t}{n_e}\frac{\omega\omega_{g,t}}{\omega^2-\omega_\parallel^2}\,(dv)^3 + Z_t^2\phi_1^s\int\frac{F_t}{n_e}\frac{\omega_\parallel^2}{\omega^2-\omega_\parallel^2}\,(dv)^3$$
$$- Z_k^2\phi_0\int\frac{T_t\partial_{E_k}F_k}{n_e}\frac{\omega\omega_{g,k}}{\omega^2-\omega_\parallel^2}\,(dv)^3 - Z_k^2\phi_1^s\int\frac{T_t\partial_{E_k}F_k}{n_e}\frac{\omega_\parallel^2}{\omega^2-\omega_\parallel^2}\,(dv)^3. \tag{B.21}$$

To solve this system, six integrals need to be computed:

$$I_1 = \int\frac{F_t}{n_e}\frac{\omega\omega_{g,t}}{\omega^2-\omega_\parallel^2}\,(dv)^3, \tag{B.22}$$

$$I_2 = \int\frac{F_t}{n_e}\frac{\omega_{g,t}^2}{\omega^2-\omega_\parallel^2}\,(dv)^3, \tag{B.23}$$

$$I_3 = \int\frac{F_t}{n_e}\frac{\omega_\parallel^2}{\omega^2-\omega_\parallel^2}\,(dv)^3, \tag{B.24}$$

$$I_4 = \int\frac{T_t\partial_{E_k}F_k}{n_e}\frac{\omega\omega_{g,k}}{\omega^2-\omega_\parallel^2}\,(dv)^3, \tag{B.25}$$

$$I_5 = \int\frac{T_t\partial_{E_k}F_k}{n_e}\frac{\omega_{g,k}^2}{\omega^2-\omega_\parallel^2}\,(dv)^3, \tag{B.26}$$

$$I_6 = \int\frac{T_t\partial_{E_k}F_k}{n_e}\frac{\omega_\parallel^2}{\omega^2-\omega_\parallel^2}\,(dv)^3, \tag{B.27}$$

where I_1, I_2 and I_3 are integrals over the thermal distribution function, while I_4, I_5 and I_6 are integrals over the kinetic distribution function.

Regarding the three integrals over the thermal distribution function, we find after calculus

$$I_1 = -\frac{n_t}{n_e}\frac{\sqrt{T_t m_t}}{e_t B}\frac{qk_r}{\sqrt{2}}\left[\mathcal{Z}(\Omega_t)(1+2\Omega_t^2)+2\Omega_t\right], \tag{B.28}$$

$$I_2 = -\frac{n_t}{n_e}\frac{T_t m_t}{e_t^2B^2}q^2k_r^2\left[\mathcal{Z}(\Omega_t)(\frac{1}{\Omega_t}+2\Omega_t+2\Omega_t^3)+3+2\Omega_t^2\right], \tag{B.29}$$

$$I_3 = -\frac{n_t}{n_e}[1+\Omega_t\mathcal{Z}(\Omega_t)], \tag{B.30}$$

where Ω_t is the frequency of the mode normalized as follows:

$$\Omega_t = \sqrt{\frac{m_t}{2T_t}}qR\omega. \tag{B.31}$$

Regarding the three integrals over the kinetic distribution function, the derivative of

the kinetic distribution function according the the kinetic energy reads

$$\partial_{E_k} F_k = -\frac{n_k}{2T_t\tau_k}\left(\frac{m_k}{2\pi T_t\tau_k}\right)^{\frac{3}{2}}\left[e^{-\frac{m_k\left(v_\parallel-\bar{v}_\parallel\right)^2+2\mu_k B}{2T_t\tau_k}}+e^{-\frac{m_k\left(v_\parallel+\bar{v}_\parallel\right)^2+2\mu_k B}{2T_t\tau_k}}\right] + \frac{n_k}{2T_t\tau_k}\frac{\bar{v}_\parallel}{v_\parallel}\left(\frac{m_k}{2\pi T_t\tau_k}\right)^{\frac{3}{2}}\left[e^{-\frac{m_k\left(v_\parallel-\bar{v}_\parallel\right)^2+2\mu_k B}{2T_t\tau_k}}-e^{-\frac{m_k\left(v_\parallel+\bar{v}_\parallel\right)^2+2\mu_k B}{2T_t\tau_k}}\right]. \tag{B.32}$$

We find after calculus

$$I_4 = \frac{n_k}{2n_e}\frac{\sqrt{T_t m_k}}{e_k B}\frac{\sqrt{2}qk_r}{\sqrt{\tau_k}}\left\{\left[\mathcal{Z}\left(\frac{\Omega_k-\bar{u}_\parallel}{\sqrt{\tau_k}}\right)\left[1-\frac{\bar{u}_\parallel}{\Omega_k}\right]+\mathcal{Z}\left(\frac{\Omega_k+\bar{u}_\parallel}{\sqrt{\tau_k}}\right)\left[1+\frac{\bar{u}_\parallel}{\Omega_k}\right]\right]\left[\frac{\Omega_k^2}{\tau_k}+\frac{1}{2}\right] + 2\frac{\Omega_k}{\sqrt{\tau_k}}-\frac{\bar{u}_\parallel}{\Omega_k}\mathcal{Z}\left(\frac{\bar{u}_\parallel}{\sqrt{\tau_k}}\right)\right\}, \tag{B.33}$$

$$I_5 = \frac{n_k}{2n_e}\frac{T_t m_k}{e_k^2 B^2}2q^2k_r^2\left\{\left[\mathcal{Z}\left(\frac{\Omega_k-\bar{u}_\parallel}{\sqrt{\tau_k}}\right)\left[1-\frac{\bar{u}_\parallel}{\Omega_k}\right]+\mathcal{Z}\left(\frac{\Omega_k+\bar{u}_\parallel}{\sqrt{\tau_k}}\right)\left[1+\frac{\bar{u}_\parallel}{\Omega_k}\right]\right]\left[\frac{\Omega_k^3}{\tau_k^{3/2}}+\frac{\Omega_k}{\sqrt{\tau_k}}+\frac{\sqrt{\tau_k}}{2\Omega_k}\right] + 2\frac{\Omega_k^2}{\tau_k}+3-\frac{\bar{u}_\parallel\sqrt{\tau_k}}{\Omega_k^2}\mathcal{Z}\left(\frac{\bar{u}_\parallel}{\sqrt{\tau_k}}\right)\right\}, \tag{B.34}$$

$$I_6 = \frac{n_k}{2n_e}\frac{1}{\tau_k}\left\{\mathcal{Z}\left(\frac{\Omega_k-\bar{u}_\parallel}{\sqrt{\tau_k}}\right)\frac{\Omega_k}{\sqrt{\tau_k}}\left[1-\frac{\bar{u}_\parallel}{\Omega_k}\right]+\mathcal{Z}\left(\frac{\Omega_k+\bar{u}_\parallel}{\sqrt{\tau_k}}\right)\frac{\Omega_k}{\sqrt{\tau_k}}\left[1+\frac{\bar{u}_\parallel}{\Omega_k}\right]+2\right\}, \tag{B.35}$$

where Ω_k is the frequency of the mode, normalized as

$$\Omega_k = \sqrt{\frac{m_k}{2T_t}}qR\omega, \tag{B.36}$$

and $\bar{u}_\parallel$ is the position of the bump-on-tail in the $v_\parallel$ direction, normalized as

$$\bar{u}_\parallel = \sqrt{\frac{m_k}{2T_t}}\bar{v}_\parallel. \tag{B.37}$$

Reporting those expressions of I_1 to I_6 into equations (B.20) and (B.21), and using a linear combination of those two equations to get rid of ϕ_1^s, one gets the dispersion relation with ϕ_0 in factor. When the mode exists, ϕ_0 is non null, which means that it can be removed from the relation. We thus get the following dispersion relation:

$$\frac{1}{q^2}+A_1(\Omega_t)+A_2(\Omega_k)-\frac{\left[N_1(\Omega_t)+N_2(\Omega_k)\right]^2}{D_1(\Omega_t)+D_2(\Omega_k)}=0, \tag{B.38}$$

with

$$A_1(\Omega_t) = \frac{n_e}{n_t+n_k\frac{m_k}{m_t}}\frac{n_t}{n_e}\left\{\mathcal{Z}(\Omega_t)\left[\Omega_t^3+\Omega_t+\frac{1}{2\Omega_t}\right]+\Omega_t^2+\frac{3}{2}\right\}, \tag{B.39}$$

$$A_2(\Omega_k) = \frac{m_k}{m_t}\frac{n_e}{n_t + n_k\frac{m_k}{m_t}}\frac{n_k}{2n_e}\Bigg\{\left[\mathcal{Z}\left(\frac{\Omega_k - \bar{u}_\parallel}{\sqrt{\tau_k}}\right)\left[1 - \frac{\bar{u}_\parallel}{\Omega_k}\right] + \mathcal{Z}\left(\frac{\Omega_k + \bar{u}_\parallel}{\sqrt{\tau_k}}\right)\left[1 + \frac{\bar{u}_\parallel}{\Omega_k}\right]\right]\left[\frac{\Omega_k^3}{\tau_k^{3/2}} + \frac{\Omega_k}{\sqrt{\tau_k}} + \frac{\sqrt{\tau_k}}{2\Omega_k}\right] + 2\frac{\Omega_k^2}{\tau_k} + 3 - \frac{\bar{u}_\parallel\sqrt{\tau_k}}{\Omega_k^2}\mathcal{Z}\left(\frac{\bar{u}_\parallel}{\sqrt{\tau_k}}\right)\Bigg\}, \tag{B.40}$$

$$N_1(\Omega_t) = Z_t\sqrt{\frac{n_e}{n_t + n_k\frac{m_k}{m_t}}}\frac{n_t}{n_e}\left\{\mathcal{Z}(\Omega_t)\left[\Omega_t^2 + \frac{1}{2}\right] + \Omega_t\right\}, \tag{B.41}$$

$$N_2(\Omega_k) = Z_k\frac{1}{\sqrt{\tau_k}}\sqrt{\frac{m_k}{m_t}}\sqrt{\frac{n_e}{n_t + n_k\frac{m_k}{m_t}}}\frac{n_k}{2n_e}\Bigg\{\left[\mathcal{Z}\left(\frac{\Omega_k - \bar{u}_\parallel}{\sqrt{\tau_k}}\right)\left[1 - \frac{\bar{u}_\parallel}{\Omega_k}\right] + \mathcal{Z}\left(\frac{\Omega_k + \bar{u}_\parallel}{\sqrt{\tau_k}}\right)\left[1 + \frac{\bar{u}_\parallel}{\Omega_k}\right]\right]\left[\frac{\Omega_k^2}{\tau_k} + \frac{1}{2}\right] + 2\frac{\Omega_k}{\sqrt{\tau_k}} - \frac{\bar{u}_\parallel}{\Omega_k}\mathcal{Z}\left(\frac{\bar{u}_\parallel}{\sqrt{\tau_k}}\right)\Bigg\}, \tag{B.42}$$

$$D_1(\Omega_t) = Z_t^2\frac{n_t}{n_e}\{\mathcal{Z}(\Omega_t)\Omega_t + 1\} + \frac{T_t}{T_e}, \tag{B.43}$$

$$D_2(\Omega_k) = \frac{Z_k^2}{\tau_k}\frac{n_k}{2n_e}\left\{\mathcal{Z}\left(\frac{\Omega_k - \bar{u}_\parallel}{\sqrt{\tau_k}}\right)\frac{\Omega_k}{\sqrt{\tau_k}}\left[1 - \frac{\bar{u}_\parallel}{\Omega_k}\right] + \mathcal{Z}\left(\frac{\Omega_k + \bar{u}_\parallel}{\sqrt{\tau_k}}\right)\frac{\Omega_k}{\sqrt{\tau_k}}\left[1 + \frac{\bar{u}_\parallel}{\Omega_k}\right] + 2\right\}. \tag{B.44}$$

Appendix C

Non-linear parametric decay model derivation

We here consider a non-linear model taking into account three waves: two ITG modes and an EGAM. The aim is to describe a situation in which the two ITG modes have a positive non-linear growth rate, while the EGAM has a large amplitude compared to the ITG, and which can be considered to be steady-state. In the equations derived in the present appendix, the linear part is an ITG mode, while the non-linear part (from the $\mathbf{E} \times \mathbf{B}$ drift velocity) comprises the other ITG mode and the EGAM.

The derivation of the linear part is similar to that described in Appendix A. A difference is that in the present appendix, a local equation is derived, while in Appendix A the poloidal shape of the ITG linear mode was derived. However, the global structure derived in Appendix A is taken into account in Section 5.3.3 to discuss the pertinence of the solutions obtained in the present appendix.

C.1 Gyrokinetic Vlasov equation

We use the gyrokinetic model described in Section 1.3.1 to derive the non-linear equation describing the interaction between ITG and EGAM in the framework of the parametric decay model. The following variables are used: $(\mathbf{x}_\mathrm{G}, v_\parallel, \mu)$, where the subscript G denotes the gyro-centre position. $v_\parallel$ is the parallel velocity, μ is the magnetic moment. The latter is an adiabatic invariant, which means that $d_t \mu = 0$.

We here consider an electrostatic perturbation. This means that the magnetic field fluctuations are not taken into account: $\mathbf{B}(\mathbf{x}_\mathrm{G}, t) = \mathbf{B}_\mathrm{eq}(\mathbf{x}_\mathrm{G})$. The equilibrium electric potential is assumed to be null; the electric potential is therefore reduced to its perturbed part $\tilde{\phi}$. In agreement with the gyrokinetic hypotheses, $e\tilde{\phi}/T_i$ is assumed to be of order 1 in ρ_*.

The distribution function of gyro-centres f_G is decomposed into an equilibrium part

$f_{\mathrm{G,eq}}$ and a perturbed part $\tilde{f}_{\mathrm{G}}$:

$$f_{\mathrm{G}}(\mathbf{x}_{\mathrm{G}}, v_{\parallel}, \mu, t) = f_{\mathrm{G,eq}}(\mathbf{x}_{\mathrm{G}}, v_{\parallel}, \mu) + \tilde{f}_{\mathrm{G}}(\mathbf{x}_{\mathrm{G}}, v_{\parallel}, \mu, t). \tag{C.1}$$

The perturbation of the distribution function is assumed to be of order 1 in ρ_*: $\tilde{f}_{\mathrm{G}}/f_{\mathrm{G,eq}} \sim \rho_*$.

The gyrokinetic equation reads, at first order in ρ_*:

$$\partial_t f_{\mathrm{G}} + \mathbf{v}_{\mathrm{G}\perp} \cdot \boldsymbol{\nabla}_{\perp} f_{\mathrm{G}} + v_{\parallel} \nabla_{\parallel} f_{\mathrm{G}} + d_t v_{\parallel} \cdot \partial_{v_{\parallel}} f_{\mathrm{G}} = 0, \tag{C.2}$$

with

$$\mathbf{v}_{\mathrm{G}\perp} = \mathbf{v}_{\mathrm{E}} + \mathbf{v}_g, \tag{C.3}$$

$$\mathbf{v}_{\mathrm{E}} = \frac{\mathbf{b} \times \boldsymbol{\nabla} J_0 \tilde{\phi}}{B}, \tag{C.4}$$

$$\mathbf{v}_g = \frac{m v_{\parallel}^2 + \mu B}{eB} \frac{\mathbf{b} \times \boldsymbol{\nabla} B}{B} + \frac{m v_{\parallel}^2}{eB} \frac{\mathbf{rot}\ \mathbf{B}}{B}\bigg|_{\perp}. \tag{C.5}$$

In this expression, $\mathbf{v}_{\mathrm{E}}$ is the electric drift velocity, $\mathbf{v}_g$ the gradient and curvature drift velocity and J_0 is the gyro-average operator. The magnetic field $\mathbf{B}$ is to be evaluated at the gyro-centre position. The last term in the expression of $\mathbf{v}_g$, that is to say $\frac{m v_{\parallel}^2}{eB} \frac{\mathbf{rot}\ \mathbf{B}}{B}\big|_{\perp}$, can be neglected when the plasma has a low β, which is what we will here consider.

Still up to the first order in ρ_* and at low β,

$$d_t v_{\parallel} = -\frac{e}{m} \nabla_{\parallel} J_0 \tilde{\phi} + v_{\parallel} \mathbf{v}_{\mathrm{E}} \cdot \frac{\boldsymbol{\nabla} B}{B}. \tag{C.6}$$

In this expression, only highly passing particles are considered, which means that the term in $\mu \nabla_{\parallel} B$ has not been taken into account.

In addition to ρ_*, a second small parameter is introduced, $\delta \sim k_{\perp} \rho_i$, with the following ordering:

$$\rho_* \ll \delta \ll 1, \tag{C.7}$$

were ρ_i is the ion Larmor radius and $k_{\perp}$ represents a characteristic value of the perpendicular wave vector. In terms of the notations that are used below, $k_{\perp}$ here means either k_{θ}, K_1, K_2 or k_r. Taking into account δ, the following orderings are considered for the

ITG:

$$\frac{e\tilde{\phi}_{1,2}}{T_i} \sim \rho_* \delta^{-1}, \tag{C.8}$$

$$\frac{\tilde{f}_{\mathrm{G}1,2}}{f_{\mathrm{G,eq}}} \sim \rho_* \delta^{-3}, \tag{C.9}$$

where $\tilde{\phi}_{1,2}$ is the ITG mode 1, 2 perturbed electric potential and $\tilde{f}_{\mathrm{G}1,2}$ is the ITG mode 1, 2 perturbed gyro-centre distribution function.

As for the EGAM, the following orderings are considered:

$$\frac{e\tilde{\phi}_{\mathrm{E}}}{T_i} \sim \rho_* \delta^{-2}, \tag{C.10}$$

$$\frac{\tilde{f}_{\mathrm{GE}}}{f_{\mathrm{G,eq}}} \sim \rho_* \delta^{-1}, \tag{C.11}$$

where $\tilde{\phi}_{\mathrm{E}}$ is the EGAM perturbed electric potential, and $\tilde{f}_{\mathrm{GE}}$ is the EGAM perturbed gyro-centre distribution function.

The EGAM being the pump wave, the corresponding electric potential perturbation is deemed to be one order of magnitude larger in δ than the ITG waves. In addition, those orderings correspond to the idea that the non-linear term in the $\mathbf{E} \times \mathbf{B}$ velocity is dominant over other non-linearities. The $\tilde{f}_{\mathrm{G}}/f_{\mathrm{G,eq}}$ ordering then ensues from the EGAM and ITG gyrokinetic equations.

In the computation, we will keep terms up to order 1 in ρ_* and -1 in δ. $J_0 - 1$ applied to perturbed fields is of order δ^2: $J_0 - 1 \approx \frac{1}{2}\frac{\mu B}{T_i}\rho_i^2 \nabla_\perp^2$. $ak_\perp = k_\perp \rho_i a/\rho_i$ is of order $\delta\rho_*^{-1}$ (a is the value of the minor radius of the tokamak). $a\boldsymbol{\nabla}_\perp \ln f_{\mathrm{G,eq}}$ is assumed to be of order δ^{-3}.

The equilibrium terms are removed from the gyrokinetic equation: their sum is null since they satisfy the equilibrium gyrokinetic equation. Out of the non-linear terms, the $\tilde{\mathbf{v}}_{\mathrm{E}} \cdot \boldsymbol{\nabla}_\perp \tilde{f}_{\mathrm{G}}$ term is assumed to be dominant. We therefore remove all non-linear terms but this one. With the conventions here adopted, the gyrokinetic equation reads

$$\begin{aligned}\partial_t \tilde{f}_{\mathrm{G}1} + \frac{\mathbf{b} \times \boldsymbol{\nabla} J_0 \tilde{\phi}_1}{B} \cdot \boldsymbol{\nabla}_\perp f_{\mathrm{G,eq}} + \frac{\mathbf{b} \times \boldsymbol{\nabla} J_0 \tilde{\phi}_{\mathrm{E}}}{B} \cdot \boldsymbol{\nabla}_\perp \tilde{f}_{\mathrm{G}2} + \frac{m v_\parallel^2 + \mu B}{eB} \frac{\mathbf{b} \times \boldsymbol{\nabla} B}{B} \cdot \boldsymbol{\nabla}_\perp \tilde{f}_{\mathrm{G}1} \\ + v_\parallel \nabla_\parallel \tilde{f}_{\mathrm{G}1} - \frac{e}{m} \nabla_\parallel J_0 \tilde{\phi}_1 \, \partial_{v_\parallel} f_{\mathrm{G,eq}} + v_\parallel \frac{\mathbf{b} \times \boldsymbol{\nabla} J_0 \tilde{\phi}_1}{B} \cdot \frac{\boldsymbol{\nabla} B}{B} \partial_{v_\parallel} f_{\mathrm{G,eq}} = 0.\end{aligned} \tag{C.12}$$

In particular, the non-linear term $\frac{\mathbf{b} \times \boldsymbol{\nabla} J_0 \tilde{\phi}_2}{B} \cdot \boldsymbol{\nabla}_\perp \tilde{f}_{\mathrm{GE}}$ does not appear in this equation as its order in δ is too high.

A Maxwellian distribution function is assumed for the equilibrium distribution func-

tion:

$$f_{\mathrm{G,eq}} = n_i \left(\frac{m}{2\pi T_i} \right)^{3/2} e^{-\frac{m v_\parallel^2}{2T_i} - \frac{\mu B}{T_i}}. \tag{C.13}$$

Therefore:

$$\boldsymbol{\nabla}_\perp f_{\mathrm{G,eq}}|_{v_\parallel,\mu} = \mathbf{e}_r \frac{\partial}{\partial r} f_{\mathrm{G,eq}} \bigg|_{\varepsilon,\mu} - \frac{\mu \boldsymbol{\nabla}_\perp B}{T_i} f_{\mathrm{G,eq}}, \tag{C.14}$$

$$\partial_{v_\parallel} f_{\mathrm{G,eq}} = -\frac{m v_\parallel}{T_i} f_{\mathrm{G,eq}}. \tag{C.15}$$

Taking into account those last two relations, and after having removed high order terms, the gyrokinetic equation reads

$$\begin{aligned} &\partial_t \tilde{f}_{\mathrm{G1}} + \frac{\mathbf{b} \times \boldsymbol{\nabla} J_0 \tilde{\phi}_1}{B} \cdot \mathbf{e}_r \frac{\partial}{\partial r} f_{\mathrm{G,eq}} \bigg|_{\varepsilon,\mu} + \frac{\mathbf{b} \times \boldsymbol{\nabla} J_0 \tilde{\phi}_{\mathrm{E}}}{B} \cdot \boldsymbol{\nabla}_\perp \tilde{f}_{\mathrm{G2}} \\ &\quad + \frac{m v_\parallel^2 + \mu B}{eB} \frac{\mathbf{b} \times \boldsymbol{\nabla} B}{B} \cdot \boldsymbol{\nabla}_\perp \tilde{f}_{\mathrm{G1}} + v_\parallel \nabla_\parallel \tilde{f}_{\mathrm{G1}} + \frac{e v_\parallel}{T_i} \nabla_\parallel \tilde{\phi}_1 \; f_{\mathrm{G,eq}} = 0. \end{aligned} \tag{C.16}$$

In the case of concentric circular poloidal sections, this equation can be recast as

$$\begin{aligned} &\partial_t \tilde{f}_{\mathrm{G1}} - \frac{\partial_\theta J_0 \tilde{\phi}_1}{rB} \partial_r f_{\mathrm{G,eq}} + \frac{\mathbf{b} \times \boldsymbol{\nabla} J_0 \tilde{\phi}_{\mathrm{E}}}{B} \cdot \boldsymbol{\nabla}_\perp \tilde{f}_{\mathrm{G2}} - v_g \left(\sin\theta \partial_r + \frac{\cos\theta}{r} \partial_\theta \right) \tilde{f}_{\mathrm{G1}} \\ &\quad + v_\parallel \left(\frac{\partial_\varphi}{R} + \frac{\partial_\theta}{qR} \right) \tilde{f}_{\mathrm{G1}} + f_{\mathrm{G,eq}} \frac{e v_\parallel}{T_i} \left(\frac{\partial_\varphi}{R} + \frac{\partial_\theta}{qR} \right) \tilde{\phi}_1 = 0, \end{aligned} \tag{C.17}$$

where $v_g = \frac{m v_\parallel^2 + \mu B}{eBR}$.

The ballooning representation (see Section 2.3.1) is used to express $\tilde{\phi}_1$ and $\tilde{f}_{\mathrm{G1}}$ in the linear part of the equation, corresponding to the first ITG mode:

$$\tilde{\phi}_1(\mathbf{x}_{\mathrm{G}}, t) = \phi_1(t) e^{-i\omega_1 t} e^{in\varphi} \sum_{\ell=-\infty}^{+\infty} \hat{\Phi}_1(\theta + 2\ell\pi) e^{-inq(\theta + 2\ell\pi - \theta_1)} + c.c., \tag{C.18}$$

$$\tilde{f}_{\mathrm{G1}}\big(\mathbf{x}_{\mathrm{G}}, v_\parallel, \mu, t\big) = f_1(t) e^{-i\omega_1 t} e^{in\varphi} \sum_{\ell=-\infty}^{+\infty} \hat{F}_1\big(\theta + 2\ell\pi, v_\parallel, \mu\big) e^{-inq(\theta + 2\ell\pi - \theta_1)} + c.c., \tag{C.19}$$

where q is the safety factor and *c.c.* means *complex conjugate*. We consider the safety factor to be linear: $q = q_0 + q_0' x$, where $q_0 = q(r_0)$, $q_0' = q'(r_0)$, $x = r - r_0$ and r_0 is the position (in the small radius coordinate) of the reference resonance surface. ω_1 is the real part of the linear frequency (*i.e.* the frequency which is solution of the linear dispersion

relation). $\phi_1(t)$ and $f_1(t)$ are the amplitudes of the mode.

Keeping only the $\ell = 0$ component; defining $K_1 = n\theta_1 q_0'$ and $k_\theta = \frac{nq_0}{r_0}$, we can write the ballooning representation as follows:

$$\tilde{\phi}_1(\mathbf{x}_\mathrm{G}, t) = \phi_1(t) e^{-i\omega_1 t} e^{in\varphi} \hat{\Phi}_1(\theta) e^{-ir_0 k_\theta \theta - inq_0' x\theta + ixK_1} + c.c., \tag{C.20}$$

$$\tilde{f}_{\mathrm{G}1}\big(\mathbf{x}_\mathrm{G}, v_\parallel, \mu, t\big) = f_1(t) e^{-i\omega_1 t} e^{in\varphi} \hat{F}_1\big(\theta, v_\parallel, \mu\big) e^{-ir_0 k_\theta \theta - inq_0' x\theta + ixK_1} + c.c. \tag{C.21}$$

Inserting those expressions into equation (C.17), we get

$$\begin{aligned}
&\frac{\mathbf{b}\times\boldsymbol{\nabla} J_0 \tilde{\phi}_\mathrm{E}}{B} \cdot \boldsymbol{\nabla}_\perp \tilde{f}_{\mathrm{G}2} + \left(-i\omega_1 + \frac{f_1'}{f_1}\right) f_1(t) e^{-i\omega_1 t} e^{in\varphi} \hat{F}_1 e^{-ir_0 k_\theta \theta - inq_0' x\theta + ixK_1} \\
&\quad - \partial_\theta \left(1 + \frac{1}{2}\frac{\mu B}{T_i}\rho_i^2 \nabla_\perp^2\right) \phi_1(t) e^{-i\omega_1 t} e^{in\varphi} \hat{\Phi}_1 e^{-ir_0 k_\theta \theta - inq_0' x\theta + ixK_1} \frac{\partial_r f_{\mathrm{G,eq}}}{rB} \\
&\quad - v_g \left(\sin\theta \partial_r + \frac{\cos\theta}{r}\partial_\theta\right) f_1(t) e^{-i\omega_1 t} e^{in\varphi} \hat{F}_1 e^{-ir_0 k_\theta \theta - inq_0' x\theta + ixK_1} \\
&\quad + v_\parallel \left(\frac{\partial_\varphi}{R} + \frac{\partial_\theta}{qR}\right) f_1(t) e^{-i\omega_1 t} e^{in\varphi} \hat{F}_1 e^{-ir_0 k_\theta \theta - inq_0' x\theta + ixK_1} \\
&\quad + f_{\mathrm{G,eq}} \frac{e v_\parallel}{T_i} \left(\frac{\partial_\varphi}{R} + \frac{\partial_\theta}{qR}\right) \phi_1(t) e^{-i\omega_1 t} e^{in\varphi} \hat{\Phi}_1 e^{-ir_0 k_\theta \theta - inq_0' x\theta + ixK_1} = 0.
\end{aligned} \tag{C.22}$$

Due to ordering considerations, once out of the exponentials, θ or x do not need to be derived any more. Besides, $\frac{\rho_i^2}{T_i}$ does not have any spatial dependence (except through B, but B is here assumed to be constant). $\hat{F}_1$ and $\hat{\Phi}_1$ depend slowly on θ, and are therefore not to be derived except in parallel gradients. Equation (C.22) can therefore be recast as

$$\begin{aligned}
&\frac{\mathbf{b}\times\boldsymbol{\nabla} J_0 \tilde{\phi}_\mathrm{E}}{B} \cdot \boldsymbol{\nabla}_\perp \tilde{f}_{\mathrm{G}2} + e^{-i\omega_1 t} e^{in\varphi} e^{-ir_0 k_\theta \theta - inq_0' x\theta + ixK_1} \Bigg[(-i\omega_1 + \partial_t) f_1(t) \hat{F}_1 \\
&\quad + \frac{\left(ik_\theta + \frac{inq_0' x}{r_0}\right)\left(1 - \frac{1}{2}\frac{\mu B}{T_i} k_{\perp 1}^2 \rho_i^2\right) \phi_1(t) \hat{\Phi}_1}{B} \partial_r f_{\mathrm{G,eq}} \\
&\quad - v_g \left(\sin\theta (iK_1 - inq_0'\theta) - \cos\theta \left(ik_\theta + \frac{inq_0' x}{r_0}\right)\right) f_1(t) \hat{F}_1 \\
&\quad + v_\parallel f_1(t) \frac{\partial_\theta \hat{F}_1}{qR} + f_{\mathrm{G,eq}} \frac{e v_\parallel}{T_i} \phi_1(t) \frac{\partial_\theta \hat{\Phi}_1}{qR} \Bigg] = 0.
\end{aligned} \tag{C.23}$$

We define the perpendicular wave vector $k_{\perp 1}$ and the parallel wave vector $k_\parallel$ as follows:

$$k_{\perp 1}^2 = \left(K_1 - nq_0'\theta\right)^2 + k_\theta^2, \tag{C.24}$$

$$ik_\parallel = \frac{\partial_\theta}{qR}. \tag{C.25}$$

We define the comprehensive mode frequency Ω_1, the diamagnetic frequency ω_*, the

kinetic drift frequency ω_{g1}, and the parallel frequency $\omega_\parallel$ as follows:

$$i\Omega_1 = i\omega_1 - \partial_t, \tag{C.26}$$

$$\omega_* = -k_\theta \frac{\partial_r \ln f_{\mathrm{G,eq}}}{B}\frac{T_i}{e}, \tag{C.27}$$

$$\omega_{g1} = v_g[\sin\theta(K_1 - nq_0'\theta) - \cos\theta k_\theta], \tag{C.28}$$

$$\omega_\parallel = v_\parallel k_\parallel. \tag{C.29}$$

With those conventions, and considering that $\frac{x}{r_0}$ is small, the equation now reads

$$\begin{aligned}\frac{\mathbf{b}\times\boldsymbol{\nabla}J_0\tilde{\phi}_{\mathrm{E}}}{B}\cdot\boldsymbol{\nabla}_\perp\tilde{f}_{\mathrm{G2}} + e^{-i\omega_1 t}e^{in\varphi}e^{-ir_0k_\theta\theta - inq_0'x\theta + ixK_1}\Bigg[&- i\Omega_1 f_1(t)\hat{F}_1 \\ &- i\phi_1(t)\hat{\Phi}_1\frac{e}{T_i}\omega_*\left(1 - \frac{1}{2}\frac{\mu B}{T_i}k_{\perp 1}^2\rho_i^2\right)f_{\mathrm{G,eq}} - i\omega_{g1}f_1(t)\hat{F}_1 \\ &+ k_\parallel f_1(t)\hat{F}_1 + f_{\mathrm{G,eq}}\frac{ev_\parallel}{T_i}k_\parallel\phi_1(t)\hat{\Phi}_1\Bigg] = 0.\end{aligned} \tag{C.30}$$

In the non linear part of the equation, the EGAM is expressed as follows:

$$\tilde{\phi}_{\mathrm{E}}(\mathbf{x}_{\mathrm{G}}, t) = \frac{T_i}{e}\phi_{\mathrm{E}}(t)e^{-i\omega_{\mathrm{E}}t}e^{ik_r x}\left[\hat{\Phi}_{\mathrm{E}} + \hat{\Phi}_s\sin\theta + \hat{\Phi}_c\cos\theta\right] + c.c., \tag{C.31}$$

where $\tilde{\phi}_{\mathrm{E}}$ has been normalized to $\frac{T_i}{e}$, ω_{E} is the real part of the EGAM frequency and $\phi_{\mathrm{E}}(t)$ is the amplitude of the mode. In practice, since the EGAM is the pump wave, its amplitude is assumed to be large and vary slowly compared to the amplitudes of the daughter waves (the ITG modes). Therefore, we will consider that ϕ_{E} is a constant. $\hat{\Phi}_{\mathrm{E}}$ is the $m = 0$ component of the EGAM, where m is the poloidal mode number, while $\hat{\Phi}_s$ and $\hat{\Phi}_c$ and respectively the sine and cosine $m = 1$ poloidal components. The orderings in δ are as follows (see Appendix B):

$$\frac{\hat{\Phi}_s}{\hat{\Phi}_{\mathrm{E}}} \sim \delta, \tag{C.32}$$

$$\frac{\hat{\Phi}_c}{\hat{\Phi}_{\mathrm{E}}} \sim \delta^2. \tag{C.33}$$

In practice, taking into account those orderings, $\hat{\Phi}_s$ and $\hat{\Phi}_c$ will not appear in the final dispersion relations.

As for the second ITG mode, it is expressed in the ballooning representation as

$$\tilde{\phi}_2(\mathbf{x}_\mathrm{G}, t) = \phi_2(t) e^{-i\omega_2 t} e^{in\varphi} \hat{\Phi}_2(\theta) e^{-ir_0 k_\theta \theta - inq_0' x\theta + ixK_2} + c.c., \tag{C.34}$$

$$\tilde{f}_{\mathrm{G}2}\big(\mathbf{x}_\mathrm{G}, v_\parallel, \mu, t\big) = f_2(t) e^{-i\omega_2 t} e^{in\varphi} \hat{F}_2\big(\theta, v_\parallel, \mu\big) e^{-ir_0 k_\theta \theta - inq_0' x\theta + ixK_2} + c.c., \tag{C.35}$$

where $K_2 = n\theta_2 q_0'$, $k_\theta = \frac{nq_0}{r_0}$ and ω_2 is the real part of the linear frequency. $\phi_2(t)$ and $f_2(t)$ are the amplitudes of the mode.

To ensure interaction between the two ITG modes and the EGAM, the following relations are assumed:

$$\omega_\mathrm{E} + \omega_2 = \omega_1, \tag{C.36}$$

$$k_r + K_2 = K_1. \tag{C.37}$$

T_i in the EGAM expression is assumed to be constant. In the second ITG expression, $\hat{F}_2$ varies slowly in θ and therefore needs not be derived. Considering that $\frac{x}{r_0}$ is small, and removing high order terms, the non-linear term, here called A, reads

$$A = \frac{T_i}{e} \hat{F}_2 \phi_\mathrm{E} f_2(t) \frac{k_r \left[\hat{\Phi}_\mathrm{E} + \hat{\Phi}_s \sin\theta + \hat{\Phi}_c \cos\theta\right]}{B} k_\theta - \frac{T_i}{e} \phi_\mathrm{E} \hat{\Phi}_\mathrm{E} f_2(t) \hat{F}_2 \frac{\mu B}{2T_i} \frac{\rho_i^2 k_r^3}{B} k_\theta, \tag{C.38}$$

while the total gyrokinetic equation reads

$$f_1(t)\hat{F}_1 = -\frac{iA}{\Omega_1 + \omega_{g1}} - f_{\mathrm{G,eq}} \frac{e}{T_i} \frac{\omega_* \left(1 - \frac{1}{2}\frac{\mu B}{T_i} k_{\perp 1}^2 \rho_i^2\right) - \omega_\parallel}{\Omega_1 + \omega_{g1}} \phi_1(t) \hat{\Phi}_1 + \frac{\omega_\parallel}{\Omega_1} f_1(t) \hat{F}_1. \tag{C.39}$$

Assuming the following orderings:

$$\frac{\omega_*}{\Omega_1} \sim \delta^{-2}, \tag{C.40}$$

$$\frac{\omega_\parallel}{\Omega_1} \sim \delta, \tag{C.41}$$

$$\frac{\omega_{g1}}{\Omega_1} \sim \delta^2, \tag{C.42}$$

this expression can be recast as

$$\begin{aligned} f_1(t)\hat{F}_1 = &-f_{\mathrm{G,eq}} \frac{e}{T_i} \frac{\omega_*}{\Omega_1} \left(1 - \frac{\omega_{g1}}{\Omega_1} + \frac{\omega_\parallel}{\Omega_1} + \frac{\omega_\parallel^2}{\Omega_1^2} - \frac{1}{2}\frac{\mu B}{T_i} k_{\perp 1}^2 \rho_i^2\right) \phi_1(t) \hat{\Phi}_1 \\ &- \left(1 - \frac{\omega_{g1}}{\Omega_1} + \frac{\omega_\parallel}{\Omega_1} + \frac{\omega_\parallel^2}{\Omega_1^2}\right) \frac{iA}{\Omega_1}. \end{aligned} \tag{C.43}$$

C.2 Quasi-neutrality equation

The gyrokinetic quasi-neutrality equation reads (see Section 1.3.1)

$$n_i \frac{e}{T_e}\left(\tilde{\phi} - \left\langle \tilde{\phi} \right\rangle_{\mathrm{FS}}\right) = \mathrm{div}\left(\frac{m_i n_i}{eB^2}\boldsymbol{\nabla}_\perp \tilde{\phi}\right) + \int J_0 \cdot \left(f_{\mathrm{G,eq}} + \tilde{f}_{\mathrm{G}}\right) (dv)^3 - n_i. \tag{C.44}$$

We have here supposed that there is only one species of ions, and that its charge number is 1. The equilibrium density of ions and electrons is therefore the same, and is here called n_i. $\left\langle \tilde{\phi} \right\rangle_{\mathrm{FS}}$ is the flux-surface average of the electrostatic potential. $f_{\mathrm{G,eq}}$ is the equilibrium ion distribution function; it verifies $\int J_0 \cdot f_{\mathrm{G,eq}}\ (dv)^3 = n_i$ at order 1 in ρ_*. We assume that the electron temperature T_e is equal to the ion equilibrium temperature T_i. The spatial variations of n_i are neglected.

Using the ballooning representation, considering that $\hat{F}$ depends slowly on θ, that $\frac{x}{r_0}$ is small, and eliminating high order terms, the quasi-neutrality equation can be recast, for the linear ITG mode, as

$$n_i \frac{e}{T_i}\phi_1(t)\hat{\Phi}_1 = \int f_1(t)\hat{F}_1 \left(1 - \frac{1}{2}\frac{\mu B}{T_i}\rho_i^2\left[k_\theta^2 + \left(K_1 - n q_0' \theta\right)^2\right]\right) (dv)^3. \tag{C.45}$$

Recalling expression (C.43), this expression transforms into

$$\frac{e}{T_i}\phi_1(t)\hat{\Phi}_1 = -\int \frac{f_{\mathrm{G,eq}}}{n_i}\frac{e}{T_i}\frac{\omega_*}{\Omega_1}\left(1 - \frac{\omega_{g1}}{\Omega_1} + \frac{\omega_\parallel^2}{\Omega_1^2} - \frac{\mu B}{T_i}k_{\perp 1}^2\rho_i^2\right)\phi_1(t)\hat{\Phi}_1\ (dv)^3 + N, \tag{C.46}$$

where N is the integrated non-linear term:

$$N = -\frac{1}{n_i}\int \left(1 - \frac{\omega_{g1}}{\Omega_1} + \frac{\omega_\parallel}{\Omega_1} + \frac{\omega_\parallel^2}{\Omega_1^2} - \frac{1}{2}\frac{\mu B}{T_i}\rho_i^2 k_{\perp 1}^2\right)\frac{iA}{\Omega_1}\ (dv)^3. \tag{C.47}$$

Defining

$$\omega_n^* = -\frac{k_\theta}{B}\frac{T_i}{e}\frac{n_i'(r)}{n_i}, \tag{C.48}$$

$$\omega_p^* = -\frac{k_\theta}{B}\frac{T_i}{e}\frac{p_i'(r)}{p_i}, \tag{C.49}$$

$$v_{\mathrm{T}}^2 = \frac{T_i}{m}, \tag{C.50}$$

$$s_0 = \frac{r_0 q_0'}{q_0}, \tag{C.51}$$

where $p_i = n_i T_i$ is the ion pressure, and integrating over the velocity, the equation becomes

$$\frac{e}{T_i}\left[\frac{\Omega_1+\omega_n^*}{\omega_p^*}+\frac{2k_\theta T_i}{\Omega_1 eBR}[\cos\theta+s_0(\theta-\theta_1)\sin\theta] + v_{\mathrm{T}}^2\frac{k_\parallel^2}{\Omega_1^2}-k_\theta^2\rho_i^2\left[s_0^2(\theta-\theta_1)^2+1\right]\right]\phi_1(t)\hat{\Phi}_1 = N\frac{\Omega_1}{\omega_p^*}. \tag{C.52}$$

Let us define the fluid drift frequency ω_{gf} and the normalized poloidal wave vector k:

$$\omega_{gf} = \frac{2k_\theta T_i}{eBR} = \frac{2nq_0T_i}{er_0BR}, \tag{C.53}$$

$$k^2 = k_\theta^2\rho_i^2. \tag{C.54}$$

Let us consider the following form for the poloidal shape of the linear ITG mode:

$$\hat{\Phi}_1 = \frac{1}{\Delta_1\sqrt{2\pi}}e^{-\frac{(\theta-\theta_1)^2}{2\Delta_1^2}}, \tag{C.55}$$

where Δ_1 is a constant. Then integrating over θ, the equation becomes

$$\frac{e}{T_i}\left[\frac{\Omega_1+\omega_n^*}{\omega_p^*}+\left(\frac{\omega_{gf}}{\Omega_1}\cos\theta_1 e^{-\frac{\Delta_1^2}{2}}-k^2\right)\left(1+s_0\Delta_1^2\right)\right]\phi_1(t) = \frac{\Omega_1}{\omega_p^*}\int_{-\infty}^{\infty}N(\theta)d\theta. \tag{C.56}$$

C.3 Non-linear term

Taking into account the expression of A, and eliminating high order terms, the non-linear term N reads

$$\begin{aligned}N = &-\frac{i}{n_i\Omega_1}\int\left[\frac{T_i}{e}\hat{F}_2\phi_{\mathrm{E}}f_2(t)\frac{k_r\left[\hat{\Phi}_{\mathrm{E}}+\hat{\Phi}_s\sin\theta+\hat{\Phi}_c\cos\theta\right]}{B}k_\theta-\frac{T_i}{e}\phi_{\mathrm{E}}\hat{\Phi}_{\mathrm{E}}f_2(t)\hat{F}_2\frac{\mu B}{2T_i}\frac{\rho_i^2k_r^3}{B}k_\theta\right](dv)^3\\ &-\frac{i}{n_i\Omega_1^2}\int\omega_\parallel\left[\frac{T_i}{e}\hat{F}_2\phi_{\mathrm{E}}f_2(t)\frac{k_r\left[\hat{\Phi}_{\mathrm{E}}+\hat{\Phi}_s\sin\theta\right]}{B}k_\theta\right](dv)^3\\ &-\frac{i}{n_i\Omega_1}\int\left[\frac{\omega_\parallel^2}{\Omega_1^2}-\frac{\omega_{g1}}{\Omega_1}-\frac{1}{2}\frac{\mu B}{T_i}\rho_i^2k_{\perp1}^2\right]\left[\frac{T_i}{e}\hat{F}_2\phi_{\mathrm{E}}f_2(t)\frac{k_r\hat{\Phi}_{\mathrm{E}}}{B}k_\theta\right](dv)^3.\end{aligned} \tag{C.57}$$

Considering that

$$f_2(t)\hat{F}_2 = -f_{\mathrm{G,eq}}\frac{e}{T_i}\frac{\omega_*}{\Omega_2}\left(1-\frac{\omega_{g2}}{\Omega_2}+\frac{\omega_\parallel}{\Omega_2}+\frac{\omega_\parallel^2}{\Omega_2^2}-\frac{1}{2}\frac{\mu B}{T_i}k_{\perp2}^2\rho_i^2\right)\phi_2(t)\hat{\Phi}_2, \tag{C.58}$$

eliminating high order terms, and integrating over the velocity, one gets

$$N = \frac{i}{\Omega_1\Omega_2}\phi_{\mathrm{E}}\phi_2(t)\frac{k_r k_\theta \hat{\Phi}_{\mathrm{E}}}{B}\Bigg\{\omega_n^* - \left[\frac{\sin\theta(K_2 - nq_0'\theta) - \cos\theta k_\theta}{\Omega_2} + \frac{\sin\theta(K_1 - nq_0'\theta) - \cos\theta k_\theta}{\Omega_1}\right]\frac{2T_i}{eBR}\omega_p^* - \frac{1}{2}\rho_i^2\omega_p^*\left[k_r^2 + k_{\perp 1}^2 + k_{\perp 2}^2\right] + \left[\frac{1}{\Omega_1^2} + \frac{1}{\Omega_1\Omega_2} + \frac{1}{\Omega_2^2}\right]k_\parallel^2 v_{\mathrm{T}}^2\omega_p^*\Bigg\}\hat{\Phi}_2, \tag{C.59}$$

where

$$k_{\perp 1}^2 = \left(K_1 - nq_0'\theta\right)^2 + k_\theta^2, \tag{C.60}$$

$$k_{\perp 2}^2 = \left(K_2 - nq_0'\theta\right)^2 + k_\theta^2. \tag{C.61}$$

We can here see in particular that the EGAM $m = 1$ components $\hat{\Phi}_s$ and $\hat{\Phi}_c$ have been eliminated for ordering reasons. Therefore, ϕ_{E} and $\hat{\Phi}_{\mathrm{E}}$ now play the same role of the EGAM amplitude. We consequently assume that $\hat{\Phi}_{\mathrm{E}} = 1$, and only ϕ_{E} remains to describe the amplitude of the EGAM.

Let us consider the following form for the poloidal shape of the non-linear ITG mode:

$$\hat{\Phi}_2 = \frac{1}{\Delta_2\sqrt{2\pi}}e^{-\frac{(\theta-\theta_2)^2}{2\Delta_2^2}}, \tag{C.62}$$

where Δ_2 is a constant. Then integrating over θ, the non-linear term reads

$$\int_{-\infty}^{\infty} N(\theta)d\theta = \frac{i}{\Omega_1\Omega_2}\phi_{\mathrm{E}}\phi_2(t)\frac{k_r k_\theta}{B}\Bigg\{\omega_n^* + \left[\frac{\cos\theta_2 e^{-\frac{\Delta_2^2}{2}}}{\Omega_2}\left(s_0\Delta_2^2 + 1\right) + \frac{e^{-\frac{\Delta_2^2}{2}}}{\Omega_1}\left(s_0\cos\theta_2\Delta_2^2 - s_0(\theta_1 - \theta_2)\sin\theta_2 + \cos\theta_2\right)\right]\omega_{gf}\omega_p^* - \frac{1}{2}\rho_i^2\omega_p^* k_r^2 - k^2\omega_p^*\left[s_0^2\Delta_2^2 + \frac{1}{2}(\theta_1 - \theta_2)^2 s_0^2 + 1\right]\Bigg\}. \tag{C.63}$$

C.4 Dispersion relation

Since $k_r + K_2 = K_1$, k_r can be recast as $k_r = k_\theta s_0(\theta_1 - \theta_2)$.

The dispersion relation therefore reads

$$\frac{e}{T_i}\left[\frac{\Omega_1 + \omega_n^*}{\omega_p^*} + \left(\frac{\omega_{gf}}{\Omega_1}\cos\theta_1 e^{-\frac{\Delta_1^2}{2}} - k^2\right)\left(1 + s_0\Delta_1^2\right)\right]\phi_1(t) = \frac{i}{\Omega_2}\phi_{\mathrm{E}}\phi_2(t)\frac{s_0(\theta_1 - \theta_2)k_\theta^2}{B}\Bigg\{\frac{\omega_n^*}{\omega_p^*}$$

$$+\left[\frac{\cos\theta_2}{\Omega_2}\big(s_0\Delta_2^2+1\big)+\frac{1}{\Omega_1}\big(s_0\cos\theta_2\Delta_2^2-s_0(\theta_1-\theta_2)\sin\theta_2+\cos\theta_2\big)\right]\omega_{gf}e^{-\frac{\Delta_2^2}{2}}$$
$$-k^2\big[s_0^2\Delta_2^2+(\theta_1-\theta_2)^2s_0^2+1\big]\Bigg\}. \tag{C.64}$$

A similar dispersion relation can be written in the case where the first ITG mode enters the non-linear term of the equation, while the second ITG mode enters the linear part of the equation:

$$\frac{e}{T_i}\left[\frac{\Omega_2+\omega_n^*}{\omega_p^*}+\left(\frac{\omega_{gf}}{\Omega_2}\cos\theta_2e^{-\frac{\Delta_2^2}{2}}-k^2\right)\big(1+s_0\Delta_2^2\big)\right]\phi_2(t)=-\frac{i}{\Omega_1}\phi_{\mathrm{E}}\phi_1(t)\frac{s_0(\theta_1-\theta_2)k_\theta^2}{B}\Bigg\{\frac{\omega_n^*}{\omega_p^*}$$
$$+\left[\frac{\cos\theta_1}{\Omega_1}\big(s_0\Delta_1^2+1\big)+\frac{1}{\Omega_2}\big(s_0\cos\theta_1\Delta_1^2+s_0(\theta_1-\theta_2)\sin\theta_1+\cos\theta_1\big)\right]\omega_{gf}e^{-\frac{\Delta_1^2}{2}}$$
$$-k^2\big[s_0^2\Delta_1^2+(\theta_1-\theta_2)^2s_0^2+1\big]\Bigg\}. \tag{C.65}$$

According to (2.11), Δ_1^2 and Δ_2^2 vary like $1/q$. Therefore, assuming q is large, Δ_1^2 and Δ_2^2 can be neglected. The two dispersion relations then read

$$\frac{e}{T_i}\phi_1(t)L_1(\Omega_1,K_1)=\frac{i}{\Omega_2}\Gamma_1(\Omega_1,\Omega_2,K_1,K_2)\frac{s_0(\theta_1-\theta_2)k_\theta^2}{B}\phi_{\mathrm{E}}\phi_2(t), \tag{C.66}$$
$$\frac{e}{T_i}\phi_2(t)L_2(\Omega_2,K_2)=-\frac{i}{\Omega_1}\Gamma_2(\Omega_1,\Omega_2,K_1,K_2)\frac{s_0(\theta_1-\theta_2)k_\theta^2}{B}\phi_{\mathrm{E}}\phi_1(t), \tag{C.67}$$

where the linear parts are

$$L_1(\Omega_1,K_1)=\frac{\Omega_1+\omega_n^*}{\omega_p^*}+\frac{\omega_{gf}}{\Omega_1}\cos\theta_1-k^2, \tag{C.68}$$
$$L_2(\Omega_2,K_2)=\frac{\Omega_2+\omega_n^*}{\omega_p^*}+\frac{\omega_{gf}}{\Omega_2}\cos\theta_2-k^2; \tag{C.69}$$

and the non-linear parts are

$$\Gamma_1(\Omega_1,\Omega_2,K_1,K_2)=\frac{\omega_n^*}{\omega_p^*}$$
$$+\left[\frac{\cos\theta_2}{\Omega_1}+\frac{-s_0(\theta_1-\theta_2)\sin\theta_2+\cos\theta_2}{\Omega_2}\right]\omega_{gf}-k^2\big[1+(\theta_1-\theta_2)^2s_0^2\big], \tag{C.70}$$
$$\Gamma_2(\Omega_1,\Omega_2,K_1,K_2)=\frac{\omega_n^*}{\omega_p^*}$$
$$+\left[\frac{\cos\theta_1}{\Omega_1}+\frac{s_0(\theta_1-\theta_2)\sin\theta_1+\cos\theta_1}{\Omega_2}\right]\omega_{gf}-k^2\big[1+(\theta_1-\theta_2)^2s_0^2\big]. \tag{C.71}$$

Let us call respectively $\Omega_{\mathrm{L}1}$ and $\Omega_{\mathrm{L}2}$ the complex linear frequencies (*i.e.* the complex frequencies solutions of the linear dispersion relations) of ITG modes 1 and 2. $\Omega_{\mathrm{L}1}$ is therefore a root of expression (C.68), while $\Omega_{\mathrm{L}2}$ is a root of expression (C.69). Let us call γ_1 the imaginary part of $\Omega_{\mathrm{L}1}$ and γ_2 the imaginary part of $\Omega_{\mathrm{L}2}$. The complex linear frequencies therefore read

$$\Omega_{\mathrm{L}1} = \omega_1 + i\gamma_1, \tag{C.72}$$

$$\Omega_{\mathrm{L}2} = \omega_2 + i\gamma_2. \tag{C.73}$$

We expand L_1 and L_2 around the linear frequencies:

$$L_1(\Omega_1, K_1) = L_1(\Omega_{\mathrm{L}1}, K_1) + \frac{\partial L_1}{\partial \Omega_1} \cdot (\Omega_1 - \Omega_{\mathrm{L}1}), \tag{C.74}$$

$$L_2(\Omega_2, K_2) = L_2(\Omega_{\mathrm{L}2}, K_2) + \frac{\partial L_2}{\partial \Omega_2} \cdot (\Omega_2 - \Omega_{\mathrm{L}2}), \tag{C.75}$$

where $L_1(\Omega_{\mathrm{L}1}, K_1) = 0$ and $L_2(\Omega_{\mathrm{L}2}, K_2) = 0$.

Let us recall the definition of Ω_1 and Ω_2:

$$i\Omega_1 = i\omega_1 - \partial_t, \tag{C.76}$$

$$i\Omega_2 = i\omega_2 - \partial_t. \tag{C.77}$$

The dispersion relations read

$$\frac{e}{T_i}\left[\frac{1}{\omega_p^*} - \frac{\omega_{gf}}{\Omega_{\mathrm{L}1}^2}\cos\theta_1\right](\partial_t - \gamma_1)\phi_1(t) = \Gamma_1(\Omega_{\mathrm{L}1}, \Omega_{\mathrm{L}2}, K_1, K_2)\frac{s_0(\theta_1 - \theta_2)k_\theta^2}{B\Omega_{\mathrm{L}2}}\phi_{\mathrm{E}}\phi_2(t), \tag{C.78}$$

$$\frac{e}{T_i}\left[\frac{1}{\omega_p^*} - \frac{\omega_{gf}}{\Omega_{\mathrm{L}2}^2}\cos\theta_2\right](\partial_t - \gamma_2)\phi_2(t) = -\Gamma_2(\Omega_{\mathrm{L}1}, \Omega_{\mathrm{L}2}, K_1, K_2)\frac{s_0(\theta_1 - \theta_2)k_\theta^2}{B\Omega_{\mathrm{L}1}}\phi_{\mathrm{E}}\phi_1(t). \tag{C.79}$$

We consider marginally stable ITG modes, *i.e.* $\gamma_1 = \gamma_2 = 0$. The dispersion relations thus have the following shape:

$$\partial_t\phi_1(t) = \Lambda_1\phi_{\mathrm{E}}\phi_2(t), \tag{C.80}$$

$$\partial_t\phi_2(t) = \Lambda_2\phi_{\mathrm{E}}\phi_1(t), \tag{C.81}$$

where

$$\Lambda_1(\omega_1,\omega_2,K_1,K_2)=\frac{T_i}{e}\frac{s_0(\theta_1-\theta_2)k_\theta^2\Gamma_1(\omega_1,\omega_2,K_1,K_2)}{\omega_2 B\left[\frac{1}{\omega_p^*}-\frac{\omega_{gf}}{\omega_1^2}\cos\theta_1\right]}, \tag{C.82}$$

$$\Lambda_2(\omega_1,\omega_2,K_1,K_2)=-\frac{T_i}{e}\frac{s_0(\theta_1-\theta_2)k_\theta^2\Gamma_2(\omega_1,\omega_2,K_1,K_2)}{\omega_1 B\left[\frac{1}{\omega_p^*}-\frac{\omega_{gf}}{\omega_2^2}\cos\theta_2\right]}. \tag{C.83}$$

Differentiating equation (C.80) according to t assuming that Λ_1 is time independent, and then using equation (C.81) to substitute $\partial_t\phi_2$, one gets

$$\partial_{tt}\phi_1(t)=\Lambda_1\Lambda_2\phi_{\mathrm{E}}^2\phi_1(t). \tag{C.84}$$

Similarly, differentiating equation (C.81) according to t assuming that Λ_2 is time independent, and then using equation (C.80) to substitute $\partial_t\phi_1$, one gets

$$\partial_{tt}\phi_2(t)=\Lambda_1\Lambda_2\phi_{\mathrm{E}}^2\phi_2(t). \tag{C.85}$$

Defining $\gamma^2=\Lambda_1\Lambda_2\phi_{\mathrm{E}}^2$, we can see that ϕ_1 and ϕ_2 have the same exponential evolution $e^{\pm\gamma t}$.

We now need to check under which conditions $\gamma^2=\Lambda_1\Lambda_2\phi_{\mathrm{E}}^2$ can be positive, a situation which corresponds to non-linearly unstable modes.

C.5 Sign of γ^2

The sign of γ^2 is the same as the sign of

$$D=-\frac{\Gamma_1(\omega_1,\omega_2,K_1,K_2)\Gamma_2(\omega_1,\omega_2,K_1,K_2)}{\omega_1\omega_2\left[\frac{1}{\omega_p^*}-\frac{\omega_{gf}}{\omega_1^2}\cos\theta_1\right]\left[\frac{1}{\omega_p^*}-\frac{\omega_{gf}}{\omega_2^2}\cos\theta_2\right]}. \tag{C.86}$$

Let us define the following normalized frequencies:

$$\bar{\Omega}_n=\frac{\omega_n^*}{\omega_p^*}, \tag{C.87}$$

$$\bar{\Omega}_g=\frac{\omega_{gf}}{\omega_p^*}, \tag{C.88}$$

$$\bar{\Omega}_1=\frac{\omega_1}{\omega_p^*}, \tag{C.89}$$

$$\bar{\Omega}_2=\frac{\omega_2}{\omega_p^*}. \tag{C.90}$$

ω_1 and ω_2 are solutions of the linear dispersion relations (C.68) and (C.69), therefore

$\bar{\Omega}_1$ and $\bar{\Omega}_2$ read

$$\bar{\Omega}_1 = \frac{k^2 - \bar{\Omega}_n}{2} + \varepsilon_1 \frac{\sqrt{\left(k^2 - \bar{\Omega}_n\right)^2 - 4\bar{\Omega}_g \cos\theta_1}}{2}, \tag{C.91}$$

$$\bar{\Omega}_2 = \frac{k^2 - \bar{\Omega}_n}{2} + \varepsilon_2 \frac{\sqrt{\left(k^2 - \bar{\Omega}_n\right)^2 - 4\bar{\Omega}_g \cos\theta_2}}{2}, \tag{C.92}$$

where $\varepsilon_1, \varepsilon_2 = \pm 1$.

With the normalized frequencies, the expression we are searching the sign of reads

$$\begin{aligned} D = -\varepsilon_1\varepsilon_2 & \frac{\frac{\bar{\Omega}_g}{\bar{\Omega}_2} s_0(\theta_1 - \theta_2)\sin\theta_1 - \bar{\Omega}_1 + \frac{\bar{\Omega}_g}{\bar{\Omega}_2}\cos\theta_1 - k^2 s_0^2(\theta_1 - \theta_2)^2}{\sqrt{\left(k^2 - \bar{\Omega}_n\right)^2 - 4\bar{\Omega}_g \cos\theta_1}} \\ & \times \frac{-\frac{\bar{\Omega}_g}{\bar{\Omega}_1} s_0(\theta_1 - \theta_2)\sin\theta_2 - \bar{\Omega}_2 + \frac{\bar{\Omega}_g}{\bar{\Omega}_1}\cos\theta_2 - k^2 s_0^2(\theta_1 - \theta_2)^2}{\sqrt{\left(k^2 - \bar{\Omega}_n\right)^2 - 4\bar{\Omega}_g \cos\theta_2}}. \end{aligned} \tag{C.93}$$

Notations

Latin letters

a minor radius of the plasma on the equatorial plane

a, b letters used to designate undetermined ions species

$\bar{a} = a\sqrt{\kappa_a}$ average minor radius of the plasma

$\mathbf{A}$ equilibrium magnetic vector potential

A non linear term before integration in velocity, defined in Appendix C (three wave parametric interaction model)

A_1 term of the GAM and EGAM dispersion relations, defined in Sections 4.1.2 and 4.1.3

A_2 term of the EGAM dispersion relation, defined in Section 4.1.3

$\mathbf{b}$ unitary vector oriented along the equilibrium magnetic field

$\mathbf{B}$ equilibrium magnetic field

$\tilde{\mathbf{B}}$ perturbed magnetic field

B norm of the equilibrium magnetic field

B_0 norm of the equilibrium magnetic field on the magnetic axis

$B_{\max} = \frac{B_0}{1-\varepsilon}$ maximum value of the magnetic field on a given flux surface

B_{P} norm of the poloidal magnetic field

$c.c.$ complex conjugate

$c_{\mathrm{E}} = \int_0^{+\infty} E_k^{3/2} f_{\mathrm{E}}(E_k) dE_k$ (sawteeth stabilization modelling)

$c_{r\theta} = \int_{\rho_{\min}}^{1} \int_{-\theta_t}^{\theta_t} \frac{\rho^{\alpha+1} e^{-(\rho/\rho_k)^2}}{\sqrt{1-\Lambda_0+\Lambda_0 \varepsilon \cos\theta}} \, d\theta d\rho$ (sawteeth stabilization modelling)

C parameter in the Gaussian form assumed for the ITG poloidal shape

C constant of the order of 1-10 (three wave parametric interaction model)

C, C' arbitrary constants (relation GAM/EGAM)

$C(f)$ collision operator in the Fokker-Planck equation

$d = \frac{1}{nq_0'}$ distance between two resonance surfaces in ballooning representation

D deuterium

D EGAM dispersion relation (relation GAM/EGAM)

D expression defined in Section 5.3.2 which has the same sign as γ^2 (three wave parametric interaction model)

D_1 term of the GAM and EGAM dispersion relations, defined in Sections 4.1.2 and 4.1.3

D_2 term of the EGAM dispersion relation, defined in Section 4.1.3

div divergence

$e = 1.6 \cdot 10^{-19}$ C elementary Coulomb charge

e_i ion charge

e_s charge of ions of species s (relation GAM/EGAM, s stands either for t - thermal or k - kinetic)

$\mathbf{e}_r$ unit vector in the radial direction

$\mathbf{e}_\theta$ unit vector in the poloidal direction, in the case of circular flux surfaces

$\mathbf{e}_\varphi$ unit vector in the toroidal direction

$\tilde{\mathbf{E}}$ perturbed electric field

$E = \frac{1}{2}mv_\parallel^2 + \mu B$ kinetic energy

$E_\alpha = 3.5$ MeV energy that an alpha particle takes away from a D-T reaction

$E_s = \frac{1}{2}m_s v_\parallel^2 + \mu_s B$ kinetic energy of ions of species s (s stands either for t - thermal or k - kinetic)

$f(\mathbf{x}, \mathbf{v}, t)$ generic kinetic distribution function

f_E distribution of the fast particles in kinetic energy (sawteeth stabilization modelling)

$f_\mathrm{G} = f_t + f_k$ total ion gyro-centre distribution function (relation GAM/EGAM)

$f_\mathrm{G} = f_{\mathrm{G,eq}} + \tilde{f}_\mathrm{G}$ ion gyro-centre distribution function (linear ITG derivation, three wave parametric interaction model)

$f_{\mathrm{G,eq}}$ equilibrium ion gyro-centre distribution function (linear ITG derivation, three wave parametric interaction model)

$\tilde{f}^{\mathrm{ad}} = -\boldsymbol{\xi}_\perp \cdot \boldsymbol{\nabla} f_{\mathrm{eq}}$ adiabatic part of the perturbed ion distribution function, in the convention of [Coppi 1990] (sawteeth stabilization modelling)

$\tilde{f}_\mathrm{G}$ perturbed ion gyro-centre distribution function (linear ITG derivation, three wave

parametric interaction model)

$\tilde{f}_{\mathrm{GE}}$ EGAM part of the perturbed ion gyro-centre distribution function (three wave parametric interaction model)

$\tilde{f}_{\mathrm{G1,2}}$ ITG 1, 2 part of the perturbed ion gyro-centre distribution function (three wave parametric interaction model)

$f_{1,2}$ amplitude of the ITG 1, 2 perturbed ion gyro-centre distribution function (three wave parametric interaction model)

f_ρ radial distribution of the fast particles (sawteeth stabilization modelling)

$f_s = F_s\left(1 + \tilde{f}_s\right)$ ion gyro-centre distribution function of species s (relation GAM/EGAM, s stands either for t - thermal or k - kinetic)

$\tilde{f}_s$ perturbed ion gyro-centre distribution function of species s (relation GAM/EGAM, s stands either for t - thermal or k - kinetic)

f_{sm}^c cosine Fourier component of order m of $\tilde{f}_s$

f_{sm}^s sine Fourier component of order m of $\tilde{f}_s$

F_s equilibrium ion gyro-centre distribution function of species s (relation GAM/EGAM, s stands either for t - thermal or k - kinetic)

$F_{k,\mathrm{ICRH}} = \lambda f_\Lambda(\Lambda) f_{\mathrm{E}}(E) f_r(r)$ distribution function of the ICRH-accelerated fast particles (sawteeth stabilization modelling)

$\hat{F}_{1,2}$ poloidal envelope of the ion gyro-centre distribution function for ITG 1, 2 (three wave parametric interaction model)

$\mathbf{F}$ generic tensor of order 1, *i.e.* a vector (Section 1.4 about conventions)

F_x, F_y, F_z Cartesian coordinates of generic tensor $\mathbf{F}$ (Section 1.4 about conventions)

$\mathbf{h}$ generic small displacement (Section 1.4 about conventions)

$H = \frac{1}{2} m_i v_\parallel^2 + \mu B + e_i \phi$ ion energy

H Heaviside function

H hydrogen

He3 helium 3

$I_1, I_2, I_3, I_4, I_5, I_6$ integrals defined in Appendix B.2 (relation GAM/EGAM)

$I_b = \frac{v \tau_b}{Rq}$ (sawteeth stabilization modelling)

$I_c = \langle \cos\theta \rangle_b$ (sawteeth stabilization modelling)

$I_d = \langle \cos\theta \rangle_b + s\langle \theta \sin\theta \rangle_b$ (sawteeth stabilization modelling)

$I_q = \langle \cos(q\theta) \rangle_b$ (sawteeth stabilization modelling)

$I(\Lambda_0) = \Lambda_0 I_b \frac{I_c I_d - I_q^2}{I_d}$ (sawteeth stabilization modelling)

$I(\psi) = \frac{qR^2}{\mathcal{J}}$ toroidal covariant component of the magnetic field

$J = 2\int_{-\theta_t}^{\theta_t} m_i v_\parallel dl$ longitudinal invariant

$\mathbf{J}$ equilibrium current density

$\tilde{\mathbf{J}}$ perturbed current density

$\tilde{\mathbf{J}}_\mathbf{k}$ perturbed fast particle current density

$\mathcal{J} = (\boldsymbol{\nabla}\psi \times \boldsymbol{\nabla}\theta \cdot \boldsymbol{\nabla}\phi)^{-1}$ Jacobian of the Cartesian coordinates with respect to the (ψ, θ, φ) coordinates

$\mathbf{k}_\mathrm{E}$ EGAM wave vector (three wave parametric interaction model)

$\mathbf{k}_{1,2}$ ITG 1, 2 wave vector (three wave parametric interaction model)

$k = k_\theta \rho_i$ normalized poloidal wave vector

k_r GAM/EGAM radial wave vector (relation GAM/EGAM, three wave parametric interaction model)

$k_\theta = \frac{nq_0}{r_0}$ poloidal wave vector

$k_\perp$ characteristic perpendicular wave vector of the perturbation

$k_\perp = \sqrt{(K_0 - nq_0'\theta)^2 + k_\theta^2}$ perpendicular wave vector (linear ITG derivation)

$k_{\perp 1,2} = \sqrt{(K_{1,2} - nq_0'\theta)^2 + k_\theta^2}$ perpendicular wave vector of ITG 1, 2 (three wave parametric interaction model)

$k_\parallel = -i\frac{\partial_\theta}{qR}$ parallel wave vector (linear ITG derivation, three wave parametric interaction model)

$K_0 = nq_0'\theta_0$ radial wave number in ballooning representation

$K_{1,2} = nq_0'\theta_{1,2}$ radial wave number of ITG mode 1, 2 (three wave parametric interaction model)

$K(x)$ position-dependent radial wave vector (three wave parametric interaction model)

ℓ mode number in ballooning representation which allows the 2π-periodicity in θ to be respected

$\ln\Lambda$ Coulomb logarithm

$L_{1,2}$ linear dispersion relation for ITG 1, 2 (three wave parametric interaction model)

$L_p = \frac{r}{p}\frac{dp}{dr}$ characteristic pressure gradient length

$L_{\mathrm{T}} = \frac{r}{T}\frac{dT}{dr}$ characteristic temperature gradient length

m poloidal mode number

m mass

$m_e = 9.1 \cdot 10^{-31}$ kg electron mass

m_i ion mass

m_s mass of ions of species s (s stands either for t - thermal or k - kinetic)

n neutron

n toroidal mode number

n density

n_e equilibrium electron density

$\tilde{n}_e$ perturbed electron density

n_i equilibrium ion density

$\hat{n}_i$ peak equilibrium ion density

n_s equilibrium ion density of species s (relation GAM/EGAM, s stands either for t - thermal or k - kinetic)

$\tilde{n}_s$ perturbed ion density of species s (relation GAM/EGAM, s stands either for t - thermal or k - kinetic)

$n_{s1}^c = \int F_s f_{s1}^c (dv)^3 / n_s$ cosine Fourier component of order 1 of the perturbed density of species s normalized to the equilibrium density (relation GAM/EGAM)

n_a, n_b density of ions of species a, b

N fusion reaction rate per time unit and per volume unit

N non linear term integrated in velocity, defined in Appendix C (three wave parametric interaction model)

N_1 term of the GAM and EGAM dispersion relations, defined in Sections 4.1.2 and 4.1.3

N_2 term of the EGAM dispersion relation, defined in Section 4.1.3

p scalar pressure

$p_i = n_i T_i$ ion equilibrium scalar pressure

$p_{\max}$ maximum value of p_i that can be withstood by a given tokamak

$\tilde{p}$ perturbed scalar pressure

$\mathbf{P}$ pressure tensor (tensor of order 2)

$P_{\text{fus}\to\text{pla}}$ power of fusion reactions transferred to the plasma

P_{loss} power of losses on the edge of the plasma (by radiation, conduction or convection)

$P_\varphi = m_i R v_\varphi - e_i \psi$ canonical momentum

$q = \frac{\mathbf{B}\cdot\boldsymbol{\nabla}\varphi}{\mathbf{B}\cdot\boldsymbol{\nabla}\theta}$ safety factor

$q_0 = q(r_0)$ value of the safety factor at the position of the reference resonance surface in ballooning representation

$q_0' = q'(r_0)$ derivative of the safety factor with respect to the minor radius coordinate, at the position of the reference resonance surface in ballooning representation

$\mathbf{Q}$ heat flux (tensor of order 1)

r minor radius coordinate

r_0 minor radius of the reference resonance surface in ballooning representation

r_1 minor radius of the $q = 1$ surface, on the equatorial plane (sawteeth stabilization modelling)

$\bar{r}_1 = r_1\sqrt{\kappa_1}$ average minor radius of the $q = 1$ surface (sawteeth stabilization modelling)

r_m minor radius of a given resonance surface in ballooning representation, defined by the relation $q(r_m) = \frac{m}{n}$

rot curl

R major radius coordinate

R_0 major radius of the magnetic axis

$s = \frac{rq'(r)}{q}$ magnetic shear

$s_0 = \frac{r_0 q_0'}{q_0}$ magnetic shear on the reference resonance surface in ballooning representation

$s_1 = \bar{r}_1 q'(\bar{r}_1)$ magnetic shear on the $q = 1$ surface

S source in the Fokker-Planck equation

t time

t_i time at which an ITG 2 burst occurs (three wave parametric interaction model)

T tritium

T_e electron temperature

T_i ion temperature

$\hat{T}_i$ peak ion temperature

T_t thermal ion temperature

$u_\parallel$ parallel fluid velocity

$\bar{u}_\parallel = \sqrt{\frac{m_k}{2T_t}}\bar{v}_\parallel$ normalized mean parallel velocity of the fast particles (relation GAM/EGAM)

$\mathbf{u}$ fluid velocity

U bounded domain defined in Section 4.3.1 (relation GAM/EGAM)

$\mathbf{v}$ particle velocity

v norm of the particle velocity

$v_\mathrm{A} = \frac{B_0}{\sqrt{\mu_0 n_i m_i}}$ Alfvén velocity

$v_{d,s} = \mathbf{v}_\mathrm{E} + \mathbf{v}_{g,s}$ drift velocity of ions of species s (s stands either for t - thermal or k - kinetic)

$\mathbf{v}_\mathrm{E} = \frac{\mathbf{E}\times\mathbf{b}}{B}$ $\mathbf{E}\times\mathbf{B}$ drift velocity

$\mathbf{v}_g = \left(\frac{m_i v_\parallel^2}{e_i B}\frac{\mathbf{b}\times\boldsymbol{\nabla}B}{B} + \frac{m_i v_\parallel^2}{e_i B}\frac{\mathbf{rot}\ \mathbf{B}}{B}\Big|_\perp\right) + \frac{\mu B}{e_i B}\frac{\mathbf{b}\times\boldsymbol{\nabla}B}{B}$ magnetic drift velocity; the **rot B** term can be neglected when β is low

$\mathbf{v}_{g,s} = \frac{m_s v_\parallel^2}{e_s B}\frac{\mathbf{b}\times\boldsymbol{\nabla}B}{B} + \frac{\mu_s B}{e_s B}\frac{\mathbf{b}\times\boldsymbol{\nabla}B}{B}$ magnetic drift velocity of ions of species s at low β (s stands either for t - thermal or k - kinetic)

$v_g = \frac{m v_\parallel^2 + \mu B}{eRB}$ norm of the magnetic drift velocity

v_{g1} normalized group velocity of ITG 1 (three wave parametric interaction model)

$v_{g,s} = \frac{m_s v_\parallel^2 + \mu_s B}{e_s RB}$ norm of the magnetic drift velocity of ions of species s at low β (s stands either for t - thermal or k - kinetic)

$v_\mathrm{T} = \sqrt{\frac{T_i}{m_i}}$ ion thermal velocity

$v_\parallel = \mathbf{v}\cdot\mathbf{b}$ parallel velocity

$\bar{v}_\parallel$ mean parallel velocity of the fast particles (relation GAM/EGAM)

$v_\perp = \mathbf{v} - v_\parallel\mathbf{b}$ perpendicular velocity

V volume of the plasma

W total internal energy of the plasma

$W_{k,\mathrm{ICRH}}$ total energy of the ICRH-accelerated fast particles (integrated over space and velocity; sawteeth stabilization modelling)

$\mathbf{x}$ position in space

x, y, z Cartesian coordinates

$x = r - r_0$ distance to the reference resonance surface in ballooning representation

$\bar{x} = \frac{r-r_0}{d}$ normalized distance to the reference resonance surface in ballooning representation

$X = \frac{x}{\rho_i}$ normalized radial coordinate (three wave parametric interaction model)

X_2 radial position marking the separation between the region in which the ITG is linearly unstable and the region in which the ITG is linearly stable (three wave parametric interaction model)

$y = \theta - \theta_0$ poloidal coordinate counted from the ballooning angle in ballooning representation (linear ITG derivation)

y_0 parameter in the Gaussian form assumed for the ITG poloidal shape (linear ITG derivation)

y_1 parameter in the Gaussian form assumed for the ITG 1 poloidal shape (three wave parametric interaction model)

$Z_i = \frac{e_i}{e}$ ion charge number

Z_t thermal ion charge number

Z_k kinetic ion charge number

$\mathcal{Z}(z) = \frac{1}{\sqrt{\pi}} \int_{-\infty}^{+\infty} \frac{e^{-t^2}}{t-z} dt$ Fried and Conte plasma dispersion function, where $z \in \mathbf{C}$

Greek letters

α constant used in the expression of the Scrape-Off Layer (SOL) width as a function of the magnetic field B

α constant used in the expression of the radial fast particle distribution function to ensure the maximum is reached on the ICRH resonance layer (sawteeth stabilization modelling)

α coefficient in the ITG equation (see Appendix A.3, linear ITG derivation)

$\beta = \beta_e + \beta_i$ ratio of the total kinetic pressure to the magnetic pressure

β_0 value of β on the magnetic axis

$\beta_e = \frac{n_e T_e}{\frac{B^2}{2\mu_0}}$ ratio of the electron kinetic pressure to the magnetic pressure

$\beta_i = \frac{n_i T_i}{\frac{B^2}{2\mu_0}}$ ratio of the ion kinetic pressure to the magnetic pressure

β_k ratio of the fast ion kinetic pressure to the magnetic pressure

γ generic mode growth rate (introduction)

γ internal kink mode growth rate (sawteeth stabilization modelling)

γ same non linear growth rate of ITG modes 1 and 2 (three wave parametric interaction model)

$\gamma_{1,2}$ linear growth rate of ITG mode 1, 2 (three wave parametric interaction model)

$\Gamma_{1,2}$ non-linear coefficient in the dispersion relation where the linear part corresponds to ITG 1, 2 (three wave parametric interaction model)

δ small parameter in the gyrokinetic ordering, verifying $\rho_* \ll \delta \ll 1$

$\delta_b \sim \frac{q\rho_i}{\sqrt{\varepsilon}}$ radial deviation from the reference flux surface, case of trapped particles

$\delta_p \sim q\rho_i$ radial deviation from the reference flux surface, case of passing particles

δT_e electron temperature perturbation, cold front (sawteeth stabilization modelling)

$\delta\hat{W} = \delta\hat{W}_{\text{MHD}} + \delta\hat{W}_{\text{kin}}$ total potential energy functional (sawteeth stabilization modelling)

$\delta\hat{W}_{\text{ICRH}}$ ICRH contribution to the potential energy functional (sawteeth stabilization modelling)

$\delta\hat{W}_{\text{kin}} = \delta\hat{W}_{\text{NBI}} + \delta\hat{W}_{\text{ICRH}}$ kinetic contribution to the potential energy functional (sawteeth stabilization modelling)

$\delta\hat{W}_{\text{MHD}}$ MHD contribution to the potential energy functional (sawteeth stabilization modelling)

$\delta\hat{W}_{\text{NBI}}$ NBI contribution to the potential energy functional (sawteeth stabilization modelling)

Δ parameter in the Gaussian form assumed for the ITG poloidal shape (linear ITG derivation)

$\Delta_{1,2}$ parameter in the Gaussian form assumed for the ITG 1, 2 poloidal shape (three wave parametric interaction model)

Δ_{X} characteristic radial extension of ITG 2 (three wave parametric interaction model)

Δ_τ characteristic time extension of ITG 2 (three wave parametric interaction model)

Δ_{τ_i} lapse of time between two ITG 2 bursts (three wave parametric interaction model)

$\Delta(r)$ Shafranov shift

$\varepsilon = \frac{r}{R_0}$ inverse aspect ratio

$\varepsilon_1 = \frac{r_1}{R_0}$ inverse aspect ratio at $q = 1$ surface

$\varepsilon_{1,2} = \pm 1$ coefficient meaning plus or minus for ITG 1, 2 (three wave parametric interaction model)

ζ parameter used to ensure consistency of the Gaussian solution with the ITG linear equation for $s_0 \gg 1$ (three wave parametric interaction model)

$\bar{\zeta}$ parameter used in [Zarzoso 2012b], comparable to $\bar{u}_{\|}$ in the present manuscript

η ratio of the number of trapped ions to the total number of ions (introduction)

$\eta = \mathrm{Im}\left(\frac{1}{2\Delta_1^2}\right)$ imaginary part of $1/2\Delta_1^2$ (three wave parametric interaction model)

θ flux coordinate poloidal angle, counted from the low field side equatorial plane

θ_0 ballooning angle (linear ITG derivation)

$\theta_{1,2}$ ballooning angle for ITG mode 1, 2 (three wave parametric interaction model)

$\theta_t > 0$ poloidal angle of banana orbit turning points

ι non-negative integer, order of a given fluid moment

$\iota_1 = \pm 1$ coefficient meaning plus or minus for ITG 1 (three wave parametric interaction model)

$\boldsymbol{\kappa} = \frac{\mathbf{b}\times\boldsymbol{\nabla}B}{B} + \frac{\mathbf{rot}\ \mathbf{B}}{B}\big|_{\perp}$ curvature of the magnetic field

κ_1 ellipticity of the $q = 1$ surface

κ_a ellipticity of the plasma at $r = a$

λ coefficient in the ITG equation (see Appendix A.3, linear ITG derivation)

λ normalisation factor in the fast particle distribution function (sawteeth stabilization modelling)

Λ generic non-linear coupling operator (three wave parametric interaction model)

$\Lambda_{1,2}$ non-linear coefficient in the dispersion relation where the linear part corresponds to ITG 1, 2 (three wave parametric interaction model)

$\bar{\Lambda}_1$ normalized non-linear coefficient in the dispersion relation where the linear part corresponds to ITG 1 (three wave parametric interaction model)

Λ in the expression $\ln\Lambda$, not the pitch coordinate; $\ln\Lambda$ is the Coulomb logarithm

$\Lambda = \frac{\mu_k B_0}{E_k}$ pitch coordinate (sawteeth stabilization modelling)

Λ_0 pitch of the ICRH-accelerated particles

μ coefficient in the ITG equation (see Appendix A.3, linear ITG derivation)

$\mu = \frac{mv_\perp^2}{2B}$ magnetic moment

$\mu_s = \frac{m_s v_\perp^2}{2B}$ magnetic moment of ions of species s (s stands either for t - thermal or k - kinetic)

$\mu_0 = 4\pi \cdot 10^{-7}$ vacuum magnetic permeability

$\boldsymbol{\xi}$ spatial displacement of a fluid element with respect to its equilibrium position (sawteeth stabilization modelling)

ξ_0 characteristic value of the spatial displacement $\boldsymbol{\xi}$ (sawteeth stabilization modelling)

$\rho = \frac{r}{\bar{a}}$ normalized minor radius coordinate

$\rho_a^2 = \frac{n_t}{n_e}\rho_t^2 + \frac{n_k}{n_e}\rho_k^2$ parameter comparable to an average Larmor radius of kinetic and thermal ions (relation GAM/EGAM)

$\rho_i = \frac{\sqrt{m_i T_i}}{eB}$ fluid ion Larmor radius

ρ_k characteristic radial length of the fast particle distribution function (sawteeth stabilization modelling)

ρ_m mass density

$\rho_\mathrm{L} = \frac{v_\perp}{\omega_c}$ kinetic Larmor radius

ρ_min minimum minor radius reachable by fast particles (sawteeth stabilization modelling)

$\rho_s^2 = \frac{m_s T_t}{e^2 B^2}$ parameter comparable to the fluid Larmor radius for ions of species s (relation GAM/EGAM, s stands either for t - thermal or k - kinetic)

$\rho_* = \frac{\rho_i}{a}$ normalized ion Larmor radius

$\sigma(v)$ cross-section of the fusion interaction between two ions having a relative velocity v

$\tau = \omega_c t$ normalized time (three wave parametric interaction model)

τ_0 time separating the lapse of time during which the EGAM is off from the lapse of time during which the EGAM is on (three wave parametric interaction model)

$\tau_\mathrm{A} = \frac{\sqrt{3}R_0}{v_\mathrm{A}}$ Alfvén time (sawteeth stabilization modelling)

τ_E characteristic energy confinement time

$\tau_i = \omega_c t_i$ normalized time at which an ITG 2 burst occurs (three wave parametric interaction model)

τ_k ratio of the fast ion distribution width to the bulk ion temperature (relation GAM/EGAM)

τ_s Spitzer slowing-down time

$\tilde{\phi}$ non-normalized perturbed electric potential

$\tilde{\phi}_{\mathrm{E}}$ EGAM part of the perturbed electric potential (three wave parametric interaction model)

$\tilde{\phi}_{1,2}$ ITG 1, 2 part of the perturbed electric potential (three wave parametric interaction model)

ϕ_{E} normalized amplitude of the EGAM perturbed electric potential (three wave parametric interaction model)

$\phi_{1,2}$ non-normalized amplitude of the ITG 1, 2 perturbed electric potential (three wave parametric interaction model)

ϕ_m^c normalized cosine Fourier component of order m of $\tilde{\phi}$

ϕ_m^s normalized sine Fourier component of order m of $\tilde{\phi}$

Φ_2 radial shape of the *ad-hoc* representation of ϕ_2 (three wave parametric interaction model)

$\hat{\Phi}$ poloidal envelope of the electric potential in ballooning representation

$\hat{\Phi}_0$ characteristic value of the ITG poloidal envelope $\hat{\Phi}$ (linear ITG derivation)

$\hat{\Phi}_{1,2}$ poloidal envelope of the electric potential for ITG 1, 2 (three wave parametric interaction model)

$\hat{\Phi}_{\mathrm{E}}$ $m = 0$ component of the EGAM (three wave parametric interaction model)

$\hat{\Phi}_c$ cosine $m = 1$ component of the EGAM (three wave parametric interaction model)

$\hat{\Phi}_s$ sine $m = 1$ component of the EGAM (three wave parametric interaction model)

$\hat{\phi}$ small scale radial envelope of the electric potential in ballooning representation

φ toroidal angle

ψ poloidal magnetic flux counted from the magnetic axis, normalized to 2π

ω frequency of the studied mode

$\omega_b \sim \frac{v_{\mathrm{T}}}{qR_0}\sqrt{\varepsilon}$ bounce frequency

$\omega_c = \frac{e_i B}{m_i}$ ion cyclotron frequency

$\omega_d \sim \frac{qv_{\mathrm{T}}}{R_0}\frac{\rho_{\mathrm{L}}}{a}$ toroidal precession frequency

ω_{E} EGAM linear real frequency (three wave parametric interaction model)

$\omega_{1,2}$ ITG 1, 2 linear real frequency (three wave parametric interaction model)

$\omega_{gf} = \frac{2k_\theta T_i}{eBR}$ fluid drift frequency (linear ITG derivation, three wave parametric interaction

model)

$\omega_{gk} = v_g[\sin\theta(K_0 - nq_0'\theta) - \cos\theta k_\theta]$ kinetic drift frequency (linear ITG derivation)

$\omega_{g1,2} = v_g[\sin\theta(K_{1,2} - nq_0'\theta) - \cos\theta k_\theta]$ kinetic drift frequency for ITG 1, 2 (three wave parametric interaction model)

$\omega_{g,s} = v_{g,s}k_r$ drift frequency of ions of species s (relation GAM/EGAM, s stands either for t - thermal or k - kinetic)

$\omega_{\mathrm{GAM}} \sim \frac{v_\mathrm{T}}{R}$ GAM frequency

$\omega_{\mathrm{ITG}} \sim k_\theta \rho_i \frac{v_\mathrm{T}}{L_p}$ ITG mode frequency

$\omega_* = -k_\theta \frac{\partial_r \ln f_{\mathrm{G,eq}}}{B} \frac{T_i}{e}$ kinetic diamagnetic frequency (linear ITG derivation, three wave parametric interaction model)

$\omega_n^* = -\frac{k_\theta}{B}\frac{T_i}{e}\frac{n_i'(r)}{n_i}$ density diamagnetic frequency

$\omega_p^* = -\frac{k_\theta}{B}\frac{T_i}{e}\frac{p_i'(r)}{p_i}$ pressure diamagnetic frequency

$\omega_\varphi = \frac{v_\parallel}{R}$ toroidal passing frequency

$\omega_\parallel = v_\parallel k_\parallel = -\frac{v_\parallel}{qR} i\partial_\theta$ transit frequency (linear ITG derivation, three wave parametric interaction model)

$\omega_\parallel = \frac{v_\parallel}{qR}$ transit frequency (introduction, relation GAM/EGAM)

$\Omega_{1,2} = \omega_{1,2} + i\partial_t$ comprehensive ITG 1, 2 frequency (three wave parametric interaction model)

$\Omega_{\mathrm{L}1,2} = \omega_{1,2} + i\gamma_{1,2}$ linear complex frequency of ITG mode 1, 2 (three wave parametric interaction model)

$\bar{\Omega}_{\mathrm{L}1} = \frac{\Omega_{\mathrm{L}1}}{\omega_p^*}$ normalized linear complex frequency of ITG mode 1 (three wave parametric interaction model)

$\bar{\Omega}_{1,2} = \frac{\omega_{1,2}}{\omega_p^*}$ normalized ITG 1, 2 real frequency (three wave parametric interaction model)

$\Omega_\parallel = \frac{v_\mathrm{T}}{qR\omega}$ normalized fluid transit frequency (linear ITG derivation)

$\bar{\Omega}_c = \frac{\omega_c}{\omega_p^*}$ normalized ion cyclotron frequency (three wave parametric interaction model)

$\Omega_g = \frac{\omega_{gf}}{\omega}$ normalized fluid drift frequency (linear ITG derivation)

$\bar{\Omega}_g = \frac{\omega_{gf}}{\omega_p^*}$ normalized fluid drift frequency (three wave parametric interaction model)

$\Omega_k = qR\sqrt{\frac{m_k}{2T_t}}\omega$ GAM/EGAM frequency normalized to the kinetic ion velocity (relation GAM/EGAM)

$\Omega_n^* = \frac{\omega_n^*}{\omega}$ normalized density diamagnetic frequency (linear ITG derivation)

$\bar{\Omega}_n = \frac{\omega_n^*}{\omega_p^*}$ normalized density diamagnetic frequency (three wave parametric interaction model)

$\Omega_p^* = \frac{\omega_p^*}{\omega}$ normalized pressure diamagnetic frequency (linear ITG derivation)

$\Omega_t = qR\sqrt{\frac{m_t}{2T_t}}\omega$ GAM/EGAM frequency normalized to the thermal ion velocity (relation GAM/EGAM)

$\Omega_{t,\mathrm{EGAM}} = qR\sqrt{\frac{m_t}{2T_t}}\omega_{\mathrm{EGAM}}$ normalized EGAM frequency (c)

$\Omega_{t,\mathrm{GAM}} = qR\sqrt{\frac{m_t}{2T_t}}\omega_{\mathrm{GAM}}$ normalized GAM frequency (relation GAM/EGAM)

$\Omega_{k,\mathrm{GAM}} = qR\sqrt{\frac{m_k}{2T_t}}\omega_{\mathrm{GAM}}$ normalized GAM frequency (relation GAM/EGAM)

Other

$\langle\cdot\rangle_b$ average over the bounce motion

$\langle\cdot\rangle_{q<1}$ average over the volume within the $q = 1$ surface

$\langle\cdot\rangle_{FS}$ average over a magnetic flux surface

$\langle\cdot\rangle_t$ average over time

$\langle\cdot\rangle_v$ average over velocity weighted by the relevant distribution function (introduction)

$\langle\cdot\rangle_x$ average over space

$\boldsymbol{\nabla}$ gradient

$\boldsymbol{\nabla}_\perp = \boldsymbol{\nabla} - \mathbf{b}(\mathbf{b}\cdot\boldsymbol{\nabla})$ perpendicular gradient

$\nabla_\parallel = \mathbf{b}\cdot\boldsymbol{\nabla}$ parallel gradient

Bibliography

[Adams 1993] J. M. Adams, O. N. Jarvis, G. J. Sadler, D. B. Syme and N. Watkins. *The JET neutron emission profile monitor.* Nuclear Instruments and Methods in Physics Research Section A: Accelerators, Spectrometers, Detectors and Associated Equipment, vol. 329, pages 277 – 290, 1993. (Cited on page 56.)

[Angelino 2006] P. Angelino, A. Bottino, R. Hatzky, S. Jolliet, O. Sauter, T. M. Tran and L. Villard. *Effects of plasma current on nonlinear interactions of ITG turbulence, zonal flows and geodesic acoustic modes.* Plasma Physics and Controlled Fusion, vol. 48, no. 5, page 557, 2006. (Cited on pages 2, 30, and 40.)

[Angioni 2002] C. Angioni, A. Pochelon, N. N. Gorelenkov, K. G. McClements, O. Sauter, R. V. Budny, P. C. de Vries, D. F. Howell, M. Mantsinen, M. F. F. Nave, S. E. Sharapov and contributors to the EFDA-JET Workprogramme. *Neutral beam stabilization of sawtooth oscillations in JET.* Plasma Physics and Controlled Fusion, vol. 44, no. 2, page 205, 2002. (Cited on pages 29, 33, 49, and 51.)

[Arnichand 2014] H. Arnichand and S. Hacquin, private correspondence, 2014. IRFM, CEA. (Cited on pages 43 and 44.)

[Aydemir 1992] A. Y. Aydemir. *Nonlinear studies of m=1 modes in high-temperature plasmas.* Physics of Fluids B: Plasma Physics (1989-1993), vol. 4, no. 11, pages 3469–3472, 1992. (Cited on page 29.)

[Berk 2006] H. L. Berk, C. J. Boswell, D. Borba, A. C. A. Figueiredo, T. Johnson, M. F. F. Nave, S. D. Pinches, S. E. Sharapov and JET EFDA contributors. *Explanation of the JET n = 0 chirping mode.* Nuclear Fusion, vol. 46, no. 10, page S888, 2006. (Cited on pages 42 and 45.)

[Berk 2010] H. L. Berk and T. Zhou. *Fast excitation of EGAM by NBI.* Nuclear Fusion, vol. 50, no. 3, page 035007, 2010. (Cited on pages 30 and 42.)

[Bernabei 2000] S. Bernabei, M. G. Bell, R. V. Budny, E. D. Fredrickson, N. N. Gorelenkov, J. C. Hosea, R. Majeski, E. Mazzucato, C. K. Phillips, G. Schilling and

J. R. Wilson. *Nature of Monster Sawteeth and Their Relationship to Alfvén Instabilities in Tokamaks.* Phys. Rev. Lett., vol. 84, pages 1212–1215, Feb 2000. (Cited on pages 59 and 64.)

[Bernabei 2001] S. Bernabei, R. V. Budny, E. D. Fredrickson, N. N. Gorelenkov, J. C. Hosea, C. K. Phillips, R. B. White, J. R. Wilson, C. C. Petty, R. I. Pinsker, R. W. Harvey and A. P. Smirnov. *The combined effect of EPMs and TAEs on energetic ion confinement and sawtooth stabilization.* Nuclear Fusion, vol. 41, no. 5, page 513, 2001. (Cited on pages 59 and 64.)

[Biancalani 2014] A. Biancalani, A. Bottino, Ph. Lauber and D. Zarzoso. *Numerical validation of the electromagnetic gyrokinetic code NEMORB on global axisymmetric modes.* Nuclear Fusion, vol. 54, no. 10, page 104004, 2014. (Cited on pages 45, 77, and 78.)

[Biglari 1989] H. Biglari, P. H. Diamond and M. N. Rosenbluth. *Toroidal ion-pressure-gradient-driven drift instabilities and transport revisited.* Physics of Fluids B: Plasma Physics (1989-1993), vol. 1, no. 1, pages 109–118, 1989. (Cited on page 35.)

[Biglari 1990] H. Biglari, P. H. Diamond and P. W. Terry. *Influence of sheared poloidal rotation on edge turbulence.* Physics of Fluids B: Plasma Physics (1989-1993), vol. 2, no. 1, pages 1–4, 1990. (Cited on page 38.)

[Boswell 2006] C. J. Boswell, H. L. Berk, D. N. Borba, T. Johnson, S. D. Pinches and S. E. Sharapov. *Observation and explanation of the JET chirping mode.* Physics Letters A, vol. 358, no. 2, pages 154 – 158, 2006. (Cited on page 42.)

[Bottino 2011] A. Bottino, T. Vernay, B. Scott, S. Brunner, R. Hatzky, S. Jolliet, B. F. McMillan, T. M. Tran and L. Villard. *Global simulations of tokamak microturbulence: finite-β effects and collisions.* Plasma Physics and Controlled Fusion, vol. 53, no. 12, page 124027, 2011. (Cited on pages 45 and 72.)

[Brix 2008] M. Brix, N. C. Hawkes, A. Boboc, V. Drozdov, S. E. Sharapov and JET-EFDA Contributors. *Accuracy of EFIT equilibrium reconstruction with internal diagnostic information at JET.* Review of Scientific Instruments, vol. 79, no. 10, 2008. (Cited on page 49.)

[Brizard 2007] A. J. Brizard and T. S. Hahm. *Foundations of nonlinear gyrokinetic theory.* Rev. Mod. Phys., vol. 79, pages 421–468, Apr 2007. (Cited on pages 19 and 90.)

[Bussac 1975] M. N. Bussac, R. Pellat, D. Edery and J. L. Soule. *Internal Kink Modes in Toroidal Plasmas with Circular Cross Sections.* Phys. Rev. Lett., vol. 35, pages 1638–1641, Dec 1975. (Cited on pages 29 and 30.)

[Buttery 2004] R. J. Buttery, T. C. Hender, D. F. Howell, R. J. La Haye, S. Parris, O. Sauter, C. G. Windsor and JET-EFDA Contributors. *On the form of NTM onset scalings.* Nuclear Fusion, vol. 44, no. 5, page 678, 2004. (Cited on page 32.)

[Chakrabarti 2007] N. Chakrabarti, R. Singh, P. K. Kaw and P. N. Guzdar. *Nonlinear excitation of geodesic acoustic modes by drift waves.* Physics of Plasmas (1994-present), vol. 14, no. 5, 2007. (Cited on page 41.)

[Chapman 2011] I. T. Chapman. *Controlling sawtooth oscillations in tokamak plasmas.* Plasma Physics and Controlled Fusion, vol. 53, no. 1, page 013001, 2011. (Cited on pages 32 and 64.)

[Chen 1984] L. Chen, R. B. White and M. N. Rosenbluth. *Excitation of Internal Kink Modes by Trapped Energetic Beam Ions.* Phys. Rev. Lett., vol. 52, pages 1122–1125, Mar 1984. (Cited on page 34.)

[Chen 2000] L. Chen, Z. Lin and R. White. *Excitation of zonal flow by drift waves in toroidal plasmas.* Physics of Plasmas (1994-present), vol. 7, no. 8, pages 3129–3132, 2000. (Cited on page 39.)

[Connor 1978] J. W. Connor, R. J. Hastie and J. B. Taylor. *Shear, Periodicity, and Plasma Ballooning Modes.* Phys. Rev. Lett., vol. 40, pages 396–399, Feb 1978. (Cited on page 35.)

[Connor 1979] J. W. Connor, R. J. Hastie and J. B. Taylor. *High Mode Number Stability of an Axisymmetric Toroidal Plasma.* Proceedings of the Royal Society of London A: Mathematical, Physical and Engineering Sciences, vol. 365, no. 1720, pages 1–17, 1979. (Cited on page 35.)

[Conway 2011] G. D. Conway, C. Angioni, F. Ryter, P. Sauter and J. Vicente. *Mean and Oscillating Plasma Flows and Turbulence Interactions across the L-H Confinement Transition.* Phys. Rev. Lett., vol. 106, page 065001, Feb 2011. (Cited on pages 2, 30, 40, 83, 103, and 106.)

[Coppi 1988] B. Coppi, R.J. Hastie, S. Migliuolo, F. Pegoraro and F. Porcelli. *Suppression of internal plasma oscillations by trapped high energy nuclei.* Physics Letters A, vol. 132, no. 5, pages 267 – 272, 1988. (Cited on pages 1 and 33.)

[Coppi 1989] B. Coppi, P. Detragiache, S. Migliuolo, F. Pegoraro and F. Porcelli. *Quiescent window for global plasma modes.* Phys. Rev. Lett., vol. 63, pages 2733–2736, Dec 1989. (Cited on pages 1 and 33.)

[Coppi 1990] B. Coppi, S. Migliuolo, F. Pegoraro and F. Porcelli. *Global modes and high-energy particles in ignited plasmas.* Physics of Fluids B, vol. 2, no. 5, pages 927–943, 1990. (Cited on pages 34 and 142.)

[Diamond 2001] P. H. Diamond, S. Champeaux, M. Malkov, A. Das, I. Gruzinov, M. N. Rosenbluth, C. Holland, B. Wecht, A. I. Smolyakov, F. L. Hinton, Z. Lin and T. S. Hahm. *Secondary instability in drift wave turbulence as a mechanism for zonal flow and avalanche formation.* Nuclear Fusion, vol. 41, no. 8, page 1067, 2001. (Cited on page 39.)

[Diamond 2005] P. H. Diamond, S.-I. Itoh, K. Itoh and T. S. Hahm. *Zonal flows in plasma - a review.* Plasma Physics and Controlled Fusion, vol. 47, no. 5, page R35, 2005. (Cited on page 39.)

[Drake 1988] J. F. Drake, P. N. Guzdar and A. B. Hassam. *Streamer Formation in Plasma with a Temperature Gradient.* Phys. Rev. Lett., vol. 61, pages 2205–2208, Nov 1988. (Cited on page 35.)

[Edery 1992] D. Edery, X. Garbet, J.-P. Roubin and A. Samain. *Variational formalism for kinetic-MHD instabilities in tokamaks.* Plasma Physics and Controlled Fusion, vol. 34, no. 6, page 1089, 1992. (Cited on page 29.)

[Eich 2011] T. Eich, B. Sieglin, A. Scarabosio, W. Fundamenski, R. J. Goldston and A. Herrmann. *Inter-ELM Power Decay Length for JET and ASDEX Upgrade: Measurement and Comparison with Heuristic Drift-Based Model.* Phys. Rev. Lett., vol. 107, page 215001, Nov 2011. (Cited on page 9.)

[Elfimov 2014] A. G. Elfimov, A. I. Smolyakov and R. M. O. Galvão. *Geodesic mode instability driven by the electron current in tokamak plasmas.* Physics Letters A, vol. 378, no. 10, pages 800 – 803, 2014. (Cited on page 68.)

[Eriksson 1993] L.-G. Eriksson, T. Hellsten and U. Willen. *Comparison of time dependent simulations with experiments in ion cyclotron heated plasmas.* Nuclear Fusion, vol. 33, no. 7, page 1037, 1993. (Cited on pages 49 and 52.)

[Eriksson 2013] J. Eriksson, C. Hellesen, E. Andersson Sundén, M. Cecconello, S. Conroy, G. Ericsson, M. Gatu Johnson, S. D. Pinches, S. E. Sharapov, M. Weiszflog and JET EFDA contributors. *Finite Larmor radii effects in fast ion measurements with neutron emission spectrometry.* Plasma Physics and Controlled Fusion, vol. 55, no. 1, page 015008, 2013. (Cited on page 52.)

[Fisher 2012] R. K. Fisher, D. C. Pace, G. J. Kramer, M. A. Van Zeeland, R. Nazikian, W. W. Heidbrink and M. García-Muñoz. *Beam ion losses due to energetic particle*

geodesic acoustic modes. Nuclear Fusion, vol. 52, no. 12, page 123015, 2012. (Cited on page 42.)

[Fried 1961] B. D. Fried and S. D. Conte. The plasma dispersion function. Academic Press, 1961. (Cited on page 68.)

[Fu 2008] G. Y. Fu. *Energetic-Particle-Induced Geodesic Acoustic Mode*. Physical Review Letters, vol. 101, page 185002, Oct 2008. (Cited on pages 30, 42, 45, 65, and 77.)

[Février 2015] O. Février and J.-H. Ahn, private correspondence, 2015. IRFM, CEA. (Cited on page 33.)

[Garbet 2001] X. Garbet. Instabilités, turbulence, et transport dans un plasma magnétisé. Thèse d'Habilitation à Diriger des Recherches, Université de Provence (Aix-Marseille I), 2001. (Cited on page 111.)

[Gassner 2012] T. Gassner, K. Schoepf, S. E. Sharapov, V. G. Kiptily, S. D. Pinches, C. Hellesen, J. Eriksson and JET-EFDA contributors. *Deuterium beam acceleration with 3rd harmonic ion cyclotron resonance heating in Joint European Torus: Sawtooth stabilization and Alfvén eigenmodes*. Physics of Plasmas (1994-present), vol. 19, no. 3, 2012. (Cited on pages 47, 50, 56, 59, and 64.)

[Gatu Johnson 2008] M. Gatu Johnson, L. Giacomelli, A. Hjalmarsson, J. Källne, M. Weiszflog, E. Andersson Sundén, S. Conroy, G. Ericsson, C. Hellesen, E. Ronchi, H. Sjöstrand, G. Gorini, M. Tardocchi, A. Combo, N. Cruz, J. Sousa and S. Popovichev. *The 2.5-MeV neutron time-of-flight spectrometer TOFOR for experiments at JET*. Nuclear Instruments and Methods in Physics Research Section A: Accelerators, Spectrometers, Detectors and Associated Equipment, vol. 591, no. 2, pages 417 – 430, 2008. (Cited on page 52.)

[Girardo 2014] J.-B. Girardo, D. Zarzoso, R. Dumont, X. Garbet, Y. Sarazin and S. Sharapov. *Relation between energetic and standard geodesic acoustic modes*. Physics of Plasmas (1994-present), vol. 21, no. 9, 2014. (Cited on page 65.)

[Girardo 2015] J.-B. Girardo, S. Sharapov, R. Dumont, J. Eriksson, M. Fitzgerald, X. Garbet, N. Hawkes, V. Kiptily, M. Mantsinen, Y. Sarazin, M. Schneider and JET Contributors. *Stabilization of Sawteeth with 3rd Harmonic Deuterium ICRF-Accelerated Beam in JET Plasmas*. Submitted to Physics of Plasmas (1994-present), 2015. (Cited on page 47.)

[Glasser 1977] A. H. Glasser. *Ballooning Modes in Axisymmetric Toroidal Plasmas*. Proceedings of the Finite Beta Theory Workshop, Varenna, pages 55 – 65, 1977. (Cited on page 35.)

[Goldston 2012] R. J. Goldston. *Heuristic drift-based model of the power scrape-off width in low-gas-puff H-mode tokamaks.* Nuclear Fusion, vol. 52, no. 1, page 013009, 2012. (Cited on page 9.)

[Gorelenkov 2014] N. N. Gorelenkov, S.D. Pinches and K. Toi. *Energetic particle physics in fusion research in preparation for burning plasma experiments.* Nuclear Fusion, vol. 54, no. 12, page 125001, 2014. (Cited on page 28.)

[Grandgirard 2008] V. Grandgirard, Y. Sarazin, X. Garbet, G. Dif-Pradalier, Ph. Ghendrih, N. Crouseilles, G. Latu, E. Sonnendrücker, N. Besse and P. Bertrand. *Computing ITG turbulence with a full-f semi-Lagrangian code.* Communications in Nonlinear Science and Numerical Simulation, vol. 13, no. 1, pages 81 – 87, 2008. Vlasovia 2006: The Second International Workshop on the Theory and Applications of the Vlasov Equation. (Cited on pages 40, 42, 43, and 83.)

[Graves 2005] J. P. Graves. *Internal kink mode stabilization and the properties of auxiliary heated ions.* Physics of Plasmas (1994-present), vol. 12, no. 9, 2005. (Cited on page 29.)

[Graves 2011] J. P. Graves, I. T. Chapman, S. Coda, T. Johnson, M. Lennholm, J. I. Paley, O. Sauter and JET-EFDA Contributors. *Recent Advances in Sawtooth Control.* Fusion Science and Technology, vol. 59, no. 3, pages 539 – 548, 2011. (Cited on page 49.)

[Graves 2012] J. P. Graves, I. T. Chapman, S. Coda, M. Lennholm, M. Albergante and M. Jucker. *Control of magnetohydrodynamic stability by phase space engineering of energetic ions in tokamak plasmas.* Nature Communications, vol. 3, page 624, 2012. (Cited on pages 32 and 64.)

[Guzdar 2008] P. N. Guzdar, N. Chakrabarti, R. Singh and P. K. Kaw. *Excitation of geodesic acoustic modes by ion temperature gradient modes.* Plasma Physics and Controlled Fusion, vol. 50, no. 2, page 025006, 2008. (Cited on page 41.)

[Hager 2012] R. Hager and K. Hallatschek. *Nonlinear Dispersion Relation of Geodesic Acoustic Modes.* Phys. Rev. Lett., vol. 108, page 035004, Jan 2012. (Cited on page 41.)

[Hahm 1995] T. S. Hahm and K. H. Burrell. *Flow shear induced fluctuation suppression in finite aspect ratio shaped tokamak plasma.* Physics of Plasmas (1994-present), vol. 2, no. 5, pages 1648–1651, 1995. (Cited on page 38.)

[Hahm 1999] T. S. Hahm, M. A. Beer, Z. Lin, G. W. Hammett, W. W. Lee and W. M. Tang. *Shearing rate of time-dependent $E\times B$ flow.* Physics of Plasmas (1994-present), vol. 6, no. 3, pages 922–926, 1999. (Cited on page 38.)

[Hallatschek 2001] K. Hallatschek and D. Biskamp. *Transport Control by Coherent Zonal Flows in the Core/Edge Transitional Regime.* Physical Review Letters, vol. 86, pages 1223–1226, Feb 2001. (Cited on pages 2, 30, 40, 83, 103, and 106.)

[Hasegawa 1979] A. Hasegawa, C. G. Maclennan and Y. Kodama. *Nonlinear behavior and turbulence spectra of drift waves and Rossby waves.* Physics of Fluids (1958-1988), vol. 22, no. 11, pages 2122–2129, 1979. (Cited on page 39.)

[Hazeltine 1990] R. D. Hazeltine and W. A. Newcomb. *Inversion of the ballooning transformation.* Physics of Fluids B: Plasma Physics (1989-1993), vol. 2, no. 1, pages 7–10, 1990. (Cited on page 35.)

[Hazeltine 2003] R. D. Hazeltine and J. D. Meiss. Plasma confinement. Dover Publications, 2003. (Cited on page 3.)

[Hellesen 2010a] C. Hellesen, M. Gatu Johnson, E. Anderson Sundén, S. Conroy, G. Ericsson, E Ronchi, H. Sjöstrand, M. Weiszflog, G. Gorini, M. Tardocchi, T. Johnson, V. G. Kiptily, S. D. Pinches, S. E. Sharapov and JET-EFDA Contributors. *Neutron emission generated by fast deuterons accelerated with ion cyclotron heating at JET.* Nuclear Fusion, vol. 50, no. 2, page 022001, 2010. (Cited on page 52.)

[Hellesen 2010b] C. Hellesen, M. Gatu Johnson, E. Andersson Sundén, S. Conroy, G. Ericsson, J. Eriksson, G. Gorini, T. Johnson, V. G. Kiptily, S. D. Pinches, S. E. Sharapov, H. Sjöstrand, M. Nocente, M. Tardocchi, M. Weiszflog and JET EFDA contributors. *Measurements of fast ions and their interactions with MHD activity using neutron emission spectroscopy.* Nuclear Fusion, vol. 50, no. 8, page 084006, 2010. (Cited on page 52.)

[Hellesen 2013] C. Hellesen, M. Gatu Johnson, E. Andersson Sundén, S. Conroy, G. Ericsson, J. Eriksson, H. Sjöstrand, M. Weiszflog, T. Johnson, G. Gorini, M. Nocente, M. Tardocchi, V. G. Kiptily, S. D. Pinches, S. E. Sharapov and JET EFDA Contributors. *Fast-ion distributions from third harmonic ICRF heating studied with neutron emission spectroscopy.* Nuclear Fusion, vol. 53, no. 11, page 113009, 2013. (Cited on pages 51, 52, and 53.)

[Hellsten 2015] T. Hellsten, T. Johnson, S. Sharapov, V. Kiptily, J. Eriksson, M. Mantsinen, M. Schneider, F. Rimini, M. Tsalas and JET contributors. *RF Heating for Fusion Product Studies.* 21st Topical Conference on Radiofrequency Power in Plasmas, Lake Arrowhead, California, USA, 2015. (Cited on page 49.)

[Horton 1981] W. Horton, D.-I. Choi and W. M. Tang. *Toroidal drift modes driven by ion pressure gradients.* Physics of Fluids (1958-1988), vol. 24, no. 6, pages 1077–1085, 1981. (Cited on page 35.)

[Horton 1988] W. Horton, B. G. Hong and W. M. Tang. *Toroidal electron temperature gradient driven drift modes.* Physics of Fluids (1958-1988), vol. 31, no. 10, pages 2971–2983, 1988. (Cited on page 35.)

[Huysmans 1991] G. T. A. Huysmans, J. P. Goedbloed and W. Kerner. *Isoparametric Bicubic Hermite Elements for Solution of the Grad-Shafranov Equation.* International Journal of Modern Physics C, vol. 02, no. 01, pages 371–376, 1991. (Cited on page 49.)

[ITER 1999] Physics Basis Editors ITER. *Chapter 5: Physics of energetic ions.* Nuclear Fusion, vol. 39, no. 12, page 2471, 1999. (Cited on page 59.)

[Itoh 2005] K. Itoh, K. Hallatschek and S.-I. Itoh. *Excitation of geodesic acoustic mode in toroidal plasmas.* Plasma Physics and Controlled Fusion, vol. 47, no. 3, page 451, 2005. (Cited on page 41.)

[Jakubowski 2002] M. Jakubowski, R. J. Fonck and G. R. McKee. *Observation of Coherent Sheared Turbulence Flows in the DIII-D Tokamak.* Phys. Rev. Lett., vol. 89, page 265003, Dec 2002. (Cited on pages 2, 30, 40, 83, 103, and 106.)

[Johnson 2011] T. Johnson, A. Salmi, G. Steinbrecher, L.-G. Eriksson, T. Hellsten, L. J. Höök, M. Schneider and ITM-TF contributors. *Library for RF Interactions in Orbit Following Codes.* AIP Conference Proceedings, vol. 1406, no. 1, pages 373–376, 2011. (Cited on pages 49 and 52.)

[Jolliet 2007] S. Jolliet, A. Bottino, P. Angelino, R. Hatzky, T. M. Tran, B. F. Mcmillan, O. Sauter, K. Appert, Y. Idomura and L. Villard. *A global collisionless PIC code in magnetic coordinates.* Computer Physics Communications, vol. 177, no. 5, pages 409 – 425, 2007. (Cited on page 72.)

[Kadomtsev 1970] B. B. Kadomtsev and O. P. Pogutse. *Turbulence in Toroidal Systems.* In M. A. Leontovich, editor, Reviews of Plasma Physics, pages 249–400. Consultants Bureau, New York, 1970. (Cited on page 35.)

[Kadomtsev 1975] B. B. Kadomtsev. *Disruptive instability in tokamaks.* Sov. J. Plasma. Phys., vol. 1, page 389, Sept-Oct 1975. (Cited on pages 29 and 32.)

[Kolesnichenko 2013] Ya. I. Kolesnichenko, B. S. Lepiavko and V. V. Lutsenko. *Geodesic acoustic mode in tokamaks: local consideration and eigenvalue analysis.* Plasma Physics and Controlled Fusion, vol. 55, no. 12, page 125007, 2013. (Cited on pages 30 and 42.)

[Kramer 2004] G. J. Kramer, S. E. Sharapov, R. Nazikian, N. N. Gorelenkov and R. V. Budny. *Observation of Odd Toroidal Alfvén Eigenmodes.* Phys. Rev. Lett., vol. 92, page 015001, Jan 2004. (Cited on page 58.)

[Lee 1977] Y. C. Lee and J. W. Van Dam. *Kinetic Theory of Ballooning Instabilities.* Proceedings of the Finite Beta Theory Workshop, Varenna, pages 93 – 101, 1977. (Cited on page 35.)

[Loarte 1999] A. Loarte, S. Bosch, A .Chankin, S. Clement, A. Herrmann, D. Hill, K. Itami, J. Lingertat, B. Lipschultz, K. McCormick, R. Monk, G. D. Porter, M. Shimada and M. Sugihara. *Multi-machine scaling of the divertor peak heat flux and width for L-mode and H-mode discharges.* Journal of Nuclear Materials, vol. 266-269, pages 587 – 592, 1999. (Cited on page 9.)

[Lütjens 2010] H. Lütjens and J.-F. Luciani. *XTOR-2F: A fully implicit Newton-Krylov solver applied to nonlinear 3D extended MHD in tokamaks.* Journal of Computational Physics, vol. 229, no. 21, pages 8130 – 8143, 2010. (Cited on page 33.)

[Malkov 2001] M. A. Malkov, P. H. Diamond and A. Smolyakov. *On the stability of drift wave spectra with respect to zonal flow excitation.* Physics of Plasmas (1994-present), vol. 8, no. 5, pages 1553–1558, 2001. (Cited on page 39.)

[Matthews 2011] G. F. Matthews, M. Beurskens, S. Brezinsek, M. Groth, E. Joffrin, A. Loving, M. Kear, M.-L. Mayoral, R. Neu, P. Prior, V. Riccardo, F. Rimini, M. Rubel, G. Sips, E. Villedieu, P. de Vries, M. L. Watkins and EFDA-JET contributors. *JET ITER-like wall – overview and experimental programme.* Physica Scripta, vol. 2011, no. T145, page 014001, 2011. (Cited on page 48.)

[Mikhailovskii 1997] A. B. Mikhailovskii, G. T. A. Huysmans, W. O. K. Kerner and S. E. Sharapov. *Optimization of Computational MHD Normal-Mode Analysis for Tokamaks.* Plasma Physics Reports, vol. 23, no. 10, page 844, 1997. (Cited on pages 49 and 50.)

[Miki 2007] K. Miki, Y. Kishimoto, N. Miyato and J. Q. Li. *Intermittent Transport Associated with the Geodesic Acoustic Mode near the Critical Gradient Regime.* Phys. Rev. Lett., vol. 99, page 145003, Oct 2007. (Cited on pages 2, 30, and 40.)

[Mirnov 1971] S. V. Mirnov and I. B. Semenov. *The Nature of the Large-Scale Instabilities in the Tokamak.* Soviet Physics Journal of Experimental and Theoretical Physics, vol. 33, no. 6, pages 1134–1137, 1971. (Cited on pages 34 and 43.)

[Miyato 2004] N. Miyato, Y. Kishimoto and J. Li. *Global structure of zonal flow and electromagnetic ion temperature gradient driven turbulence in tokamak plasmas.*

Physics of Plasmas (1994-present), vol. 11, no. 12, pages 5557–5564, 2004. (Cited on pages 2, 30, 40, 41, 83, 103, and 106.)

[Mora 2011] P. Mora and J.-M. Rax. *Fusion thermonucléaire.* Cours donné à l'Ecole Polytechnique, polycopié, 2011. (Cited on pages 3 and 4.)

[Nagashima 2005] Y. Nagashima, K. Hoshino, A. Ejiri, K. Shinohara, Y. Takase, K. Tsuzuki, K. Uehara, H. Kawashima, H. Ogawa, T. Ido, Y. Kusama and Y. Miura. *Observation of Nonlinear Coupling between Small-Poloidal Wave-Number Potential Fluctuations and Turbulent Potential Fluctuations in Ohmically Heated Plasmas in the JFT-2M Tokamak.* Phys. Rev. Lett., vol. 95, page 095002, Aug 2005. (Cited on pages 2, 30, and 40.)

[Nakano 2009] T. Nakano, N. Asakura, H. Kubo, J. Yanagibayashi and Y. Ueda. *Tungsten accumulation in H-mode plasmas of JT-60U.* Nuclear Fusion, vol. 49, no. 11, page 115024, 2009. (Cited on page 32.)

[Nave 2003] M. F. F. Nave, J. Rapp, T. Bolzonella, R. Dux, M. J. Mantsinen, R. Budny, P. Dumortier, M. von Hellermann, S. Jachmich, H. R. Koslowski, G. Maddison, A. Messiaen, P. Monier-Garbet, J. Ongena, M. E. Puiatti, J. Strachan, G. Telesca, B. Unterberg, M. Valisa, P. de Vries and contributors to the JET-EFDA Workprogramme. *Role of sawtooth in avoiding impurity accumulation and maintaining good confinement in JET radiative mantle discharges.* Nuclear Fusion, vol. 43, no. 10, page 1204, 2003. (Cited on page 32.)

[Nazikian 2008] R. Nazikian, G. Y. Fu, M. E. Austin, H. L. Berk, R. V. Budny, N. N. Gorelenkov, W. W. Heidbrink, C. T. Holcomb, G. J. Kramer, G. R. McKee, M. A. Makowski, W. M. Solomon, M. Shafer, E. J. Strait and M. A. Van Zeeland. *Intense Geodesic Acousticlike Modes Driven by Suprathermal Ions in a Tokamak Plasma.* Phys. Rev. Lett., vol. 101, page 185001, Oct 2008. (Cited on pages 42, 44, 45, 73, and 80.)

[Nicolas 2013] T. Nicolas. *Sawtooth driven particle transport in tokamak plasmas.* PhD thesis, 2013. (Cited on pages 30 and 32.)

[NRL 2011] Naval Research Laboratory NRL. Plasma formulary. 2011. (Cited on page 61.)

[Pearlstein 1969] L. D. Pearlstein and H. L. Berk. *Universal Eigenmode in a Strongly Sheared Magnetic Field.* Phys. Rev. Lett., vol. 23, pages 220–222, Aug 1969. (Cited on page 97.)

[Pinches 1998] S. D. Pinches, L. C. Appel, J. Candy, S. E. Sharapov, H. L. Berk, D. Borba, B. N. Breizman, T. C. Hender, K. I. Hopcraft, G. T. A. Huysmans and W. Kerner. *The HAGIS self-consistent nonlinear wave-particle interaction model.* Computer Physics Communications, vol. 111, no. 1-3, pages 133 – 149, 1998. (Cited on page 49.)

[Porcelli 1991] F. Porcelli. *Fast particle stabilisation.* Plasma Physics and Controlled Fusion, vol. 33, no. 13, page 1601, 1991. (Cited on pages 1, 24, 29, 33, 34, 48, 49, 50, 55, 57, and 105.)

[Porcelli 1992] F. Porcelli, R. Stankiewicz, H. L. Berk and Y. Z. Zhang. *Internal kink stabilization by high-energy ions with nonstandard orbits.* Physics of Fluids B: Plasma Physics (1989-1993), vol. 4, no. 10, pages 3017–3023, 1992. (Cited on pages 29 and 57.)

[Porcelli 1996] F. Porcelli, D. Boucher and M. N. Rosenbluth. *Model for the sawtooth period and amplitude.* Plasma Physics and Controlled Fusion, vol. 38, no. 12, page 2163, 1996. (Cited on pages 29 and 33.)

[Pütterich 2010] T. Pütterich, R. Neu, R. Dux, A. D. Whiteford, M. G. O'Mullane, H. P. Summers and the ASDEX Upgrade Team. *Calculation and experimental test of the cooling factor of tungsten.* Nuclear Fusion, vol. 50, no. 2, page 025012, 2010. (Cited on page 32.)

[Qiu 2010] Z. Qiu, F. Zonca and L. Chen. *Nonlocal theory of energetic-particle-induced geodesic acoustic mode.* Plasma Physics and Controlled Fusion, vol. 52, no. 9, page 095003, 2010. (Cited on pages 30, 42, and 45.)

[Ramisch 2003] M. Ramisch, U. Stroth, S. Niedner and B. Scott. *On the detection of Reynolds stress as a driving and damping mechanism of geodesic acoustic modes and zonal flows.* New Journal of Physics, vol. 5, no. 1, page 12, 2003. (Cited on pages 2, 30, 40, 83, 103, and 106.)

[Rax 2005] J.-M. Rax. Physique des plasmas. Dunod, 2005. (Cited on page 3.)

[Rax 2011] J.-M. Rax. Physique des tokamaks. Editions de l'Ecole Polytechnique, 2011. (Cited on pages 3 and 8.)

[Romanelli 1989] F. Romanelli. *Ion temperature-gradient-driven modes and anomalous ion transport in tokamaks.* Physics of Fluids B, vol. 1, no. 5, pages 1018–1025, 1989. (Cited on pages 88 and 89.)

[Romanelli 1990] F. Romanelli and S. Briguglio. *Toroidal semicollisional microinstabilities and anomalous electron and ion transport.* Physics of Fluids B, vol. 2, no. 4, pages 754–763, 1990. (Cited on pages 88 and 89.)

[Saigusa 1998] M. Saigusa, H. Kimura, Y. Kusama, G. J. Kramer, T. Ozeki, S. Moriyama, T. Oikawa, Y. Neyatani and T. Kondoh. *Systematic study of toroidicity-induced Alfvén eigenmodes at low-q discharges in JT-60U.* Plasma Physics and Controlled Fusion, vol. 40, no. 9, page 1647, 1998. (Cited on pages 58, 59, and 64.)

[Sarazin 2002] Y. Sarazin, M. Bécoulet, P. Beyer, X. Garbet, Ph. Ghendrih, T. C. Hender, E. Joffrin, X. Litaudon, P. J. Lomas, G. F. Matthews, V. Parail, G. Saibene and R. Sartori. *Edge issues in ITB plasmas in JET.* Plasma Physics and Controlled Fusion, vol. 44, no. 11, page 2445, 2002. (Cited on pages 61, 62, and 64.)

[Sarazin 2006] Y. Sarazin, V. Grandgirard, G. Dif-Pradalier, E. Fleurence, X. Garbet, Ph. Ghendrih, P. Bertrand, N. Besse, N. Crouseilles, E. Sonnendrücker, G. Latu and E. Violard. *Impact of large scale flows on turbulent transport.* Plasma Physics and Controlled Fusion, vol. 48, no. 12B, page B179, 2006. (Cited on pages 40, 42, 43, and 83.)

[Sarazin 2009] Y. Sarazin. *Toroidal ITG: linear study.* Private notes, 2009. (Cited on page 111.)

[Sarazin 2010] Y. Sarazin, V. Grandgirard, J. Abiteboul, S. Allfrey, X. Garbet, Ph. Ghendrih, G. Latu, A. Strugarek and G. Dif-Pradalier. *Large scale dynamics in flux driven gyrokinetic turbulence.* Nuclear Fusion, vol. 50, no. 5, page 054004, 2010. (Cited on pages 40, 42, 43, and 83.)

[Sasaki 2012] M. Sasaki, K. Itoh, S.-I. Itoh and N. Kasuya. *Zonal flows induced by symmetry breaking with existence of geodesic acoustic modes.* Nuclear Fusion, vol. 52, no. 2, page 023009, 2012. (Cited on pages 2, 30, and 40.)

[Schneider 2005] M. Schneider, L.-G. Eriksson, V. Basiuk and F. Imbeaux. *On alpha particle effects in tokamaks with a current hole.* Plasma Physics and Controlled Fusion, vol. 47, no. 12, page 2087, 2005. (Cited on pages 49, 51, and 52.)

[Schneider 2011] M. Schneider, L.-G. Eriksson, I. Jenkins, J. F. Artaud, V. Basiuk, F. Imbeaux, T. Oikawa, JET-EFDA contributors and ITM-TF contributors. *Simulation of the neutral beam deposition within integrated tokamak modelling frameworks.* Nuclear Fusion, vol. 51, no. 6, page 063019, 2011. (Cited on pages 49, 51, and 52.)

[Smolyakov 2010] A.I. Smolyakov, C. Nguyen and X. Garbet. *Electromagnetic effects on geodesic acoustic and beta-induced Alfvén eigenmodes.* Nuclear Fusion, vol. 50, no. 5, page 054002, 2010. (Cited on page 45.)

[Stix 1975] T. H. Stix. *Fast-wave heating of a two-component plasma.* Nuclear Fusion, vol. 15, no. 5, page 737, 1975. (Cited on pages 51 and 53.)

[Storelli 2014] A. Storelli, private correspondence, 2014. LPP Ecole Polytechnique/IRFM, CEA. (Cited on page 40.)

[Sugama 2006] H. Sugama and T.-H. Watanabe. *Collisionless damping of geodesic acoustic modes.* Journal of Plasma Physics, vol. 72, pages 825–828, 12 2006. (Cited on page 77.)

[Sugama 2008] H. Sugama and T.-H. Watanabe. *Erratum: Collisionless damping of geodesic acoustic modes.* Journal of Plasma Physics, vol. 74, pages 139–140, 2 2008. (Cited on page 77.)

[Tagger 1977] M. Tagger, G. Laval and R. Pellat. *Trapped ion mode driven by ion magnetic drift resonance in a fat torus.* Nuclear Fusion, vol. 17, no. 1, page 109, 1977. (Cited on page 35.)

[Tang 1977] W. M. Tang, J. C. Adam and David W. Ross. *Residual trapped-ion instabilities in tokamaks.* Physics of Fluids (1958-1988), vol. 20, no. 3, pages 430–435, 1977. (Cited on page 35.)

[Waelbroeck 1989] F. L. Waelbroeck. *Current sheets and nonlinear growth of the m=1 kink-tearing mode.* Physics of Fluids B: Plasma Physics (1989-1993), vol. 1, no. 12, pages 2372–2380, 1989. (Cited on pages 29 and 32.)

[Wahlberg 2009] C. Wahlberg. *Low-frequency magnetohydrodynamics and geodesic acoustic modes in toroidally rotating tokamak plasmas.* Plasma Physics and Controlled Fusion, vol. 51, no. 8, page 085006, 2009. (Cited on page 45.)

[Waltz 1994] R. E. Waltz, G. D. Kerbel and J. Milovich. *Toroidal gyro-Landau fluid model turbulence simulations in a nonlinear ballooning mode representation with radial modes.* Physics of Plasmas (1994-present), vol. 1, no. 7, pages 2229–2244, 1994. (Cited on page 38.)

[Waltz 2008] R. E. Waltz and C. Holland. *Numerical experiments on the drift wave-zonal flow paradigm for nonlinear saturation.* Physics of Plasmas (1994-present), vol. 15, no. 12, 2008. (Cited on pages 2, 41, 83, 103, and 106.)

[Wesson 2011] J. Wesson. Tokamaks. Oxford University Press, 4th edition, 2011. (Cited on pages 3, 4, and 6.)

[White 1988] R. B. White, P. H. Rutherford, P. Colestock and M. N. Bussac. *Sawtooth Stabilization by Energetic Trapped Particles.* Phys. Rev. Lett., vol. 60, pages 2038–2041, May 1988. (Cited on page 29.)

[White 1989] R. B. White, M. N. Bussac and F. Romanelli. *High-β, Sawtooth-Free Tokamak Operation Using Energetic Trapped Particles.* Phys. Rev. Lett., vol. 62, pages 539–542, Jan 1989. (Cited on page 29.)

[Winsor 1968] N. Winsor, J. L. Johnson and J. M. Dawson. *Geodesic Acoustic Waves in Hydromagnetic Systems.* Physics of Fluids (1958-1988), vol. 11, no. 11, pages 2448–2450, 1968. (Cited on pages 2, 30, and 40.)

[Xu 2012] M. Xu, G. R. Tynan, P. H. Diamond, P. Manz, C. Holland, N. Fedorczak, S. Chakraborty Thakur, J. H. Yu, K. J. Zhao, J. Q. Dong, J. Cheng, W. Y. Hong, L. W. Yan, Q. W. Yang, X. M. Song, Y. Huang, L. Z. Cai, W. L. Zhong, Z. B. Shi, X. T. Ding, X. R. Duan and Y. Liu. *Frequency-Resolved Nonlinear Turbulent Energy Transfer into Zonal Flows in Strongly Heated L-Mode Plasmas in the HL-2A Tokamak.* Phys. Rev. Lett., vol. 108, page 245001, Jun 2012. (Cited on pages 2, 30, 40, 83, 103, and 106.)

[Zabiego 1994] M. Zabiego, X. Garbet, A. Becoulet, F. Nguyen and B. Saoutic. *Sawtooth stabilization with on-axis ICRH on Tore Supra.* Nuclear Fusion, vol. 34, no. 11, page 1489, 1994. (Cited on page 29.)

[Zakharov 1993] L. Zakharov, B. Rogers and S. Migliuolo. *The theory of the early nonlinear stage of m=1 reconnection in tokamaks.* Physics of Fluids B: Plasma Physics (1989-1993), vol. 5, no. 7, pages 2498–2505, 1993. (Cited on pages 29 and 32.)

[Zarzoso 2012a] D. Zarzoso. *Kinetic description of the interaction between energetic particles and waves in fusion plasmas.* PhD thesis, 2012. (Cited on page 38.)

[Zarzoso 2012b] D. Zarzoso, X. Garbet, Y. Sarazin, R. Dumont and V. Grandgirard. *Fully kinetic description of the linear excitation and nonlinear saturation of fast-ion-driven geodesic acoustic mode instability.* Physics of Plasmas (1994-present), vol. 19, no. 2, 2012. (Cited on pages 30, 42, 73, 75, 77, 78, 80, 83, 107, and 150.)

[Zarzoso 2013] D. Zarzoso, Y. Sarazin, X. Garbet, R. Dumont, A. Strugarek, J. Abiteboul, T. Cartier-Michaud, G. Dif-Pradalier, Ph. Ghendrih, V. Grandgirard, G. Latu, C. Passeron and O. Thomine. *Impact of Energetic-Particle-Driven Geodesic Acoustic Modes on Turbulence.* Phys. Rev. Lett., vol. 110, page 125002, Mar 2013. (Cited on pages 2, 42, 83, 85, 86, 102, 103, 106, and 107.)

[Zarzoso 2014] D. Zarzoso, A. Biancalani, A. Bottino, Ph. Lauber, E. Poli, J.-B. Girardo, X. Garbet and R. J. Dumont. *Analytic dispersion relation of energetic particle driven geodesic acoustic modes and simulations with NEMORB.* Nuclear Fusion, vol. 54, no. 10, page 103006, 2014. (Cited on pages 72, 78, and 80.)

[Zhang 2010] H. S. Zhang and Z. Lin. *Trapped electron damping of geodesic acoustic mode*. Physics of Plasmas (1994-present), vol. 17, no. 7, 2010. (Cited on page 80.)

[Zonca 2008] F. Zonca and L. Chen. *Radial structures and nonlinear excitation of geodesic acoustic modes*. EPL (Europhysics Letters), vol. 83, no. 3, page 35001, 2008. (Cited on pages 41, 45, 68, 76, 78, 86, and 87.)